This electronic thesis or dissertation has been downloaded from the King's Research Portal at https://kclpure.kcl.ac.uk/portal/

KING'S College LONDON

Characterisation and Representation of Arrhythmia Substrates

Williams, Steven Edwin

Awarding institution:
King's College London

The copyright of this thesis rests with the author and no quotation from it or information derived from it may be published without proper acknowledgement.

END USER LICENCE AGREEMENT

Unless another licence is stated on the immediately following page this work is licensed

under a Creative Commons Attribution-NonCommercial-NoDerivatives 4.0 International

licence. https://creativecommons.org/licenses/by-nc-nd/4.0/

You are free to copy, distribute and transmit the work

Under the following conditions:

- Attribution: You must attribute the work in the manner specified by the author (but not in any way that suggests that they endorse you or your use of the work).
- Non Commercial: You may not use this work for commercial purposes.
- No Derivative Works - You may not alter, transform, or build upon this work.

Any of these conditions can be waived if you receive permission from the author. Your fair dealings and other rights are in no way affected by the above.

Take down policy

If you believe that this document breaches copyright please contact librarypure@kcl.ac.uk providing details, and we will remove access to the work immediately and investigate your claim.

Download date: 05. May. 2023

Characterisation and Representation of Arrhythmia Substrates

Dr. Steven Edwin Williams

BSc MBChB MRCP

A dissertation submitted for the degree of

Doctor of Philosophy

Division of Imaging Sciences and Biomedical Engineering
School of Medicine
King's College London
University of London

Table of Contents

Abstract

Cardiac arrhythmias arise from a variety of structural and electrical substrates and range in clinical presentation from asymptomatic to severely disabling or life threatening. Existing techniques for the characterisation of arrhythmia substrates include surface electrocardiography and intracardiac mapping together with ultrasound, computed tomography and magnetic resonance imaging. In this thesis I study a spectrum of arrhythmia characterisation techniques to improve the understanding of complex arrhythmia mechanisms. The role of surface electrocardiography and intra-cardiac contact mapping together with cardiac magnetic resonance imaging are studied in a variety of atrial and ventricular arrhythmias as well as in an animal model of atrial ablation. Arrhythmia characterisation techniques result in large quantities of data that are frequently considered in combination with other modalities and visualised within the 3-dimensional nature of cardiac structures. Since no techniques are currently available to display multiple parameters without loss of fidelity of either parameter, I developed a new system for data representation. Termed Dot Mapping, this system allows two or more datasets to be concurrently displayed by using separate visual entities (colour and dots) for each. The function, development and feasibility of the system are studied. In summary, this thesis explores and develops a number of techniques for assessing arrhythmia substrates, including surface electrocardiography, intra-cardiac mapping and cardiac magnetic resonance imaging. New (and existing) data thus created are displayed using a new data representation technique designed to optimise the co-display of multiple related modalities.

Table of Figures

List of Tables

Abbreviations

AAD	Antiarrhythmic drug
ADC	Analogue to digital convertor
AF	Atrial fibrillation
AI	Ablation index
ANOVA	One-way analysis of variance
AP	Action potential
APD	Action potential duration
ARP	Absolute refractory period
AT	Atrial tachycardia
ATP	Adenosine triphosphate
b-SSFP	Balanced steady state free precession
CAD-VF	Coronary artery disease-related ventricular fibrillation
CF	Contact force
CMR	Cardiovascular magnetic resonance
CS	Coronary sinus
CSp	Coronary sinus pacing
CT	Computer tomography
CTI	Cavotricuspid isthmus
DAD	Delayed afterdepolarisations
DC	Direct current
DE-MRI	Delayed enhancement magnetic resonance imaging
EAD	Early afterdepolarisations
EAM	Electroanatomic mapping
ECG	Electrocardiography
ECGI	Electrocardiographic imaging
ED	Electrogram duration
ER	Early repolarisation
ERP	Effective refractory period
EV	Electrogram voltage

FB	Fibrosis burden
FRP	Functional refractory period
Hb	Haemoglobin
HF	High force
HRA	High right atrium
HRAp	High right atrial pacing
ID-VF	Idiopathic ventricular fibrillation
IIR	Image intensity ratio
IR	Inversion recovery time
IVC	Inferior vena cava
JPE	J-point elevation
LA	Left atrium
LAA	Left atrial appendage
LASP	Left atrial sphericity
LAT	Local activation time
LF	Low force
LGE	Late gadolinium enhancement
LV	Left ventricle
LVEF	Left ventricular ejection fraction
LVOT	Left ventricular outflow tract
MIP	Maximum intensity projection
MRI	Magnetic resonance imaging
NHS	National Health Service
PAF	Paroxysmal atrial fibrillation
PEFA	Paced electrogram fractionation analysis
PMVT	Polymorphic ventricular tachycardia
PPI	Post-pacing interval
PRR	Post-repolarisation refractoriness
PsAF	Persistent atrial fibrillation
PV	Pulmonary vein
PVC	Premature ventricular complex

RA	Right atrium
RF	Radiofrequency
RRP	Relative refractory period
RV	Right ventricle
RVOT	Right ventricular outflow tract
SD	Standard deviation
SR	Sinus rhythm
SVC	Superior vena cava
T2W	T2-weighted
TCL	Tachycardia cycle length
TE	Echo time
TFE	Turbo field echo
TR	Repetition time
VF	Ventricular fibrillation
VT	Ventricular tachycardia
WCT	Wilson's central terminal

Thesis Outline

Cardiac arrhythmias arise from a variety of structural and electrical substrates and range in clinical presentation from asymptomatic to severely disabling or life threatening. Existing techniques for the characterisation of arrhythmia substrates include surface electrocardiography and intracardiac mapping together with ultrasound, computed tomography and magnetic resonance imaging. In this thesis I study a spectrum of arrhythmia characterisation techniques to improve understanding of complex arrhythmia mechanisms before developing a new technique for the representation (display) of these arrhythmia substrates.

The role of surface electrocardiography in risk-stratifying the early repolarization phenotype is covered first (Chapter 2). Although sudden cardiac death arising from idiopathic ventricular fibrillation has been associated with early repolarization, the finding of early repolarization on the ECG of an otherwise-well individual is of uncertain significance. The early repolarization phenotype is itself similar to the ECG appearances of hypothermia. Therefore I studied whether therapeutic hypothermia could augment the ECG appearances substantially differentially in a group of idiopathic ventricular fibrillation survivors compared to a control group consisting of coronary artery disease-related ventricular fibrillation survivors.

Chapters 3 and 4 focus on the role of intra-cardiac mapping in characterising atrial arrhythmia substrates. Local activation mapping is performed by recording the timing of a local electrogram compared to a fixed (usually intracardiac) reference electrogram. The use of local activation time mapping in atrial tachycardias allows arrhythmia mechanism diagnosis and appropriate targeting of ablation therapy, but the optimal mapping density for local activation mapping is not currently known. In Chapter 3 this optimal sampling density is explored, using both simulated and clinical data. The impacts of chamber geometry complexity and activation pattern complexity on the optimal sampling density are characterised.

Intra-cardiac mapping has also been used to characterise local electrical properties in various arrhythmia states, frequently in order to guide ablation. However, to date, procedural success rates in paroxysmal atrial fibrillation have been variable. I hypothesised that varying degrees of electrical remodelling may therefore be demonstrable within a clinically homogeneous population of paroxysmal atrial

fibrillation patients. Chapter 4 develops techniques to characterise regional atrial electrophysiology whilst using supporting evidence from simulation experiments to provide a detailed characterisation of these patients.

In addition to electrical remodelling, structural remodelling has also been identified in atrial fibrillation, and in Chapter 5 the comparison between cardiac magnetic resonance and local electrophysiology is made. Together these modalities provide a tool for characterising the atrial fibrillation substrate which could in the future be used to guide treatment strategies.

In the final chapter of this section (Chapter 6), several arrhythmia characterisation modalities are combined to assess ablation lesion formation in a porcine model. The creation of effective ablation lesions is crucial to the success of ablation procedures, but ineffective ablation lesions can also themselves become arrhythmogenic by for example altering local conductivities and providing substrate for re-entry. This chapter uses intracardiac mapping, imaging and histological assessment to examine the impact of catheter-myocardium contact force on the creation of linear ablation lesions.

Finally, arrhythmia characterisation techniques result in large quantities of data that are frequently considered in combination with other modalities and visualised within the 3-dimensional nature of cardiac structures. Since no techniques are currently available to display multiple parameters without loss of fidelity of either parameter, Chapter 7 develops a new system for data representation. Termed Dot Mapping, this system allows two or more datasets to be concurrently displayed by using separate visual entities (colour and dots) for each. The function, development and feasibility of the system are studied.

In summary, this thesis explores and develops a number of techniques for assessing arrhythmia substrates, including surface electrocardiography, intra-cardiac mapping and cardiac magnetic resonance imaging. New (and existing) data thus created are displayed using a new data representation technique designed to optimise the co-display of multiple related modalities.

SECTION ONE: BACKGROUND AND LITERATURE REVIEW

1 Background

In this section I will firstly outline the electrophysiological basis of arrhythmias before describing the key techniques used for *in vivo* arrhythmia characterisation. I will then highlight some of the clinical contexts in which these techniques are applied and in doing so identify the first aims of this thesis. Finally, I will review the technologies used for clinical representation of arrhythmia substrates, identifying scope for further work. Aims are therefore split into two categories: arrhythmia characterisation (prefixed 'C') and arrhythmia representation (prefixed 'R').

1.1 Cardiac Electrophysiology

Molecular Basis of Cardiac Electrophysiology

Ionic Equilibrium and Transmembrane Potential

The lipid bilayer forming the cardiomyocyte cell membrane is impermeable to water-soluble ions. Ion channels spanning the cell membrane allow for the passive movement of ions, driven by electrostatic and chemical gradients. These gradients may oppose each other, such that there exists a point where the forces are exactly opposite. In this situation there is no net movement of the ion across the cell membrane and the ion is said to be in equilibrium. Due to the existence of a chemical gradient in addition to an electrical gradient, at ionic equilibrium there will be a net accumulation of charge on one side of the membrane. This equilibrium potential for a specific ion is termed the Nernst potential (E_{ion}). The transmembrane potential (E_m) at ionic equilibrium is found by calculating a weighted average of the E_{ion} of all the ions for which the membrane is permeable. The weighting for a particular ion is calculated as the ratio of the conductance of the membrane for that ion to the total membrane conductance.

In addition to passive movement, cardiomyocytes maintain an excess of negative ions inside the cell membrane, resulting in polarisation of the cell membrane and a negative transmembrane potential (E_m). The cell membrane demonstrates both a capacitance and a resistance. The small transmembrane potential results in accumulation of oppositely charged ions on the intracellular and extracellular aspects of the cell membrane, and since the membrane is thin, the resulting electrical potential gradient is extremely high. Whilst

this membrane capacitance is fixed, the membrane resistance varies depending on the conductance of membrane ion channels. For a particular ion, membrane conductance is termed g_{ion}. Since conductance is simply the inverse of resistance, and given Ohm's law ($E = I \times R$), then the current generated by a particular ion is given by the following relationship:

$$I_{ion} = g_{ion} \times (E_m - E_{ion}) \qquad \textbf{Equation 1-1}$$

A net inward current (generated by influx of positively charged ions (e.g. Na^+ or Ca^{2+}) or efflux of negatively charged ions (e.g. Cl^-)) results in depolarization of the transmembrane potential whilst an outward current (generated typically by efflux of positively charged K^+ ions) results in hyperpolarisation of the transmembrane potential. The transmembrane potential (E_m) hence depends on membrane conductances for Na^+, K^+, Ca^{2+} and Cl^- ions, which are determined by the activity of specific ion channels, transporters and exchangers.

Cardiac Action Potential

The cardiac action potential is an 'all-or-nothing' response characterised by dramatic changes in membrane conductances and transmembrane potential that is triggered by an abrupt change in E_m usually as a result of an electric current from an adjacent cell. Activation of adjacent cardiomyocytes is triggered by changes in capacitive currents. In contrast to ionic currents (generated by movement of ions across the cell membrane), capacitive currents arise from an accumulation of electrons at the extracellular aspect of the cell membrane as the depolarization wave approaches. The electrons reduce the extracellular positive charge and the intracellular negative charge correspondingly falls. The net effect of these capacitive currents is to increase E_m towards zero. Once the E_m passes a threshold of around -65mV, Na^+ channels in the cell membrane open resulting in a rapid influx of positively charged ions and a cascade of subsequent ion channel events that give rise to the cardiac action potential (see Figure 1-1).

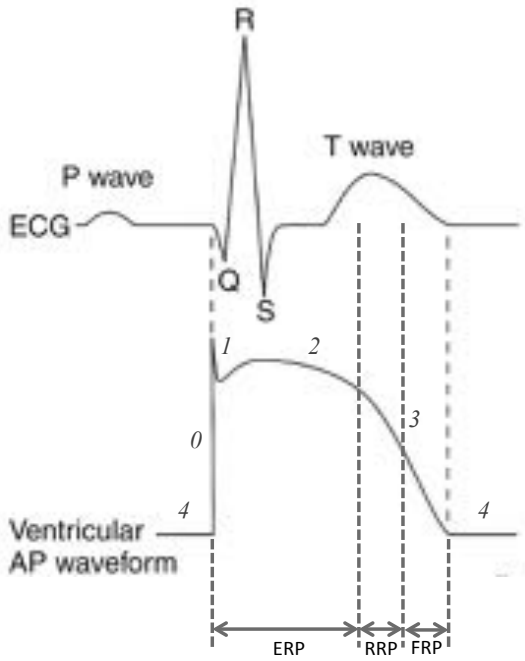

Figure 1-1. Schematic Diagram of Ventricular Action Potential and Surface ECG

The standard surface ECG with P, QRS and T-waves is shown with respect to the underlying ventricular action potential. Phases of the action potential (italic numerals) and refractory periods are shown. ERP, effective refractory period; RRP, relative refractory period; FRP, functional refractory period. Adapted from (1).

The cardiac action potential is divided into five phases, numbered 0-4, and beginning with the resting membrane potential (Phase 4). During Phase 4, resting membrane potential is dependent on passive movement of Na^+, K^+, Ca^{2+} and Cl^- ions. Since the resting membrane is highly permeable to K^+ ions (owing to the presence of the inwardly rectifying K^+ channels (K_{ir})), the resting membrane potential is clamped close to the Nernst potential for K^+, i.e. E_m is close to E_k. The Na^+-K^+ adenosine triphosphatase pump (Na^+-K^+ pump) also contributes to resting E_m, by facilitating the energy-dependent movement of Na^+ and K^+ against their chemical gradients. The net effect of these channels is to maintain the resting transmembrane potential around -85mV. Following initial depolarisation of the cell membrane above the threshold potential, Phase 0 of the action potential is triggered. In atrial and ventricular myocytes as well as His-Purkinje fibres, Phase 0 is characterised by a rapid upstroke dependent on fast inward Na^+ currents, termed the 'fast response action potential'. In contrast, sinus node and atrioventricular node cells have action potentials characterised by a slow upstroke dependent on L-type voltage-gated Ca^{2+} currents. Following the depolarisation phase of the action potential, three repolarisation phases occur: early repolarisation (Phase 1), plateau phase (Phase 2) and rapid repolarisation (Phase 3). Early repolarisation in Phase 1 returns the membrane

potential near to 0mV and is mediated primarily by the transient outward K^+ current (I_{to}) with further contributions from the Na^+-Ca^{2+} exchanger. During the plateau phase (Phase 2), Ca^{2+} ions enter the cell through L-type Ca^{2+} channels (I_{CaL}), but this depolarizing inward current is balanced by repolarizing outward potassium currents (ultra-rapidly (I_{Kur}), rapidly (I_{Kr}) and slowly (I_{Ks}) activating delayed outward rectifying currents). Overall, therefore, there is no net movement of charge during Phase 2. The duration of Phase 2 varies between types of cardiomyocytes, with atrial and His-Purkinje cells characterised by the shortest and longest Phase 2 durations, respectively. Finally, Phase 3 is the final rapid repolarization, restoring E_m back to the resting membrane potential. Time-dependent inactivation of I_{CaL} together with delayed outward rectifying currents (I_{Kr} and I_{Ks}) and inwardly rectifying K^+ currents (I_{K1} and I_{KAch}) are responsible for final repolarization.

Excitability

An action potential is triggered when a charge applied to the cardiomyocyte results in a reduction of the transmembrane potential (E_m) above the threshold value for excitation. The charge required for excitation defines the excitability of the cell. When excitability is reduced, a greater external charge is required to trigger the action potential. During Phase 0, excitability is reduced by increased (i.e. less negative) E_m as more Na^+ channels become progressively inactivated as the E_m rises above -70mV to -50mV (when all the Na^+ channels are inactivated). In contrast, towards the end of Phase 3 of the action potential, sufficient Na^+ channels are available to trigger rapid depolarization, and E_m is relatively close to the threshold potential, resulting in supernormal excitability. A number of states, including Na^+ channel blockade with class I antiarrhythmic drugs and myocardial ischemia reduce cardiomyocyte excitability.

Refractoriness

Refractoriness refers to the period following excitation during which the cardiomyocytes remain unexcitable. Further excitation requires the transmembrane potential to recover toward the resting membrane potential. Refractoriness is thus related to, but generally slightly shorter than, the action potential duration. A phenomenon termed post-repolarisation refractoriness (PRR) is however described whereby myocardial tissue remains non-excitable even after the transmembrane potential has returned to the resting membrane potential. PRR typically occurs in cells depending on the I_{CaL} current for

excitation (over and above I_{Na}) and has been documented in sinoatrial/atrioventricular nodal cells (2, 3), in the post-ischaemic state (4, 5) and in atrial tissue preparations (6). Since the recovery of Ca^{2+} channels from inactivation may continue into phase 4 of the action potential, recovery of excitability in these myocytes may require a time interval that is longer than the action potential duration. Although physiological states promoting PRR have been described, for example hypoxia, acidosis and hyperkalaemia, the underlying cellular mechanisms of PRR are currently debated (7). Regardless of the relative contribution of APD and/or PRR to overall refractoriness, refractoriness itself is a crucial determinant of arrhythmogenesis since it dictates the maximal frequency of activation.

A number of terminologies have been applied to describe refractory periods in terms of cellular activation and the action potential (see Figure 1-1). During Phase 0, 1 and 2 of the action potential, no stimulus regardless of size can elicit a further action potential: this period is termed the absolute refractory period (ARP). The effective refractory period (ERP) refers to the ARP plus the early portion of Phase 3 when non-propagated cellular depolarisation can be triggered. During the ERP, an applied stimulus will not result in propagation of the depolarization wave. The relative refractory period (RRP) refers to a period during Phase 3 when cellular activation may be triggered by a larger-than-normal stimulus. During the RRP, further cellular activation is inhibited but not impossible. A stimulus applied during the RRP will result in a lower amplitude action potential with less rapid Phase 0, and at a tissue scale propagation is also inhibited resulting in a reduction in conduction velocity. ERP, RRP and additionally the functional refractory period (FRP), have also been given clinical definitions as outlined in Table 1-1.

Table 1-1. Refractory Periods

Type	Definition
ERP	The longest coupling interval that fails to be conducted over the structure
RRP	The 'input' interval to a structure at which the 'output' interval just begins to differ from the 'input' interval
FRP	The shortest 'output' coupling interval that can be elicited from a tissue or structure by an 'input' interval.

Conduction

Cardiac excitation relies on the propagation of an action potential from one cardiomyocyte to the next (termed a regenerative action potential). Conduction velocity

refers to the speed of depolarisation across the myocardium and depends on both active and passive cell membrane properties (i.e. ion channel conductances and action potential formation) as well as tissue-scale properties (cellular coupling and geometry). During conduction, adjacent cardiomyocytes exist in a source-sink relationship. Initially, an excited cardiomyocyte acts as a (capacitive) current source for adjacent non-excited cell(s) (sink). Gradually the transmembrane potential of the non-excited cell(s) rises above the threshold potential, at which point an action potential is triggered and the non-excited (sink) cell becomes an excited (source) cell acting as a source for the next non-excited cell. A number of resistances act against current propagation from source to sink, including intracellular resistance (within the cell), intercellular resistance (relating to gap junctions) and extracellular resistance provided by the interstitial fluid. The mathematical relationship between these resistances (i.e. conductances) is well described (see Continuous Propagation Models, p. 44).

Given the dependence of conduction on the generation of a capacitive current, it follows that conduction velocity is dependent on both the action potential amplitude and the rate of change of transmembrane potential (i.e. the steepness of Phase 0 of the action potential). Conduction velocity therefore depends upon the factors influencing I_{Na}, which (as discussed above) include the resting membrane potential E_m at the time of stimulation, the availability of Na^+ channels and the electrochemical gradient of Na^+. These observations explain both the rapid conduction seen in His-Purkinje tissue (with a high concentration of Na^+ channels) and the conduction delay seen in nodal tissue (with a very slow I_{CaL}-dependent Phase 0).

Electrophysiological Mechanisms of Cardiac Arrhythmias

At a cellular level, arrhythmia may occur due to automaticity (spontaneous impulse generation), triggered activity (arising from after-depolarisations) and re-entry (perpetual activation of the origin site by the returning original depolarisation wave). Clinical characterisation of arrhythmia mechanisms depends on the ability to record cardiac activation *in vivo*, but relating clinical arrhythmias to underlying cellular mechanisms is challenging. Automaticity, triggered activity and re-entry are considered further below.

Automaticity

Automaticity is a normal property of cells within the sinus node, atrioventricular node and His-Purkinje system. Arrhythmias may arise from enhanced normal automaticity as

well as abnormal automaticity occurring in atrial or ventricular myocytes. Normal automaticity in pacemaker regions depends at least in part on the action of I_f (the funny current) (8). I_f is an inward current carried in the I_f channel with mixed permeability to both Na^+ and K^+. It activates during repolarisation when E_m falls to -50mV and completely activates at -100mV, leading to a depolarisation that triggers Ca^{2+} influx resulting in triggering of the action potential. Whilst atrial and ventricular myocytes do also have an I_f, the range of activation is significantly more negative than the resting transmembrane potential (e.g. -120 to -170mV), and hence abnormal automaticity occurring in these cells is not I_f-dependent (9). However, automaticity can be seen in these cells when the resting membrane potential is abnormally high (e.g. depolarization to -70 to -30mV vs. -85mV). A variety of candidate mechanisms for abnormal automaticity have been identified including a dependence on the delayed rectifier I_K current and intracellular sarcoplasmic calcium release causing activation of inward Ca^{2+} currents. Clinically, automatic arrhythmias often initiate with acceleration ('warm-up') and terminate after deceleration ('warm-down'). They are susceptible to suppression by overdrive pacing, which is usually followed by gradual re-acceleration of the tachycardia.

Triggered Activity

Triggered activity refers to excitation occurring due to afterdepolarisations consequent to a preceding impulse (10, 11). Afterdepolarisations may occur just before (phase 2), during (phase 3) or after (phase 4) repolarisation. Afterdepolarisations are referred to as early (EAD) when they occur during repolarisation phases 2 or 3 and delayed (DAD) when they occur after repolarisation in phase 4. When an EAD/DAD reaches membrane threshold potential a further action potential is triggered, which may in turn result in a sustained arrhythmia for example by initiating abnormal automaticity, subsequent triggered activity or re-entry (12). Both EADs (13) and DADs (14) have been described in pulmonary venous myocardial sheaths, although their exact relationship to the pathogenesis human atrial fibrillation remains uncertain (15).

EADs are caused by any imbalance in the net repolarising current during phase 2 and phase 3 of the action potential. During phase 2, inward currents carried through incompletely inactivated Na^+ channels (16) and the slow inward Ca^{2+} current (17) are offset by outward currents carried by rapidly activating I_{Kr} and slowly activating I_{Ks} delayed rectifier currents (18). There is a slight net excess of outward currents, which shifts membrane potential gradually in a negative direction, until such time as phase 3

and complete repolarisation occur. Any imbalance of these currents that results in a region of net inward current can prevent repolarisation (19) and potentially lead to an EAD. A number of states may pre-dispose to EAD occurrence including hypoxia, elevated pCO_2 and elevated catecholamines, as well as exposure drugs such as sotalol and procainamide which prolong the repolarisation phase of the action potential (12). There is also a relationship between heart rate and EADs. As heart rate increases, shorter APD is associated with lower amplitude EADs, likely due to augmentation of the delayed rectifier potassium current (20). Similarly, at slower heart rates, prolongation of APD reflects a decrease in the net outward current and an increase in the likelihood of EAD formation and bradycardia-induced arrhythmias (21).

DADs are membrane potential oscillations occurring after completion of repolarization and are caused by alterations of sarcoplasmic calcium handling (22) resulting in increased intracellular calcium concentration. In the presence of elevated [Ca^{2+}] reuptake of Ca^{2+} by the sarcoplasmic reticulum may be incomplete by the end of the action potential and there may be further release of Ca^{2+} from the sarcoplasmic reticulum (23). In turn the increased level of cytoplasmic calcium may lead to altered sarcolemmal conductance and an inward movement of charge carried by sodium ions creating an overall transient inward current causing the DAD (24, 25). The consequences of elevated cytosolic calcium are clearly demonstrated during digitalis toxicity where inhibition of the Na^{+}-K^{+} pump causes elevation of the intracellular sodium concentration which in turn activates the Na^{+}-Ca^{2+} exchange mechanism causing a rise in intracellular calcium and frequent ventricular ectopy (26). Elevated catecholamines have also been associated with DADs in both the atrium (27) and ventricle (28). As for EADs, heart rate is also a key determinant of DADs, although the opposite relationship is seen with more rapid stimulation being associated with higher amplitude DADs that are more likely to reach threshold for triggered activity (29).

Clinically, arrhythmias due to triggered activity show a variable response to overdrive pacing. If pacing is fast enough for a long enough duration, then the rate of triggered activity slows and may stop. However, if the pacing rate is only slightly faster than tachycardia, then it can cause overdrive acceleration of the tachycardia.

Re-entry and the Excitable Gap

In sinus rhythm (and during focal tachycardias), the activation wave expires following complete activation of the myocardium, since the period of excitation is significantly shorter than the refractoriness of the tissue. In contrast, during re-entry the depolarisation wave re-enters tissue that it has previously depolarised at a time when local repolarisation has already occurred. In doing so, repeated depolarisations of the original tissue can occur in a process of self-perpetuation. Re-entry can only occur when certain conditions are met: 1) unidirectional block is required for initiation; and 2) the circuit activation time must be longer than the refractory period of the tissue (30). Unidirectional block can occur if there is anatomical asymmetry of the conduction tissue, or if there is functional asymmetry in excitability (31). The second condition implies that there must be an excitable gap – i.e. that the circuit is long enough such that tissue at the trailing edge of the wave front has time to become excitable before return of the leading edge of the next wave front. The concept of the excitable gap depends on the wavelength of the re-entrant circuit. Wavelength is defined as the product of conduction velocity and effective refractory period and determines the distance travelled by the depolarisation wave relative to the refractory period of the tissue. Hence, increased conduction velocity or refractoriness both increase wavelength, reduce the excitable gap and ultimately require a greater re-entrant path length to support re-entry.

1.2 Arrhythmia Substrate Characterisation Techniques

Surface Electrocardiography

From the beginning of the 19th century a number of key discoveries paved the way for the development of modern surface electrocardiography (ECG), one of the most ubiquitous investigations in modern cardiology. That the beating heart is associated with an electric current was first demonstrated using the 'rheoscopic frog'. In this experiment the cut nerve of a frog's leg connected to the epicardial surface of the ventricle would cause twitching of the frog's leg in time with the heart beat (32). These early findings were later confirmed using the astatic galvanometer (33) and, following the invention of more sensitive galvanometers, transmembrane potentials (i.e. action potentials) were shown to accompany muscular contraction (34). Eventually, in 1887, the first human electrocardiogram was recorded at St Mary's Medical School (35) using the capillary electrometer (see Figure 1-2). This device consisted of a column of mercury within a glass

tube. The technique was subsequently refined allowing identification of atrial and ventricular components of the waveform together with the first measurements of mammalian (canine) atrioventricular delay (later to be termed the *PR* interval) (36).

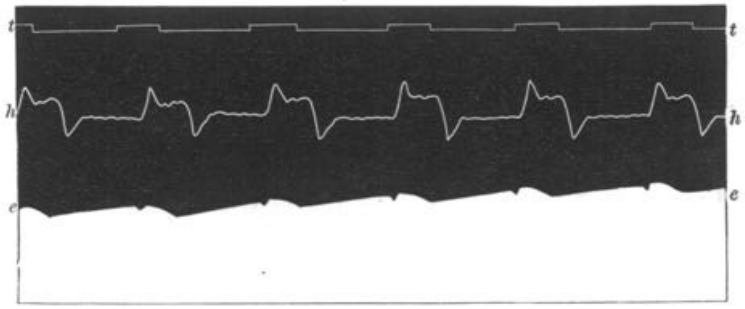

Figure 1-2. First In Man Electrocardiograph

The first electrical recording of the heart was made in 1887 by Waller, a physiologist in London. Line e-e – mercury capillary electrometer, line h-h – heart motion from lever cardiograph. Reproduced (35)

Several innovations in the first half of the 20th century then followed, progressing toward the standard 12-lead ECG still in use today. Use of a refined capillary electrometer allowed demonstration of 5 deflections in the electrocardiogram, and mathematical correction for inertia and friction in the capillary system resulted in the familiar 'PQRST' waveforms (37) (Figure 1-3). Subsequently, the string galvanometer was invented, which was a highly sensitive device not requiring mathematical correction of the acquired waveform (38). The string galvanometer propelled electrocardiography from research to clinical practice, using three leads connected to the left arm, right arm and left leg arranged in bipolar configuration. It was not until 1928 that non-mechanical amplification of the ECG was described, using vacuum tubes rather than the string galvanometer (39).

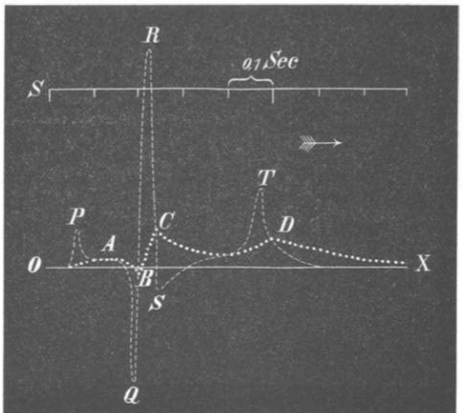

Figure 1-3. Electrocardiogram Recorded by Einthoven

The uncorrected deflections ABCD were converted to the familiar PQRST waveform by a mathematical correction accounting for inertia in the capillary system. Reproduced from (37)

Whilst the early electrocardiogram in the coronal plane was useful for detecting arrhythmias, including atrial fibrillation (delirium cordis, (40)) and myocardial infarction (41), the 3-lead configuration in use resulted in 'silent' areas of the heart (42). This observation led to the invention of the 'central terminal' created by joining the three limb leads together via 5kΩ resistors in order to create a single ground terminal (43). A roving electrode could then be used to record unipolar surface electrograms (termed V) anywhere on the body in reference to the central terminal. Eventually, combined American Heart Association / Cardiac Society of Great Britain guidelines were published recommending the V1-V6 chest lead positions that are still in use today (44).

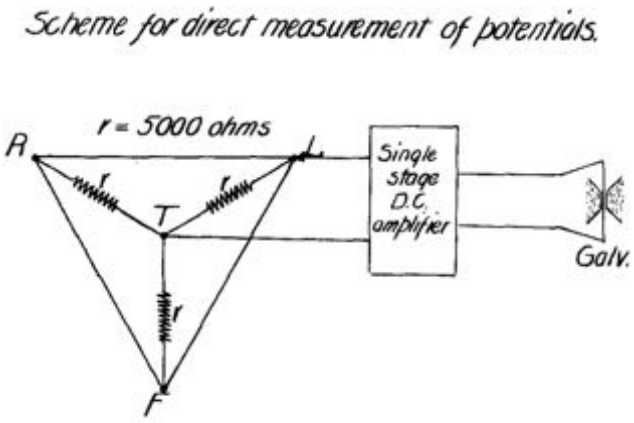

Fig. 1.—Diagram illustrating the method of leading used to record the potential variations of a single electrode. Electrodes on the right arm (*R*), left arm (*L*), and left leg (*F*) are connected through equal resistances of 5,000 ohms to a central terminal (*T*). The central terminal and an exploring electrode, or one of the extremity electrodes as indicated here, are connected to the input terminals of a vacuum-tube amplifier with a balanced plate circuit in which the string galvanometer is inserted.

Figure 1-4. Wilson's Central Terminal

To create a central terminal, or ground, each of the limb leads (right hand, left hand and left foot) is connected together via 5kΩ resistors. Reproduced from (43).

One final innovation in the creation of the 12 lead ECG came with the development of the augmented limb leads. The standard 3-lead ECG provided leads in 60° intervals in the frontal plane. In order to provide a more detailed coverage (e.g. 30°) in the coronal plane, unipolar limb leads (VL, VR, VF) were created (43). Owing to the low amplitude signal found in VL, VR and VF a method was derived to amplify ('augment') their signal, resulting in the now-familiar leads termed a-VL, a-VR and a-VF (45). The eventual configuration of the standard limb leads, augmented limb leads and chest leads, as defined by the American Heart Association (46) is shown in Figure 1-5. Although this system remains in use today, the position of the chest leads does limit the diagnostic yield of the surface ECG. Indeed, adaptations to the standard positions have been suggested in order

to improve this including the addition of a right sided precordial lead in right ventricular infarction (47) and the use of posterior leads (V8 and V9) in posterior ventricular infarction (48). As an extension, ECG systems recording tens or hundreds of leads (termed body surface potential mapping) have been studied in a wide range of cardiac conditions, but are limited by their complexity of both use and interpretation (49).

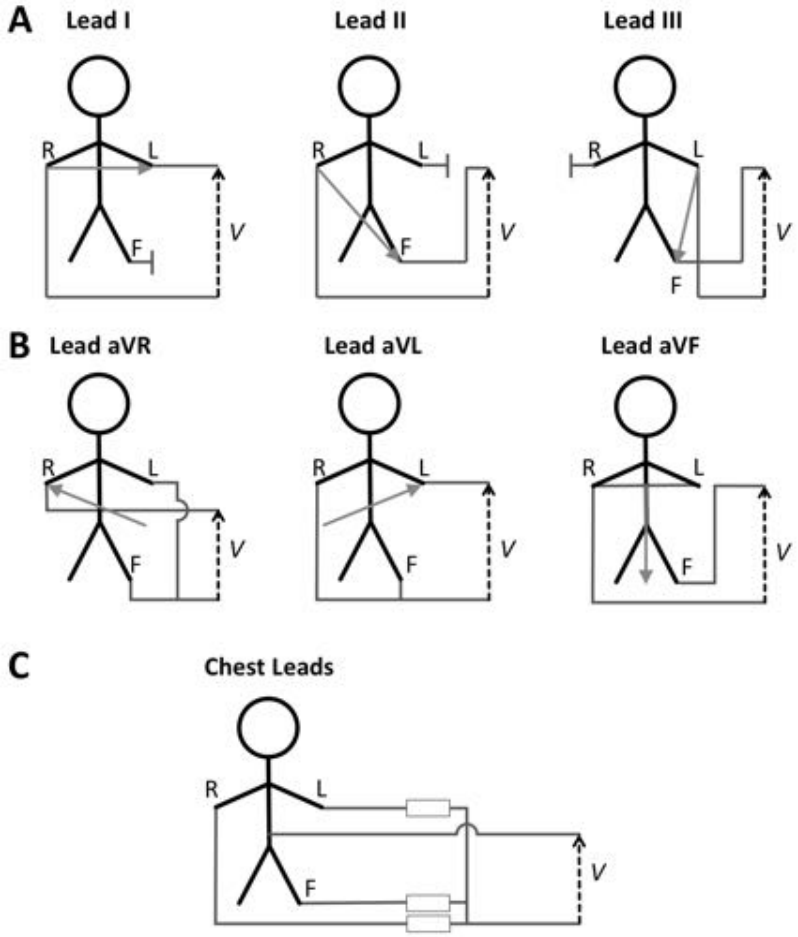

Figure 1-5. Configuration of Standard ECG Leads

A – Standard bipolar limb leads; **B** – Augmented limb leads. **C** – Unipolar chest leads with Wilson's central terminal. Resistors (boxes) are usually 5kΩ.

Whilst the surface ECG can reveal important information about the arrhythmia (e.g. rate, A-V relationship) and is frequently in itself diagnostic, determining the specific underlying mechanism and/or cardiac activation pattern requires more advanced techniques. These include intracardiac contact and non-contact mapping and body surface potential mapping. These techniques are addressed in the following sections.

Intracardiac Contact Mapping

Intracardiac mapping catheters are used to record electrograms from cardiac structures, with the resulting electrograms being compared to other intracardiac and surface recordings. The catheters may be positioned once at the start of the procedure and then remain stationary (e.g. in the case of CS or HRA catheters), or may be roving catheters recording electrograms from multiple sites as required (e.g. in the case of the mapping/ablation catheter). Electrograms may be recorded from intracardiac catheters in unipolar or bipolar configuration (50). In the case of unipolar recordings, the electrogram is recorded as the potential difference between an intra-cardiac electrode and an indifferent reference electrode, for example Wilson's central terminal (WCT). In the case of bipolar recordings, the potential difference is recorded between two closely spaced intracardiac electrodes. Since far-field and signal noise is present on both recording channels in a bipolar recording, bipolar recordings frequently have substantially higher signal-to-noise ratio than unipolar recordings. Nevertheless, identification of local activation time using unipolar recordings is very accurate owing to the close relationship between the steepest negative gradient of the unipolar signal and the onset of phase 0 of the local action potential (51). Furthermore unipolar signals give information about the direction of activation, with positive deflections occurring as the depolarisation wave approaches, and negative deflections occurring as the depolarisation wave travels away from the recording electrode. In contrast, assigning local activation time to bipolar recordings is more error prone, especially in the context of complex fractionated signals, and bipolar recordings give less information about the direction of activation.

Activation Mapping

Since activation mapping is performed during tachycardia, a stable, inducible tachycardia is a prerequisite for activation mapping. Bipolar recordings are generally used for activation mapping due to their improved signal to noise ratio and rejection of far field signal components. A sampling frequency of 1000Hz and a band pass filter of 30-250Hz are typically used for activation mapping of atrial arrhythmias, in order to highlight signal components most representative of local activation (50). Catheter positions are traditionally assessed with fluoroscopy, although electroanatomic mapping systems permit minimisation or even elimination of radiation exposure during mapping (see below). Local activation is taken as the time from the reference electrogram to a fixed characteristic (e.g. electrogram peak or onset) of the electrogram of the most distal bipole

of the mapping catheter. By considering the timing of local electrograms recorded with the mapping catheter to a fixed reference (e.g. atrial appendage electrogram for atrial tachycardias or QRS onset for ventricular tachycardias) it is possible to deduce the mechanism of tachycardia.

Schematic representations of focal and re-entrant tachycardias are shown in Figure 1-6.

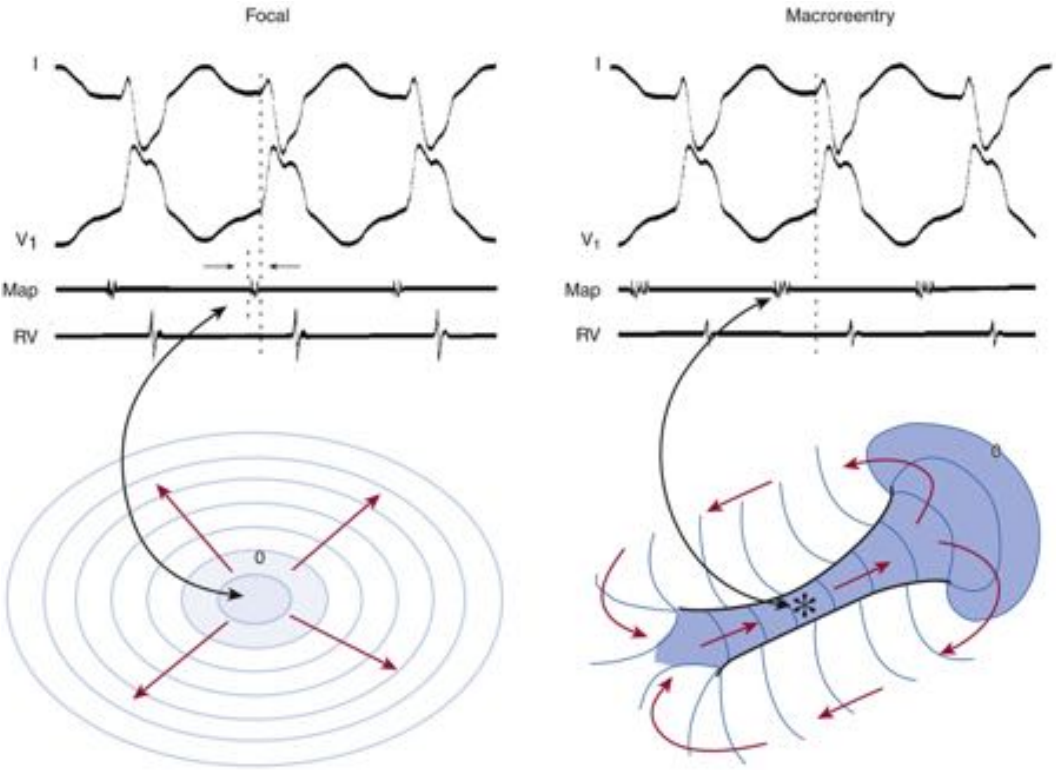

Figure 1-6. Focal vs. Macro-re-entrant Ventricular Tachycardia

Left – schematic representation of a focal tachycardia with corresponding surface ECG, mapping catheter and RV apex electrograms. **Right** – schematic representation of a re-entrant tachycardia with corresponding surface ECG, mapping catheter and RV apex electrograms. Notice the diastolic potential on Map recorded from the critical isthmus. Reproduced from (1).

In the case of a focal tachycardia, the goal is to locate the earliest activity within the chamber of interest. The following general sequence is typically employed. 1) Analysis of the surface ECG provides an initial estimate of the location of the tachycardia. 2) Analysis of activation sequences on a limited number of static intracardiac catheters (e.g. placed at the high right atrium, bundle of His, coronary sinus or right ventricular apex) refines the initial estimate to identify the region of interest. 3) A mapping catheter is manoeuvred into position and used to 'explore' the region of interest, searching for the site of earliest activation. Unipolar signals may then be used to confirm the exact site of

origin of the focal tachycardia, with a 'QS' morphology signifying that activation spreads away centrifugally from the catheter location.

In the case of macro-re-entrant tachycardias, the goal is to locate the critical isthmus of the tachycardia (see Figure 1-6). The critical isthmus is identified as the site with continuous diastolic activity, or with an isolated mid-diastolic potential. Identification of the critical isthmus is challenging due to a number of factors. 'Bystander' pathways (false isthmus) may complicate mapping but have no relevance to the tachycardia mechanism whilst sites of late activation may appear to display diastolic potentials. In order to determine whether an isthmus is true or false it is necessary to identify whether the diastolic potential represents a site required for maintenance of the tachycardia (52). A fixed relationship between the diastolic potential and the subsequent tachycardia beat during cycle length changes (spontaneously or due to pacing) is consistent with, but does not prove, that the diastolic potential represents the location of the critical isthmus. Further manoeuvres (e.g. entrainment, see below) are necessary to finally confirm the correct site has been identified.

Aside from assessing timing of local depolarisation (and therefore the tachycardia mechanism), analysis of the bipolar electrogram morphology can yield valuable information about local activation and/or underlying atrial substrate. Normal activation shows a simple electrogram with single peaks. Double potentials may be seen at any lines of block, including the crista terminalis in the normal atrium (53), due to previous ablation (54) or at sites of previous incisions (55). Fractionated potentials may be seen at sites of localised re-entry, but also at sites of atrial fibrosis or discontinuous conduction.

Entrainment Mapping

Entrainment mapping is a technique used to detect the presence (and circuit) of re-entry (56). During tachycardia, pacing distant to the tachycardia circuit may result in one of three outcomes. 1) The paced beat may reach the tachycardia circuit when the circuit is still refractory and have no effect on the tachycardia. 2) The paced beat may reach the tachycardia circuit early enough in the refractory period that it blocks in the orthodromic direction but still collides antidromically with the last beat of tachycardia, resulting in termination of the tachycardia. 3) The paced beat may reach the tachycardia circuit during the 'excitable gap', propagate in the antegrade direction and collide with the previous tachycardia cycle in the retrograde direction. Where this 'resetting' of the tachycardia

occurs reproducibly the tachycardia is said to be entrained (57). Note should be made that the degree of advancement of the tachycardia depends both on stimulus prematurity and conduction slowing in response to prematurity within the tachycardia circuit. In order to prove the presence of re-entry, four entrainment criteria have been identified (Table 1-2). Recently, a fifth criterion has been proposed that can assist with identification of single or double loop re-entry (58). Demonstration of any one criterion is sufficient to prove the presence of re-entry.

Table 1-2. Criteria for Entrainment

	Criteria for Entrainment
1	During overdrive pacing that fails to interrupt tachycardia, the demonstration of constant fusion beats in the electrocardiogram, except for the last captured beat, which is not fused.
2	During overdrive pacing at two rates that fail to interrupt tachycardia, the demonstration of constant fusion beats of the ECG at each rate, but different degrees of constant fusion at each rate (progressive fusion).
3	During overdrive pacing that interrupts the tachycardia, the demonstration of localized conduction block to a site(s) for 1 beat followed by activation of that site(s) by the next paced beat from a different direction and with a shorter conduction time.
4	During overdrive pacing at two rates that fail to interrupt tachycardia, the demonstration of a change in conduction time to and electrogram morphology at an electrogram recording site.

Criteria 1 and 2 are ECG criteria, whilst criteria 3 and 4 are electrogram criteria. Adapted from (59).

Following cessation of the overdrive pacing train, the post-pacing interval (PPI) can be measured, as the time from the last pacing stimulus to the next non-paced recorded electrogram at the pacing site. In order for PPI measurements to be valid, entrainment of the tachycardia must first be demonstrated. When the pacing site lies on the tachycardia circuit, the time from the final paced stimulus to the return electrogram will be equal to the tachycardia cycle length (TCL). As the pacing site moves progressively farther from the circuit the PPI prolongs, since the final paced stimulus must travel to the circuit, around the circuit and back to the recording site. Hence the PPI is equal to the TCL plus the conduction time from the pacing site to the tachycardia circuit and back to the pacing site. Entrainment mapping is typically used to examine whether candidate regions identified from activation mapping are indeed part of the tachycardia circuit.

Intracardiac Non-contact Mapping

As an alternative to contact mapping, which records single bipolar electrograms or limited numbers of electrograms individually, the ESI non-contact mapping system (St Jude Medical, St Paul, MN) provides a tool to record many thousands of extrapolated electrograms simultaneously. Its major advantage is that it can document activation timing from large regions of a cardiac chamber from a single beat. This can be particularly

useful when the tachycardia may not be sufficiently sustained to allow conventional mapping to be performed. The non-contact mapping system consists of a balloon multi-electrode array with 64 electrodes, a reference electrode located on the shaft of the catheter in the blood pool and a processing station. The multi-electrode array is positioned within the chamber of interest and the balloon inflated such that the 64 electrodes all record far-field signals. Prior to inflation a geometric model of the endocardial surface of the chamber is created (see Anatomical Representation, p.58). Given the known quantities of the shape of the balloon, the shape of the chamber and the potential field across the balloon, the system then computes the potential field across the surface of the chamber (using the Laplace equation). This is an inverse problem solved using the boundary element method. In doing so it becomes possible to estimate the unipolar electrograms found at a large number (e.g. 3000) of sites on the endocardial surface and, just as for contact mapping with unipolar signals, activation time can then be assigned as the steepest negative gradient of the calculated unipolar electrograms. Thus an estimated local activation time map can be created from a single beat, which is particularly useful for non-sustained, or haemodynamically unstable ventricular arrhythmias (60, 61). Non-contact mapping has also been applied in the atrium where simultaneous electrical recordings across the whole chamber can permit the assessment of the spatiotemporal characteristics of AF (62, 63).

Despite these advantages, non-contact mapping does suffer from a number of limitations. Since the calculation of virtual unipolar electrograms depends on the geometrical relationship between the balloon and cardiac chamber, any inaccuracies in the chamber geometry (including changes in volume loading or contraction pattern during tachycardia) can adversely affect the accuracy of the virtual electrograms. Furthermore, increased distance between the balloon and the chamber wall also reduce the accuracy of mapping, limiting the use of non-contact mapping in large chambers. Finally, the presence of the balloon in small chambers (e.g. the left atrium) can hinder manipulation of the mapping catheter around the inflated balloon.

Electrocardiographic Imaging

The solution to the inverse Laplace equation has also been applied to body surface potential mapping using three dimensional cross sectional imaging (usually computed tomography) to determine the geometrical relationship between the body surface and epicardial surface of the heart. Recovery of epicardial potentials from body surface

potentials in this way (the so-called inverse problem of electrophysiology) is an ill-posed problem [1] sensitive to noise and requiring regularization [2] of the solution. Two mathematical processes are involved in the calculation of epicardial potentials. Discretization[3] of Laplace's equation in the volume between body surface and epicardial surface is achieved using the boundary element method allowing the transfer matrix relating epicardial potentials to body surface potentials to be determined. Inverse solutions such as Tikhonov regularization or the generalized minimal residual method are then required to solve the inverse of this problem and compute epicardial potentials from the transfer matrix and body surface potentials (64–66). More recently these techniques have been applied in humans (67, 68) resulting in production of a commercially available system for electrocardiographic imaging (ECGI). The process of combining body surface potential recordings with three-dimensional heart-torso geometry to reconstruct an epicardial electroanatomic map is outlined in Figure 1-7.

ECGI is a promising clinical tool for non-invasive risk stratification, arrhythmia diagnosis, intervention planning and evaluation as well as a research tool for studying mechanisms and properties of arrhythmias. ECGI has been validated in ventricular arrhythmias using comparisons with intra-operative multi-electrode mapping (68) and comparisons with known right ventricular (RV) and left ventricular (LV) pacing sites (69). ECGI has been validated in atrial arrhythmias using comparisons with intracardiac contact mapping (70, 71), and known sites of left atrial (LA) pacing (72). ECGI has also been employed for substrate assessment in atrial fibrillation, including identification of zones of low voltage (73). Atrial activation patterns in AF have been assessed using ECGI, finding most commonly multiple wavelets and focal sources with rotors found more rarely (72). Another study was able to identify rotors in all patients studied with AF (74). Since ECGI has been shown to have a resolution of ~6mm for both ventricular and atrial activation (68, 72), the true ability of ECGI to detect rotor activation in AF (especially in the presence of wave break) remains uncertain.

[1] An 'ill-posed' problem (in the sense of Hadamard (360)) is one in which the solution is not unique, or the solution does not vary continuously with the input data.

[2] 'Regularization' refers to a group of mathematical techniques that impose constraints on input data in order to force uniqueness in the solution (i.e. converting an ill-posed problem to a well-posed problem).

[3] 'Discretization' is the process of transferring a continuous function (e.g. the relationship between body surface and epicardial potentials) into a form suitable for the calculation of numerical solutions.

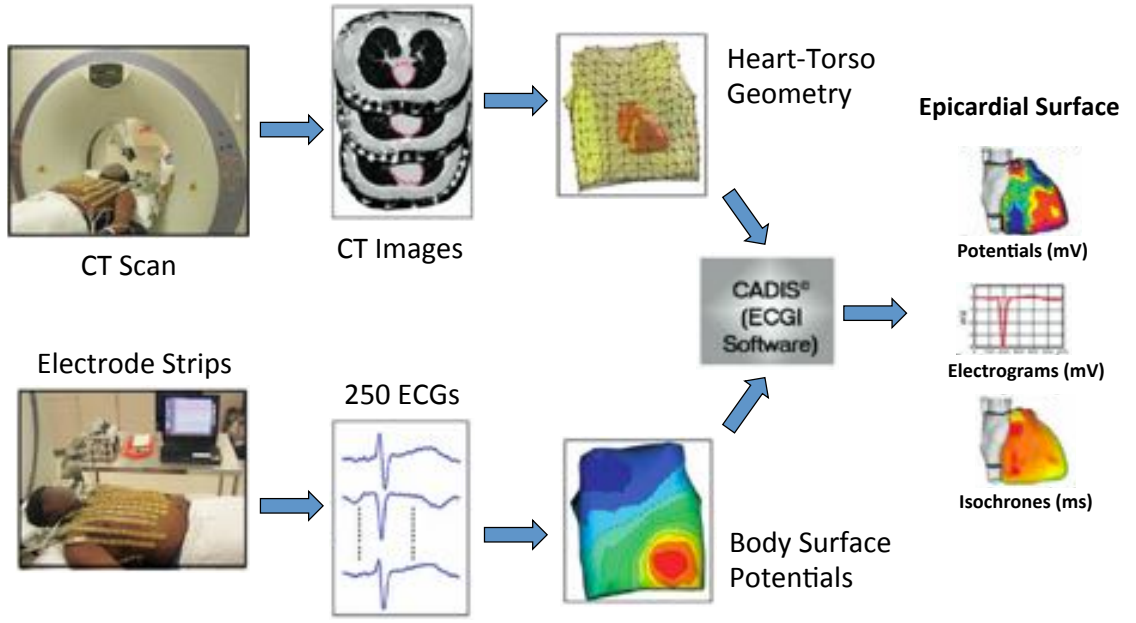

Figure 1-7. Electrocardiographic Imaging

Body surface potentials are recorded using a multi-electrode ECG vest. Cardiac and torso geometries are obtained from transverse CT images. Processing software (see text) solves the inverse problem to calculate epicardial potentials from surface potentials and the heart-torso geometrical relationship. Adapted from (71).

Cardiovascular Magnetic Resonance

Cardiovascular Magnetic Resonance (CMR) is a non-invasive technique that has evolved over the past decade to allow comprehensive assessment of cardiac anatomy and function. Late enhancement CMR with gadolinium-based contrast agents has greatly improved the imaging of ventricular (75) and atrial (76–78) myocardial tissue composition and fibrosis. Such non-invasive identification of physical tissue characteristics offers the possibility of non-invasive characterisation of tissue electrical properties and ultimately arrhythmia mechanisms.

Physical Basis of CMR Tissue Characterisation

T1 and T2 Relaxation Times

In CMR the pixel signal intensity is based on the relaxation of protons in a static magnetic field (typically 1.5 or 3 Tesla) characterized by 2 distinct magnetic resonance relaxation parameters: 1) the T_1 or spin-lattice relaxation time and 2) the T_2 or spin-spin relaxation time. The T_1 relaxation time is the time constant defining the rate of recovery of magnetization along the longitudinal (z) axis following a radiofrequency pulse. The T_2

relaxation time is the time constant defining the loss of magnetization (and therefore signal) in the transverse (*xy*) plane following radiofrequency excitation.

Since the magnetic resonance characteristics of protons depends on their immediate molecular environment the T_1 and T_2 relaxation times vary between tissue types (e.g. fat, myocardium or blood) and also within the same tissue depending on its pathological state (e.g. inflammation, oedema or fibrosis). These inherent differences can be exploited by specific CMR sequences in order to reveal the molecular environment within the tissue and are further enhanced by the use of gadolinium-based contrast agents.

Late Gadolinium Enhanced CMR

Late gadolinium enhanced (LGE) imaging uses a T_1-dependent inversion recovery technique to exploit the significant shortening of T_1 relaxation times by gadolinium contrast agents. The pixel signal intensity is therefore dependent upon the local temporal gadolinium concentration. Gadolinium is a small rare-earth metal element that is prepared as a chelate and injected intravenously from where it can enter the interstitial space in the myocardium. In normal myocardium, the interstitial space is minimal, but it is expanded in certain pathological states (e.g. fibrosis, inflammation, infarction or infiltration) so that sufficient gadolinium to be detected may be present. Furthermore, gadolinium washes out of tissue capillary beds within minutes, but takes 10-30 minutes to wash out from the interstitial space. By imaging within this window using an inversion time where normal myocardium has a net magnetization vector of zero (and therefore appears black or 'nulled') the difference with normal myocardium (from which gadolinium has washed out) can be exploited (79, 80).

<u>Imaging Ventricular Fibrosis with LGE</u>

The first clinical application of myocardial LGE was in acute and chronic myocardial infarction imaging (81–83) with animal studies showing a close correlation between areas of LGE in the ventricle and areas of scar on histology (84). During the chronic phase of infarction, when dense fibrotic scar replaces infarcted myocardium, LGE accurately and reproducibly determines infarct size (85). Subsequently the assessment of myocardial fibrosis by LGE in non-ischaemic cardiomyopathies has been assessed. Different patterns of LGE have been demonstrated according to the underlying aetiology, and LGE CMR now forms an important part of the assessment in new-onset myocardial dysfunction (86–88).

Imaging Atrial Fibrosis with LGE

Atrial wall imaging with LGE poses a greater challenge since the wall of the LA is several times thinner than the left ventricular myocardium and therefore greater spatial resolution is required. Over the past few years, technological developments and novel imaging sequences have made LA LGE CMR possible although with significant remaining limitations. A recent series of studies has suggested that LA LGE both before and after catheter ablation can help predict the chance of recurrence of AF by identifying the extent of pre-existing fibrosis and post-ablation scar (77, 78, 89–91). It is proposed that this may allow a more individualized approach to AF ablation.

Atrial LGE Imaging Protocols

Sequences for LA LGE imaging vary between centres, particularly depending on the MRI scanner manufacturer and the magnetic field strength. In general, they involve a series of planning scans, an anatomical scan for LA and PV segmentation and a 3D inversion recovery (IR) LGE sequence 20-25 minutes following the injection of a gadolinium-based contrast agent. In our institution, scans are performed in a 1.5T Philips Achieva MR scanner (Philips Medical Systems, Best, The Netherlands) using a 32 channel surface coil (Invivo, Orlando, Florida, USA). The 3D LGE sequence is a respiratory-navigated, ECG-triggered IR turbo field echo (TFE) acquisition, with a pixel resolution of 1.3 x 1.3 x 4 mm^3, reconstructed to 2 mm slice thickness (typical repetition time (TR) and TE are 6.2 ms and 3.0 ms respectively). The IR delay time is determined from a Look-Locker sequence to achieve partial suppression of both ventricular myocardium and blood. The scan is acquired in a four-chamber orientation, typically with 30-40 slices to allow for complete coverage of the LA.

3D reconstruction of atrial CMR requires segmentation of the LA and PVs as well as the more challenging segmentation of the LGE information. Such image processing is necessary for the integration of late enhancement data with functional and electrical data but is also met with significant challenges (76, 78, 92). Whilst there is good image contrast between healthy and enhanced myocardium in the ventricle, this is not so for the atrium where the wall is much thinner and image contrast is lower. Additionally atrial LGE is susceptible to image artefacts (motion and partial volume effect) as the wall may only be a few pixels wide. The method used here (adapted from (92)) first involves registration of the 2D information from the LGE scan and the anatomical scan. Automated segmentation of the LA 3D anatomy from the anatomical scan is then performed. A maximum intensity projection (MIP) is used, whereby the maximum signal intensity within ±3mm of the 3D surface is selected as the LGE

signal intensity for that point on the shell. Signal intensities are displayed as a number of standard deviations from the mean intensity of the atrial blood pool, or as a ratio of the atrial wall to atrial blood pool signal intensities.

Predicting Ablation Success with CMR

Ablation for persistent AF is notable for lower initial and repeat success rates and increased recurrence rates (93). Electrical and structural remodelling of the atrium (see above) is one limiting factor in the success of ablation for persistent AF (94). In some hands it has been shown possible to measure the quantity of left atrial fibrosis (classified as mild (<15%), moderate (15-35%) and severe (>35%) LGE) with CMR and demonstrate increased 6-month recurrence rates with increasing LGE intensity (78). This work has led to the development of the Utah classification system: Utah I (<5% enhancement), Utah II (5-20% enhancement), Utah III (21-35% enhancement) and Utah IV (>35% enhancement) (90, 91), again showing that the extent of pre-existing LGE is predictive of AF recurrence. The authors suggest a more extensive ablation strategy is appropriate in those with more enhancement and that in Utah IV, ablation is unlikely to be successful. Despite these findings, other cohorts fail to show pre-ablation LGE in any patients (76) casting doubt over the current resolution of CMR to detect atrial fibrosis.

Computational Modelling

With advances in computer technology electro-anatomically accurate computer models of the atria (integrating information from the molecular to organ scale) have established computational electrophysiology as a technique able to provide unique insights into pathophysiological processes affecting the human heart.

Multiple Scales of Computational Electrophysiology

Computational electrophysiology is usually applied with a 'bottom-up' approach spanning multiple levels and scales (see Table 1-3).

Table 1-3. Levels and Scales of Computational Electrophysiology

Modeling Level	Features
Molecular level	Channel gating kinetics
Membrane level	Integration of the effects of ionic currents, pumps and ion exchangers
Cellular level	Summation of the contribution of each ionic current to the overall ionic concentration
Tissue level	Myocyte coupling and spatially heterogeneous ionic models

Organ level	Reproduction of cardiac anatomy
Clinician level	Simulation of measurement devices including intracardiac catheters or ECG leads

In this section atrial cell models, propagation models (tissue level) and geometry and structural models (organ level) will be considered.

Atrial Cell Models

The atrial cell membrane consists of a dielectric lipid bilayer and acts as a capacitor. The electric charge per unit area of the membrane Q_m is given by the product of the membrane potential V_m and the membrane capacitance per unit area C_m (Equation 1-2).

$$Q_m = C_m V_m \qquad \textbf{Equation 1-2}$$

The total ionic current I_{ion} per unit area is responsible for variations in V_m according to Equation 1-3 and Equation 1-4, where s represents all dynamic variables of the cell and the function g describes the dynamics of those variables:

$$C_m \frac{dV_m}{d_t} = -I_{ion}(V_m, s) + I_{stim}(t) \qquad \textbf{Equation 1-3}$$

$$\frac{ds}{dt} = g(V_m, s) \qquad \textbf{Equation 1-4}$$

An external current I_{stim} is used to trigger an action potential. All cell models conform to this prototype, but differ in their specification of the variables (s), their dynamics (g) and their effects of the membrane potential (I_{ion}). In turn, I_{ion} is defined as the sum of a number of ion channel, pump and ion-exchanger currents.

A number of atrial cell models have been published, relying heavily on the mathematical formulation introduced by Hodgkin and Huxley for neuronal cells (95). A simple implementation of this cell model is given below:

```
function [data] = hodghux(Vo, dt, dep, delay)
% HODGHUX Solves the Hodgkin-Huxley cell model.
%
% Usage:
%   data = hodghux(Vo, dt, dep, delay)
%
% Where:
%   Vo - is the resting membrane value (eg 0mV)
%   dt - is the time interval to compute the model (eg 0.01ms)
%   dep - is the depolarising voltage to be applied
%   delay is the time to the extrastim - set at <0 for no extrastim.
%
```

```
% HODGHUX creates a Hodgkin Huxley model.
%   Variable definitions:
%   Vo - initial membrane potential
%   gK - potassium ion conductance
%   gNa - sodium ion conductance
%   gL - leakage ion conductance
%   VK - potassium ion potential difference
%   VNa - sodium ion potential difference
%   VL - leakage ion potential difference
%   Cm - membrane capacitance
%
%   Derived variable definitions:
%   m, n , h - voltange/time dependent gating variables
%   alphaM, alphaN, alphaH, betaM, betaN, betaH - rate constants
%
% Author: Steven Williams (2012)
% Modifications -
%
% Info on Code Testing:
% ------------------------------------------------------------------
% data = hodghux(0, 0.01, 20, 0);
% ------------------------------------------------------------------
%
% ------------------------------------------------------------------
% code
% ------------------------------------------------------------------

% ---------- Initialise output variable ---------- %
data = NaN(10000,1);

% ---------- Constans Initialisation begins ---------- %
gK = 36;
gNa = 120;
gL = 0.3;
VK = -12;
VNa = 115;
VL =  10.6;
Cm = 1;

% ---------- Function Definitions ---------- %
% Calculate rate constant values
    function [output] = alphaMCalc(volt)
        output = 0.1 * ((25 - volt) / ( exp((25-volt)/10)-1));
    end
    function [output] = betaMCalc(volt)
        output = 4 * (exp(-volt/18));
    end
    function [output] = alphaHCalc(volt)
        output = 0.07 * (exp(-volt/20));
    end
    function [output] = betaHCalc(volt)
        output = 1 / (exp((30-volt)/10)+1);
    end
    function [output] = alphaNCalc(volt)
        output = 0.01 * ((10-volt)/(exp((10-volt)/10)-1));
    end
    function [output] = betaNCalc(volt)
        output = 0.125 * (exp(-volt/80));
    end

% Calculate dvdt
    function [output] = dvdtCalc(volt)
        output = Cm -((gK * (n^4) * (volt - VK)) + (gNa * (m^3) * h * (volt-VNa)) + (gL *
(volt - VL)));
    end

% Calcuate rate of change of rate constants
    function [output] = dmdtCalc()
        output = (alphaM * (1 - m)) - (betaM * m);
    end
    function [output] = dndtCalc()
        output = (alphaN * (1 - n)) - (betaN * n);
    end
    function [output] = dhdtCalc()
        output = (alphaH * (1 - h)) - (betaH * h);
    end

% Calculate values of m, n and h
    function [output] = mCalc()
        output = alphaM / (alphaM + betaM);
    end
    function [output] = nCalc()
```

```
        output = alphaN / (alphaN + betaN);
    end
    function [output] = hCalc()
        output = alphaH / (alphaH + betaH);
    end

% Calculate initial rate constant values
alphaM = alphaMCalc(Vo);
betaM = betaMCalc(Vo);
alphaN = alphaNCalc(Vo);
betaN = betaNCalc(Vo);
alphaH = alphaHCalc(Vo);
betaH = betaHCalc(Vo);

% Calculate the steady stage values of m, n , h
m = mCalc();
n = nCalc();
h = hCalc();

% Calculate dvdt
dvdt = dvdtCalc(Vo);

% Calculate rate of change of m, n, h
dmdt = dmdtCalc();
dndt = dndtCalc();
dhdt = dhdtCalc();

V = Vo + dep;

for i = 1:10000
    % Calculate new rate constants with the new membrane voltage
    alphaM = alphaMCalc(V);
    betaM = betaMCalc(V);
    alphaN = alphaNCalc(V);
    betaN = betaNCalc(V);
    alphaH = alphaHCalc(V);
    betaH = betaHCalc(V);

    % Calculate rate of change of m, n, h
    dmdt = dmdtCalc();
    dndt = dndtCalc();
    dhdt = dhdtCalc();

    % Calcuate the new values of m, n and h
    m = m + dmdt * dt;
    n = n + dndt * dt;
    h = h + dhdt * dt;

    % Calculate the new value for dvdt
    dvdt = dvdtCalc(V);

    % Calculate and save the new value for V
    if i == delay
        V = V + dvdt * dt + 100;
    else
        V = V + dvdt * dt;
    end
    data(i) = V;
end
end
```

In recent years the availability of increasing experimental detail has led to the refinement of these models. The first such models described the action potential (AP) in terms of transmembrane ion channels with little focus on intracellular calcium dynamics (96, 97). These models could provide good representations of the morphological changes seen in the AP in AF by, for example, reducing the transient outward current (I_{to}), ultrarapid delayed rectifier current (I_{Kur}) and L-type calcium current ($I_{Ca,L}$) by experimentally-

measured amounts (98). Notably however, the rate-dependent behaviour of these models is dissimilar, largely due to differences in intracellular calcium handling (99).

Subsequent refinements of these models have: 1) improved the potassium current description to better represent repolarisation and rate-dependence of the transient outward potassium current (I_t), I_{Kur} and the AP duration (100); and 2) improved the description of subcellular calcium dynamics to account for a delay between peripheral and central sarcoplasmic reticulum calcium release (101). Noting the presence of an extensive t-tubular network in atrial myocytes and remodelling of this network in AF allows accurate representation of AP and calcium dynamics in human atrial myocytes in sinus rhythm and AF states (102).

Continuous Propagation Models

To formulate continuous models describing current movement in cardiac tissue, the tissue is considered as three separate domains (the intracellular medium, extracellular medium and cell membranes) occupying the same physical space (Ω_{myo}). The intracellular potential ϕ_i, the cell state s and the extracellular potential ϕ_e become fields $\phi_i(\boldsymbol{x})$, $s(\boldsymbol{x})$ and $\phi_e(\boldsymbol{x})$ defined on Ω_{myo}. The transmembrane potential V_m is given by:

$$V_m = \phi_i - \phi_e \qquad \textbf{Equation 1-5}$$

Assuming the intracellular medium is continuous, the current flows are described by a continuity equation expressing the conservation of electric charge:

$$\frac{\delta \rho_i}{\delta t} + \nabla \cdot \mathbf{j}_i = I_{src,i} \qquad \textbf{Equation 1-6}$$

where ρ_i is the charge density, $\mathbf{j}_i$ is the current density in the intracellular medium and $I_{src,i}$ is a current source term. A similar expression can be written for the extracellular medium. The charge density, current density and current source are given by Equation 1-7, Equation 1-8 and Equation 1-9, respectively:

$$\rho_i = C_m V_m S_v \qquad \textbf{Equation 1-7}$$

$$\mathbf{j}_i = -\boldsymbol{\sigma}_i \nabla \phi_i \qquad \textbf{Equation 1-8}$$

$$I_{src,i} = -I_{ion} S_v \qquad \textbf{Equation 1-9}$$

where, S_v is the area of membrane per unit volume and $\boldsymbol{\sigma}_i$ is the conductivity tensor. Combining Equation 1-6, Equation 1-7, Equation 1-8 and Equation 1-9 and rearranging leads to:

$$C_m \frac{\delta V_m}{\delta t} = S_v^{-1} \nabla \cdot \boldsymbol{\sigma}_i \nabla \phi_i - I_{ion} \qquad \textbf{Equation 1-10}$$

Similarly, charges in the extracellular medium form the other side of the capacitor such that $\rho_e + \rho_i = 0$, $I_{src,e} + I_{src,i} = 0$ and $\mathbf{j}_e = -\boldsymbol{\sigma}_e \nabla \phi_e$ leading to:

$$-C_m \frac{\delta V_m}{\delta t} = S_v^{-1} \nabla \cdot \boldsymbol{\sigma}_e \nabla \phi_e + I_{ion} \qquad \textbf{Equation 1-11}$$

The complete system, known as the *bidomain equations*, is usually written as:

$$S_v^{-1} \nabla \cdot \boldsymbol{\sigma}_i \nabla \phi_i = C_m \frac{\delta V_m}{\delta t} + I_{ion} \qquad \textbf{Equation 1-12}$$

$$\nabla \cdot (\boldsymbol{\sigma}_i \nabla \phi_i + \boldsymbol{\sigma}_e \nabla \phi_e) = 0 \qquad \textbf{Equation 1-13}$$

If the anisotropy ratios are equal the bidomain equations can be decoupled and Equation 1-10 and Equation 1-11 combined to give the *monodomain equation*:

$$C_m \frac{\delta V_m}{\delta t} = S_v^{-1} \nabla \cdot \boldsymbol{\sigma} \nabla V_m - I_{ion} \qquad \textbf{Equation 1-14}$$

In the following chapters, the bidomain and monodomain equations were solved using the Cardiac Arrhythmia Research Package (103).

1.3 Clinical Contexts

Normal Heart Ventricular Arrhythmias

The assessment of patients presenting with ventricular arrhythmias (premature ventricular complexes (PVCs), monomorphic ventricular tachycardia VT, polymorphic VT (PMVT), ventricular fibrillation (VF)) includes 12-lead ECG, 2-dimensional echocardiogram, non-invasive tests of functional ischemia, coronary angiography and cardiovascular magnetic resonance imaging. In the absence of demonstrable structural heart disease, the majority of ventricular arrhythmias have an excellent prognosis, but a minority of patients are susceptible to life-threatening arrhythmias. Arrhythmia substrate characterisation in these two groups is considered separately below.

Non-Life-Threatening

Non-life-threatening ventricular arrhythmias may still cause significant symptoms and/or tachycardia-related cardiomyopathy. Tachycardia-related cardiomyopathy can result in a significant reduction in ejection fraction although the precise ectopy burden at which this occurs is quite variable between patients: >30,000 ectopic beats (104), >17,000 ectopic beats (105), >16% ectopic beats (106), >20% ectopic beats (107), and >24% ectopic beats (108). However, even once a pre-defined ectopic beat threshold is reached, tachycardia-related cardiomyopathy is still rare (104, 106). Although non-life-threatening ventricular arrhythmias may originate from any location in the heart, including the mitral annulus, tricuspid annulus and papillary muscles, the two most common forms are outflow tract and idiopathic left ventricular tachycardia.

Life-Threatening

A number of genetic syndromes leading to abnormal ion channel function are associated with ventricular arrhythmias and sudden cardiac death. ECG phenotypes, but not family history, have been used for risk stratification (109). Although secondary prevention with implantable cardioverter-defibrillators is mandated, primary prevention should be based on risk stratification and the availability of medical therapy (see below).

Long QT Syndrome

The hallmark of the long QT syndromes is prolongation of the QT interval (QTc >440ms in males and >460ms in females) with or without T-wave abnormalities. Prolongation of repolarisation owing to decreased outward potassium currents or increased inward sodium currents during phase 2 of the action potential results in a predisposition to early afterdepolarisations and torsade de pointes VT (see Triggered Activity, p. 25). A number of genes have been identified with LQT1 (KCNQ1, α subunit of I_{Ks}), LQT2 (KCNH2, α subunit of I_{Kr}) and LQT3 (SCN5A, α subunit of I_{Na}) accounting for >90% of genotyped long QT syndrome cases (110). Clinical triggers vary between the long QT syndrome phenotypes, with LQT1 being associated with physical exertion, LQT2 with auditory stimulation or emotional stress and LQT3 with arrhythmias during rest or sleep. The ECG shows broad-based T-waves in LQT1, notched T-waves in LQT2 and long ST segments in LQT3 although there is considerable overlap. Characterisation of the arrhythmia substrate in long QT syndromes involves clinical scoring (111), exercise testing, epinephrine challenge and genetic testing.

Brugada Syndrome

The Brugada syndrome with its characteristic ECG manifestations of coved precordial ST-segment elevation and complete or incomplete right bundle branch block may present with syncope or cardiac arrest (112, 113). Substrate characterisation in the Brugada syndrome involves both rest ECG and provocation studies with sodium channel blocking agents (e.g. ajmaline, flecainide or procainamide) as well as long-term ECG monitoring. Genetic mutations in SCN5A (BrS1) lead to loss of function of sodium channels and clinical overlap with the LQT3 phenotype (114, 115). Risk stratification involves considering the presence of spontaneous Brugada ECG pattern and syncope, and notably family history does not predict risk of syncope and/or sudden cardiac death events (116).

Catecholaminergic PMVT

Catecholaminergic PMVT is characterised by polymorphic or bidirectional VT and presents clinically with exertional syncope and sudden cardiac death. Mutations of the cardiac ryanodine receptor (RyR2, autosomal dominant inheritance) and the calsequestrin 2 gene (CASQ2, autosomal recessive inheritance) have been identified. Both of these genes encode proteins important in calcium handling with mutations leading to excess intracellular calcium and delayed afterdepolarisations (see Triggered Activity, p. 25). Whilst the resting ECG is normal, exercise induces bidirectional VT preceded by increasing frequency of premature ventricular complexes when the sinus rate reaches 120 to 130 beats per minute.

Idiopathic Ventricular Fibrillation

Idiopathic ventricular fibrillation is defined as the presence of ventricular fibrillation in the absence of structural heart disease or an identifiable genetic syndrome. It may present with episodes of ventricular fibrillation (VF) or polymorphic ventricular tachycardia (PMVT) associated with syncope or sudden cardiac death. VF and PMVT are triggered by premature ventricular complexes which can typically be mapped to the distal Purkinje system or right ventricular outflow tract (117).

The early repolarisation ECG pattern (QRS-ST junction ("J-point") elevation ≥0.1mV in inferolateral leads) has been associated with idiopathic VF (118). Analysis of the ST segment has been suggested to help differentiate benign from malignant J-point elevation, with a horizontal/descending ST segment, but not ascending ST segment, being

associated with risk of sudden cardiac death (119). However, the early repolarisation phenotype occurs frequently in the normal population without determining future syncopal or sudden cardiac death events (120). In contrast to the other normal heart arrhythmias described above, risk stratification in patients with the early repolarisation phenotype is less well described. This leads to the following aim:

C1 *Examine the role of the surface ECG, augmented by therapeutic hypothermia, in characterising the arrhythmia substrate in idiopathic ventricular fibrillation.*

Atrial Tachycardia

Atrial tachycardias are classified as either focal or macro-re-entrant (121). Additionally a third mechanistic group termed localised re-entry has been described, most frequently described after catheter ablation for persistent AF (122).

Diagnosis of Atrial Tachycardia

Where a clinical diagnosis is sought to guide ablation, intra-cardiac contact mapping (see Intracardiac Contact Mapping, p. 31) is usually required. Even given the logical approach to intra-cardiac mapping described above, mapping can frequently be a challenging and time consuming process. The optimal sampling density for atrial tachycardias is not known. This leads to the following aim:

C2 *Determine the optimal point sampling density for intracardiac contact mapping in the diagnosis of tachycardia mechanism in a variety of atrial tachycardias.*

Focal Atrial Tachycardia

Focal atrial tachycardias may account for up to 15% of all supraventricular arrhythmias (123). They are characterised by a single site of origin with centrifugal electrical activation spreading away from that site. Typical sites of origin include the crista terminalis, tricuspid annulus, coronary sinus os, superior vena cava and RA appendage. The underlying mechanism may be abnormal automaticity, triggered activity or micro-re-entry (see above). Focal ATs show gradual rates of onset and termination. Focal atrial tachycardias are most often seen in the absence of structural heart disease (124).

The surface ECG may be diagnostic in focal AT. P waves are separated by an isoelectric interval consistent in all ECG leads where it is not obscured by a rapid ventricular

response rate. Assuming normal atrial conduction, algorithms have been proposed to localise the source from the surface ECG (125). A positive P-wave in lead V1 suggests a left atrial origin, whilst a negative P-wave in lead V1 suggest a right atrial origin (126). In the presence of surgical scars or ablation lesions, localisation of the focal origin from the surface ECG is less reliable.

Pharmacotherapy has traditionally been the first line treatment for focal AT, using rate-limiting drugs such as cardio-selective beta-blockers and non-dihydropyridine calcium channel antagonists or Class Ic (e.g. flecainide or propafenone) or Class III (e.g. sotalol or amiodarone) antiarrhythmic agents for tachycardia management. Owing to poor efficacy and side effects of pharmacological treatment, catheter ablation is now first line therapy for recurrent/incessant tachycardia or tachycardia-induced cardiomyopathy (127). Ablation has an acute success rate of 85-90% (128), complications (including recurrence) are rare, and good recovery of LV function is seen in the case of tachycardia induced cardiomyopathy (129).

Macro-re-entrant Atrial Tachycardia (Including Atrial Flutter)

Macro-re-entrant atrial tachycardias are characterised by continuous activation of a large circuit around a central obstacle. The obstacle may be anatomic (e.g. pulmonary veins, mitral or tricuspid annulus, surgical or spontaneous scar) or functional (e.g. crista terminalis). Macro-re-entrant atrial tachycardias include cavotricuspid isthmus (CTI) dependent atrial flutter (both typical and reverse typical) and non-CTI dependent macro-re-entry. Typically, macro-re-entrant tachycardias show a sudden onset and termination.

CTI dependent atrial flutter occurs around a circuit bounded anteriorly by the tricuspid annulus and posteriorly by the crista terminalis and Eustachian ridge (130). Activation is counter clockwise (typical atrial flutter) in the majority of cases resulting in inferior to superior septal activation and superior to inferior lateral wall activation, whilst 10% see the opposite direction of activation (reverse typical atrial flutter) (131). The CTI itself provides a critical isthmus for the circuit and therefore an ablation target (132, 133). Associations of CTI dependent flutter include ischaemic heart disease, valvular heart disease, cardiomyopathy, any cause of increased RA pressure, age and male sex (134). Approximately one third of patients with CTI dependent flutter will later develop AF (135).

Non-CTI dependent macro-re-entry tachycardias include mitral isthmus-dependent macro-re-entry, roof-dependent macro-re-entry and scar-related macro-re-entry. Additionally, macro-re-entry may occur around areas of spontaneous fibrosis in the LA or RA (136). Substrates for scar-related macro-re-entry include surgical scars, suture lines or prosthetic patches following correction of congenital heart disease as well as scars arising from surgical or catheter ablation of AF. With more extensive LA ablation for persistent AF, up to 50% of cases may subsequently develop a macro-re-entrant atrial tachycardia (137). Since gaps in ablation lines result in conduction slowing, and an increased likelihood of developing post ablation atrial tachycardia, an important goal is to ensure that the ablation energy delivered forms effective, contiguous and transmural lesions. This leads to the following aim for this thesis:

C5 Assess the impact of contact force in the creation of effective linear ablation lesions.

Catheter ablation of CTI dependent flutter has high efficacy and low complication rates. Catheter ablation has been shown to be superior to antiarrhythmic therapy with maintenance of sinus rhythm seen in 80-92% of patients undergoing a single catheter ablation procedure, compared to 36% of patients receiving drug therapy (138, 139). Success rates are improved by the use of pacing manoeuvres to confirm bidirectional block across the CTI (140). Drug therapy is rarely effective for non-CTI dependent macro-re-entry, and catheter ablation using advanced mapping techniques (see above) is more likely to offer a cure. Due to the complexity of the circuits involved however, success rates are more variable than for CTI-dependent flutter.

Localised Re-Entry

Localised re-entry is characterised by a small re-entry circuit, typically 1-2cm in size. Localised re-entry is most commonly seen following catheter ablation for persistent AF (141). Even in the presence of an apparently focal tachycardia, up to three quarters may actually be the result of localised re-entry (122). Whether they are drivers for atrial fibrillation or just a consequence of ablation is not known.

Atrial Fibrillation

Epidemiology, Classification and Impact

Atrial fibrillation (AF), a supraventricular tachyarrhythmia characterised by uncoordinated atrial activation, is the most common sustained cardiac arrhythmia (142).

The prevalence of AF increases with age from 0.5% in the 6th decade to at least 9% in the 9th decade and each year around 46,000 people in the United Kingdom are affected with the condition (143, 144). In 2004, it was estimated that the direct cost of AF constituted approximately 1% of the NHS budget (145). Moreover owing to an aging population, a rising prevalence of chronic heart disease and also improved diagnosis, there has been a 66% rise in hospital admissions for AF over the past two decades (142). AF is more prevalent in men than women, and whilst the prevalence of AF in women is constant the prevalence of AF in men has more than doubled from the 1970s to the 1990s (146).

AF is classified according to the duration of episodes (142). Given the occurrence of two or more episodes AF is said to be recurrent and classified as "paroxysmal" or "persistent". Paroxysmal AF involves self-terminating episodes lasting <7 days (and usually <24 hours). Persistent AF involves episodes lasting >7 days. AF is termed permanent when cardioversion does not terminate the arrhythmia (or is not attempted due to a low anticipated chance of success). The term "lone AF" refers to AF occurring in young patients (<65 years) with structurally normal hearts and no evidence of other causative pathology.

AF leads to deterioration in atrial mechanical function, stasis of blood, endothelial damage and consequently a significantly increased long-term risk of stroke (147, 148). In the Framingham study, the presence of AF independently increased mortality in men by 1.5 fold and in women by 1.9 fold (149). With an increasingly elderly population, the prevalence of AF is set to rise, conferring substantial mortality, morbidity and economic burden.

The treatment of AF involves the treatment of any underlying causes (e.g. hypertension), drugs to control the heart rate or maintain sinus rhythm, anticoagulant drugs to reduce the risk of stroke and, increasingly, catheter ablation in selected patients for symptom control.

Electrophysiological Basis of AF

Automatic Focus Theory

The possibility of a focal trigger of atrial fibrillation has long been suggested by experimental studies (150) and a pivotal development in the understanding of human AF was the demonstration of paroxysmal AF triggered by pulmonary vein (PV) ectopy (151,

152). Although PVs are the most common source of ectopy, foci have also been found in the superior caval vein, ligament of Marshall, left posterior free wall, crista terminalis and coronary sinus.

Multiple Wavelet Theory

For many years the multiple-wavelet hypothesis overshadowed automaticity as the primary driver of AF. In this theory fractionation of wave fronts propagating throughout the atria results in the formation of multiple self-perpetuating wavelets (153). Increasing atrial size, shortening refractory period and slowing conduction velocity increase the number of wavelets present and the likelihood of AF persistence.

Importance of the Atrial Substrate

Whilst experimental (154) and clinical (155) mapping studies support an automatic focus over multiple wavelets as the trigger of AF, the importance of the atrial substrate in maintaining AF remains. For example in some patients with persistent AF, PVI may terminate AF whereas in others AF persists following PVI but does not recur after cardioversion. Specific electrophysiological differences can be observed in the atria of AF patients including increased dispersion of atrial refractoriness and greater ability to induce AF (156), widespread distribution of abnormal fractionated electrograms predictive of progression to persistent AF (157) and prolonged intra-atrial conduction in patients with persistent AF following successful cardioversion to sinus rhythm (158).

In canine models of AF, characterized by different extents of electrical and structural remodelling, mechanisms of AF perpetuation appear to relate to abnormalities of the substrate (159, 160). In models with primary atrial electrical remodelling (i.e. rapid atrial pacing or methylcholine infusion), AF is characterized by multiple high frequency areas and multiple wavelets. However, in models with primary atrial structural remodelling (i.e. mitral regurgitation or heart failure), AF is characterized by a stable high frequency area consistent with the presence of micro-re-entry giving rise to a focal rotor or a focal impulse source. Recently, localized rotors and/or focal impulse sources have also been identified in a high proportion of cases of human AF (97%) with their ablation associated with significantly higher acute and short term success than conventional ablation strategies (161). Despite these remarkable results other mapping studies have not demonstrated the presence of stable foci or rotors (162), or only demonstrated organized patterns in a minority of cases (163).

In summary, altered refractoriness and conduction with spatial heterogeneity throughout the atria may provide a milieu for the maintenance of AF, and support the initiation of AF in response to a focal trigger, but the relative contributions of trigger and substrate to the initiation and/or maintenance and/or progression of AF is unclear.

Electrical and Structural Remodelling in AF

The natural history of AF is characterised by a gradual worsening over time, with progressively longer episodes of arrhythmia eventually leading to persistent AF. Such progression is potentially explained by the finding that AF itself produces changes in atrial function and structure.

Electrical Remodelling

The concept of tachycardia-induced atrial electrical remodelling was introduced by two independent experimental studies (164, 165). In a dog model of prolonged rapid atrial pacing, the atrial ERP was reduced by about 15% and there was increased dispersion of atrial refractoriness (165). In goats, AF maintained by automatic burst atrial pacing in response to sinus rhythm, resulted in an even more marked shortening of atrial refractory period from 146±19ms to 81±22ms and a loss (or even reversal) of the normal rate adaptation of the refractory period (164). Significantly, these studies showed that long-term rapid atrial pacing led to a progressive increase in the susceptibility to AF. After 6 weeks of rapid atrial pacing, episodes of AF lasting >15 minutes could be induced in 82% of the dogs. In 10 out of 11 goats, after maintaining AF for 7.1±4.8 days, the arrhythmia sustained itself for >24 hours, compared to periods of only 6±3 s at the start of the experiment.

In humans, electrical remodelling with decreased right atrial action potential duration (APD) has been reported (166) and reversal of electrical remodelling has been demonstrated following treatment of AF by DC cardioversion (167). In pacemaker patients with detected atrial tachyarrhythmias, increased P-wave duration without shortening of the atrial effective refractory period (ERP) is observed (168) which is similar to the atrial electrical changes noted in the rapid ventricular pacing canine heart failure model (169).

Structural Remodelling

In addition to electrical remodelling, structural remodelling involving myocardial fibrosis is inextricably linked to the progression of AF (170, 171). Structural remodelling contributes synergistically with electrical remodelling to form the arrhythmogenic substrate in AF. There is an increase in atrial fibrosis, not only in patients with AF and underlying heart disease, but also in patients with lone AF (172, 173) and furthermore there appears to be a positive correlation between the extent of fibrosis and the persistence of AF (78).

Rapid atrial pacing in the dog causes atrial fibrosis (174) comparable with many clinical forms of AF (169). Notably, in this canine model atrial fibrosis causes localised regions of conduction slowing and increased conduction heterogeneity, consistent with the electrical remodelling seen in humans. In other canine models of AF fibrosis is also observed, but AF becomes sustained before fibrosis occurs (160).

In canine models of AF with heart failure, induced by ventricular tachypacing, there is electrical as well as structural remodelling with pronounced interstitial fibrosis (175). After cessation of pacing and a 5-week recovery period there was complete recovery of the electrical remodelling but AF vulnerability was still higher than baseline suggesting that structural remodelling leads to continued AF susceptibility (175).

Catheter Ablation of AF

Although the AFFIRM study demonstrated that rhythm control conferred no prognostic benefit over rate control, a sub-study of this trial has shown that if sinus rhythm (SR) could be achieved without the use of anti-arrhythmic drugs there may be a substantial mortality benefit (176). Pharmacological management has been the mainstay of treatment for AF but is limited by concerns about efficacy, side effects and safety. Therefore catheter ablation has emerged as an effective and potentially curative approach for patients with symptomatic paroxysmal and persistent AF, who have failed drug therapy. The demonstration that paroxysmal AF is frequently triggered by ectopy arising from within the PVs has led to the emergency of PV isolation (PVI) as a widely practised therapy for this arrhythmia and even as a first line therapy in selected patients (152, 177). Whilst it was first suggested to ablate only PVs with foci of spontaneous activity (152, 178), high recurrence rates, the increasing recognition that all PVs can initiate AF and technological developments mean it is now routine practice to isolate all four PVs (142).

In the context of PVI for paroxysmal AF, incomplete or non-transmural circumferential ablation lesions may lead to immediate or delayed reconnection of the PVs, which can be documented in many cases of AF recurrence (179, 180). Reconnection is possibly due to an acute inflammatory response at the time of ablation causing tissue oedema and temporary electrical isolation of the PVs whilst at the same time preventing delivery of sufficient radiofrequency energy to cause tissue necrosis (181).

The demonstration of non-PV ectopy initiating paroxysmal AF has led to modification of ablation procedures to include supplementary ablation in selected patients (182, 183). Whilst paroxysmal AF is usually caused by foci from the thoracic veins it is recognised that pulmonary vein isolation alone is unlikely to be sufficient for the catheter ablation of persistent AF (93). An alternative anatomic approach targets complex fractionated electrograms either as an adjunct to, or instead of, pulmonary vein isolation (184). Recently, a further approach suggests mapping to identify electrical rotors or focal impulses as targets for ablation (161). All of these approaches, with the exception of rotor-ablation that is pending assessment, have variable success rates when performed in unselected patients in multiple centres (93). Indeed the addition of CFE ablation or linear ablation to PVI alone has failed to increase freedom from AF in a large multicentre randomised controlled trial (185). Hence, there is currently no agreed strategy to identify which patients are likely to benefit from each of these strategies, or indeed which are likely to benefit from none. This observation leads to the following two aims for this thesis:

C3 *Develop a tool to quantify electrical remodelling in paroxysmal AF and determine if population heterogeneities are present that could be used to predict response to catheter ablation.*

C4 *Examine the role of CMR in predicting the electrical substrate in patients with a spectrum of AF disease severity.*

1.4 Arrhythmia Substrate Representation Techniques

Electrogram Display

The aim of electrogram display processes is to represent cardiac electrical signals in a clinically relevant way with minimal artefact. In modern electrophysiological procedures, electrograms are represented digitally, but a variety of inventive methods have previously

been used to record cardiac activation, including the capillary electrometer, string galvanometer and amplifier electrograph.

The first device that was sufficiently sensitive to record the surface electrocardiogram was the capillary electrometer (186). This device consisted of a glass capillary tube filled with mercury and immersed in sulphuric acid. Owing to the collection of charge on the meniscus of the mercury, the surface of the mercury moved as a potential difference was applied between the mercury and the sulphuric acid. By using photographic paper, the movement of the mercury could be recorded over time. Just as in modern recording systems, the capillary electrometer was subject to sources of error. In particular friction between the mercury column and the capillary tube resulted in a non-linear relationship between the applied electric potential and the movement of the column. This error was partially overcome through mathematical correction of the recorded waveform (37), which although resulting in effective correction, was computationally expensive.

The capillary electrometer was superseded with the invention of the string galvanometer (38, 187). The string galvanometer consists of a long silver-coated (hence electrically-conductive) filament passed under tension between electromagnets. Movement of an electric current within the filament resulted in displacement of the filament, and this displacement after magnification was again recorded on photographic paper. The string galvanometer had much higher sensitivity than the capillary electrometer achieving sufficiently high quality recordings to enter clinical practice.

A sometimes-overlooked stage in the development of electrogram detection and display technologies was the invention of the ‘amplifier electrograph’ which, for the first time, relied on electronic amplification of the ECG signal (using vacuum tubes), rather than the mechanical amplification relied on with the string galvanometer (39). Similarly a further important innovation was reported with the invention of a 'liquid jet recorder' (mingograph) for recording the electrical data (188). Compared to the use of photographic paper, this device provided an instant representation of the cardiograph.

Eventually, digital systems were introduced to facilitate the display, storage and retrieval of electrogram information. Two important parameters describe the performance of an analogue to digital convertor (ADC): sampling rate and resolution. According to information theory, analogue signals must be sampled at a frequency at least double the maximal frequency in the signal (189). Put another way, the maximal signal frequency

that can be recorded by an ADC is half of the sampling frequency, this being known as the Nyquist frequency (190). If a component of the input signal exceeds the Nyquist frequency, then aliasing results. Resolution determines the accuracy to which the digital signal processing system can represent each signal sample. For example, with a resolution of 12 bits, the amplification system can encode each signal sample into one of 2^{12} (4096) discrete levels. That is, given a maximum input amplitude of 10mV, then the smallest change in signal that can be recorded is 2.44μV (10mV ÷ 4096). Typically, intracardiac electrograms are sampled at 1024Hz with a resolution of 12- to 16-bits.

Electroanatomic Mapping Systems

Electroanatomic mapping systems provide a number of functions facilitating complex electrophysiology procedures. All conventional electroanatomic mapping systems provide three key features: catheter location, anatomical representation and map construction.

Catheter location

Three main technologies facilitate catheter location in mainstream mapping systems: electromagnetic catheter location, impedance based catheter location and electric field based catheter location. A fourth technology combining cross sectional imaging and fluoroscopy has also been proposed (191).

Electromagnetic catheter location depends on the creation of three independent magnetic fields by an electromagnetic attachment positioned below the operating table (192). The intracardiac catheters compatible with this system contain three distally embedded orthogonally orientated coils in which currents are induced by the magnetic fields. Measurement of these currents allows the orientation and position of the tip to be calculated. Electromagnetic catheter location was first used in the Carto system (Biosense Webster, Diamond Bar, CA, USA).

Impedance based catheter location (introduced in the Carto 3 system, Biosense Webster, Diamond Bar, CA, USA) has been used in clinical systems to supplement electromagnetic catheter location (193). Six body surface patches are applied to the thorax. A small current is passed through the catheter electrodes allowing the impedance between the electrode and each of the surface patches to be calculated. Initially, the relationship between impedance and position is unknown, but by manoeuvring a magnetic-based catheter

throughout the field of interest this relationship is determined. Thereafter electrodes on the catheter shaft (or indeed non-magnetic locator catheters) may be visualised.

Electric field based catheter location depends on the creation of three high frequency electric fields within the patient using surface patches (194). By measuring the potential of each field at an intracardiac electrode, the distance between the electrode and the source patch is calculated allowing the position of the electrode to be determined. Importantly, this method only determines relative electrode positions meaning a stable reference catheter is usually used (e.g. the CS catheter). Later versions of this system allow one of the body surface patches to be used for the reference. Whilst this mitigates against inadvertent movement of the intracardiac reference, it is more sensitive to changes in intra-thoracic impedance during the procedure. Electric field based catheter location is used in the Velocity platform (St Jude Medical).

Anatomical Representation

Electroanatomic mapping systems can represent cardiac anatomy determined during the mapping procedure, or predetermined using cross sectional imaging. By establishing the anatomical limits of catheter movement the internal extent (i.e. endocardial surface) may be defined. This method typically represents the available geometry accurately, but does not necessarily represent the entire chamber anatomy. For example, pulmonary venous ostia may be effectively represented, whilst if the catheter has not been placed in the appendage then it will not be represented. Cardiac chamber geometry represented in this way has been shown to faithfully represent chamber shape determined by CT imaging (195). Nevertheless, the accuracy of the chamber geometry depends on a number of factors. In particular the interpolating algorithm type and sensitivity must be sufficient to smooth areas of the geometry sampled sparsely whilst not resulting in the formation of 'false' regions of geometry.

An alternative approach is to merge anatomical information from cross sectional imaging, typically CT or MRI. Cross sectional imaging has the advantage of representing the entire chamber without requiring an extensive map creation phase during the mapping procedure, but the chamber shell must be registered to fiducial markers determined by catheter positions on the day of the procedure. For the left atrium, points including the PV ostia, atrial roof and mitral valve annulus are typically selected for initial registration. Selection of suitable fiducial points is crucial to the successful registration of the cross-

sectional geometry. Even with careful registration this process can be challenging. For example defining appropriate anatomical landmarks such as the mitral annulus across different modalities (electroanatomic mapping vs. cross sectional imaging) can result in registration errors. Furthermore, loading conditions may result in variations of chamber geometry between the day of the scan and the day of the mapping procedure. In this regard hybrid labs combining fluoroscopy, electroanatomic mapping and cross sectional imaging are likely to be beneficial.

Electroanatomic Map Display

With ever increasing complexity in electrophysiological datasets comes an increasing requirement to represent those data in a clinically meaningful way. Electrophysiological data typically varies in multiple dimensions including time, magnitude and direction as well as varying across the complicated three-dimensional geometry of the heart. Meanwhile, data display techniques are limited in the number of dimensions that can be represented. Hence a number of strategies are employed to reduce the complexity of electrophysiological data in order that it may be displayed to the operator. For example, electrical data varying in two dimensions (e.g. time and magnitude) can be reduced to one of these dimensions by assigning a local activation time relative to a fixed reference electrogram or by determining magnitude (i.e. voltage) within a window of interest. Once the dimensionality of the data is reduced, it can be represented within a three-dimensional geometry, for example by colouring the cardiac surface according to activation time (isochronal activation map) or by electrogram voltage (voltage map).

One mapping technique has been designed which avoids the need to reduce the dimensionality of electrical data (196). By drawing the electrograms as moving bars normal to a surface, the polarity and magnitude of the electrogram can be represented as bar colour and size respectively. In this way spatial distribution of the electrograms is maintained whilst at the same time also representing both the timing and magnitude of the electrograms. Further development of this system has allowed the display of two datasets by representing the first with moving bars and the second with geometry surface colouring (197). The display of two datasets in this context is limited to electrogram data plus a scalar field. It is not possible for instance to display two static scalar fields using this technique.

In order to display multiple such datasets on a single cardiac chamber shell a number of techniques have previously been used. For example, user input can be sought to switch between display of one or other dataset, an alpha channel can be used to add transparency to one set of data, or two 'linked scenes' can be displayed with alternative datasets drawn side by side. All of these methods of multiple data set display have limitations, including reductions in fidelity of one or other datasets and the reliance on human perception to determine the spatial relationship between datasets. This observation leads to the following two aims:

R1 *Develop a system for concomitant representation of multiple electrophysiological parameters within a 3D geometry.*

R2 *Validate that system to assess dataset display fidelity and ease of dataset integration.*

1.5 Aims for this Thesis

The aims of this thesis are subdivided into arrhythmia characterisation and arrhythmia representation techniques and introduced in the above sections. They are summarised below.

Characterisation of Arrhythmia Substrates

C1 *Examine the role of surface ECG in characterising the arrhythmia substrate in the context of idiopathic ventricular fibrillation.*

C2 *Determine the optimal point sampling density for intra-cardiac contact mapping in the diagnosis of tachycardia mechanism in a variety of atrial tachycardias.*

C3 *Develop a tool to quantify electrical remodelling in paroxysmal AF and determine if population heterogeneities are present that could be used to predict response to catheter ablation.*

C4 *Examine the role of CMR in predicting the electrical substrate in patients with a spectrum of AF disease severity.*

C5 *Assess the impact of contact force in the creation of effective linear ablation lesions.*

Representation of Arrhythmia Substrates

R1 *Develop a system for concomitant representation of multiple electrophysiological parameters within a 3D geometry.*

R2 *Validate that system to assess dataset display fidelity and ease of dataset integration.*

I begin in the next chapter by addressing aim C1 and the role of the surface ECG in arrhythmia substrate characterisation.

SECTION TWO: CHARACTERISATION OF ARRHYTHMIA SUBSTRATES

2 Surface Electrocardiography: Early Repolarization in Hypothermia

2.1 Introduction

Early repolarization (ER) is a common ECG finding, with a prevalence of 5-13% (198, 199). Previously, ER was thought to be a benign variant, or a marker of cardiovascular health (200, 201). However, robust data now indicate that ER is a marker of elevated ventricular fibrillation (VF) risk and cardiac arrest. This is true in otherwise-healthy individuals (idiopathic VF) (198, 199, 202, 203) and in those with coronary artery disease (204–206). The degree of ER, quantified as J-point elevation (JPE) magnitude, appears to determine arrhythmia risk. Thus patients with JPE magnitude >0.2 mV have around double the risk of cardiac arrhythmic death as those with JPE defined using the conventional threshold (≥0.1 mV) (198). Similarly, JPE magnitude in patients with ER who have experienced an episode of VF is around twice that seen in those without arrhythmia (207).

ER syndrome is part of a spectrum of conditions, including the Brugada syndrome, collectively termed the J-wave syndromes (208). These conditions are defined by J-point elevation, terminal QRS complex slurring and ST segment elevation. A similar ionic mechanism appears to be responsible for each of the J-wave syndromes: an enhanced net repolarizing current gives rise to a marked epicardial action potential notch and hence a J-wave (209). Elevated ventricular arrhythmia risk in the J-wave syndromes therefore likely results from increased transmural dispersion of repolarization. Although J-waves are a well-established feature of hypothermia, usually being referred to as Osborn waves in this context (210, 211), interactions between hypothermia and ER have not previously been studied in a clinical context.

The motivation for examining this relationship arises from arrhythmia substrate characterisation methods employed in other settings, where exogenous effects are used to provoke characteristic ECG changes to provide a clinical diagnosis or risk stratification. For example, in the exercise tolerance test the effect of an increased sinus rate is useful in establishing the diagnosis of catecholaminergic polymorphic ventricular tachycardia

(see Catecholaminergic PMVT, p. 47). Similarly the ajmaline test serves to apply sodium channel blockade in selected individuals to reveal the Brugada ECG pattern and aid in risk stratification of these patients (see Brugada Syndrome, p. 47). There have also been isolated case reports of hypothermia revealing a Brugada-type ECG pattern (212).

This study hypothesised that the effect of therapeutic on the magnitude of JPE may be greater in idiopathic VF (ID-VF) than coronary artery disease-related VF (CAD-VF) arrest survivors, leading to the possible development of a diagnostic tool for risk stratification of patients with early repolarisation. Data obtained from a population of adult survivors of cardiac arrest treated with therapeutic hypothermia was used to investigate interactions between ER and hypothermia.

2.2 Methods

All survivors of sudden cardiac arrest with an initial rhythm of VF treated at the critical care unit at St. Thomas' Hospital, London between 2005 and 2012 were assessed for inclusion. Data collection and analysis for this study were part of on-going real-time data collection processes during physician-directed patient care.

Patient Selection

Cases were eligible for inclusion if: 1) their management included therapeutic hypothermia, 2) ECGs obtained at baseline temperature and during cooling were available and 3) sufficient data (echocardiograms, coronary angiograms, cardiac magnetic resonance imaging (CMR) studies and/or electrophysiology studies) were available to determine whether the arrest was attributable to myocardial ischemia. Cases were excluded if ventricular conduction abnormalities, other underlying arrhythmic disorders or clear confounding factors such as recent cardiothoracic surgery or cocaine use were present.

Cases were classified as ID-VF if criteria specified in guidelines were met (213), that is there was no structural heart disease (as indicated by an echocardiogram showing normal biventricular dimensions and function), no coronary artery disease (as indicated by a normal coronary angiogram) and no known repolarization abnormalities. Cases were classified as CAD-VF if A) there was a pre-existing diagnosis of coronary artery disease or B) significant coronary artery disease was demonstrated on an angiogram, a significant

troponin rise from baseline was observed and regional wall motion abnormalities were present either on echocardiography or CMR.

Data Collection and Analysis

ECGs were obtained close to the mid-point of the period of therapeutic hypothermia ('cooled' ECG), during which patients' core temperatures fell to between 32 and 34°C, and again prior to discharge ('baseline' ECG). Records were digitally scanned (300dpi, 24-bit colour) and read at 4x magnification by two independent observers. ECGs were assessed for the presence of ER and the magnitude of JPE, manifest as slurring or notching of the downslope of the R wave in at least two contiguous inferior (II, III, aVF) or lateral (I, aVL, V4-6) leads. ER was assessed at typical (≥0.1mV) and high-risk (>0.2mV) amplitudes, as well as on morphological criteria alone (JPE <0.1mV). The following data were recorded for each patient: the number and location of leads displaying ER, the mean and maximum amplitudes of JPE in each lead, PR interval, QRS duration and QTc interval (derived using Bazett's formula). For each ECG displaying ER ≥0.1mV, ST segment morphology was classified as "concave/rapidly ascending" when there was >0.1mV ST segment elevation within 100ms after the J-point and the ST segment merged gradually with the T wave, or "horizontal/descending" when the ST segment elevation was ≤0.1mV within 100ms of the J-point and continued as a flat segment until T wave onset.

Statistical analysis was performed using SPSS (SPSS Inc., Chicago, IL). Categorical variables were compared using a two-tailed Fisher's exact test or an exact McNemar test for paired data as appropriate. Continuous variables were compared using a two-tailed Student's T-test (paired or unpaired as appropriate) and reported as means ± standard errors. Owing to the nature of the study, no adjustments were made for multiple comparisons. All tests were two-sided, and P values <0.05 were considered statistically significant.

2.3 Results

Of the 89 cases reviewed, 43 met the inclusion criteria. Reasons for exclusion were: paired ECGs not available (n=21), abnormal baseline ECG (n=17: left bundle branch block, right bundle branch block, paced rhythm, Brugada syndrome), insufficient clinical details to confirm VF aetiology (n=4), other confounding factors (n=4: dilated

cardiomyopathy, cardiothoracic surgery, drug use, myocarditis). Baseline characteristics are shown in Table 2-1.

Table 2-1. Demographic data

	ID-VF (n = 10)	CAD-VF (n = 33)	P value
Age (years)	42.9 ± 4.7	61.5 ± 2.3	0.0004 *
Males	8 (80%)	31 (94%)	0.23
Females	2 (20%)	2 (6%)	0.23
Hypertension	1 (10%)	14 (42%)	0.13
Hypercholesterolemia	0 (0%)	11 (33%)	0.043 *
Pre-existing coronary artery disease (previous MI or stent)	0 (0%)	11 (33%)	0.043 *
Diabetes mellitus	0 (0%)	5 (15%)	0.320
Family history of ischemic heart disease	0 (0%)	2 (6%)	1.000

VF indicates ventricular fibrillation; MI, myocardial infarction; ID-VF, idiopathic VF; CAD-VF, coronary artery disease-related VF, * indicates statistical significance.

Effect of Cooling on ER

Overall, ER pattern was present in a significantly greater proportion of patients during cooling than at baseline (32/43 during cooling vs. 22/43 at baseline, P=0.024). The mean J-point elevation (JPE) amplitude for inferolateral ECG leads was significantly greater during cooling than at baseline (0.78±0.10 mV during cooling vs. 0.56±0.09 mV at baseline, P=0.038). The maximum JPE amplitude seen in any single lead of each ECG was greater during cooling than at baseline (1.15±0.15 mV during cooling vs. 0.68±0.11 mV at baseline, P=0.002). Figure 2-1 illustrates typical ID-VF and CAD-VF cases in which ER morphology was augmented by cooling.

Temperature-dependent Prevalence of ER in ID-VF and CAD-VF Arrest Survivors

When defining the presence of ER as any JPE (manifest as terminal QRS notching or slurring) with or without ST segment elevation, ER was more common among survivors of ID-VF as compared to CAD-VF both at baseline (80.0% vs. 42.4%) and during cooling (100% vs. 66.7%), but the difference reached statistical significance only during cooling (Figure 2-2A and B). In contrast, JPE of a magnitude ≥0.1mV was present significantly more frequently in the ID-VF as compared to the CAD-VF group at baseline (70.0% vs. 27.3%, Figure 2-2C), but the significance threshold was not met during cooling (80.0% vs. 42.4%, Figure 2-2D). Finally, there was no significant difference in the prevalence of

ER between ID-VF and CAD-VF at baseline (20.0% vs. 3.0%) or during cooling (40.0% vs. 15.2%) when defining ER as a JPE magnitude >0.2mV (Figure 2-2E and F). Cooling was not associated with the de novo development of ER in either those with ID-VF (8/10 vs. 10/10, P=0.480) or CAD-VF (14/33 vs. 22/33, P=0.061) arrest.

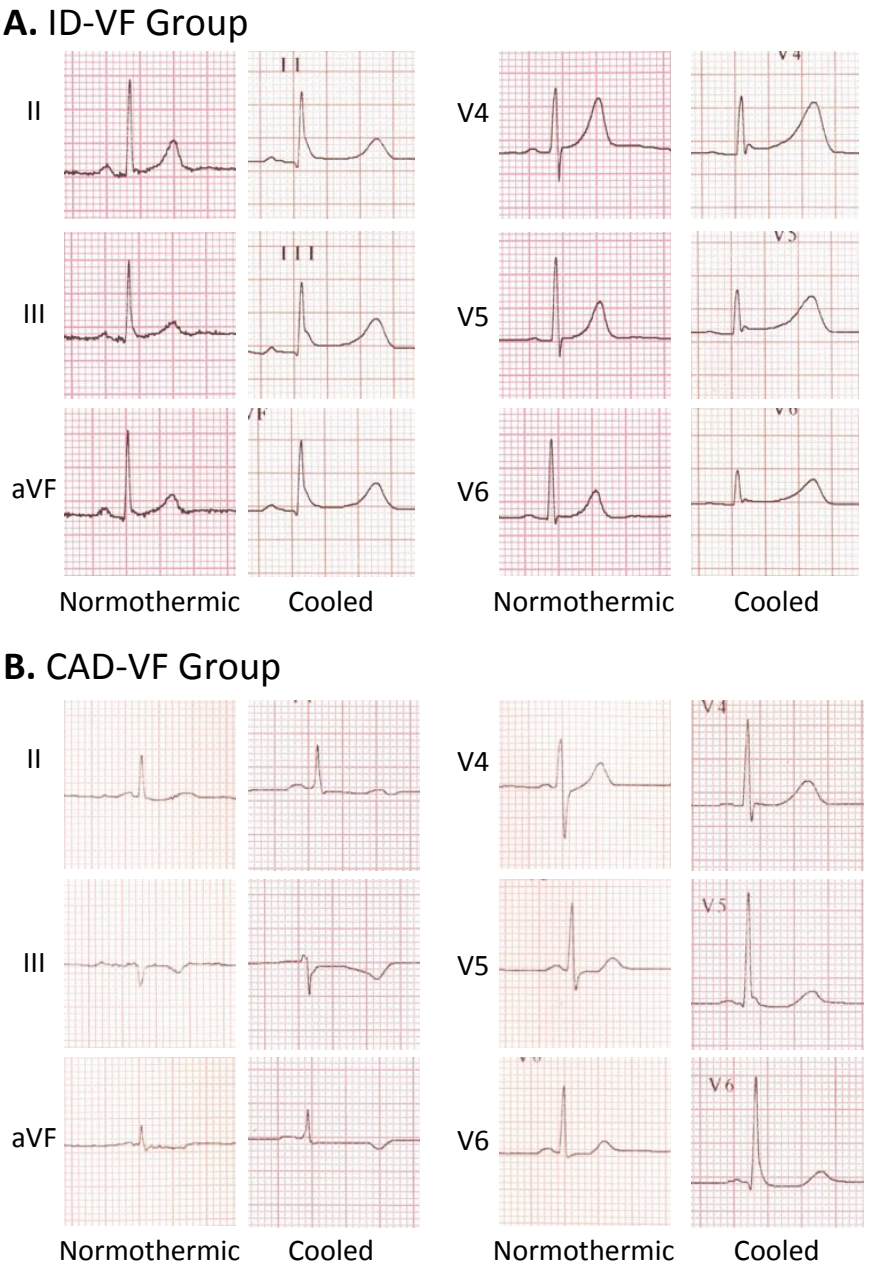

Figure 2-1 Early Repolarisation During Normothermia and Hypothermia

The early repolarisation pattern is minimal during normothermia (temperature 37ºC, leftmost 'baseline' ECGs of each panel) but substantially augmented during hypothermia (33ºC, rightmost 'cooled' ECGs of each panel). (A) In a single ID-VF patient, terminal QRS slurring combined with ST segment elevation is seen in the inferior leads and terminal QRS notching is seen in the lateral leads during hypothermia. (B) In a single CAD-VF patient, terminal QRS slurring develops in the lateral leads during hypothermia. Baseline/normothermic ECGs were obtained following rewarming after the period of therapeutic hypothermia.

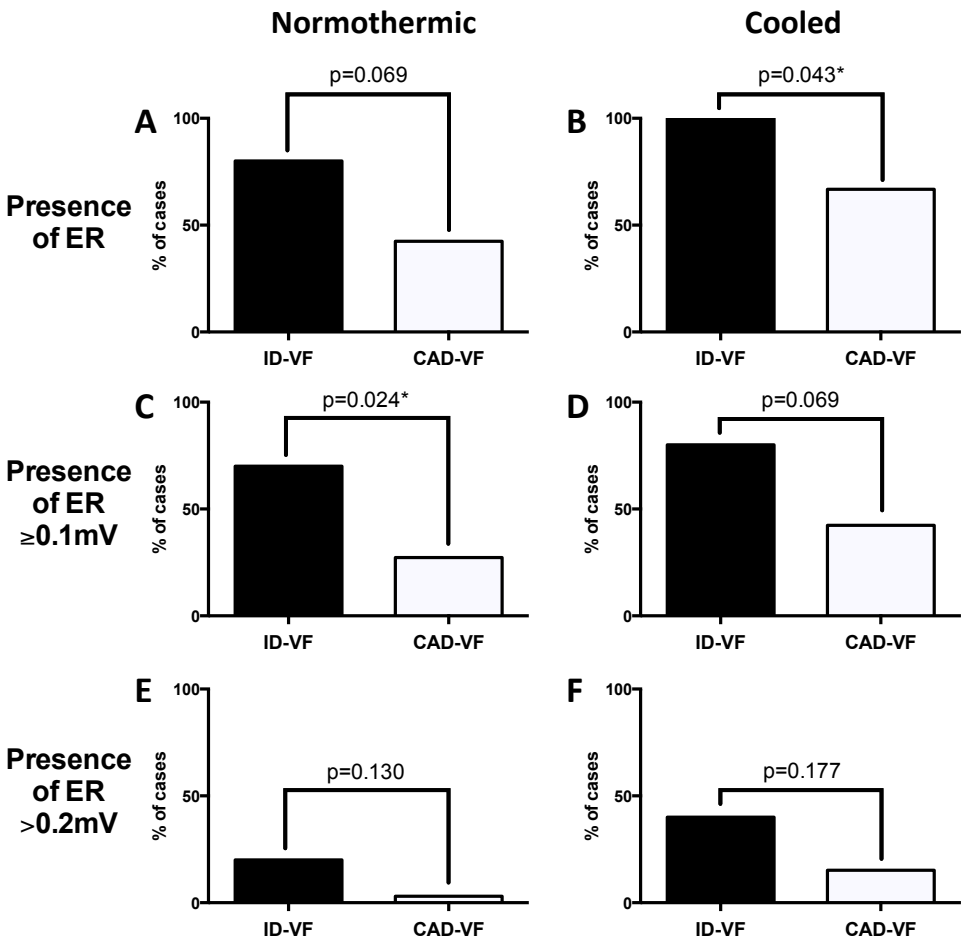

Figure 2-2. Prevalence of Early Repolarisation

The number of cases displaying early repolarisation (ER) at normothermia (left column) and when cooled (right column) is shown using thresholds of all ER (A and B), ER≥0.1mV (C and D) and ER>0.2mV (E and F). Baseline/normothermic ECGs were obtained following rewarming after the period of therapeutic hypothermia. VF indicates ventricular fibrillation; ID-VF, idiopathic VF; CAD-VF, coronary artery disease-related VF; * indicates statistical significance.

ST Segment Morphology in ID-VF and CAD-VF Arrest Survivors with ER

Considering only the cases with JPE ≥0.1mV (Figure 2-3), a greater proportion of the ID-VF group than the CAD-VF group (71.4% vs. 33.3%) displayed horizontal or down-sloping ST segments at baseline temperature. Similarly, in the CAD-VF group horizontal/down-sloping ST segments were more prevalent during hypothermia than at baseline temperature (53.8% vs. 33.3%). Neither of these differences reached statistical significance, possibly reflecting the small sample size. There was no difference between the ID-VF and CAD-VF groups in the proportion of patients with horizontal or down-sloping ST segments during hypothermia, or within the ID-VF group on cooling.

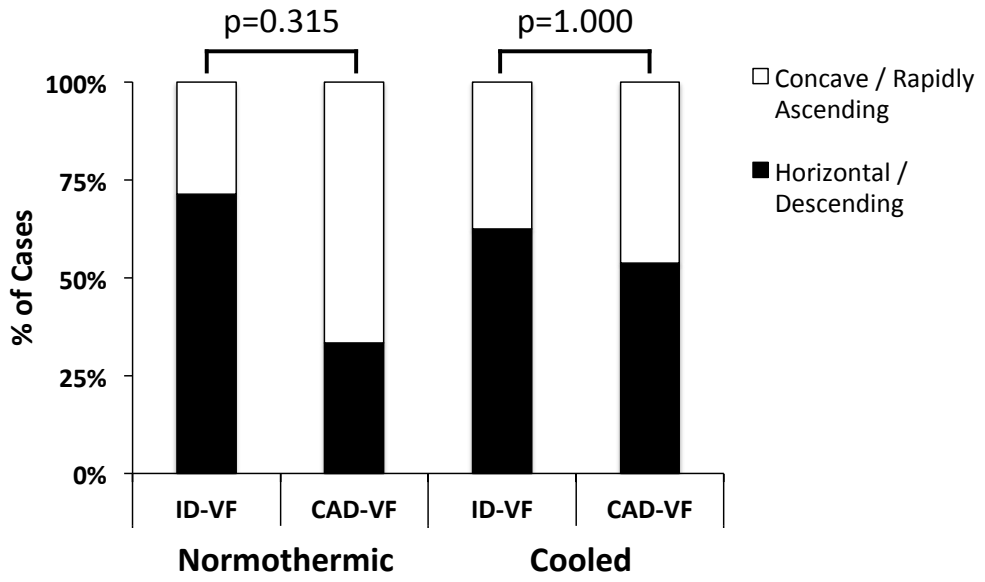

Figure 2-3. ST-segment Morphology in ID- and CAD-VF Survivors with Early Repolarisation (J-wave amplitude >0.1mV)

Proportion of cases with horizontal/down-sloping (high risk) vs. concave/up-sloping ST segments (benign) in each group at normothermia and while cooled are shown. ST segment morphology was defined according to criteria in (214). Baseline/normothermic ECGs were obtained following rewarming after the period of therapeutic hypothermia. VF indicates ventricular fibrillation; ID-VF, idiopathic VF; CAD-VF, coronary artery disease-related VF.

Temperature-dependent Amplitude of JPE in ID-VF and CAD-VF Arrest Survivors

Mean and maximum JPE amplitude were significantly greater amongst the ID-VF group, as compared to the CAD-VF group, both at baseline and during cooling (Table 2-2). Maximum, but not mean, JPE magnitude increased significantly on cooling in the ID-VF group (Figure 2-4A). Both mean and maximum JPE magnitude increased on cooling in the CAD-VF group (Figure 2-4B). There was no difference in the proportion of patients in the ID-VF group as compared to the CAD-VF group in whom JPE magnitude increased on cooling (6/10 vs. 16/33, P=0.72 for mean and 9/10 vs. 18/33, P=0.063 for maximum). Similarly, there was no difference in the magnitude of the increase in either mean or maximum JPE on cooling between the groups (ΔJPE, Table 2-2).

QRS duration and QTc intervals

QRS duration and QTc interval increased significantly on cooling in both the ID-VF and CAD-VF groups (Table 2-3). There were no differences in QRS duration or QTc interval between ID-VF and CAD-VF groups either during cooling or at baseline (all P>0.20).

Table 2-2. Magnitude of J-point Elevation

		Mean J-point elevation (mV)		
		ID-VF	**CAD-VF**	**P value**
Mean	**Baseline**	0.102 ± 0.021	0.042 ± 0.009	0.005 *
	Cooled	0.116 ± 0.018	0.070 ± 0.011	0.044 *
	Δ JPE	0.014 ± 0.053	0.028 ± 0.073	0.577
Maximum	**Baseline**	0.118 ± 0.024	0.053 ± 0.012	0.015 *
	Cooled	0.169 ± 0.029	0.099 ± 0.016	0.042 *
	Δ JPE	0.052 ± 0.065	0.046 ± 0.101	0.861

VF indicates ventricular fibrillation; ID-VF, idiopathic VF; CAD-VF, coronary artery disease-related VF; * indicates statistical significance.

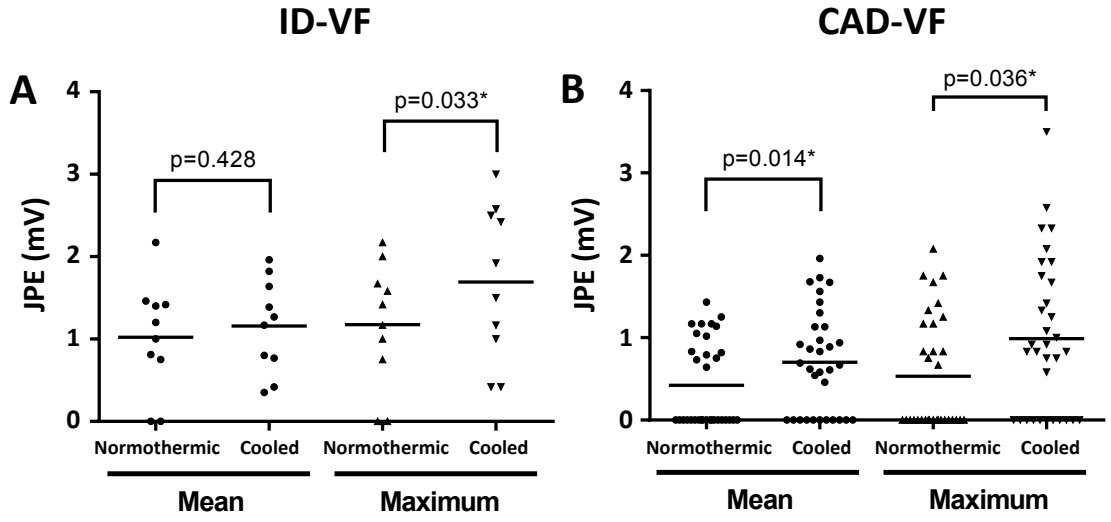

Figure 2-4. J-point Elevation at Baseline Temperature and During Hypothermia

Mean (circles) and maximum (triangles) J-point elevation at normothermia and during cooling in (A) ID-VF and (B) CAD-VF cases are shown as individual data points. Baseline/normothermic ECGs were obtained following rewarming after the period of therapeutic hypothermia. VF indicates ventricular fibrillation; ID-VF, idiopathic VF; CAD-VF, coronary artery disease-related VF; * indicates statistical significance.

Table 2-3. Other ECG parameters

		Duration (ms)		
		Baseline	**Cooled**	***P* value**
QRS duration	**ID-VF**	89.1 ± 2.3	97.9 ± 3.4	0.002 *
	CAD-VF	94.3 ± 2.2	100.5 ± 2.5	0.016 *
QTc interval	**ID-VF**	380.6 ± 37.9	493.2 ± 16.5	0.048 *
	CAD-VF	420.7 ± 4.6	472.6 ± 7.8	<0.001*

VF indicates ventricular fibrillation; ID-VF, idiopathic VF; CAD-VF, coronary artery disease-related VF; * indicates statistical significance.

2.4 Discussion

The main findings of this study are as follows. 1) Overall, ER was more common and of greater amplitude during cooling than at baseline. 2) ER amplitude was significantly greater in survivors of ID-VF arrest than survivors of CAD-VF arrest at all temperatures. 3) Whilst the prevalence of ER was not significantly increased in either group on cooling, mean JPE was increased by cooling only in survivors of CAD-VF arrest.

In recent years population-based studies have established an association between the early repolarization (ER) pattern and ventricular fibrillation (VF), whether idiopathic in nature or secondary to ischemia (118, 202, 204). At the same time, the tendency for hypothermia to result in similar electrocardiographic changes is well established (210, 211). Furthermore, in isolated cases therapeutic hypothermia itself has been described as potentially pro-arrhythmic (215). The previously common use of therapeutic hypothermia following cardiac arrest provided an important opportunity to examine in a systematic manner the impact of cooling on ER morphology in patients who have suffered either ID-VF or CAD-VF arrest. This retrospective cohort study therefore assessed the impact of therapeutic hypothermia on the prevalence, morphology and magnitude of ER in all ventricular fibrillation patients receiving therapeutic hypothermia at our critical care unit over a 7-year period.

A number of differences exist between this cohort and previously published descriptions of ER. Firstly, the overall frequency of ER in this study population is rather higher than that reported elsewhere. At baseline temperature 51% showed morphological ER. Even limiting to those patients with JPE ≥0.1mV, a widely accepted definition (118), the overall prevalence of ER in this cohort at baseline was still 37.2%. This prevalence is substantially higher than that seen in the European population overall (5%–13%) (198, 199) and also markedly higher than that described in a recent study of patients who had suffered cardiac arrests attributable to a variety of causes (3%) (216). The former likely reflects the high-risk nature of the patients in our study population and the latter differences in underlying causes for VF between our cohort and that reported in Rolfast *et al*'s study. During cooling 74% of our study population showed the ER pattern (51.2% at the 0.1mV JPE threshold). The prevalence of ER is well established to vary with core temperature: case series of patients with accidental hypothermia suggest that, given the

relatively mild degree of hypothermia used in a therapeutic setting, the prevalence of ER would be expected to be close to zero (217, 218). Rolfast *et al* report 30% prevalence in their study population during cooling.

Secondly, similarities and differences emerge between patients whose arrest was attributable to ID-VF, as compared to CAD-VF. Perhaps unsurprisingly, patients who suffered an episode of ID-VF were younger and apparently healthier than those who experienced CAD-VF. There were no differences in QRS duration or QTc between groups, though both parameters increased significantly on cooling. The latter finding has previously been established (218), with increased QTc having been described in the context of therapeutic hypothermia (216). The ER pattern was more common among survivors of ID-VF, as compared to CAD-VF, during cooling, though not at baseline temperature. Furthermore, JPE was of a greater magnitude in patients with idiopathic VF at both temperatures studied. Large magnitude JPE was seen more frequently among patients with ID-VF. This finding reached significance at baseline temperature but became less marked with the compounding influence of cooling. These observations are in keeping with a previous suggestion that the presence of ER in patients resuscitated following cardiac arrest is suggestive of a non-ischemic aetiology and that large-magnitude JPE is associated with a particularly high risk of idiopathic VF (198, 219).

This study was designed to identify differences in the effect of hypothermia between patients with ID-VF and CAD-VF. In this regard the study finds that cooling-related augmentation of J-point elevation was significant in the CAD-VF group but not the ID-VF group. This finding may be attributable to differences in the underlying mechanisms giving rise to ischemic ER, idiopathic ER or ER associated with hypothermia. Ischemic ER is most likely attributable to local activation of ATP-sensitive K^+ currents by ischemic mediators (220), and similarly idiopathic ER may result from augmentation of the transient outward current (I_{to}) resulting in a 'spike-and-dome' epicardial action potential notch and transmural voltage gradient early in repolarisation (209). Other currents influence phase 1 repolarisation and notably both blockage of I_{to} and augmentation of I_{CaL} can reduce J-point and ST segment elevation in experimental models (221). Alternatively, idiopathic ER may arise from local conduction delay causing regional dispersion of depolarisation and resulting in the same transmural gradient as before. Indeed J-point elevation associated with conduction slowing has been termed 'malignant' and may be associated with ventricular arrhythmia (222). Given these alternate mechanisms two

hypotheses arise as to the mechanism of hypothermia-induced augmentation of the ER phenotype: increased conduction delay vs. increased outward current during phase 1 repolarisation. Although the present study does not discern between these mechanisms a number of prior observations are made. In support of the conduction delay hypothesis, both severe (26°C) and therapeutic (32-34°C) hypothermia result in prolonged action potential duration (223) with significantly decreased conduction velocity (224), and on a cellular level severe hypothermia completely abolishes I_{to} (225). However in the post-ischemic setting, mild hypothermia has actually been shown to increase conduction velocity compared to the normothermic post-ischemic period (226) casting doubt on the conduction delay hypothesis as an explanation for J-point elevation augmentation in this study. In support of the altered repolarisation current hypothesis recent work in coronary-perfused canine left ventricular wedge preparations has found a key role for I_{to} in J-point elevation during hypothermia, especially in conditions modelling idiopathic ER (227). The pro-arrhythmic nature of hypothermia in the setting of the 'early repolarisation phenotype' in this model (arising from phase 2 re-entry) is consistent with reports of the pro-arrhythmic nature of therapeutic hypothermia in ER patients (215). Drugs inhibiting of I_{to} (e.g. quinidine) and augmenting I_{CaL} (e.g. milrinone) were able to reduce hypothermia-induced ER augmentation, suggesting that greater inhibition of I_{CaL} than I_{to} at the same level of hypothermia may leave I_{to} unopposed and able to accentuate the epicardial action potential notch (227).

It is also instructive to compare the present findings with other work examining the dynamicity of J waves in relation to heart rate. In one cohort, pause-dependent augmentation of J-wave amplitude was highly specific (but not sensitive) for the occurrence of idiopathic VF (207). Conversely in another cohort of non-VF patients, tachycardia (rather than bradycardia) augmentation of J waves was observed (228). Considering that I_{to} is known to be rate-dependent (209), decreasing at higher rates and increasing at lower rates, these observations support the hypothesis that early repolarisation in idiopathic VF is dependent on I_{to}. Similarly, I_{to} (or at least its surrogate, the epicardial action potential notch) is augmented by hypothermia (209). The fact that the J wave was augmented by hypothermia primarily in the CAD-VF group (but not the ID-VF) group in the present study may represent a capacity phenomenon whereby hypothermia augments the action potential notch in CAD-VF, which is already fully augmented in ID-VF. The observation that J-point elevation was greater during

normothermia in the ID-VF as compared to the CAD-VF group lends support to this hypothesis.

As will be seen later in this thesis, the combination of multiple substrate characterisation techniques may frequently be the most revealing of the underlying arrhythmia mechanism. Two recent studies serve to illustrate this point. By using CMR imaging to examine the association between ER and ventricular morphology in the absence of known structural heart disease, the presence of J-waves has been associated with abnormalities of right (but not left) ventricular morphology and function (229). Although this study did not provide any prospective follow-up data it does lead to the important hypothesis that structural right ventricular changes may help to identify patients with the ER phenotype who are at highest risk of future syncope and/or sudden cardiac death. Similarly, ECGI has been applied in patients with idiopathic VF associated with ER, and has identified areas of abnormally short activation-recovery intervals (reflecting short action potential duration) in the right ventricle (230). As with the CMR study of Takeuchi *et al*, this second study supports the hypothesis that idiopathic VF with the ER phenotype could be a right ventricular disease. However, PVC's mapped in these patients originated from the inferolateral LV, and in a further patient with idiopathic VF and ER, VF rotors anchored in the inferior-lateral LV wall (231). Given the variability of these findings, and lack of prospective follow-up data, the role of ECGI in risk stratification of ER phenotype remains to be determined.

Limitations

While this study reports the association between ER and both idiopathic and CAD-related VF, the mechanisms underlying arrhythmia in either setting cannot be conclusively identified. Traditionally ER has been associated with arrhythmia initiated by phase 2 re-entry (221, 232). It is possible, however, that patients in the CAD-VF group who had previously experienced a myocardial infarction (one third of this group) might in fact have suffered an episode of scar-related VT that subsequently deteriorated into VF. Patients in the idiopathic VF group were younger than those in the CAD-VF group. Since the prevalence of early repolarization decreases with age (233) it is possible that this confounding factor could have contributed to some of the differences observed between the ID-VF and CAD-VF groups. Finally, the baseline (normothermic) ECGs were obtained following rewarming after the arrest. Whether the same results would have been seen had pre-morbid baseline ECGs been available is not known.

2.5 Conclusions

In conclusion, the data presented in this chapter indicate that early repolarization is more strongly associated with idiopathic VF than with coronary artery disease related VF. Hypothermia increases both the prevalence and magnitude of early repolarization in cardiac arrest survivors: however, the mean amplitude of J-point elevation is increased in survivors of coronary artery disease related VF, but not of idiopathic VF.

In this chapter, I explored the use of the surface ECG to risk stratify a candidate substrate for ventricular arrhythmias. In the next chapter, the role of intracardiac electrogram analysis in the diagnosis atrial arrhythmias is examined and Aim C2 (*determine the optimal point sampling density for intra-cardiac contact mapping in the diagnosis of tachycardia mechanism in a variety of atrial tachycardias*) is addressed.

3 Intra-Cardiac Mapping: Optimized Local Activation Time Sampling Density

3.1 Introduction

In the last chapter the role of the surface ECG in arrhythmia substrate characterisation was examined. It has long been recognised that the surface ECG lacks resolution for the accurate diagnosis of both ventricular and atrial arrhythmias, and this limitation eventually resulted in the development of electroanatomic mapping systems capable of recording intracardiac electrograms and facilitating invasive arrhythmia treatments with catheter ablation techniques. Local activation time (LAT) mapping (see Intracardiac Contact Mapping, p. 31) using electroanatomic mapping systems now forms the cornerstone of invasive diagnosis of complex atrial arrhythmias.

The creation of LAT maps to determine the mechanism of an atrial tachycardia (AT) involves four key steps: 1) creation of a three dimensional model of the anatomy, 2) analysis of intracardiac electrograms to identify activation time relative to a fixed temporal reference, 3) interpolation of the activation times across the anatomical model and 4) representation of the interpolated data across the anatomical model, usually in the form of a color map.

Although the underlying technologies providing spatial localization differ between systems (magnetic-, impedance- and electric field-based), all contemporary EAM systems provide a number of core functionalities including cardiac chamber representation, catheter localization and electrophysiological data representation. Anatomic accuracy of LA electroanatomic chamber models has been compared to cross sectional imaging with CT/MRI (234), showing faithful representation of pulmonary vein dimensions and geometry. Similarly, catheter localization has been assessed both *in vitro* and *in vivo* in animal models and human subjects and has been shown to be both reproducible and highly accurate (235, 236). Despite these reports, it is notable that to date there are no studies examining the electrical accuracy of interpolated LAT maps generated with point-by-point contact mapping. Rather, recommendations on the number of sampling locations required to create an accurate map are primarily based on operator

experience (237). At the same time device manufacturers continue to innovate to increase the achievable resolution of mapping systems (238–241). Meanwhile the end goal of achieving effective diagnosis and treatment whilst minimizing procedure times for patients remains. To this end this study presents an optimal point sampling strategy for atrial arrhythmias, based on systematic analysis of *in silico* and *in vivo* LAT mapping data. The relative impact of chamber geometry complexity and activation pattern complexity on the optimal sampling density for mapping the arrhythmia is also examined.

3.2 Methods

Atrial Monolayer Model

A 4x4cm atrial tissue model was meshed using triangular elements (84,346 triangles, 42,511 nodes, average edge length Δl=0.2 mm). At each node the atrial cell membrane model developed by Nygren *et al* (242) was implemented which, in tissue simulations, is characterized by the propagation of stable re-entrant waves (97). Anisotropic conduction, with fibre orientation parallel to the *x*-axis, was used between nodes with longitudinal and transverse conductivities of 0.28 S/m and 0.026 S/m for focal and linear activation. Isotropic conduction with equal conductivities of 0.15 S/m was employed for re-entrant and spiral wave activation. Following the application of voltage stimuli (see below), electrical propagation was determined by solving the monodomain system of equations with a time step of Δt=25 ms. The Cardiac Arrhythmia Research Package (103) was used to perform atrial tissue simulations.

All stimuli were applied as transmembrane voltages (-1000mV, 1ms duration). To create uniform linear activation, a 2mm region at the left edge of the tissue was stimulated. To create focal activation a 1x1mm region close to the centre of the monolayer was stimulated. To create re-entry, a circular non-conducting region (diameter 1.5cm) was introduced at the centre of the monolayer. A dual stimulus protocol was used to initiate re-entry by delivering the second stimulus at a critical time point when half of the stimulated region remained refractory. To create spiral wave activation, two linear stimuli were used. The first stimulus activated the full height of the monolayer in a linear fashion from the leftmost edge whilst the second, critically timed stimulus, being only ¾ height initiated spiral wave re-entry. *In silico* isochronal maps were constructed from the transmembrane potential fields by calculating the time elapsed between a fixed temporal

reference and the time at which the transmembrane potential exceeded a pre-defined voltage threshold (-20mV).

In Vivo Procedures

A total of 26 electroanatomic maps were included in the analysis. Isochronal local activation time maps were created using the Carto 3 mapping system (Biosense Webster, Diamond Bar, CA, USA) by taking the activation time at each acquired point as the time from reference activation (typically an atrial coronary sinus electrogram) to earliest activation on the bipolar mapping catheter signal.

Animal Studies

Animal studies complied fully with Danish law on animal experiments. Eight male Göttingen mini-pigs (41.2±7.2kg) were pre-sedated with intramuscular azaperone (4mg/kg) and midazolam (0.5mg/kg). General anaesthesia was induced with intravenous ketamine (5mg/kg) and midazolam (0.5mg/kg), and the animals were intubated and mechanically ventilated. Anaesthesia was maintained with a continuous intravenous infusion of propofol (3mg/kg/h) and fentanyl (15μg/kg/h). Two 8F sheaths were placed percutaneously in the right femoral vein, followed by an intravenous injection of 100IU/kg heparin. Fluoroscopy was used to position a 6F decapolar reference catheter in the coronary sinus (CS) and a 7.5F ablation catheter was advanced to the RA and used to create a LAT map during proximal CS pacing. Incomplete inter-caval linear ablation was performed, with an approximately 5mm conduction gap positioned at the centre of the linear lesion, before repeat LAT mapping of the new activation detour.

Human Studies

Ten patients undergoing ablation for left atrial tachycardia were studied. Data collection for this study was part of ongoing real-time data collection processes during physician-directed patient care. All procedures were performed under general anaesthesia. Following trans-septal puncture, a 20-pole circular mapping catheter (Lasso Nav, Biosense Webster, Diamond Bar, CA, USA) was advanced and used to create a 3D geometry of the left atrium. High-density local activation time maps were constructed during tachycardia using points acquired with the ablation catheter. Coverage of the entire LA was ensured, even once tachycardia mechanism was established, with a mean number of points per map of 355±137, corresponding to a sampling point density of 2.5±0.8

points/cm^2. Local activation times were automatically assigned and all points were re-annotated to ensure correct identification of the first component of each atrial electrogram.

Local Activation Map Construction

Re-interpolated LAT maps (for both *in silico* and *in vivo* studies) were created by down-sampling the number of acquired points and performing bilinear interpolation of the resulting activation field across the 2D domain for the simulated activation patterns or 3D geometry (i.e. electroanatomic shell) for the clinical tachycardias. When performing re-interpolation on the clinical datasets, a distance threshold of 10mm was used meaning that the interpolant was only interrogated for mesh nodes lying within 10mm of an original mapped point. Points beyond this distance were assigned indeterminate local activation times and are represented as grey in the accompanying figures.

LAT Map Accuracy Quantification

For simulated activation patterns the reference map was defined as the high-resolution isochronal map created from the activation times calculated at every node. For clinical activation patterns the reference map was defined as the LAT map created by the clinical mapping system (Carto 3, Biosense Webster, Diamond Bar, CA, USA) using all available LAT points. Reference and re-interpolated maps were compared quantitatively by computing the sum of squared differences between activation times at every mesh node within a distance threshold of 10mm of an original sampling point. Results are presented per node in order to normalize for inter-case differences in the number of nodes per geometry.

Optimal Sampling Density Measurement

The optimal sampling density for each LAT map (simulated and clinical) was defined as the lowest sampling density that resulted in an error reduction rate of less than 0.05ms per mesh node per additional point sampled. This measurement was made as shown in Figure 3-1. Firstly, each map was re-interpolated with point sampling densities in the range 0.25 to 10 points/cm^2 (step size 0.125 points/cm^2, repetitions = 10). The mean LAT map accuracy (see above) for each density was plotted against sampling density and a power series of the form $f(s) = as^b + c$ was fitted to the resulting mean accuracies (where s is the sampling density). Taking the first derivative of this power series (i.e. $f'(s) = abs^{b-1}$) gives the relative improvement in map accuracy per additional point sampled. Finally, this equation was solved for $f'(s) = -0.05$ in order to determine the

sampling density at which minimal further improvement in map accuracy is achieved by further point sampling.

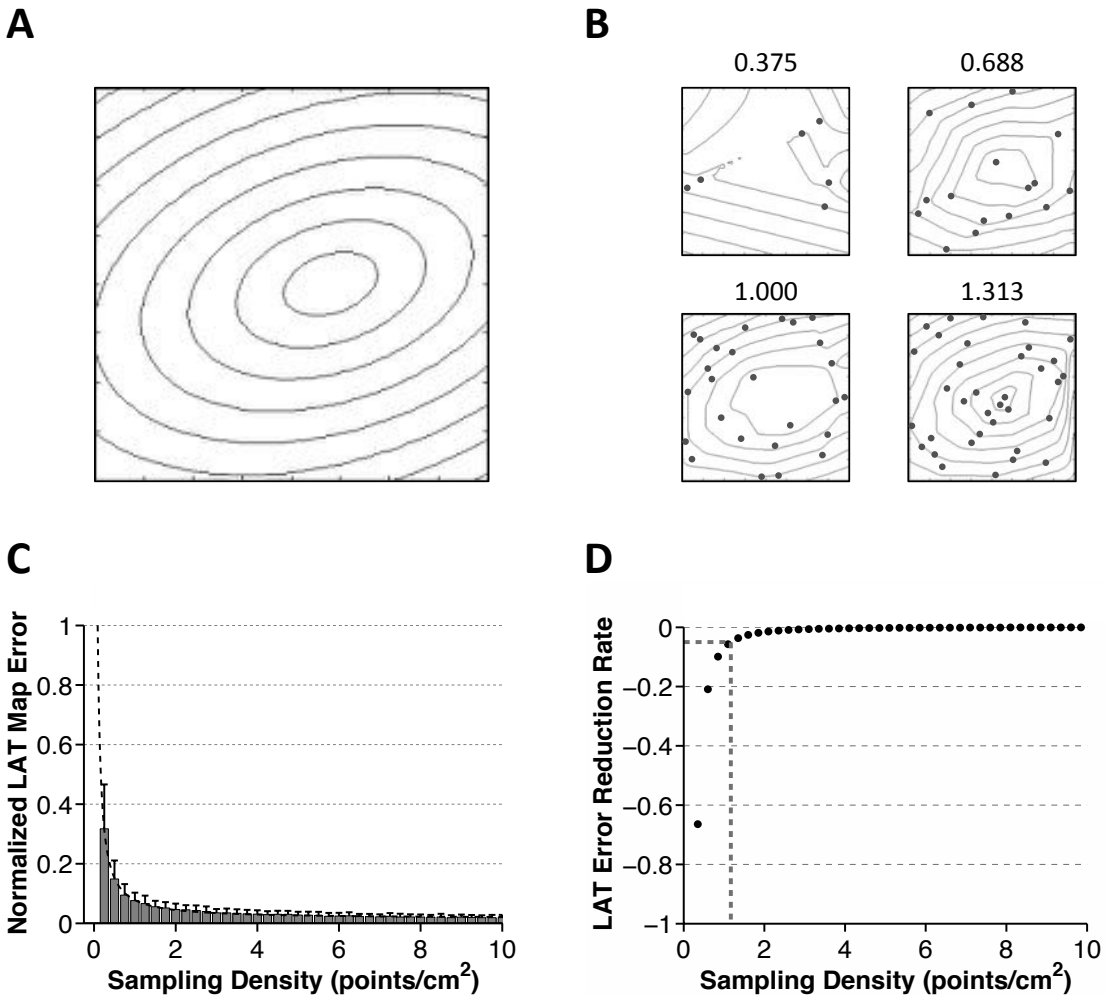

Figure 3-1. Determination of Optimal Sampling Density

A – The process is shown for a focal tachycardia in a 4x4cm monolayer with fibre orientation of 18 degrees to the *x*-axis. **B** –Activation times are re-sampled at increasing sampling density and regional activation is re-interpolated to give the resulting 'down-sampled' activation maps. **C** – Mean normalized LAT map error at each sampling density is calculated by comparing activation times at each node with the original activation times in A. **D** – Taking the first-derivative of the curve in C indicates the sampling density at which minimal further improvement in map accuracy is generated.

Data Analysis and Statistics

Custom software was written for determining the optimal sampling point density (MATLAB 8.2, The Mathworks Inc., Natick, MA). Subsequent data analysis was performed using GraphPad Prism version 6.0c (GraphPad Software, San Diego, California, USA, www.graphpad.com). Results are presented as mean±SD. Student's

unpaired *t*-test was used to compare group mean. A significance level of $P<0.05$ was considered statistically significant.

3.3 Results

Simulated Activation Patterns

Four simulated activation patterns were studied (linear, focal, spiral-wave and re-entrant activation). Initiation of these activation patterns is shown in Figure 3-2. Reference LAT maps were created from local activation times defined at every mesh node, resulting in a sampling density of ~2500 points/cm^2. In the case of linear and focal activation, local activation times were taken as the first activation of each node. In the case of spiral and re-entrant activation, a window of interest (WOI) incorporating 100% of the tachycardia cycle length (TCL) was defined. Calculated optimal sampling densities (Figure 3-7A) for focal, spiral-wave and re-entrant activation patterns were 1.09±0.14 points/cm^2, 1.44±0.49 points/cm^2, and 1.50±0.34 points/cm^2, respectively. Linear activation in a 2-dimensional domain represents a special case where map accuracy is independent of sampling density Figure 3-3.

Examples of re-interpolated isochronal LAT maps at sub-optimal, optimal and supra-optimal sampling densities for focal, re-entrant and spiral-wave activation patterns are shown in Figure 3-4, Figure 3-5 and Figure 3-6, respectively. For the focal activation pattern, sub-optimal sampling density resulted in incorrect focus localization. For the re-entrant activation pattern, sub-optimal sampling density resulted in an activation pattern more consistent with a focal source. Finally, sub-optimal sampling of the spiral-wave activation pattern failed to reveal rotational activity in the resulting re-interpolated map. Notably, in each case, there was limited morphological improvement in the isochronal map appearances at supra-optimal compared to optimal sampling densities (compare maps boxed in black in Figure 3-4, Figure 3-5 and Figure 3-6).

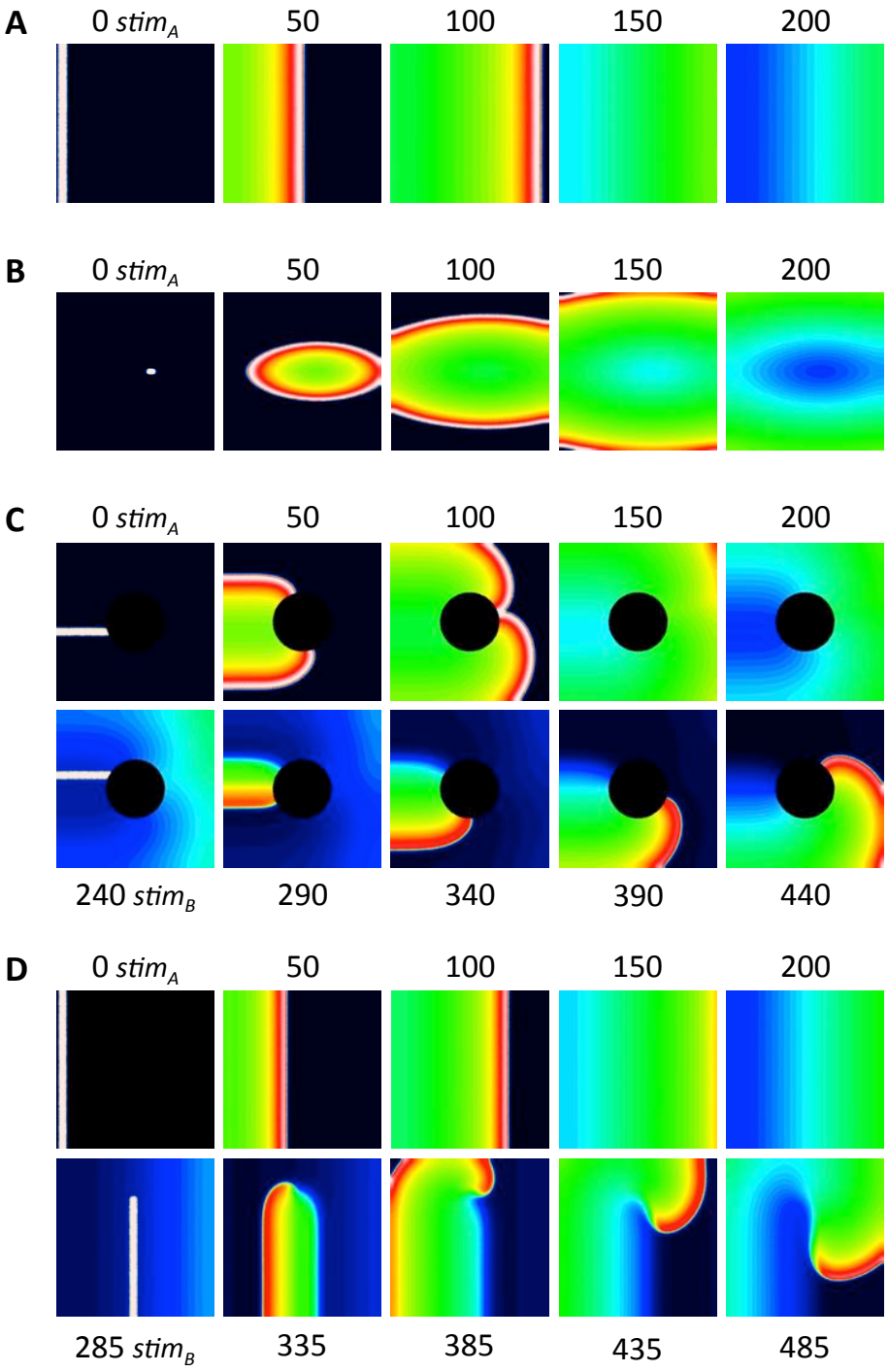

Figure 3-2. Initiation of Activation Patterns in the Atrial Monolayer

Initiation of the four atrial activation patterns studied is shown. **A** – linear activation; **B** – focal activation; **C** – re-entrant activation; **D** – spiral wave activation. Simulated regions are shown in white in the left-most column of each row.

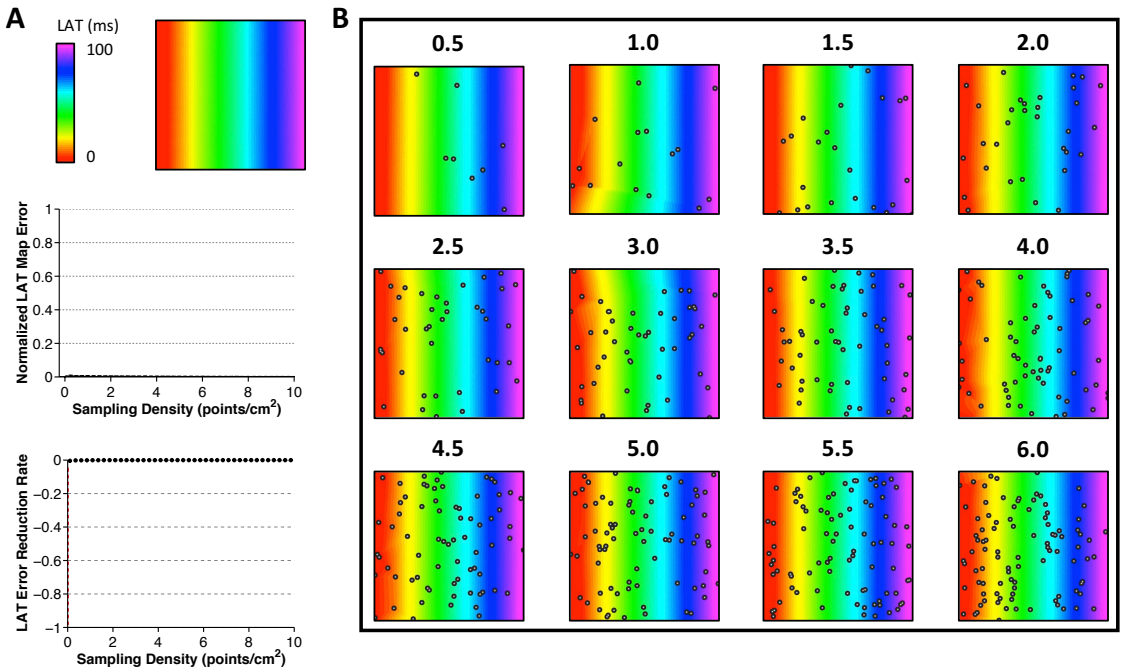

Figure 3-3. Calculation of Optimal Sampling Density for Linear Activation

Determination of optimal sampling density for linear activation is shown. **A** – (Top) Original activation pattern. (Middle) Re-interpolated LAT map errors. (Bottom) LAT map error reduction rate. **B** – Examples or re-interpolated maps at 0.5point/cm^2 intervals (red border – sub-optimal density; green border – optimal density to nearest 0.5points/cm^2; black border – supra-optimal density)

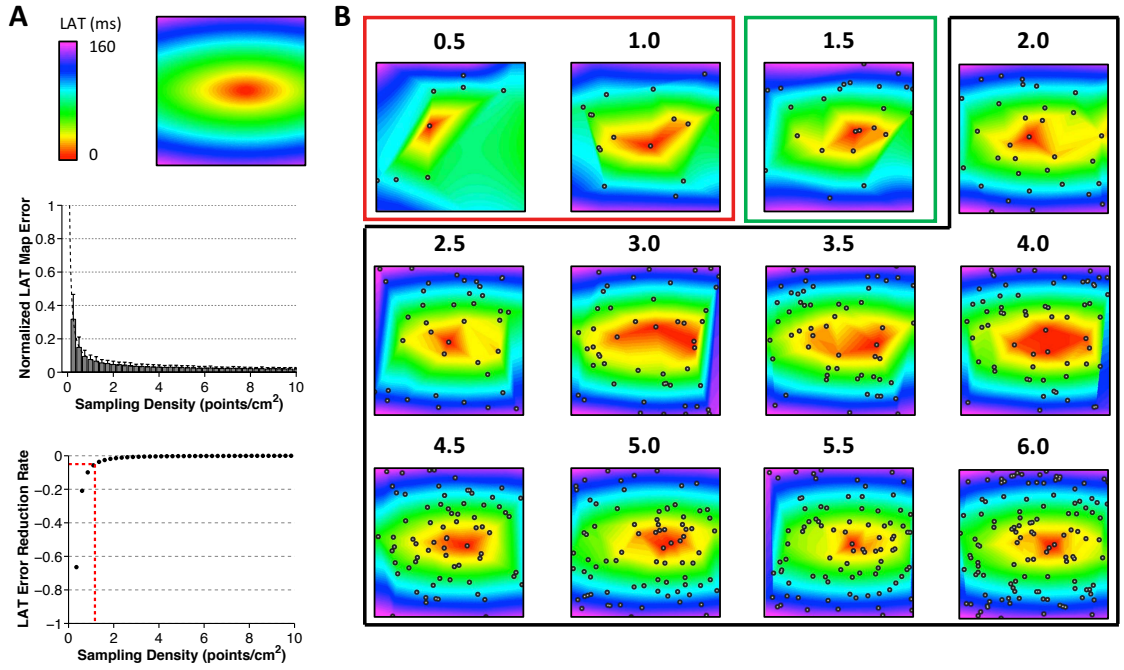

Figure 3-4. Calculation of Optimal Sampling Density for Focal Activation

Determination of optimal sampling density for linear activation is shown. **A** – (Top) Original activation pattern. (Middle) Re-interpolated LAT map errors. (Bottom) LAT map error reduction rate. **B** – Examples or re-interpolated maps at 0.5point/cm^2 intervals (red border – sub-optimal density; green border – optimal density to nearest 0.5points/cm^2; black border – supra-optimal density)

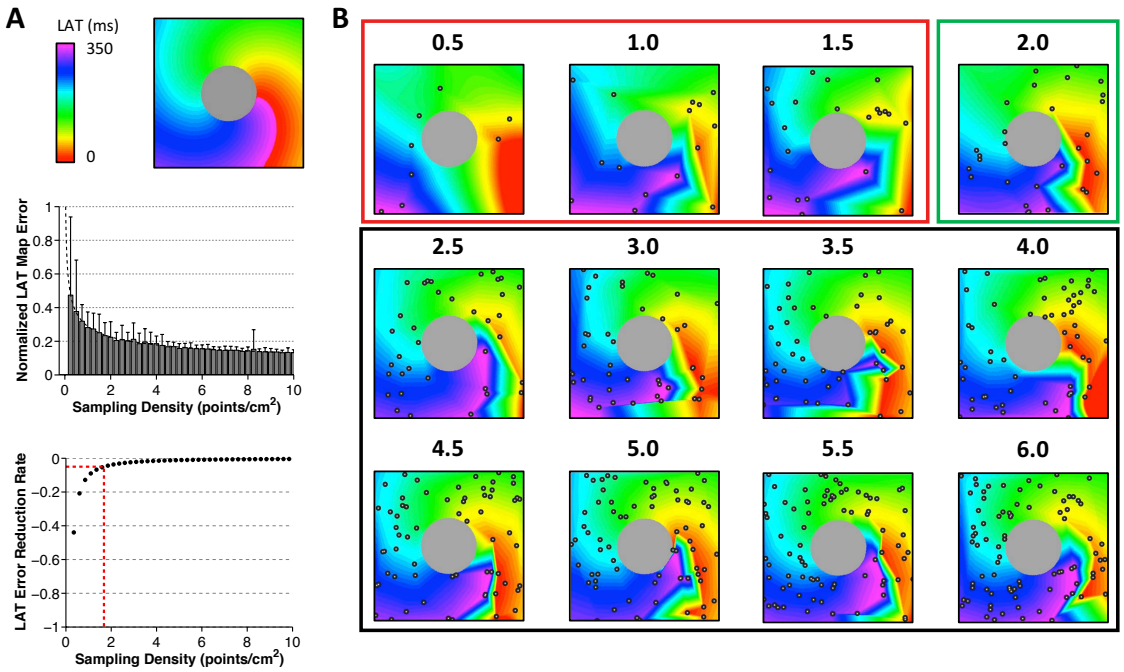

Figure 3-5. Calculation of Optimal Sampling Density for Macro-re-entry

Determination of optimal sampling density for linear activation is shown. **A** – (Top) Original activation pattern. (Middle) Re-interpolated LAT map errors. (Bottom) LAT map error reduction rate. **B** – Examples or re-interpolated maps at 0.5point/cm^2 intervals (red border – sub-optimal density; green border – optimal density to nearest 0.5points/cm^2; black border – supra-optimal density)

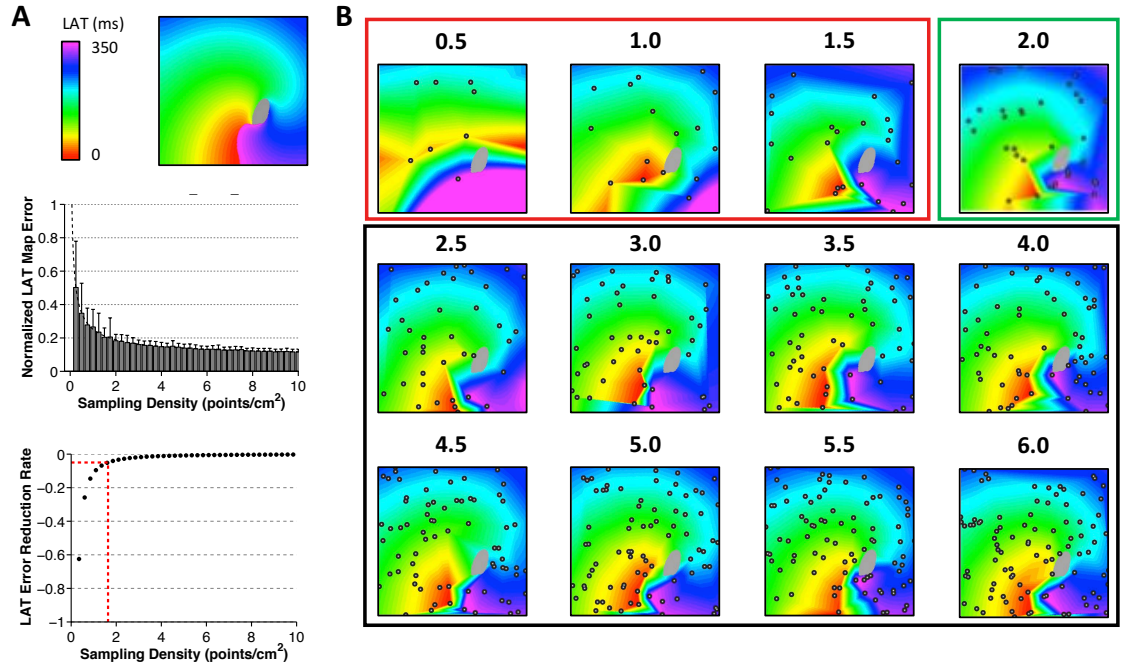

Figure 3-6. Calculation of Optimal Sampling Density for Spiral Wave Activation

Determination of optimal sampling density for linear activation is shown. **A** – (Top) Original activation pattern. (Middle) Re-interpolated LAT map errors. (Bottom) LAT map error reduction rate. **B** – Examples or re-interpolated maps at 0.5point/cm^2 intervals (red border – sub-optimal density; green border – optimal density to nearest 0.5points/cm^2; black border – supra-optimal density)

Clinical Left Atrial Tachycardias

Ten clinical left atrial tachycardias were studied (focal tachycardia, n=2; localized re-entry, n=3; macro-re-entrant tachycardia, n=5). The mean LA surface area calculated from the electroanatomic shells was 151±26cm^2 with an original sampled point density of 2.3±0.9points/cm^2. There was a trend toward higher optimal sampling densities for localized re-entry and macro-re-entry tachycardias (Figure 3-7B) but this difference did not reach statistical significance (calculated sampling densities 0.96±0.11 points/cm^2 for focal tachycardias, 1.15±0.39 points/cm^2 for macro-re-entrant tachycardias and 1.30±0.35 points/cm^2 for localized re-entry, P=0.5968). The focal tachycardia maps re-interpolated at optimal density (i.e. LAT error rate reduction <0.05ms/node/point) resulted in correct localisation of the foci of earliest activation (Figure 3-8A); anterior to the right veins in one case and posterior to the right veins in the other. In the re-entrant tachycardias (Figure 3-8B) re-interpolation at optimal sampling density resulted in the same overall map appearance, with the same macro-re-entrant circuit remaining identifiable. However, some variations in map appearance at the extremes of interpolation (e.g. beyond the pulmonary vein ostia) were identifiable. The localized re-entrant maps re-interpolated at optimum sampling density (Figure 3-8C) were remarkably similar in appearance to the original maps; but again some variations were evident in activation timing interpolated into the left-sided pulmonary veins in one case.

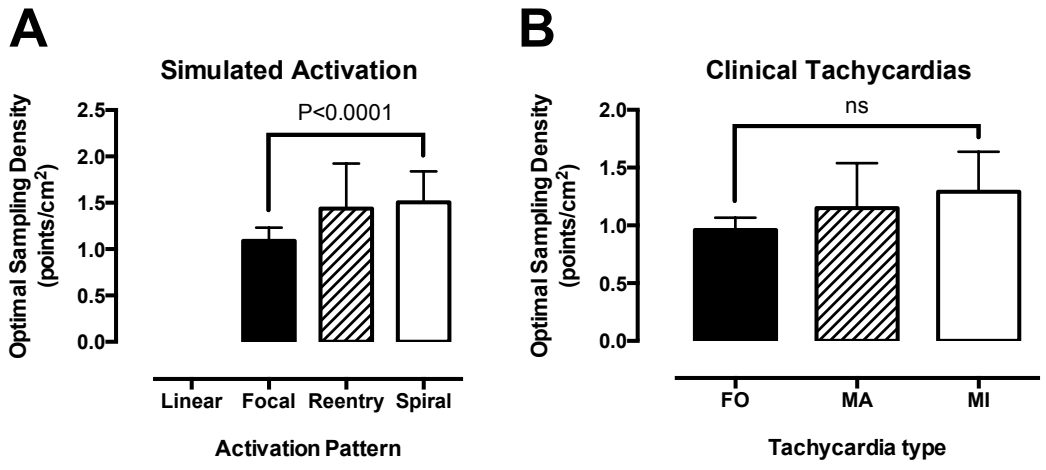

Figure 3-7. Optimal Sampling Densities

Calculated optimal sampling densities are shown for simulated activation patterns (**A**) and clinical tachycardias (**B**). FO = focal origin; MA = macro re-entry; MI = micro (localised) re-entry.

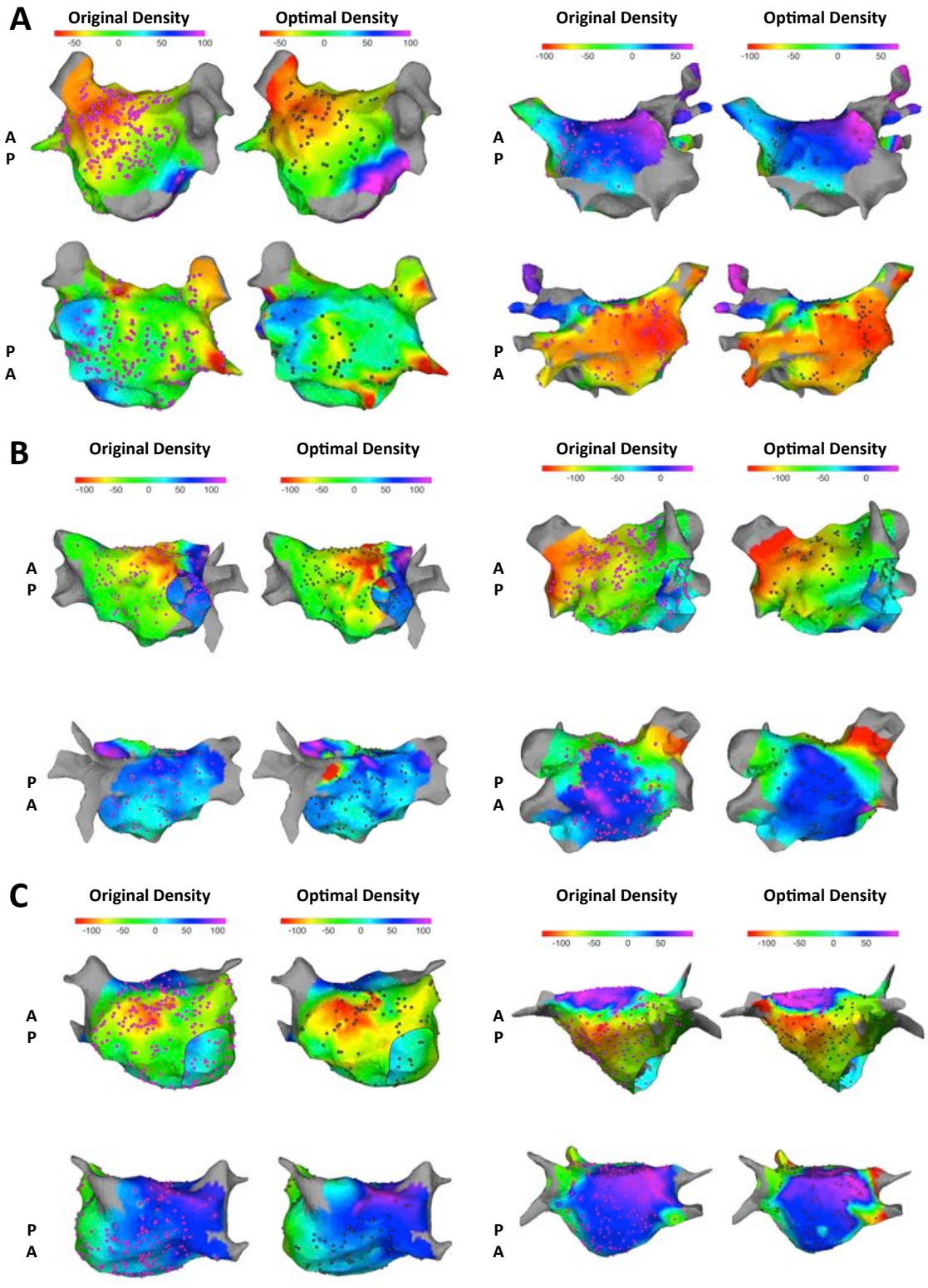

Figure 3-8. Clinical Isochronal Local Activation Time Maps

Local activation time maps for 6 example clinical tachycardias are shown. **A** – focal activation; **B** – macro-re-entry; **C** – localised re-entry. Two cases are shown per row in anterior-posterior and posterior-anterior projection. Left-most maps of each pair are the original isochronal maps produced at the time of the clinical procedure with purple dots representing sampled LAT point locations. Right-most maps of each pair are the re-interpolated maps generated at the calculated optimal sampling densities with black dots representing the re-sampled LAT point locations.

Porcine Right Atrial Activation and Chamber Geometry Complexity

Eight pre-ablation LAT maps created under proximal CS pacing were studied. In the absence of ablation, activation proceeded superiorly in a linear fashion around the tubular right atrium in all cases. After incomplete inter-caval linear ablation, a new activation detour was evident in all maps (see Figure 3-9). Mean pre-ablation optimal LAT sampling density was 0.45±0.13 points/cm^2 and mean post-ablation optimal LAT sampling density was 0.78±0.17 points/cm^2. Increasing activation morphology complexity resulted in a significant increase in the optimal LAT sampling density (P=0.0008). Even in the setting of increased activation complexity introduced by the presence of incomplete linear ablation, the overall optimal point sampling density for the geometrically-simple porcine right atrium (0.78±0.17 points/cm^2) was significantly less than that for the geometrically-complex human left atrium (1.2±0.37 points/cm^2) (P=0.0001).

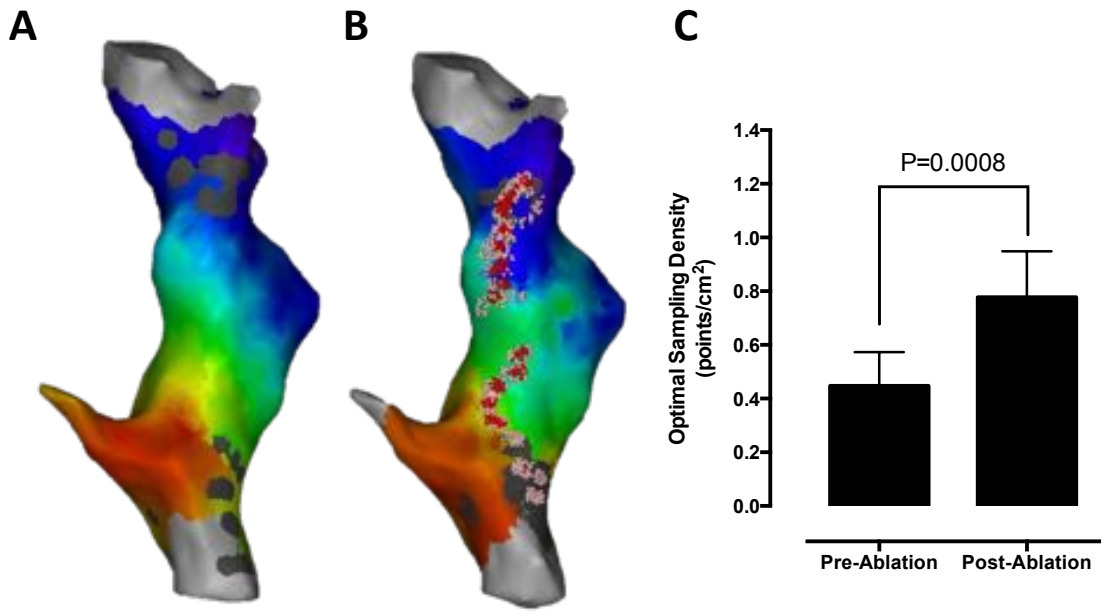

Figure 3-9. Porcine Right Atrial LAT Maps

A – Pre-ablation LAT shows uniform activation across the chamber from coronary sinus towards the right atrial appendage. **B** – Post-ablation LAT shows a new activation detour via the mid-chamber gap in the ablation line. **C** – Comparison between optimal sampling density for pre- and post-ablation LAT maps.

3.4 Discussion

The main findings of this study are as follows: 1) optimal sampling densities can be identified for a variety of tachycardia mechanisms to maximize the diagnostic yield of interpolated local activation time maps; 2) optimal sampling density is dependent on activation pattern with greater sampling densities often required to correctly reveal more

complicated activation sequences including macro-re-entry and spiral-wave activation; 3) optimal sampling density is also dependent on chamber geometry, with increasing geometric complexity necessitating an increased optimal sampling density; 4) for both focal and re-entrant clinical left atrial tachycardias there appears to be no additional benefit in performing LAT sampling at a density greater than 1.5 points/cm^2.

The aim of tachycardia activation mapping is two-fold: to determine the arrhythmia mechanism and thereby inform an ablation strategy. The ablation strategy is guided by the site of tachycardia origin (focal mechanism) or a critical isthmus of conduction (re-entrant mechanism). Three-dimensional electro-anatomic mapping systems provide a framework for visualization of electrical activation sequences as an aid to identifying the tachycardia mechanism and corresponding ablation target. Recent technological advances have enabled significant increases in the spatial resolution achievable within reasonable timescales with both established (243) and emerging (244) contact mapping platforms.

Whilst high sampling density is clearly important for substrate-mapping accuracy, for example in identifying areas of low voltage or fractionated signals (245–247) important to arrhythmogenesis, it is not known whether high-resolution mapping results in clinical benefit during activation mapping, where the primary aim is to reliably identify the tachycardia mechanism. Indeed high-resolution activation mapping is at odds with earlier strategies aiming to minimize procedure time without impacting success by providing a logical framework for directing the acquisition of LAT points (248). To this end, this study shows that in systems using interpolation methods to create isochronal LAT maps from a number of sampled LAT times, a theoretical maximal sampling density is reached at which further clinically-relevant improvements in LAT map accuracy are minimal. By using both simulated data in addition to clinical data this study has demonstrated that maximal sampling density is within the same range (0.9-1.5 points/cm^2) irrespective of the resolution at which the 'gold standard' activation sequence is defined.

The identification of atrial spiral-waves has received renewed attention recently as a strategy to identify ablation targets in atrial fibrillation (161, 249). Whilst rotors have been identified in animal (154) and computer models (250, 251) of atrial activation, there is some debate as to which technologies can reliably detect the occurrence of rotational activity in vivo (74, 252, 253). Clinical approaches to identifying rotors typically involve phase mapping in order to average activation over many cardiac cycles. This approach has successfully identified rotors in the left atrium using a 64-pole basket catheter (254).

Taking atrial endocardial surface area to be 150 cm^2 (as in this study) and assuming maximal electrode contact this equates to a sampling density of only 0.43 points/cm^2. Furthermore, suboptimal contact of the basket catheter results in even lower sampling densities (e.g. 56 electrodes equates to 0.37 points/cm^2, 48 electrodes to 0.32 points/cm^2 and 32 electrodes to 0.21 points/cm^2). All of these densities are below the optimal sampling density for spiral-wave activity identified in this study. Of note an alternative approach using dynamic voltage mapping applied to identical clinical data failed to identify sustained rotational activity in 100% (n=11) of cases (253). This result is consistent with our finding that a significantly higher sampling density of around 1.5 points/cm^2 should be required to optimally reproduce spiral-wave activity from known local activation time points.

The results presented here should not be interpreted to indicate that sampling densities above 1.5 points/cm^2 are never of clinical benefit in activation mapping. One limitation of the 'optimally' resampled clinical maps shown in Figure 3-8 is that interpolation at regions distant to the body of points (e.g. extending into the pulmonary veins or LAA) may be inaccurate. In such circumstances a local density of greater than 1.5 points/cm^2 may well be required to correctly identify the origin of a focal tachycardia. The results of this study support the argument that once an upper global sampling density of 1.5 points/cm^2 has been reached (equivalent to around 225 points for a typical LA with endocardial surface area of 150cm^2) then the tachycardia mechanism should be evident or strongly suggested. In the event where this is not the case rather than collecting further points a better approach may be to begin a new activation map perhaps with a different window of interest, reference electrogram or LAT assignment technique.

Limitations

1) In calculating the optimal sampling density for clinical tachycardias it is not possible to completely separate the effects of activation sequence complexity and chamber geometry complexity. For example, a more complex geometry in the context of an identical tachycardia may require a higher optimal sampling density. This may explain the variation in macro-re-entrant sampling densities indicated in Figure 3-7B. Similarly, regional geometric differences (e.g. PV insertion angles and geometric map resolution) may contribute to inaccuracies in the calculated optimal sampling densities.

2) A practical limitation involves the identification of 'gold standard' references maps for the clinical cases. The interpolation algorithm implemented by the commercial mapping platform is likely to have differed from the bilinear interpolation algorithm employed here. Whilst this would lead to a systematic error in the error value for an interpolated activation map it should not change the identification of the optimal sampling density (map accuracy improvement with additional sampling points (i.e. Figure 3-1D) should remain unchanged).
3) The question of whether the same optimal sampling densities would be found in other settings (e.g. complex multiple re-entry or geometrically complex ACHD cases) has not been addressed in this study, although it is reasonable to speculate that such optimal sampling densities may well be higher, but perhaps only on a regional basis.

3.5 Conclusions

In conclusion, this work demonstrates for a variety of tachycardia mechanisms that the majority of information discernible from LAT maps can be obtained with a limited sampling density strategy. The exact sampling density required depends on tachycardia mechanism and clinical characteristics. The results presented here do not attempt to guide regional variations in sampling density required for optimal LAT mapping, and this would present an obvious future research avenue for development.

In this chapter, I explored the use of intracardiac mapping to diagnose regular atrial tachycardias. Intracardiac mapping can also be used for substrate assessment in order to assess the tissue-specific electrical properties in patients with arrhythmias. In the next chapter, the role of intracardiac electrogram analysis in assessing the atrial fibrillation substrate is examined, and Aim C3 (*to develop a tool to quantify electrical remodelling in paroxysmal AF and determine if population heterogeneities are present that could be used to predict response to catheter ablation*) is addressed.

4 Intra-Cardiac Mapping: Atrial Programmed Stimulation Reveals Substrate Heterogeneity Between Paroxysmal AF Patients

4.1 Introduction

Atrial fibrillation (AF) is a diverse disease with varying extents of electrical and structural remodelling seen in patients with paroxysmal and persistent AF (245, 255, 256). However, current clinical classification systems are based solely on duration of AF episodes, rather than physiological markers of disease severity. For example, paroxysmal AF (PAF) is defined as AF lasting for less than 7 days, and persistent AF (PsAF) as AF lasting for more than 7 days (142). A number of observations suggest that within the single clinical entity of paroxysmal AF, a spectrum of disease may be present (257). Firstly, AF ablation is more successful in some patients than others, even when controlling for confounding factors including co-morbidities and left atrial dimensions. Secondly, some patients with paroxysmal AF may require multiple ablation procedures to achieve freedom from AF, whereas others may require only a single procedure. Finally, the natural history of AF varies, with differing rates of progression to PsAF seen (258).

Given this heterogeneity, a number of studies have examined clinically-measurable factors that may describe the 'severity' of AF in order to predict rates of disease progression or freedom from AF after catheter ablation. Co-morbidities including hypertension, obesity and obstructive sleep apnoea have been associated with increased AF burden and recurrence of AF after pulmonary vein isolation, but not all studies demonstrate a clear relationship between the presence of co-morbidities and AF disease severity (259). Similarly, there is debate over the predictive value of basic measures like left atrial size for outcome of pulmonary vein isolation, with some studies demonstrating a highly significant association (259, 260) and other studies demonstrating no association at all (261). The impact of AF duration on recurrence rates is also controversial. A recent study found that left atrial volume was more important than the type of atrial fibrillation in predicting long-term success of catheter ablation (262), whilst other work finds that the only positive predictor of freedom from AF is a shorter duration of AF (263). As an

alternative to quantifying clinical characteristics, other studies have examined the electrophysiological properties of the atria in patients with AF. Again however this work is characterised by variable findings. For example left atrial low voltage, shortened refractoriness and reduced conduction velocity have all been associated with increasing severity, duration or recurrence of AF in some (245, 256, 264, 265), but not all (266–268) studies. Taken together these findings serve to highlight that there is a need for improved techniques to classify atrial fibrillation in order to guide treatment strategies.

Paced electrogram fractionation analysis (PEFA) was originally used to characterise abnormal conduction in patients with hypertrophic cardiomyopathy (269, 270). The technique involves delivering pacing stimuli at progressively shorter coupling intervals from one site, and recording the response electrograms at another site. In the presence of normal conduction between pacing and recording sites, PEFA results in a single biphasic response electrogram, whereas in the presence of abnormal or discontinuous conduction, PEFA results in a fractionated electrogram response (269). Increased electrogram fractionation in PEFA has been associated with sudden cardiac death in hypertrophic cardiomyopathy, dilated cardiomyopathy and long QT syndrome, and was suggested as a tool for clinical risk stratification of these ventricular arrhythmias (271, 272).

The rationale for using PEFA analysis in substrate assessment has been addressed in both *ex vivo* tissue preparations and simulation studies. Activation mapping of isolated myocardium demonstrated that slowed conduction with activation block (the underlying substrate for re-entry) results in delayed local electrograms that contain multiple potential deflections corresponding to the individual pathways of myocardial activation (273–275). In simulation studies these electrogram morphological characteristics have been shown to arise from myocardial fibrosis and action potential abnormalities (276). Of note, these are also the key properties of the electrical and structural remodelling that is thought to underlie the AF substrate. Indeed, atrial simulation studies reveal the importance of zones of slow conduction arising from microfibrosis in the genesis of complex fractionated atrial electrograms (277). Correspondingly PEFA has previously been found to detect abnormal atrial substrate in patients with paroxysmal AF, based upon measurements from the RA and CS (278, 279).

Therefore, in this study a programmed stimulation protocol is used to quantify the left atrial electrical substrate underlying AF in a population of patients with paroxysmal atrial fibrillation. The protocol was designed to allow simultaneous measurement of atrial

conduction delay as well as morphological electrogram changes, which may be associated with atrial myocardial remodelling. The occurrence of inter-patient differences in the AF electrical substrate that may explain differing clinical presentations is examined.

4.2 Methods

Study Inception

Prior to commencing the study a number of stakeholders were involved in the development of key documentation to support the study. These included the patient information sheets, consent forms, radiation assessment, risk assessments for non-CE marked devices including software and the pacing stimulator and medical physics approval for the custom-built equipment. Once completed, and following submission through the Integrated Research Application System, ethical approval for the study was granted by the National Research Ethics Service (REC reference number: 10/H0802/77).

Patient Selection and Clinical Procedures

15 consecutive patients undergoing first time ablation for paroxysmal atrial fibrillation were studied. Patients were excluded from the study if there was a history of ischemic heart disease, cardiac surgery or structural heart disease. Anti-arrhythmic drugs, including calcium channel blockers, were stopped at least 5 half-lives before ablation. Amiodarone was stopped at least 6 months prior to ablation. All clinical procedures were performed under general anaesthesia. Following femoral access and trans-septal puncture, two 8.5 French SRO long sheaths and a PentaRay mapping catheter (Biosense Webster, Diamond Bar, CA, USA, 4-4-4mm electrode spacing) were advanced into the left atrium. Decapolar (St Jude Medical, St Paul, MN, USA) and pentapolar (Bard Electrophysiology, Lowell, MA, USA) catheters were sited in the coronary sinus and high right atrium respectively. The PentaRay catheter was manoeuvred to multiple sites in the body of the left atrium and at each site bipolar electrograms were recorded in response to pacing from the HRA and mid-CS. ‘Shadows’ of each spline of the Pentaray catheter were created using the mapping system and used to ensure that the catheter did not move during recording (Figure 4-1).

Pacing Protocol

The pacing protocol was designed to obtain a large number of S2-response electrograms (A2 electrograms) throughout the LA within a 30-minute window. The pacing protocol

was delivered using a custom-built pacing stimulator (Figure 4-2) comprising a USB digital I/O device (NI USB-6501, National Instruments, Austin, TX) connected via an optical isolator (Figure 4-3) to the external trigger of the UHS 3000 stimulator (Biotronik SE & Co. KG, Berlin, Germany). The protocol consisted of a 2-beat 470ms drive train followed by a single premature extra-stimulus. The S1S2 coupling interval was reduced in -2% steps from 350ms to 200ms or loss of capture ($S2_n = 0.98 \times S2_{n-1}$). All pacing stimuli were delivered at a voltage of at least twice threshold with a pulse width of 2ms.

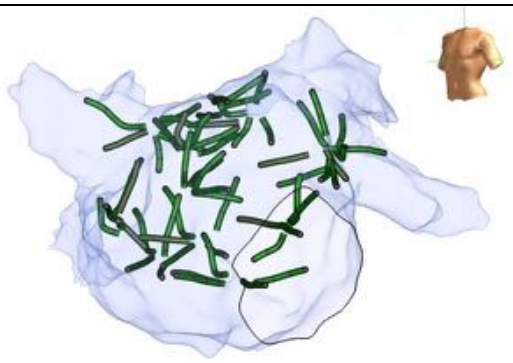

Figure 4-1. Example left atrial geometry and recording locations

Using the mapping system 'shadows' of each spline of the mapping catheter were created prior to recording and subsequently used to confirm stable catheter position throughout the recording.

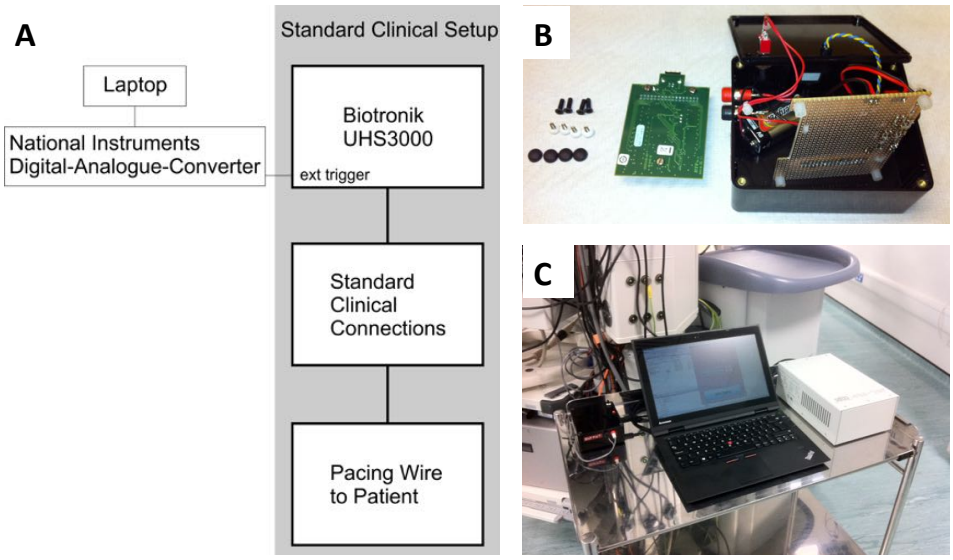

Figure 4-2. Components of the pacing stimulator

A - Block diagram. **B** - Components of the interface box. **C** - The complete set up running in the lab.

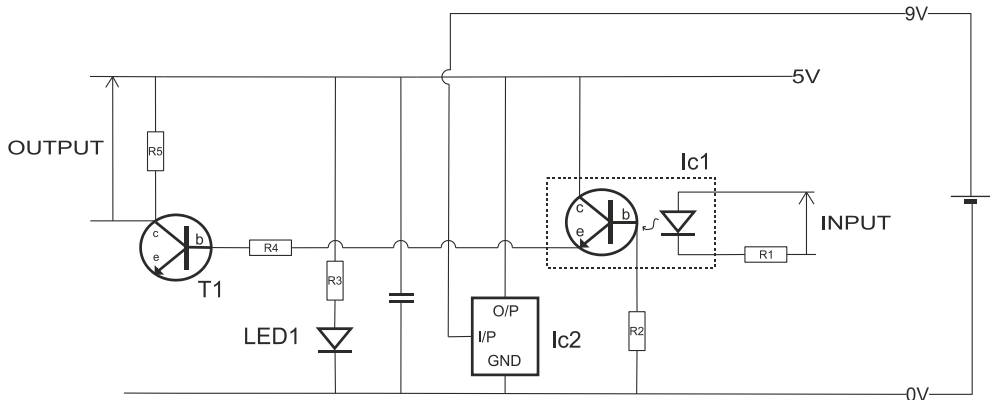

Figure 4-3. Optical isolator circuit diagram

R1 – 1kΩ; R2 – 470kΩ; R3 – 1kΩ; R5 – 4.7kΩ; Ic1 – AY44 4N25 (optoisolator); Ic2 – TS2950-50; C1 – 1.0μF; T1 – C1740. The isolator was assembled from individual components soldered onto stripboard.

Signal Processing

Electrograms were digitised using the LabSystem PRO EP Recording System (Bard Electrophysiology, Lowell, MA) at 4kHz sampling rate. All signal processing was performed offline (MATLAB 8.2, MathWorks Inc., Natick, MA). Pacing timing was determined from the paced channel (HRA or CS). The first pacing cycle was used to determine the noise threshold and discarded from subsequent analysis. As such, the longest S2 interval studied was 343ms (350ms x 0.98). A2 electrograms were rejected from analysis where the signal was far-field, there was fusion with an atrial ectopic beat or the two preceding S1 beats had failed to capture the left atrium (Figure 4-4). A band-pass filter (30-500Hz) was applied to the bipolar recordings, and the noise threshold defined as signal mean+/-3SD of the 100ms preceding the S2 component of the first cycle.

To provide a quantitative analysis of PEFA, previous work has plotted local activation against S2 coupling interval, and quantified two metrics of these conduction curves: 1) the maximal increase in electrogram duration (ΔED) after an extrastimulus; and 2) the S1S2 interval ($S1S2_{delay}$) below which the electrogram duration increased (270, 280). The previous studies of atrial PEFA derive these parameters for a limited number of recording sites, before presenting average values of $S1S2_{delay}$ and ΔED as a single observation per patient. In the present study, a large number of measurements are taken throughout the body of the LA to assess regional variation in the LA response to pacing. In order to represent all electrogram points from a region on a single conduction curve, varying path lengths (from pacing to recording site) and therefore conduction times must be accounted for. Hence in the following work the electrogram timings are normalized to the local atrial

response to drive-train pacing (A2 time) rather than the pacing extra coupling interval (S2 time). This calculation is shown schematically in Figure 4-6.

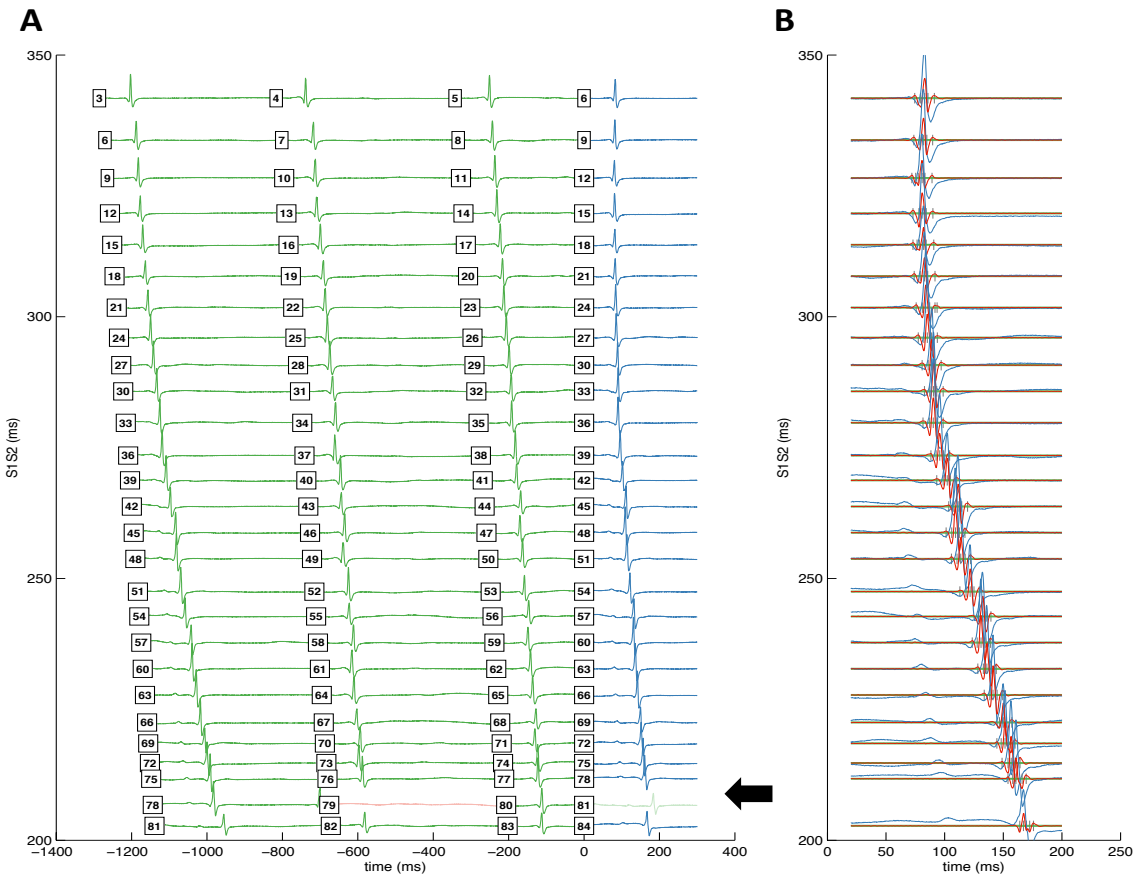

Figure 4-4. Initial Electrogram Processing

All electrograms were inspected by an external observer blinded to the clinical diagnosis. **A** - S2 electrograms were accepted for subsequent analysis (blue) where the preceding drive train captured both beats (green). Beat number 79 was annotated as inadequate quality (pink) resulting in rejection of beat 81 (arrow). **B** - the S2 electrograms accepted for analysis, with filtered electrograms overlaid in red.

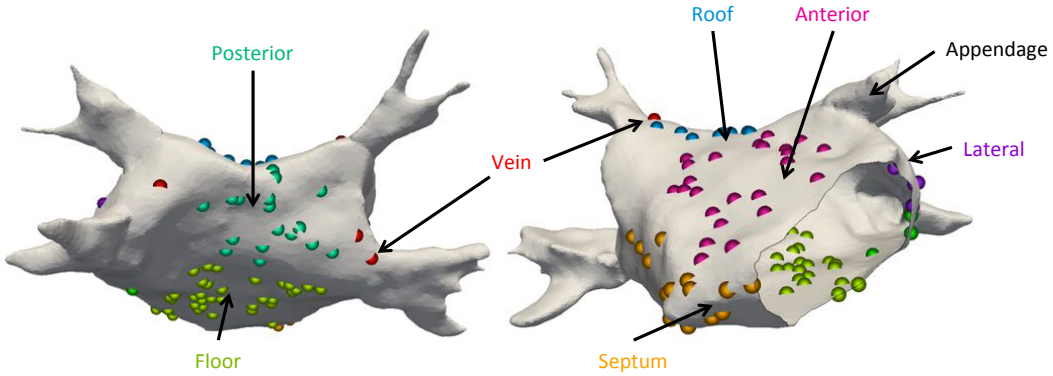

Figure 4-5. LA Regions

The LA was divided into 8 regions. *Posterior* - bounded by pulmonary veins; *Roof* - posterior to RSPV-RA line and anterior to RSPV-LSPV line; *Anterior* - from Roof to mitral annulus; *Floor* - from Posterior to mitral annulus; *Lateral* - between appendage, mitral annulus and LIPV; *Septum* - medial border of chamber between anterior and floor regions; *Veins* - within 1cm of vein ostium.

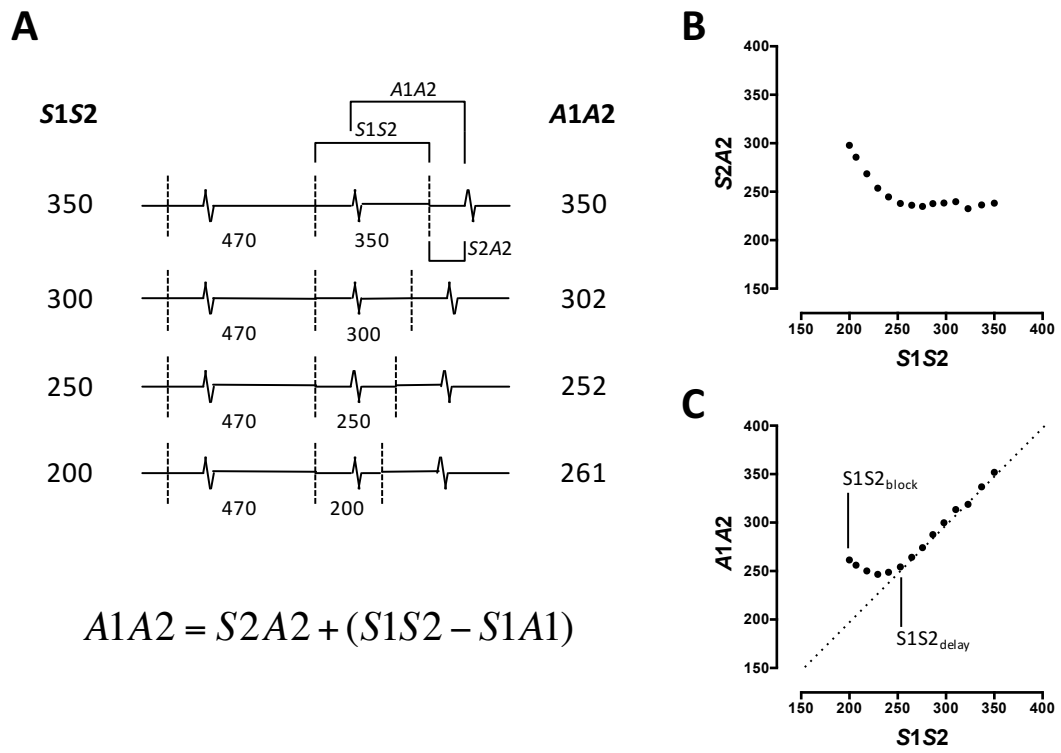

Figure 4-6. Schematic Representation of Conduction Curves

A – Pacing drive trains with measured intervals marked. **B** – Conduction curves as published in prior literature on paced fractionation. **C** – The same data as 'B' is converted into S1S2-A1A2 curves allowing determination of conduction delay and conduction block times.

LA Regional Analysis

For analysis of regional variations within the left atrium, the chamber was divided into 8 regions (Figure 4-5). The mean±SD number of recording sites for each region was 29±8 (floor), 22±10 (anterior), 21±5 (posterior), 17±7 (septum), 11±5 (roof), 9±6 (veins), 4±3 (lateral) and 4±3 (appendage). The five regions with the highest density were selected for further analysis (floor, anterior, posterior, septum, roof).

Electrogram Analysis

Conduction Delay and Conduction Block

To assess the impact of pacing rate on local electrogram timing and morphology, S1S2-A1A2 curves were plotted where each dot represents a single electrogram peak or trough. These curves were characterized by 1) a 1:1 relationship between S1S2 and A1A2 at long pacing cycle lengths (the line of identity), 2) a minimum achievable A1A2 at short cycle lengths (the flat segment) and 3) a curved transition period between the two regions. A best-fit line comprising each of these three components was fitted to the data. The best-

fit line was represented as a hyperbola with asymptotes at $y=c$ and $y=x$. In this way, the $S1S2_{block}$ was determined as the shortest S1S2 conducted to the left atrium and the $S1S2_{delay}$ was determined as the transition point between the two parts of the curve.

Pacing Latency and Conduction Path Length

To determine the impact of pacing site latency on the conduction curves, activation time within the CS close to the pacing site was measured. Pacing latency was defined as the time from pacing stimulation to detectable local activation on the next-nearest bipole to the stimulating pair showing a clear local atrial electrogram. For CS 5,6 pacing this was usually CS 7,8 or CS 9,10 bipoles. Conduction path length was measured as the geodesic distance from the site of earliest left atrial activation to the LA recording site (Figure 4-7). Distances were calculated along the surface of the left atrial geometry using the approach of Mitchell *et al* (281). A previously-published computationally efficient implementation of the algorithm (282) was employed using MATLAB 8.2 (MathWorks Inc., Natick, MA).

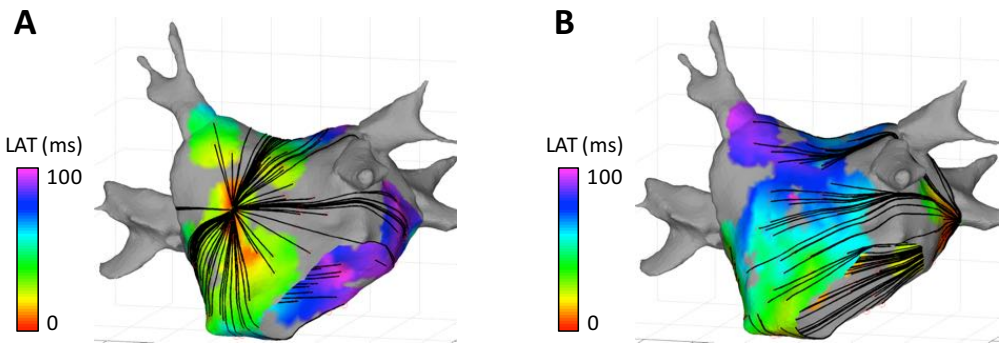

Figure 4-7. Determination of Geodesic Conduction Path Lengths

Conduction path lengths (black lines) are calculated as the geodesic distance from earliest chamber activation to local electrogram recording sites for HRA pacing (**A**) and CS pacing (**B**)

Electrogram Amplitude and Duration

Baseline electrogram amplitude and duration were determined from the longest S2 pacing cycle length analysed (S2=343ms) at each site. The rate-dependence of electrogram amplitude was quantified by calculating the gradient of the best-fit line through S1S2 vs. electrogram amplitude curves. This parameter is named ΔEV (units, mV/s) and represents the change in electrogram voltage with pacing rate. The rate-dependence of electrogram duration was quantified from S1S2-A1A2 plots for each recording site. For each S2 cycle length, the 5^{th} and 95^{th} centile of A2 electrogram components were taken as the beginning and end of local activation. Change in electrogram duration was quantified as the longest

duration between these curves minus the duration at 343ms. This parameter is named ΔED (units, ms) and represents the maximal change in electrogram duration with pacing rate.

AF Inducibility

Inducibility of AF was assessed during pacing from the HRA and CS. Sustained AF was defined as AF >30 seconds in duration (283, 284). Where AF resolved to an organised tachycardia, it was attempted to terminate the tachycardia using pacing. Electrical cardioversion was performed if AF/AT persisted beyond 5 minutes. Following electrical cardioversion, a blanking period of 10 minutes was used where no further electrical measurements were taken (267).

Atrial Simulations

To determine if the clinically observed changes in conduction could be explained by left atrial electrical remodelling two simulation experiments were employed using a 4.0x4.0cm atrial monolayer with the Courtemanche cell model implemented at each node. Firstly, anisotropy was introduced into the intra- and extra-cellular conductances to represent longitudinal fibre orientation. The model was activated by introducing a current stimulus along the leftmost edge (longitudinal activation direction) and activation times of the centre node were recorded at a transmembrane potential (V_m) of -20mV. The cell model was modified, as previously described (98), to reflect the spectrum of electrical remodelling seen in atrial fibrillation by applying reductions in I_{to} (50%), I_{Kur} (50%), and $I_{Ca,L}$ (70%) current densities and the experiment repeated. To assess the impact of changes in fibre orientation on conduction, the experiment was repeated with transverse activation direction. Secondly to determine the impact of conduction velocity and conduction velocity restitution on global LA conduction curves two activation time recording sites were used, separated by 1.5cm in the direction of propagation for both transverse and longitudinal conduction. Conduction curves were generated using the same S1S2 protocol as the clinical studies for the sinus rhythm Courtemanche model, the AF Courtemanche model and the AF model with additional reduction of I_{Na} of 52% (285). Conduction time, conduction delay and conduction velocity restitution were measured in the direction of propagation. The Cardiac Arrhythmia Research Package (103) was used to perform atrial tissue simulations. Computer scripts and for these experiments are given in Appendix B.7.

Statistical Tests

Data analysis was performed using GraphPad Prism version 6.0c (GraphPad Software, San Diego, California, USA, www.graphpad.com). Data are represented as mean±SD throughout. The Kolmogorov-Smirnov test was used to determine whether observed data differed significantly from the chosen distributions. Categorical variables were compared with the Fisher's exact test. Continuous variables were compared using a two-tailed Student's T-test. In all cases, a significance level of $P<0.05$ was considered statistically significant.

4.3 Results

Patient characteristics are shown in Table 4-1. Hypertension was present in 6 patients (15%), diabetes mellitus in 1 patient (6%) and the overall CHA_2DS_2VASc was 1.8±1.7. No patients had structural heart disease. DC cardioversion was performed in 4 (27%) patients. An operator blinded to the case details inspected the quality of every electrogram visually. Electrograms were rejected from analysis for the following reasons: lack of capture of the preceding drive train, far-field local electrogram or interference from far-field ventricular electrograms. Overall, 34.6±17.6% (HRA pacing) and 35.9±17.7% (CS pacing) of PentaRay bipolar pairs yielded suitable electrograms for further analysis.

Table 4-1. Characteristics of Paroxysmal AF Patients

Case	Sex	Age	AF Duration (years)	AF Burden (n/ month)	LA size (cm)	LVEF (%)	Prior AADs (n)	Creatinine (µmol/l)	Hb (g/dl)
1	F	68	4	<1	3.5	65	2	65	131
2	F	46	1	2	3.4	70	2	46	129
3	F	72	1	30	4.3	55	2	69	129
4	M	70	3	3	3.9	55	3	66	147
5	M	77	1	2	4.5	48	2	80	156
6	M	47	5	1	3.7	60	2	113	162
7	F	73	11	<1	3.3	60	2	79	141
8	F	69	1	<1	3.8	55	1	64	118
9	F	44	1	4	3.9	60	2	77	130
10	M	62	1	12	3.8	60	2	116	153
11	F	67	1	1	4.4	60	1	74	132
12	M	61	2	1	3.8	60	4	96	142
13	M	60	1	15	4.5	60	2	96	169
14	F	72	6	12	3.1	60	2	72	129
15	F	76	2	8	4.5	43	1	67	122

AF, Atrial Fibrillation; LA, Left Atrium; AAD, antiarrhythmic drug; LVEF, left ventricular ejection fraction; Hb, haemoglobin

Local Electrogram Morphologies

Examples of unprocessed electrograms representing the complete pacing protocol under HRA and CS pacing from each case are given on pages 102 to 131. Attention is drawn to Case 8, a female in the 7th decade, showing bidirectional paced electrogram fractionation (pages 116-117, and Figure 4-8) and Case 13, a male in the 7th decade, showing uniform bidirectional conduction without fractionation (pages 126-127, and Figure 4-9). Both of these paroxysmal AF cases had an AF duration of ~1 year and similar LA dimensions (3.8cm vs. 4.5cm). In other cases unidirectional fractionation was evident. Attention is drawn to Case 4, a male in the 8th decade, showing unidirectional paced electrogram fractionation arising primarily from CS pacing (page 108, and Figure 4-10) and Case 11, a female in the 7th decade, showing unidirectional paced electrogram fractionation arising primarily from HRA pacing (page 123, and Figure 4-11). Again, these cases had similar LA dimensions (3.9cm, vs. 4.4cm) although the duration of PAF was longer in Case 4 than Case 11 (3 years vs. 1 year). Overall, a spectrum of local electrogram morphologies was seen, ranging from early conduction delay/block without electrogram prolongation or fractionation (Figure 4-12A) to much later conduction delay/block with electrogram fractionation (Figure 4-12B). For further analysis, individual electrogram peaks were automatically detected for every local electrogram related to each S2 stimulus (S2A2 times). The first peak of each local electrogram relating to the preceding S1 stimulus was also detected (S1A1 time). By subtracting S1A1 from S2A2, the local A1A2 time for each S2-related electrogram component is derived: $A1A2 = S2A2 - S1A1$ (Figure 4-12C and D). Performing this correction for every recording site cancels the effect of conduction path length on the A2 electrogram components and allows all S2 responses for a case to be plotted on a single graph. Again, two patterns were identifiable from these curves, in keeping with the raw electrograms shown in Figure 4-12A and B.

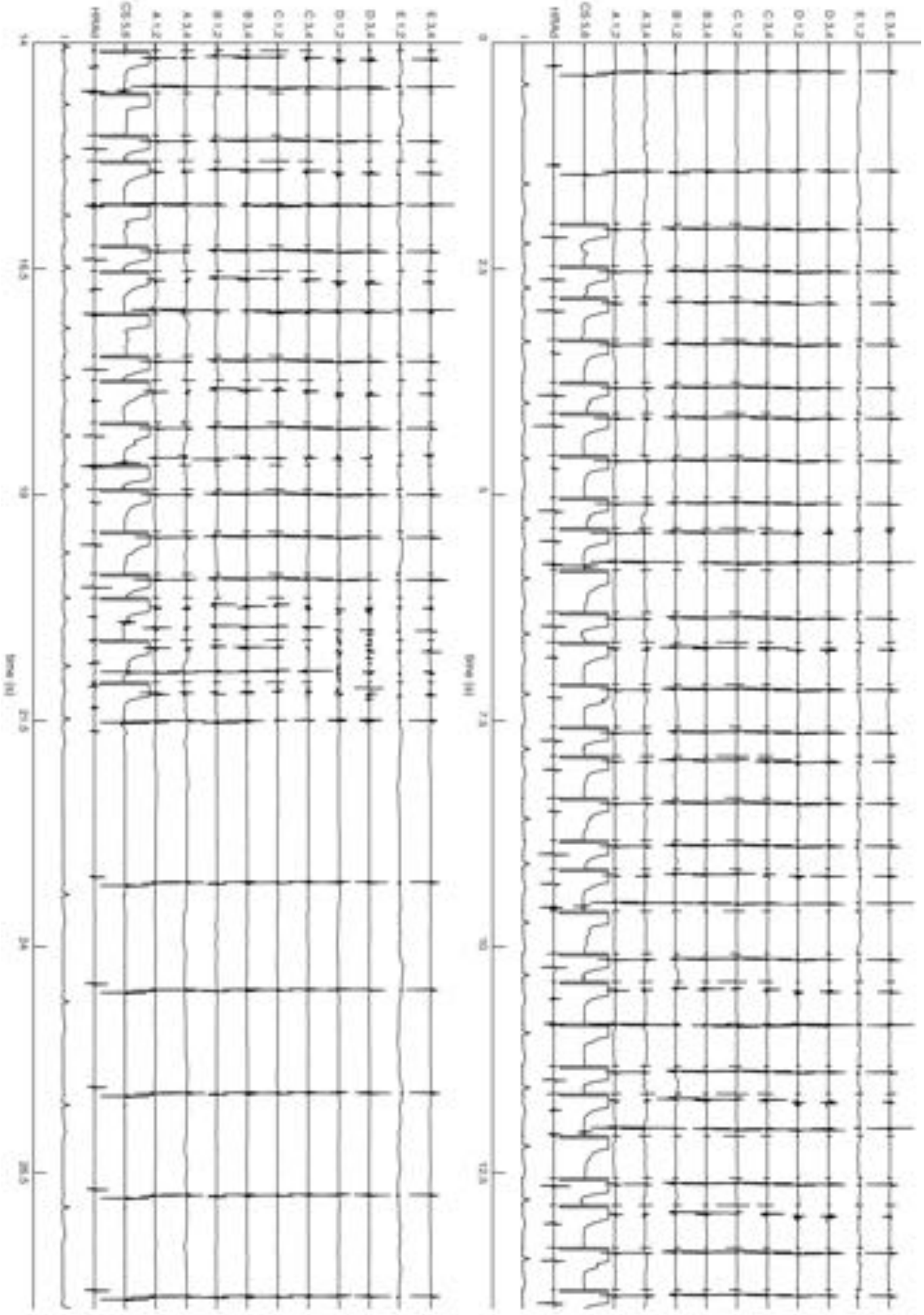

Case 1 – CS pacing

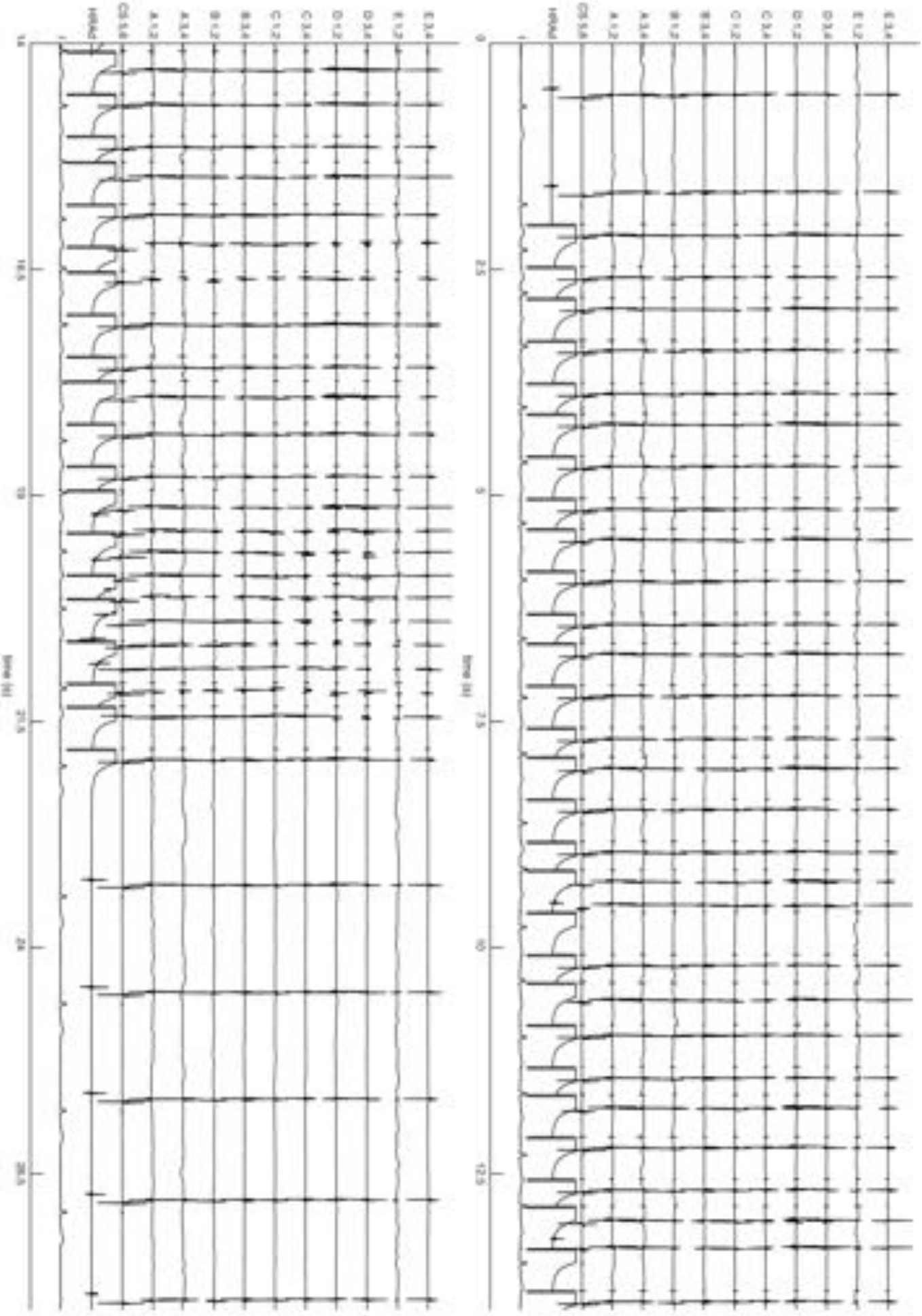

Case 1 – HRA pacing

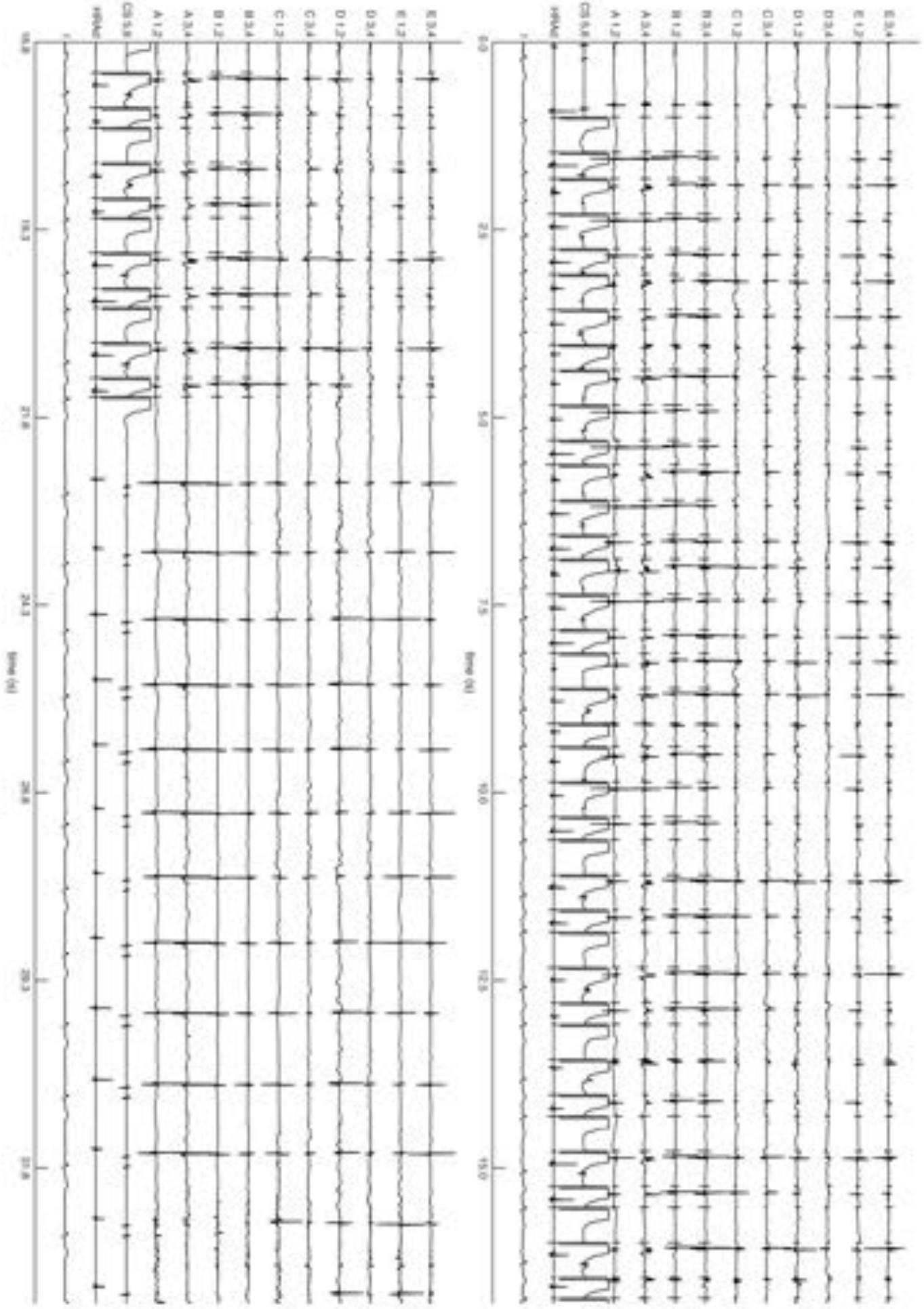

Case 2 – CS pacing

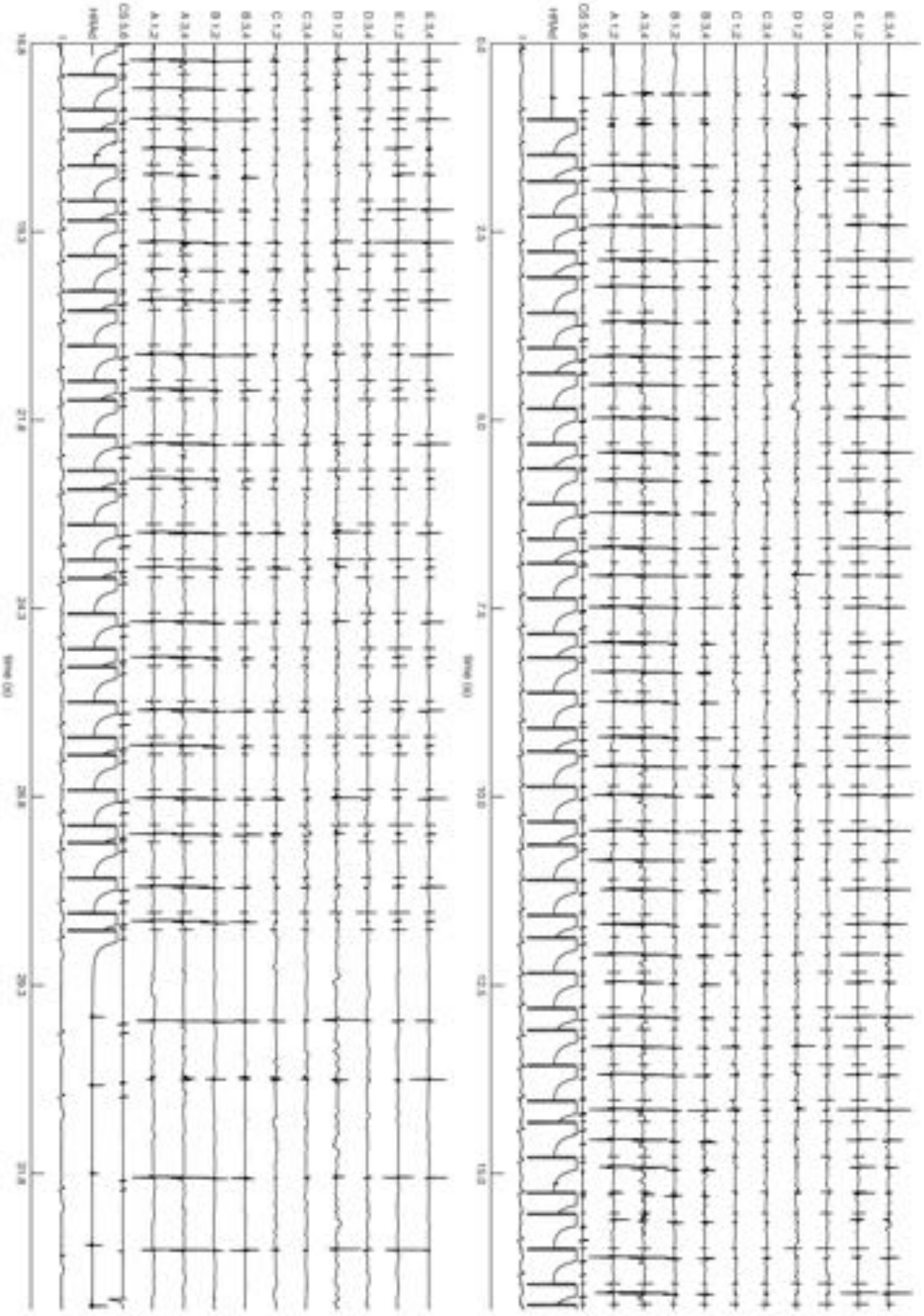

Case 2 – HRA pacing

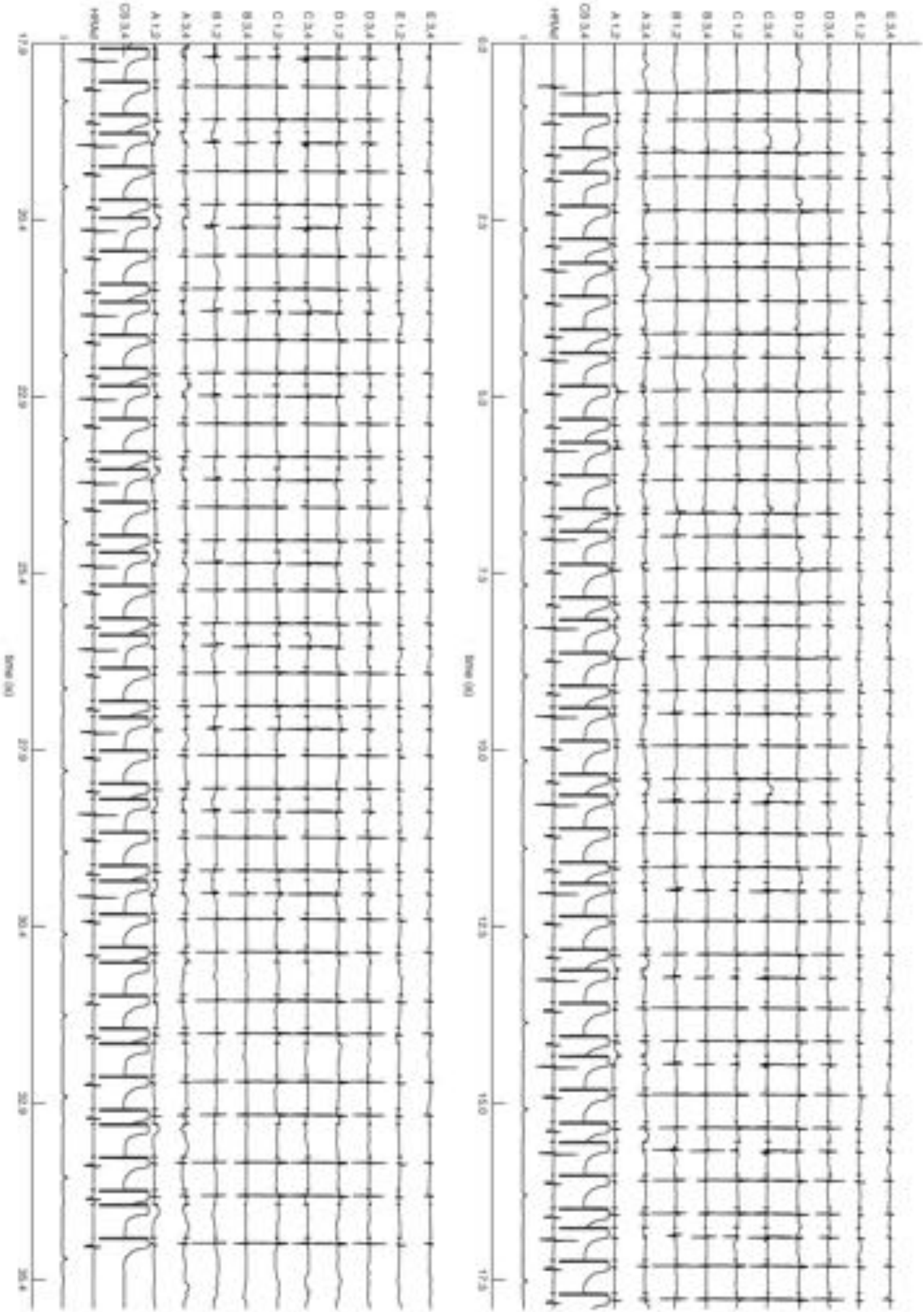

Case 3 – CS pacing

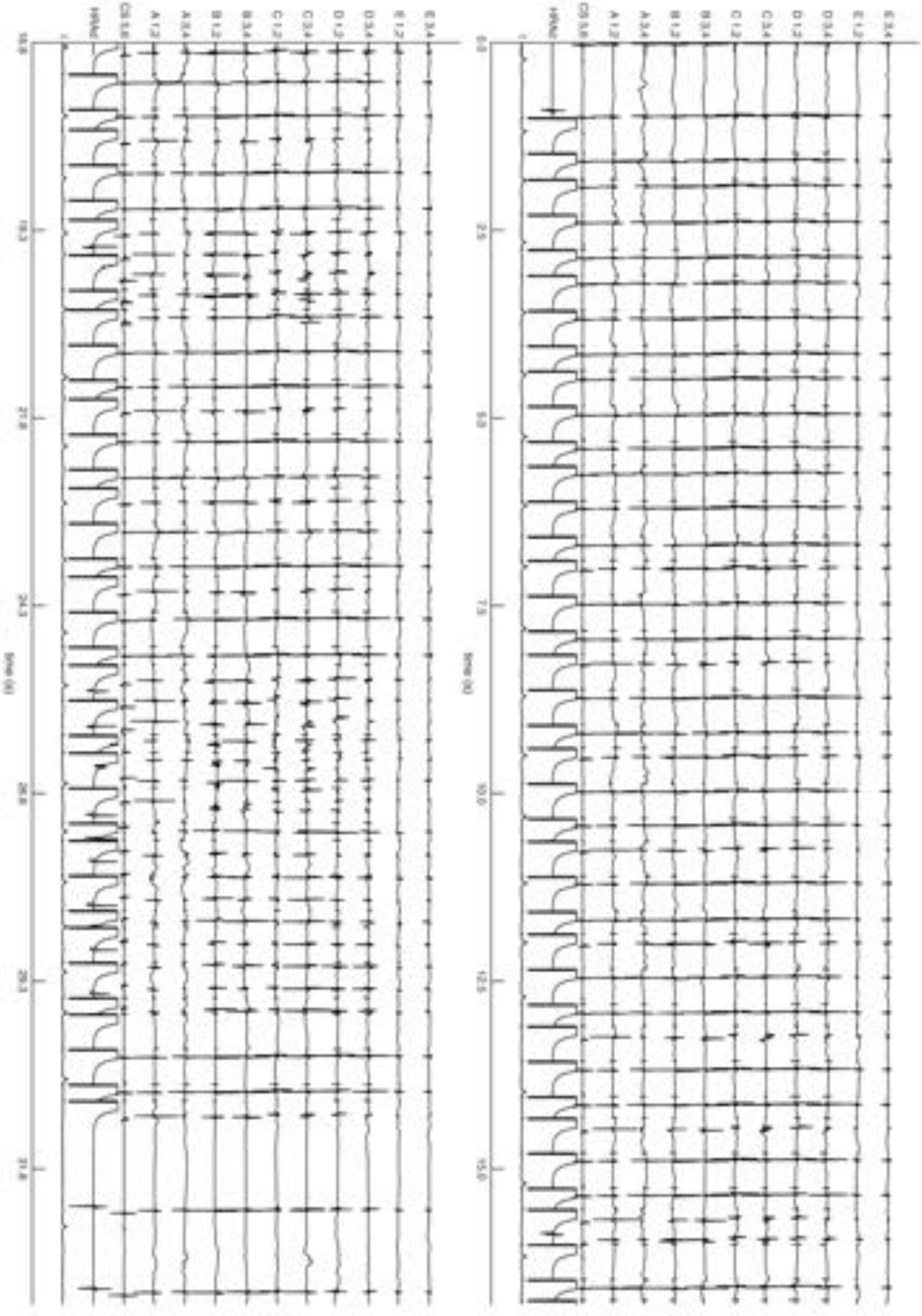

Case 3 – HRA pacing

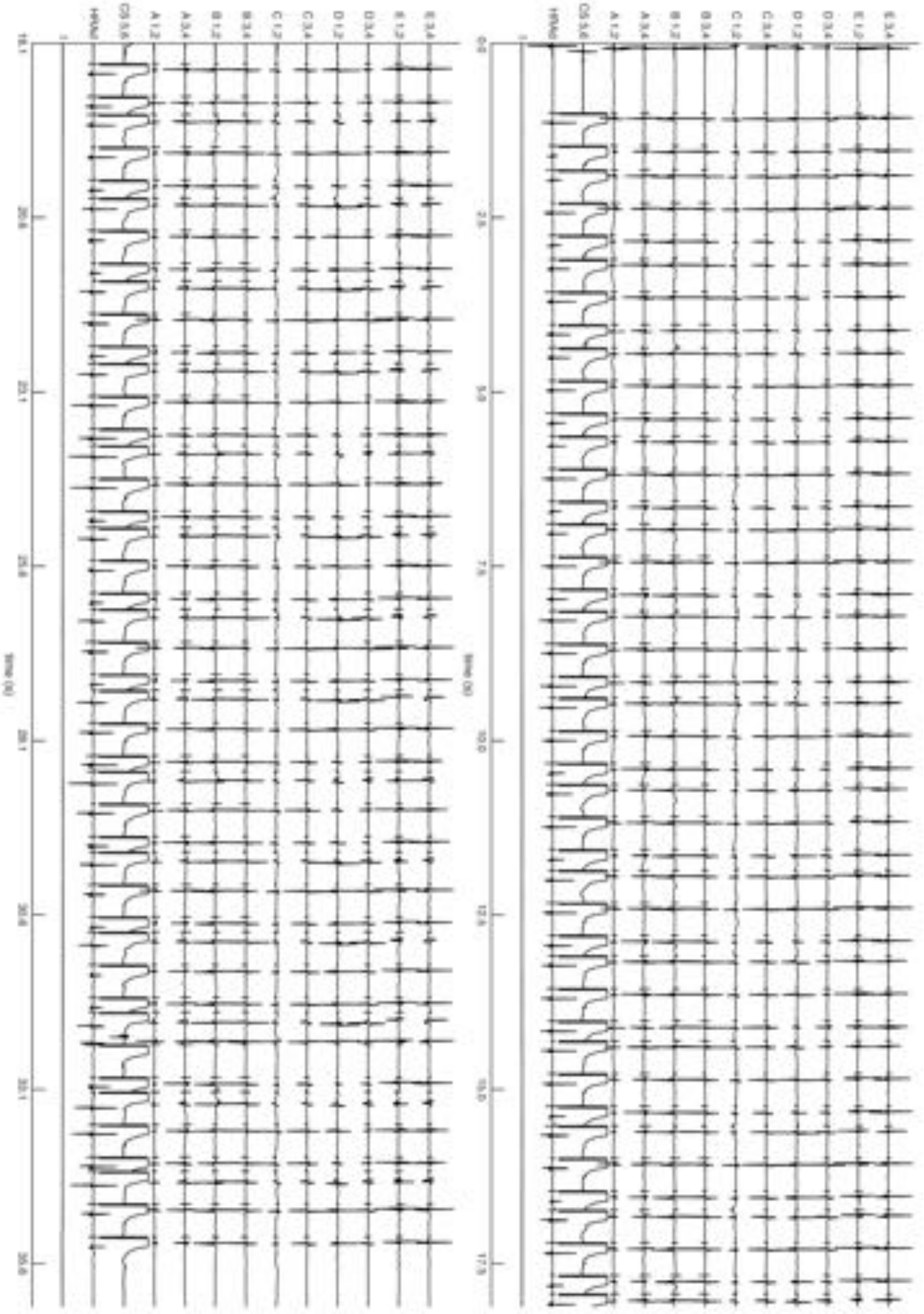

Case 4 – CS pacing

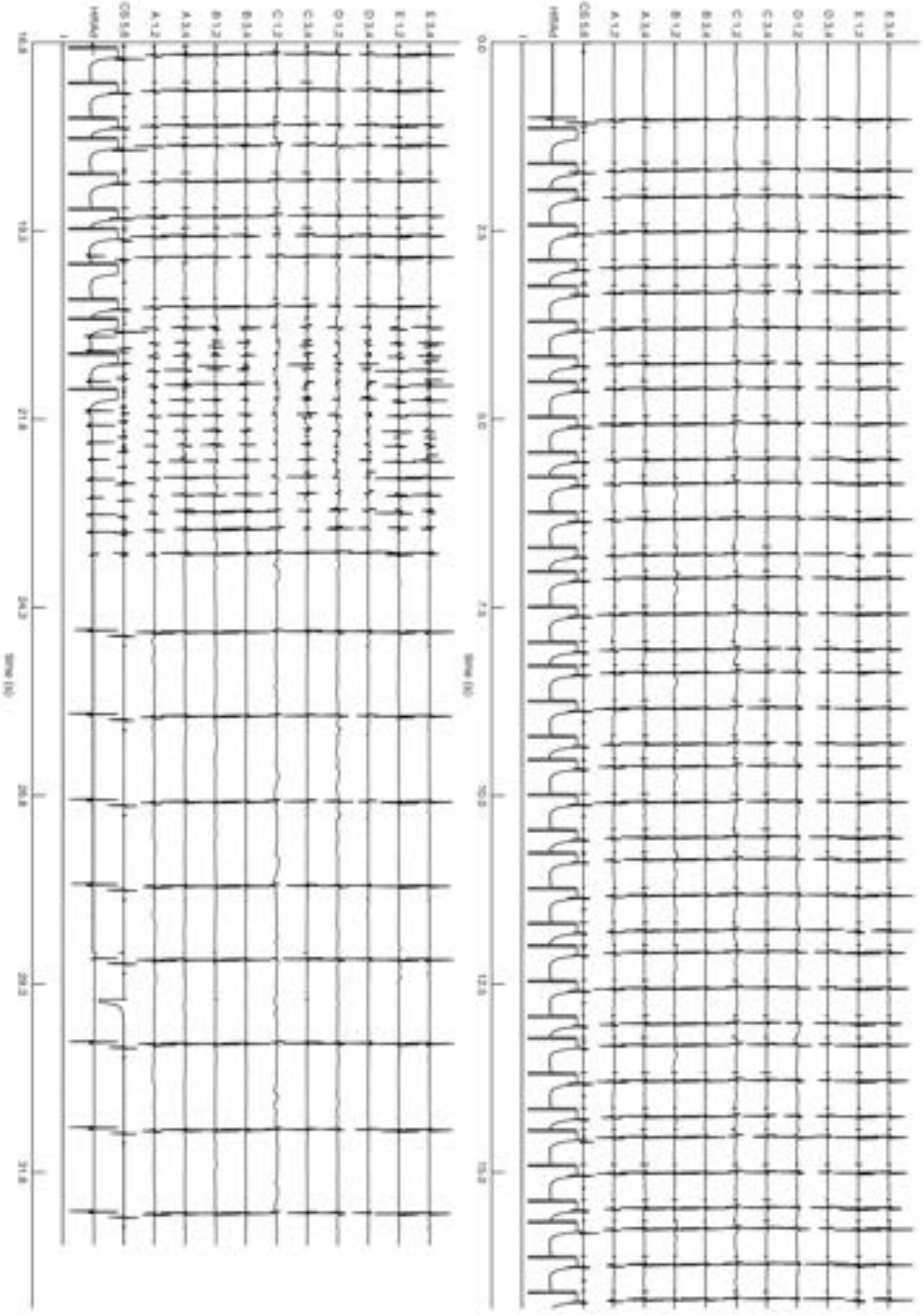

Case 4 – HRA pacing

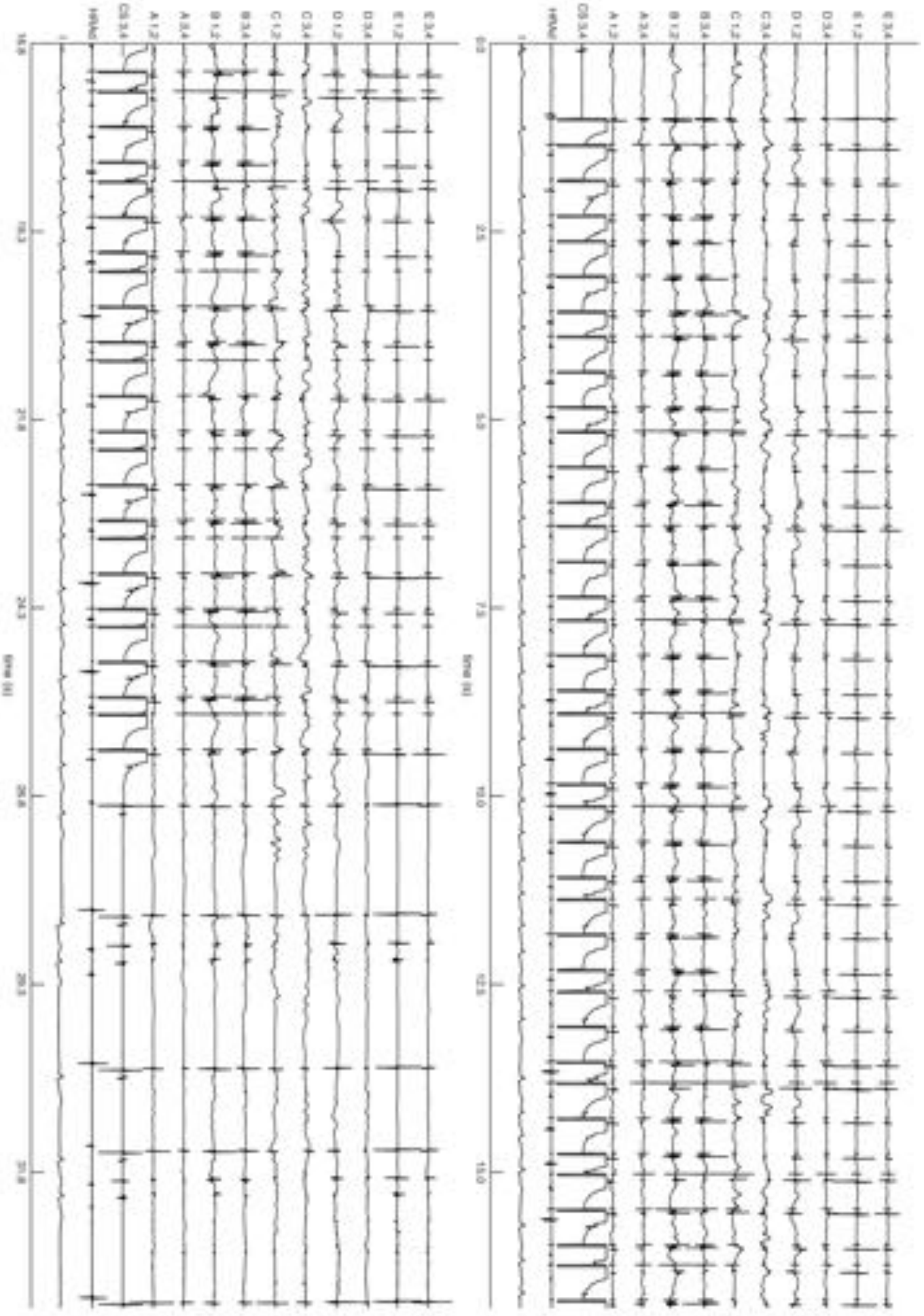

Case 5 – CS pacing

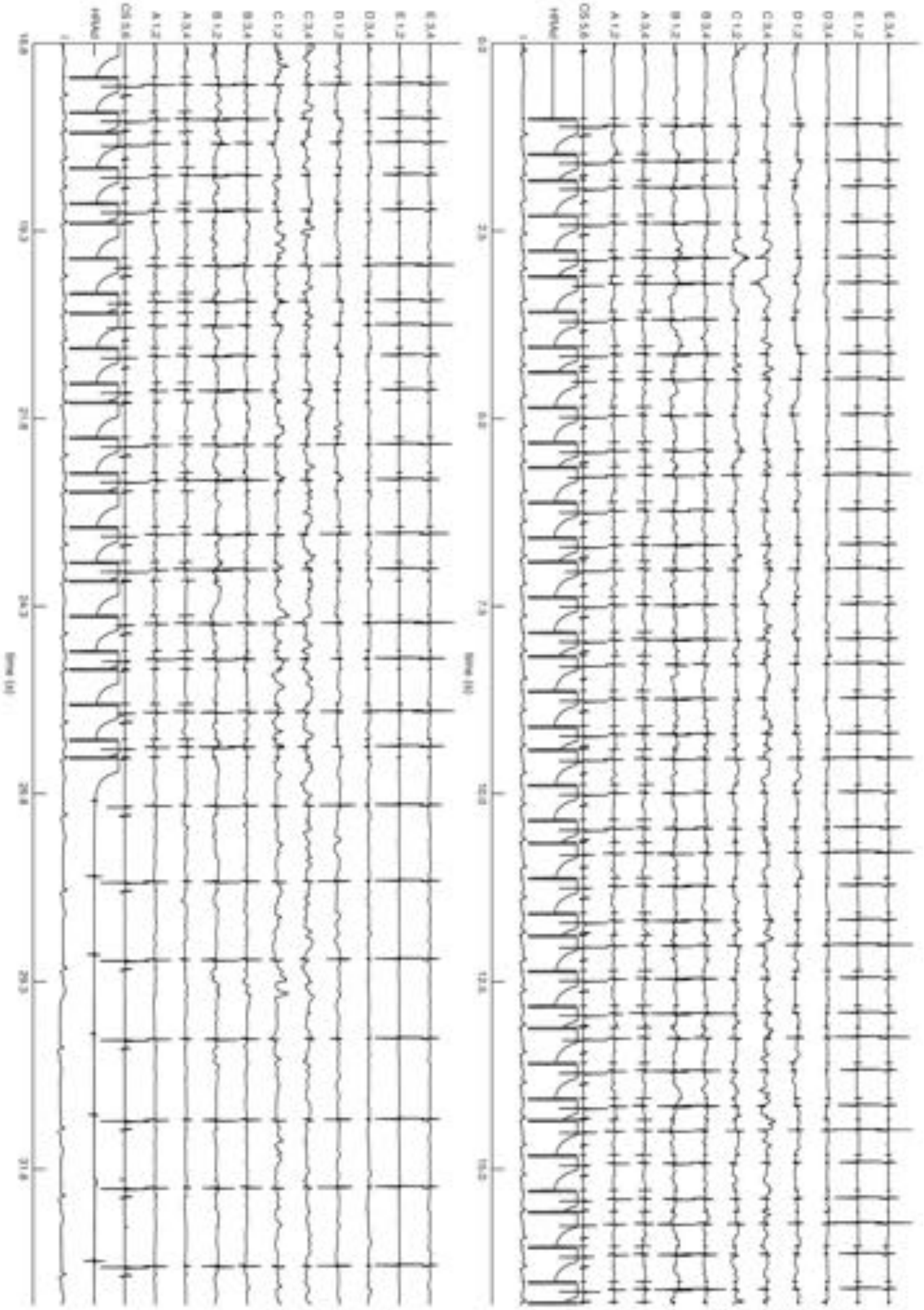

Case 5 – HRA pacing

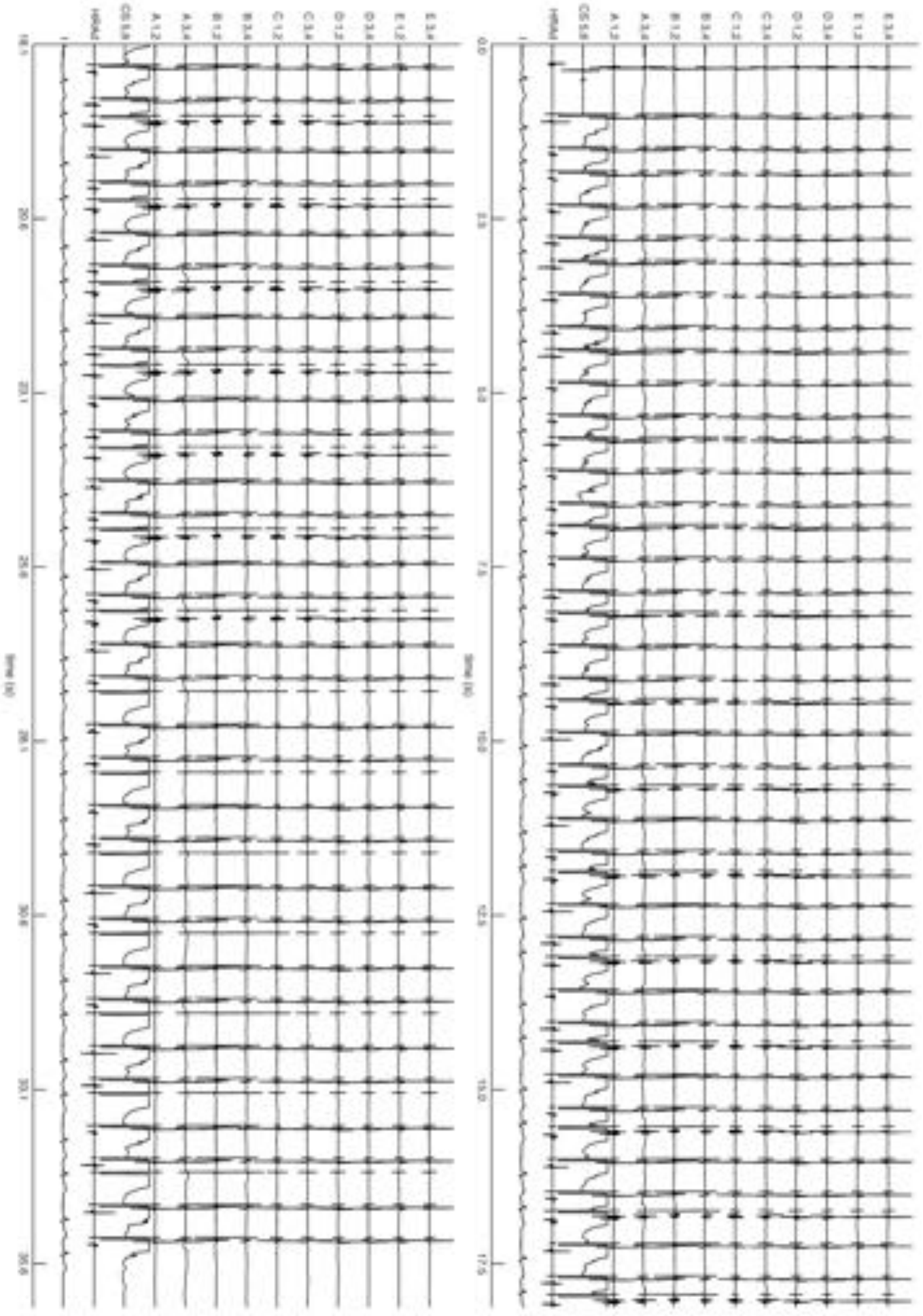

Case 6 – CS pacing

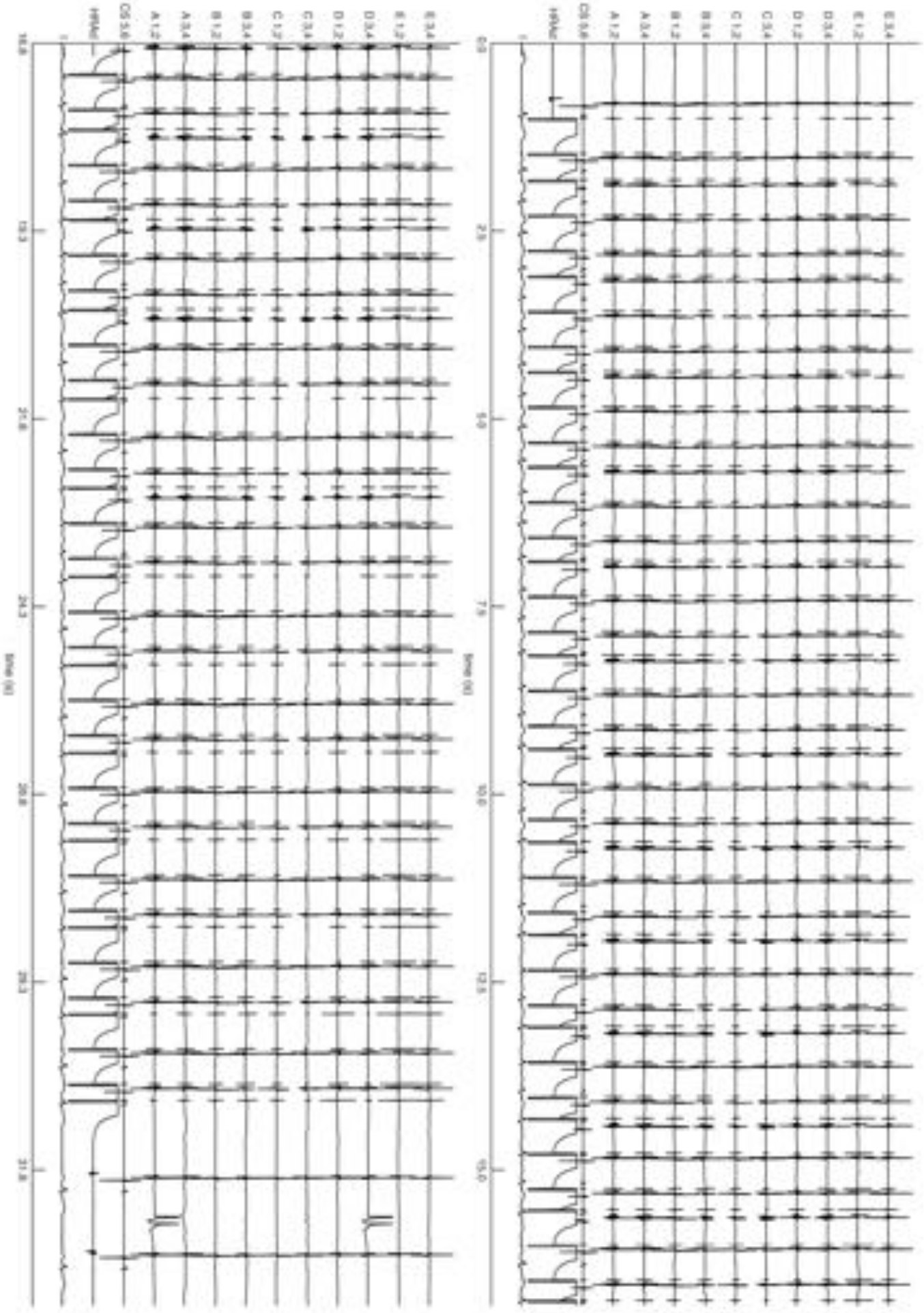

Case 6 – HRA pacing

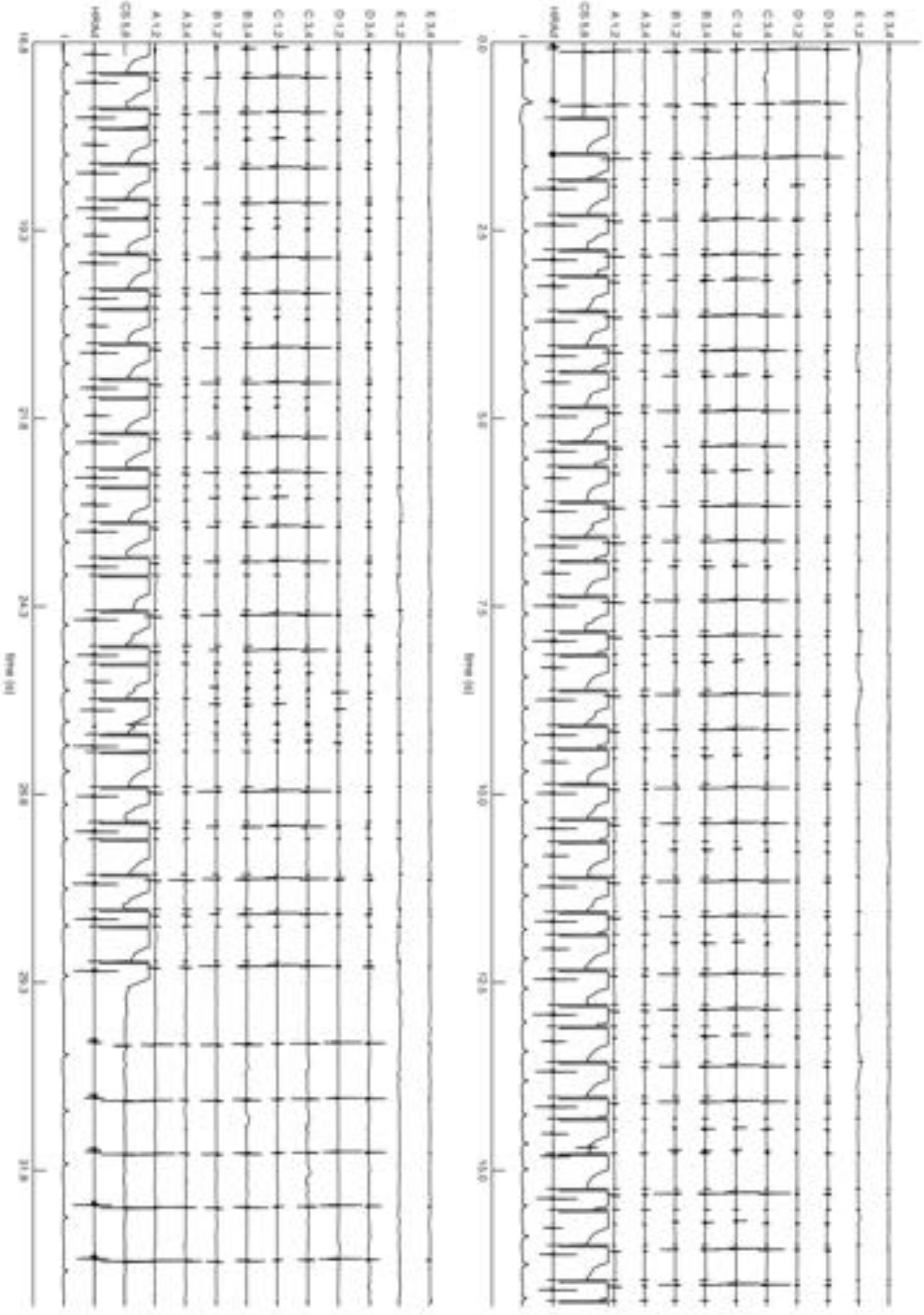

Case 7 – CS pacing

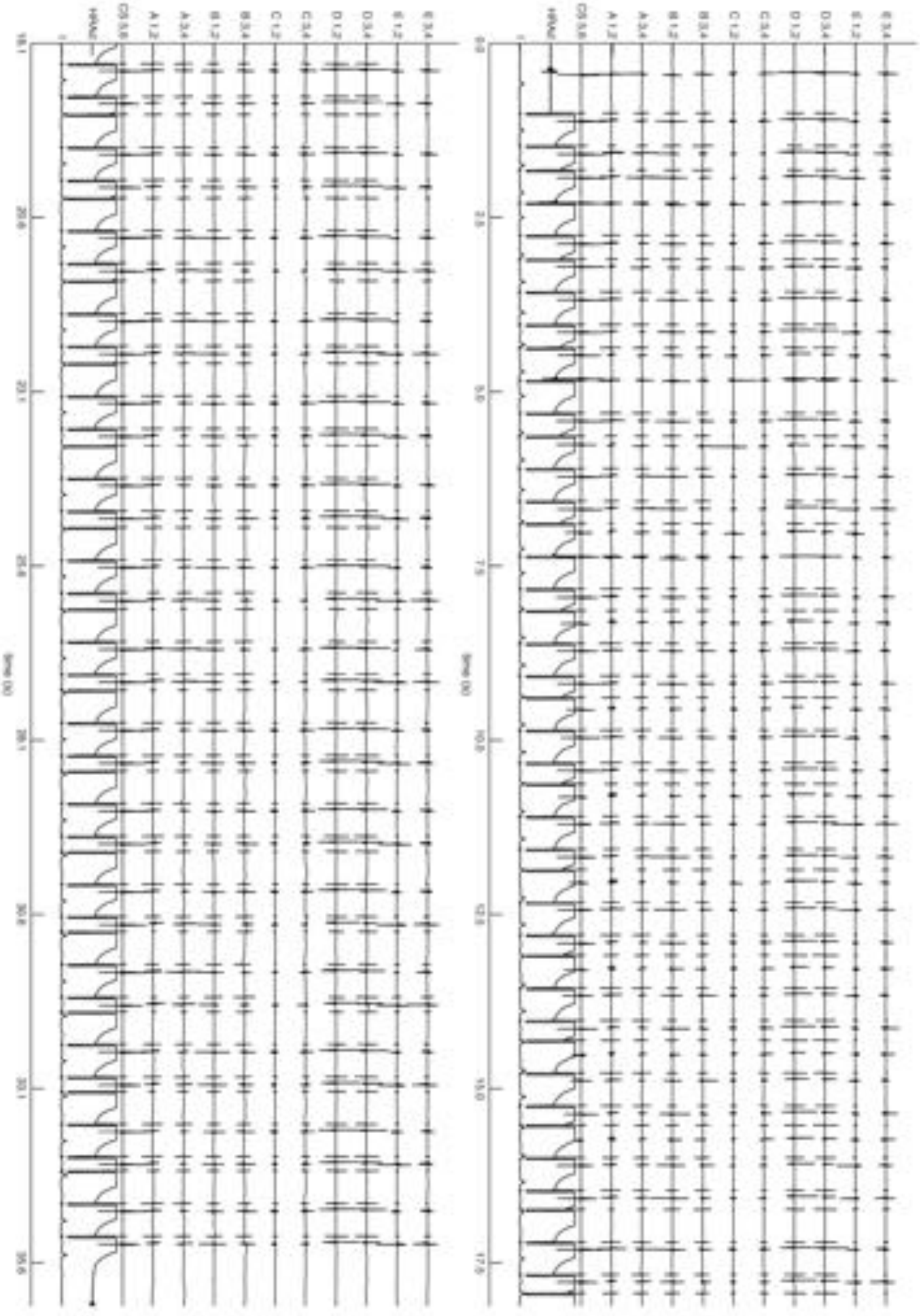

Case 7 – HRA pacing

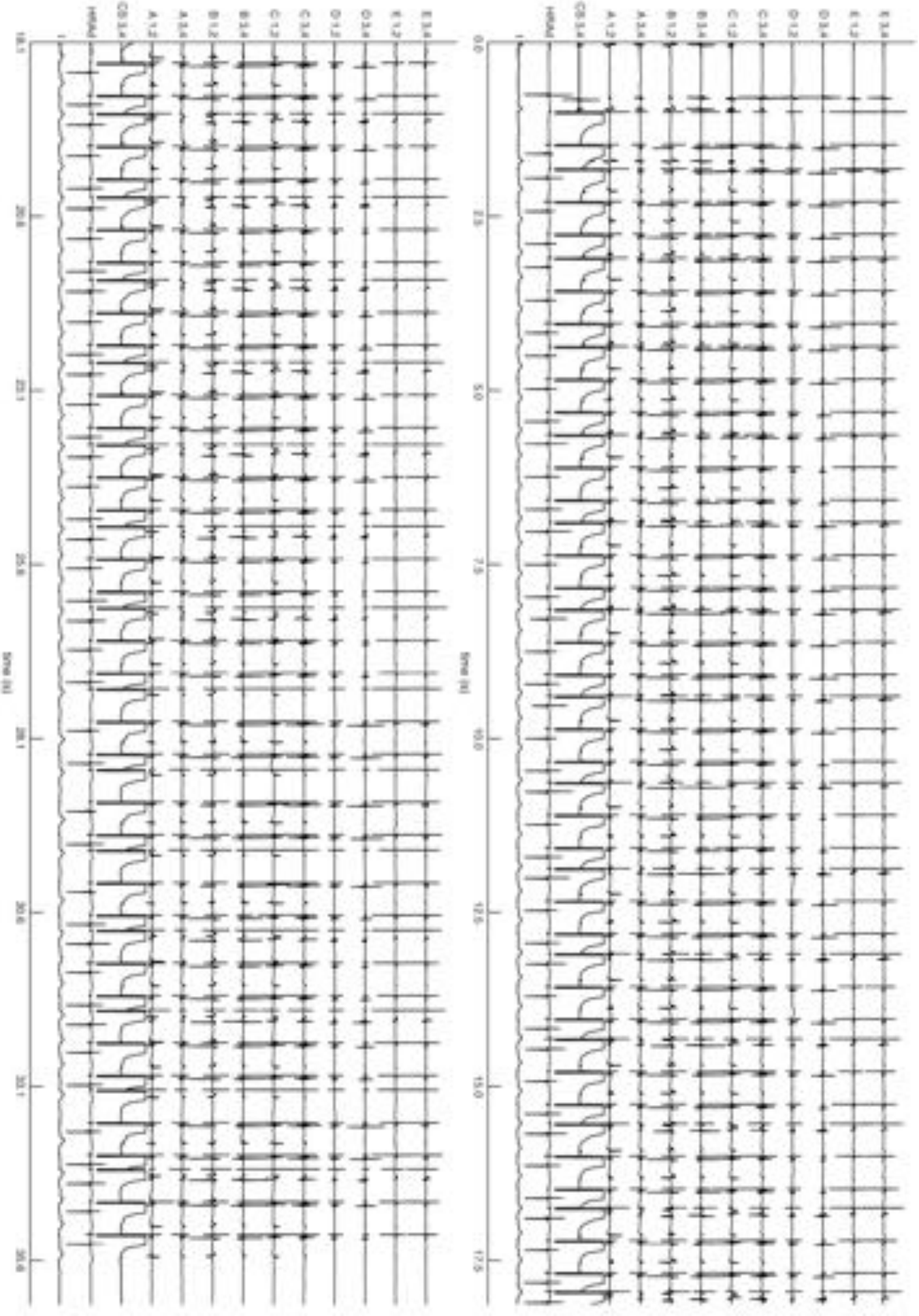

Case 8 – CS pacing

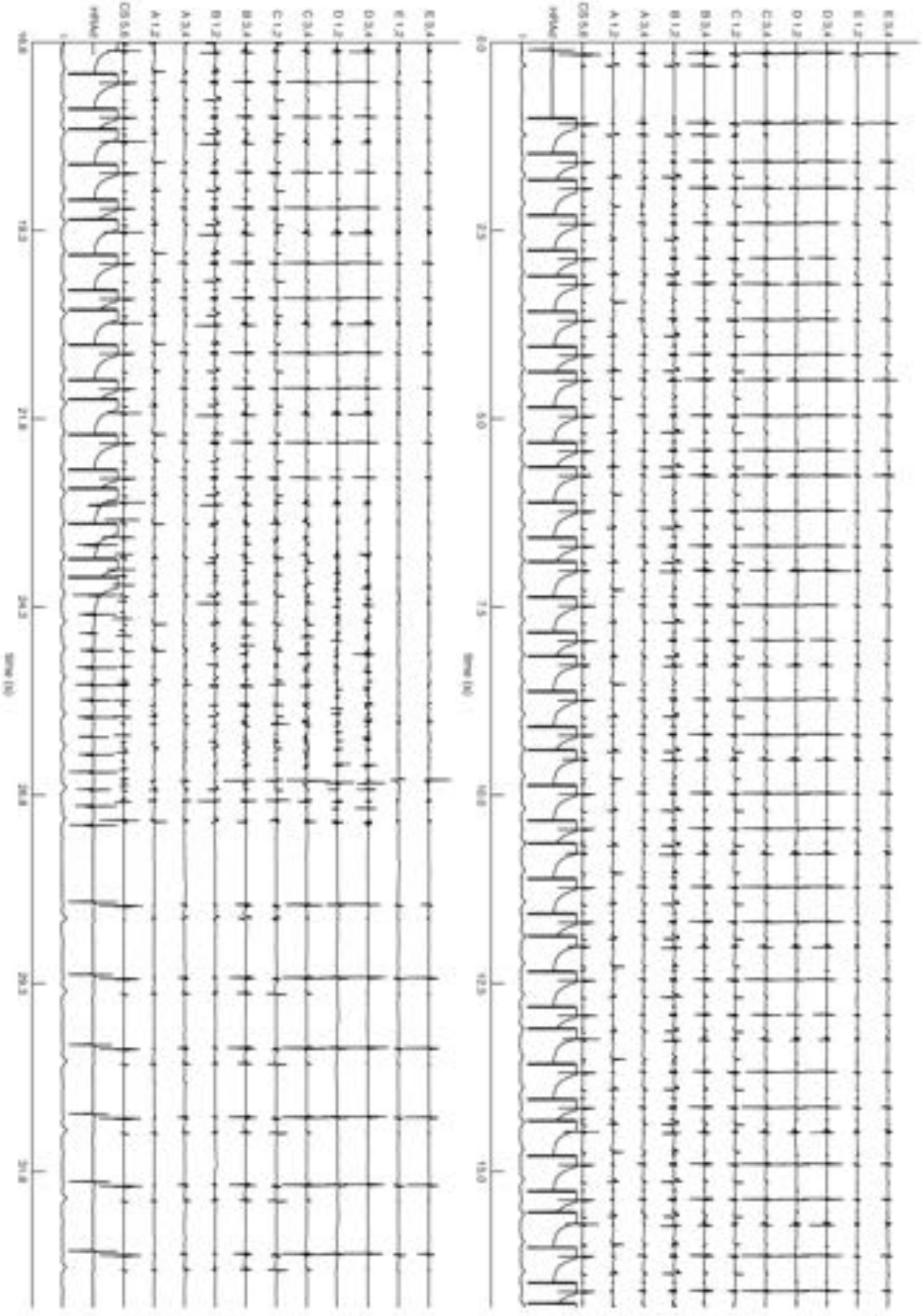

Case 8 – HRA pacing

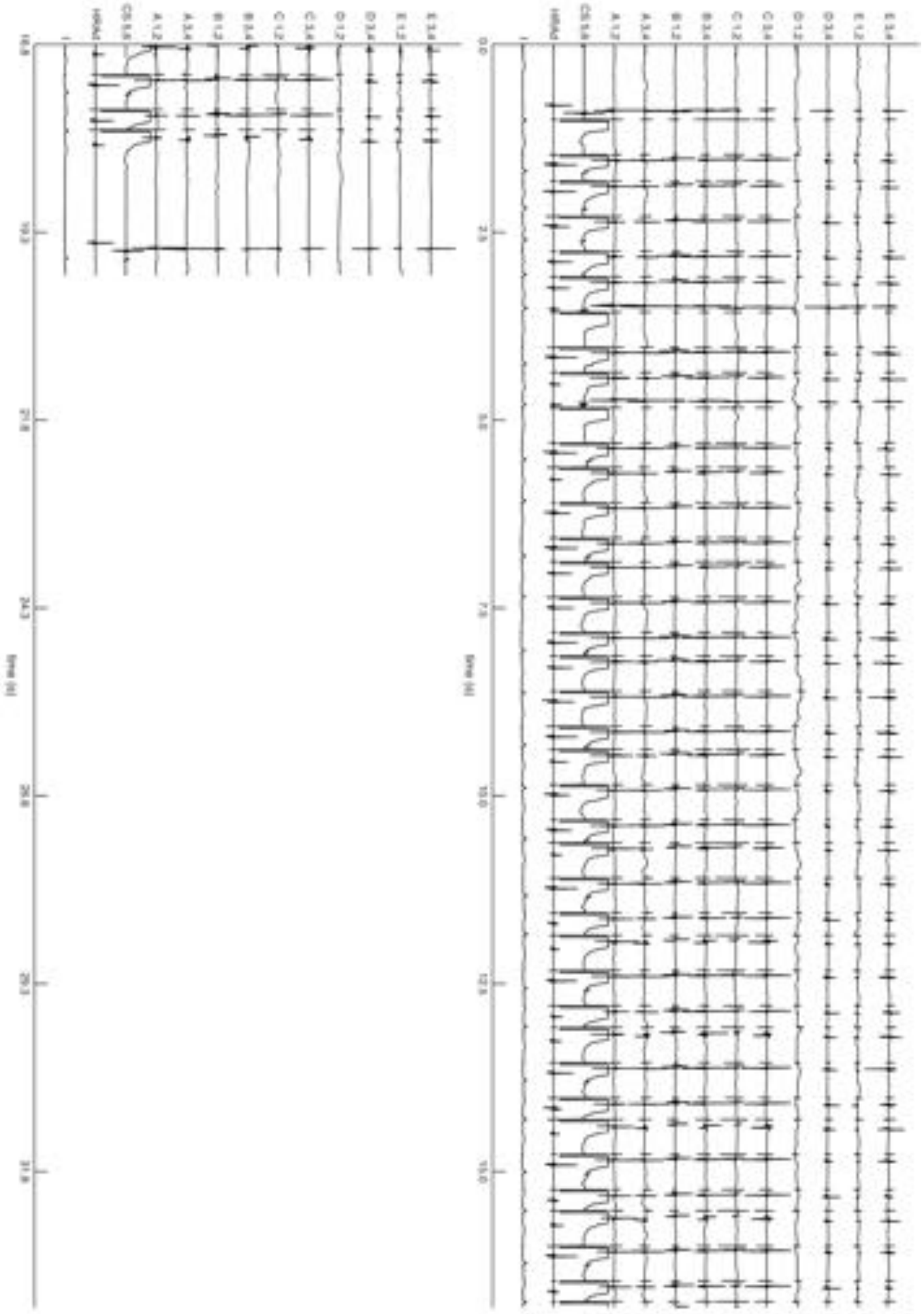

Case 9 – CS pacing

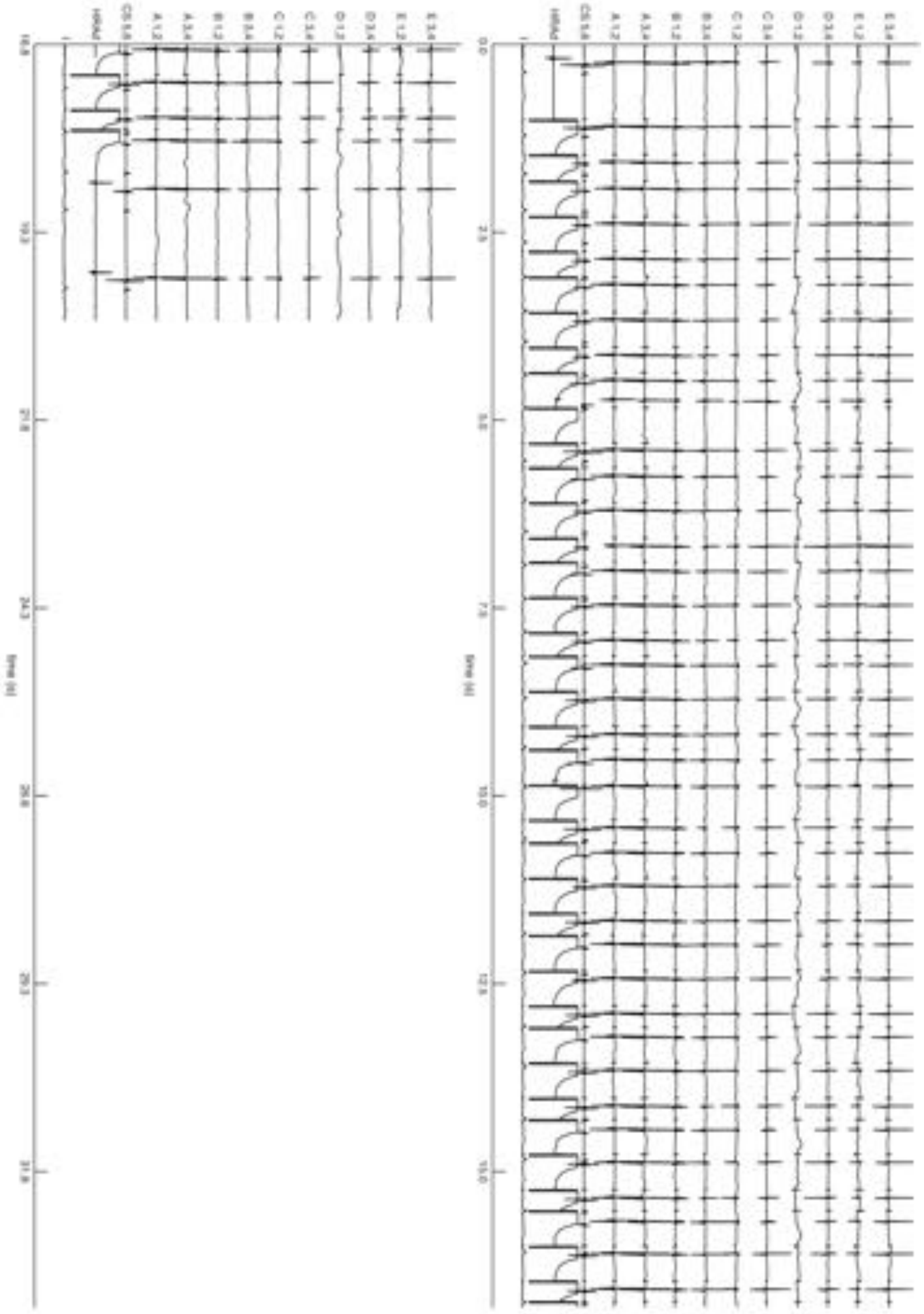

Case 9 – HRA pacing

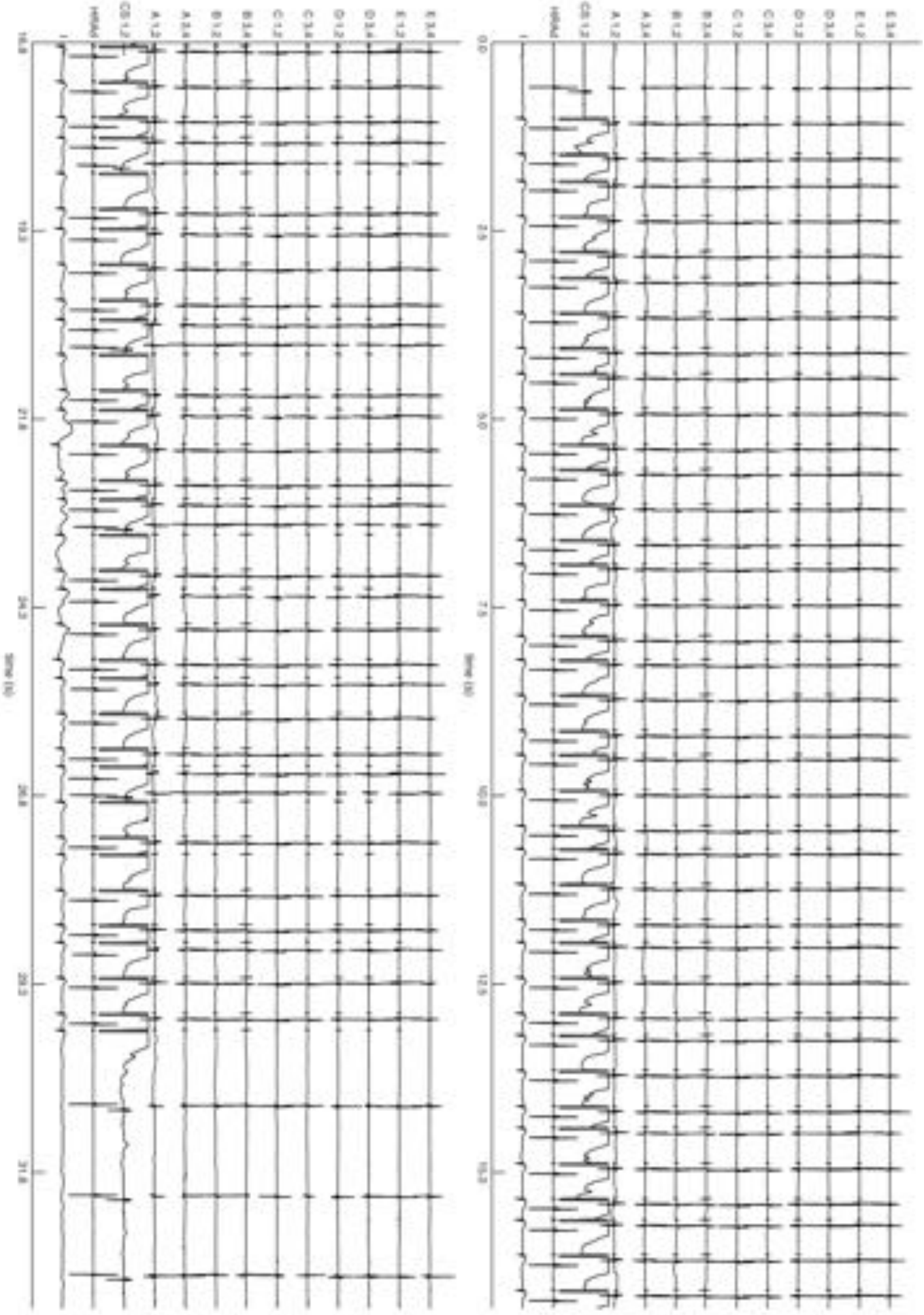

Case 10 – CS pacing

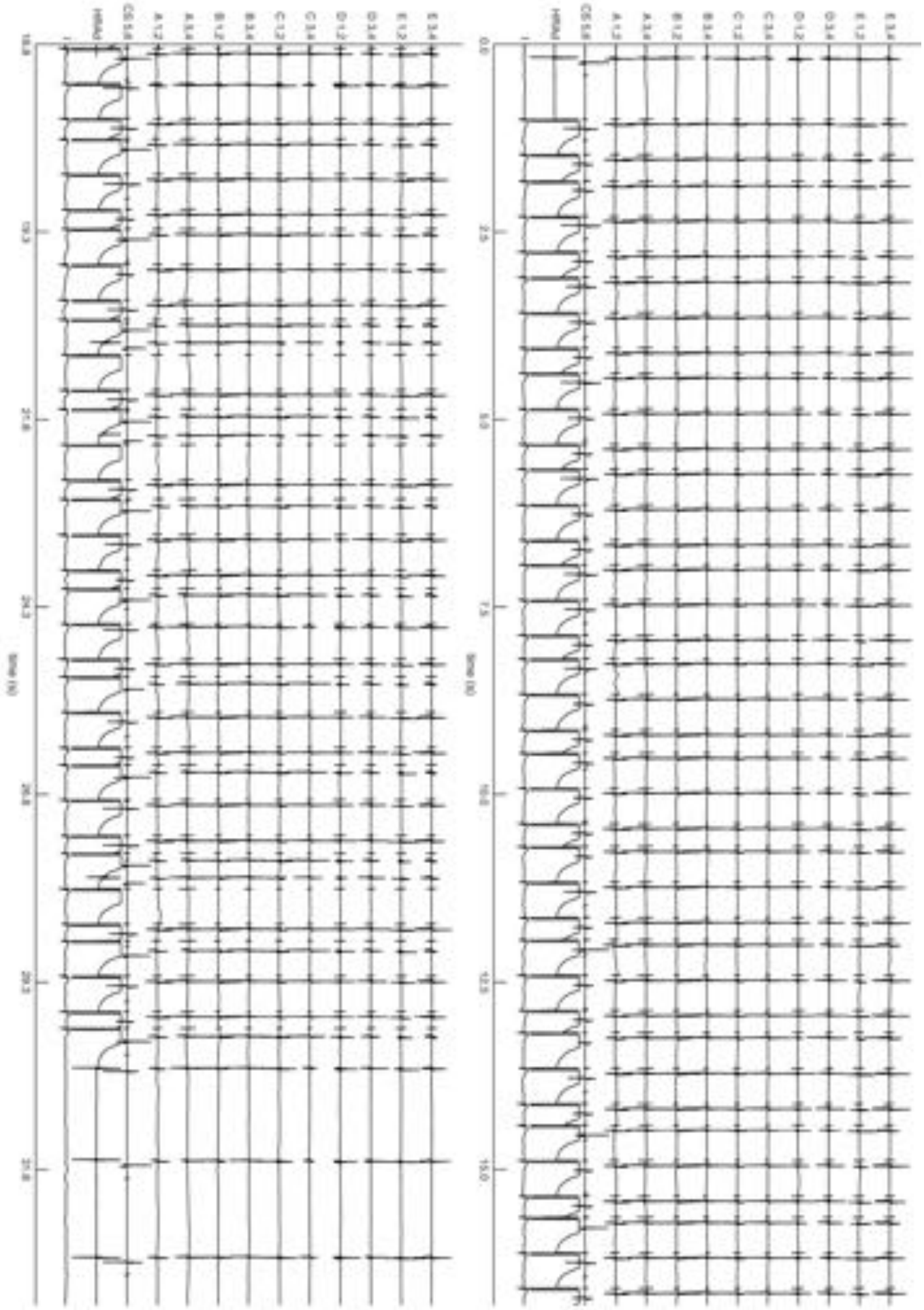

Case 10 – HRA pacing

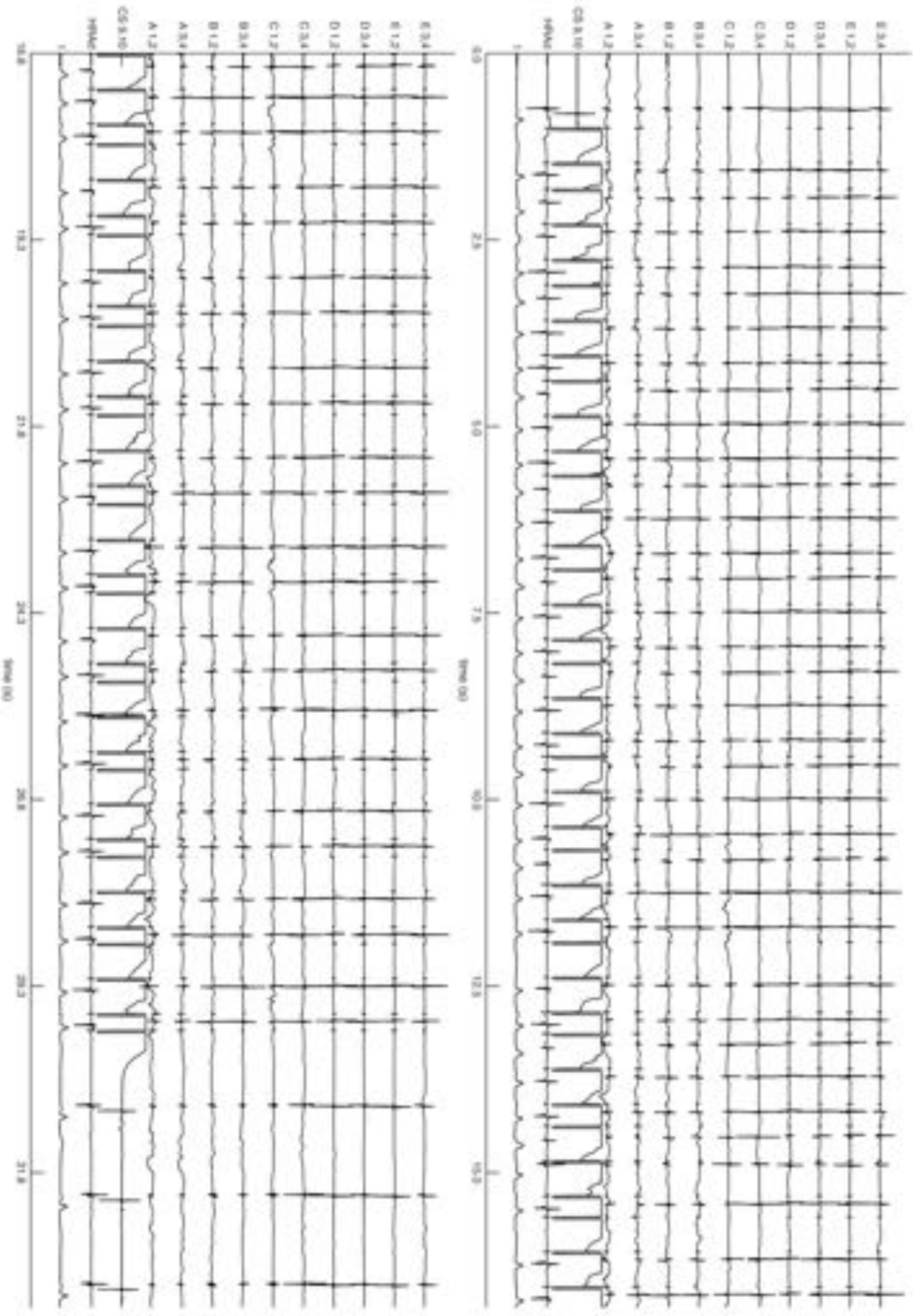

Case 11 – CS pacing

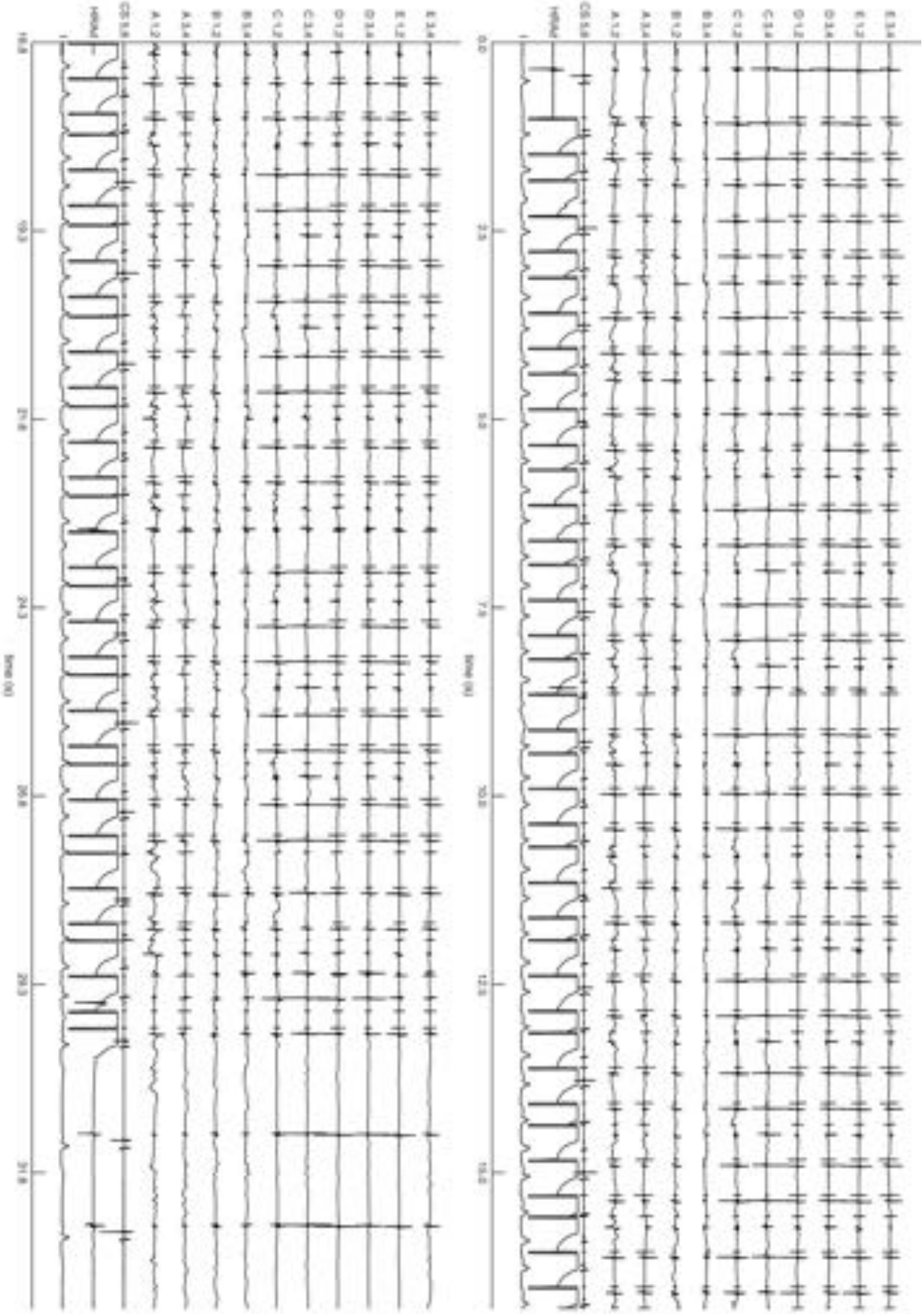

Case 11 – HRA pacing

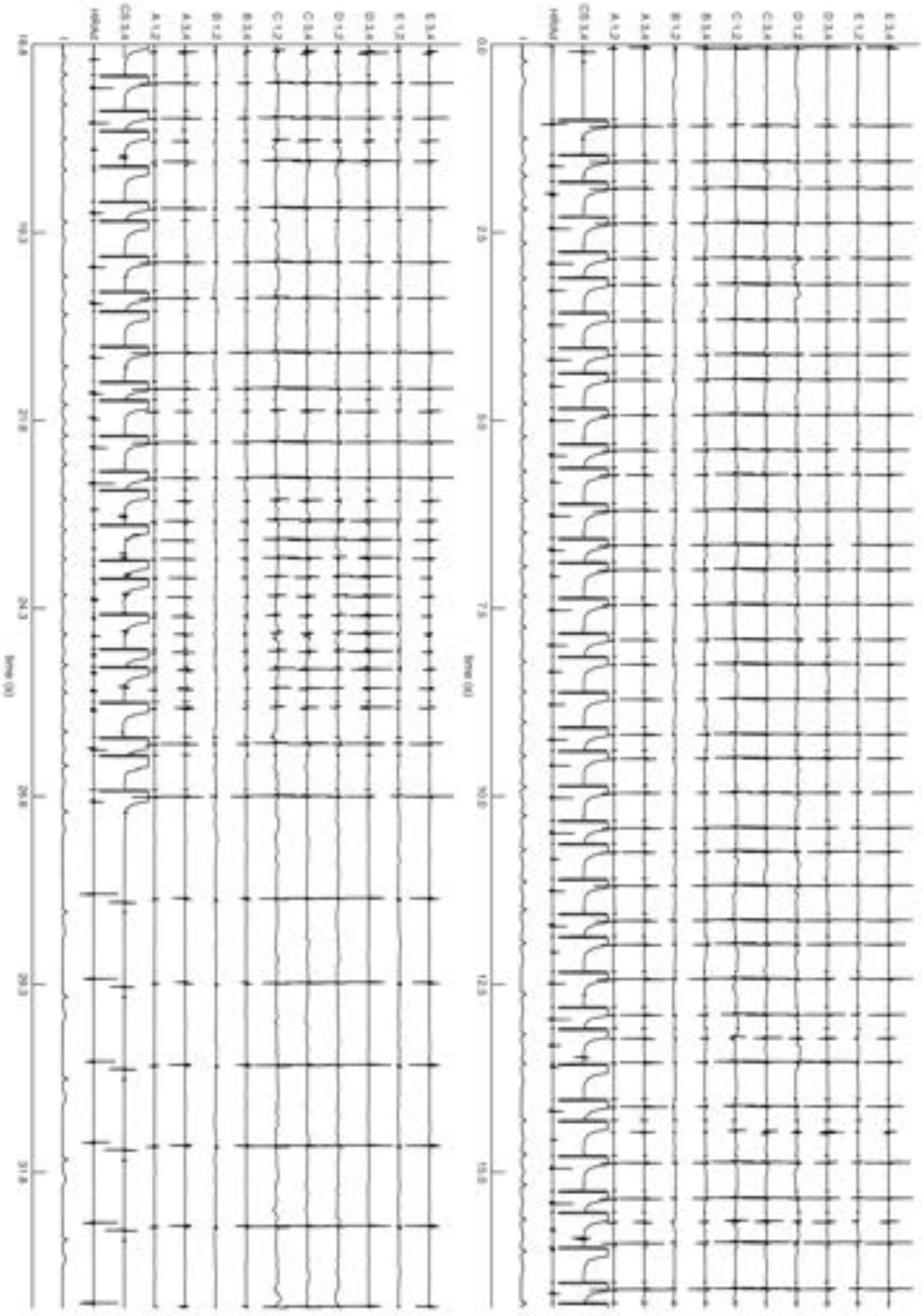

Case 12 – CS pacing

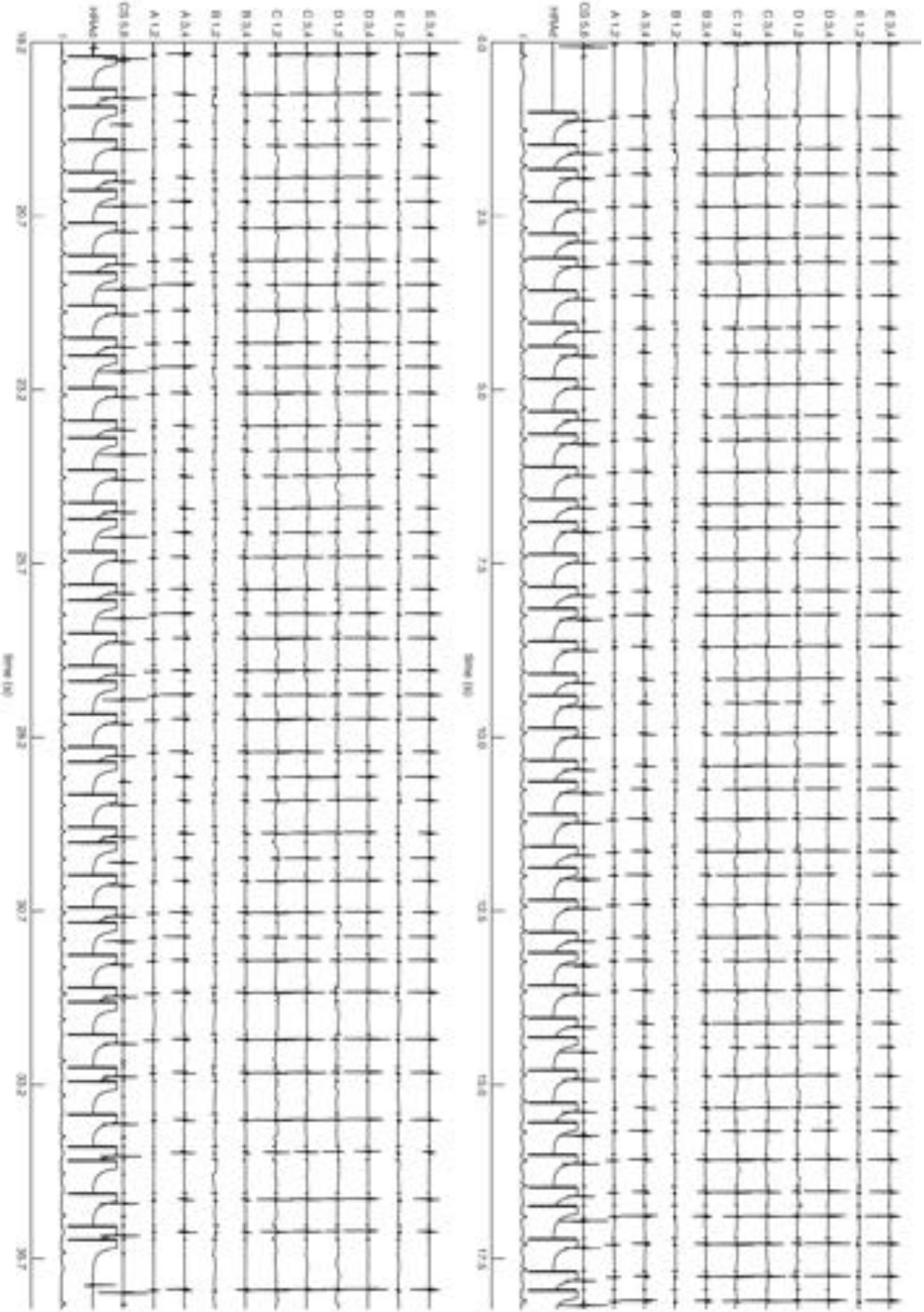

Case 12 – HRA pacing

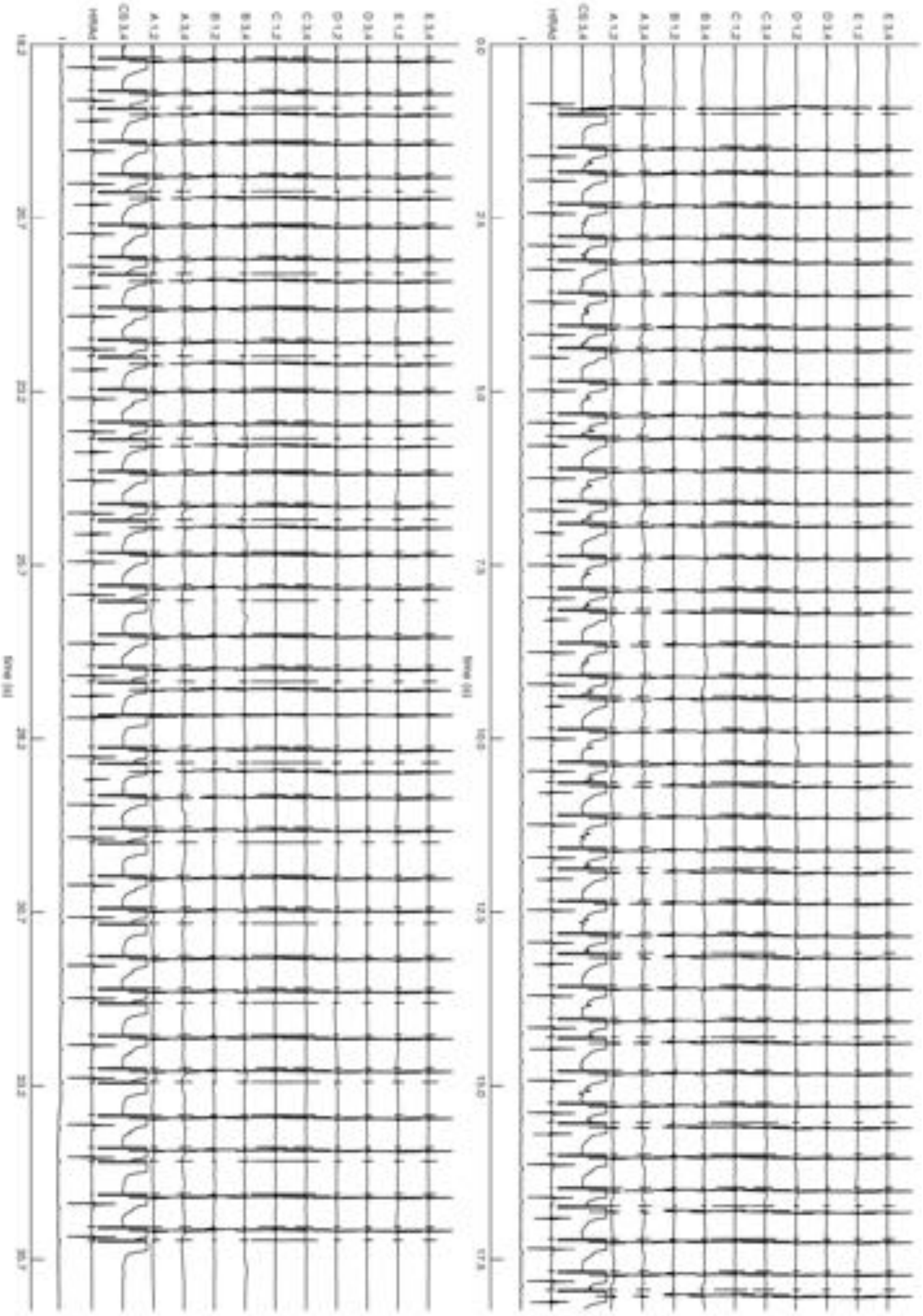

Case 13 – CS pacing

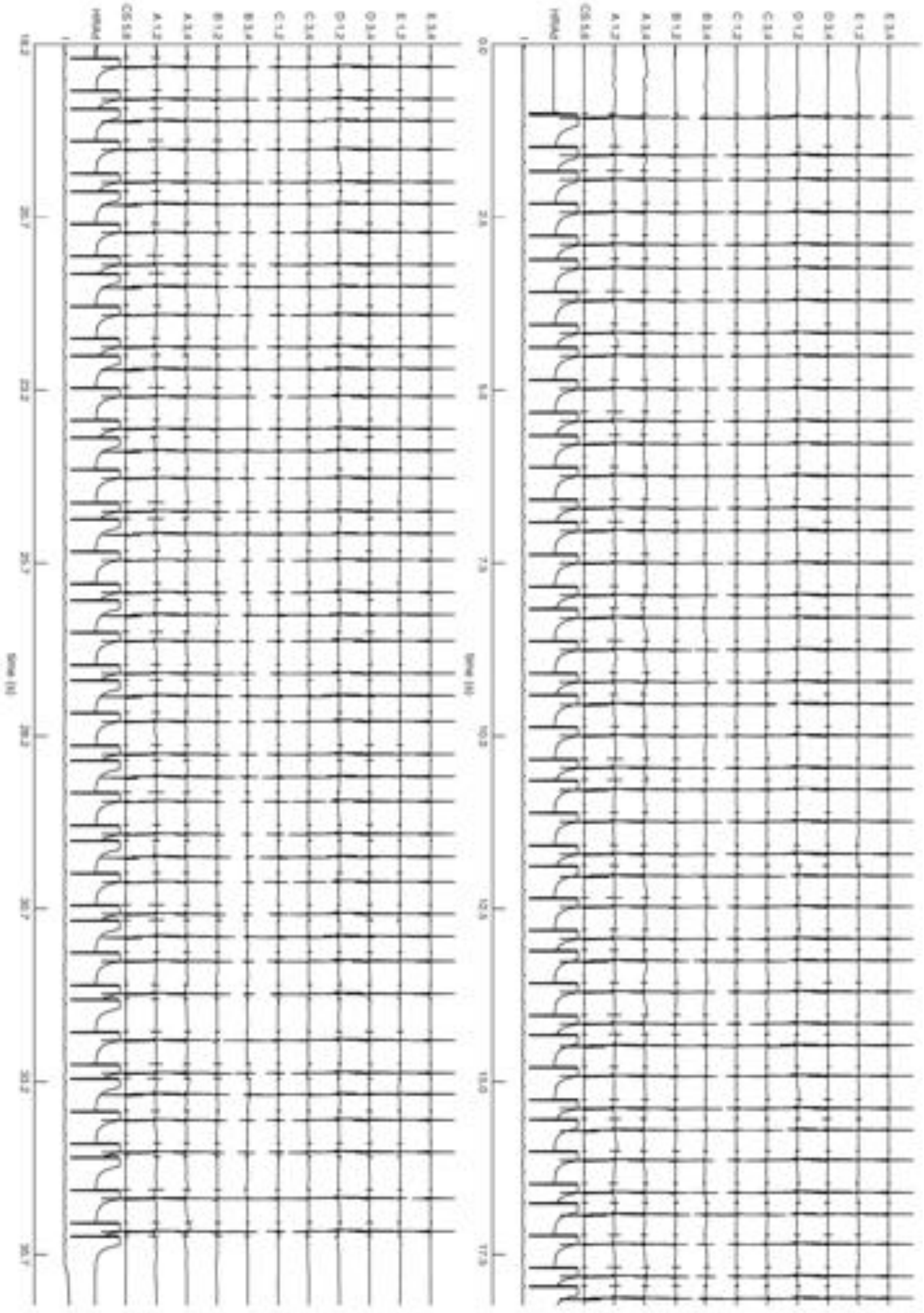

Case 13 – HRA pacing

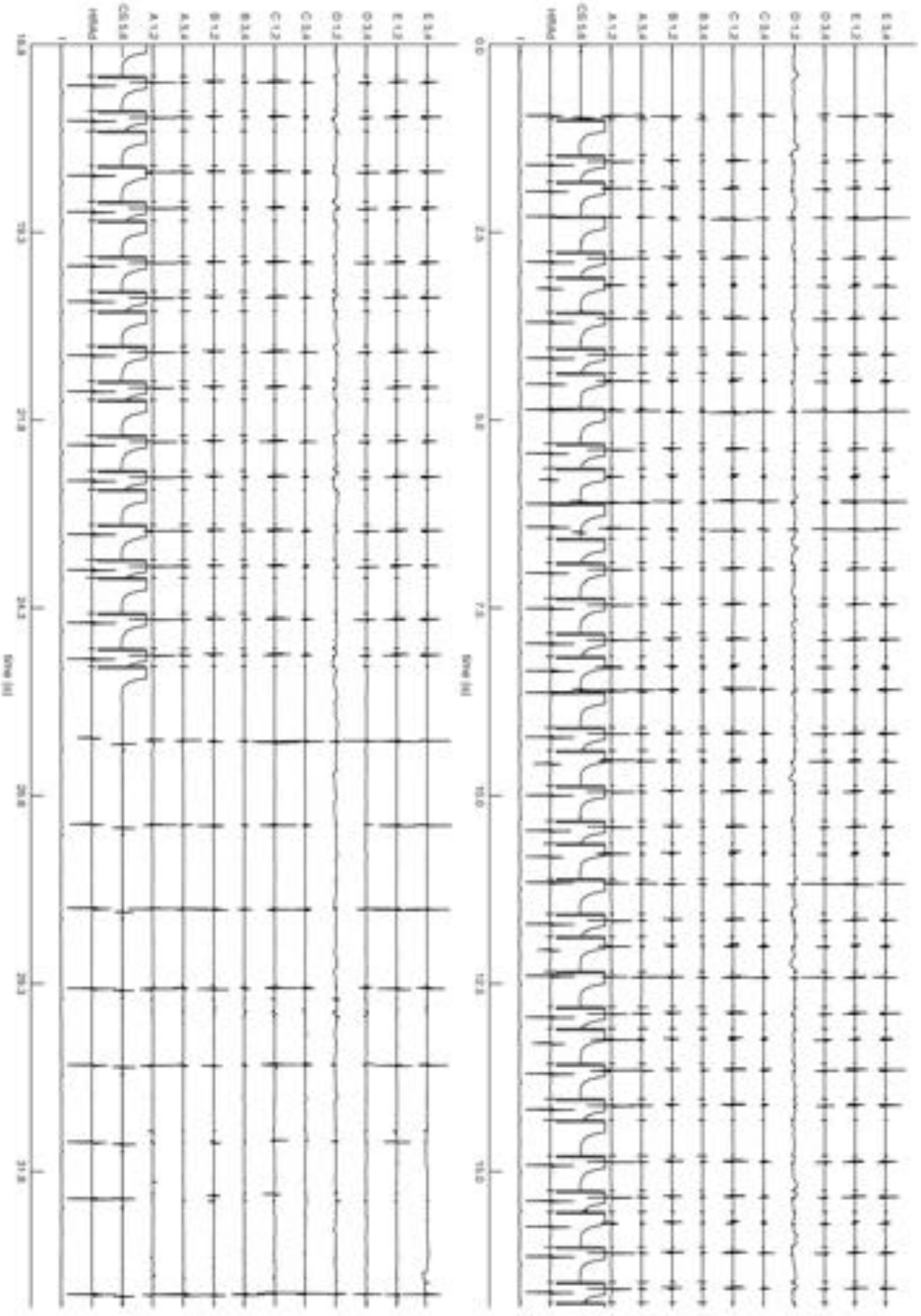

Case 14 – CS pacing

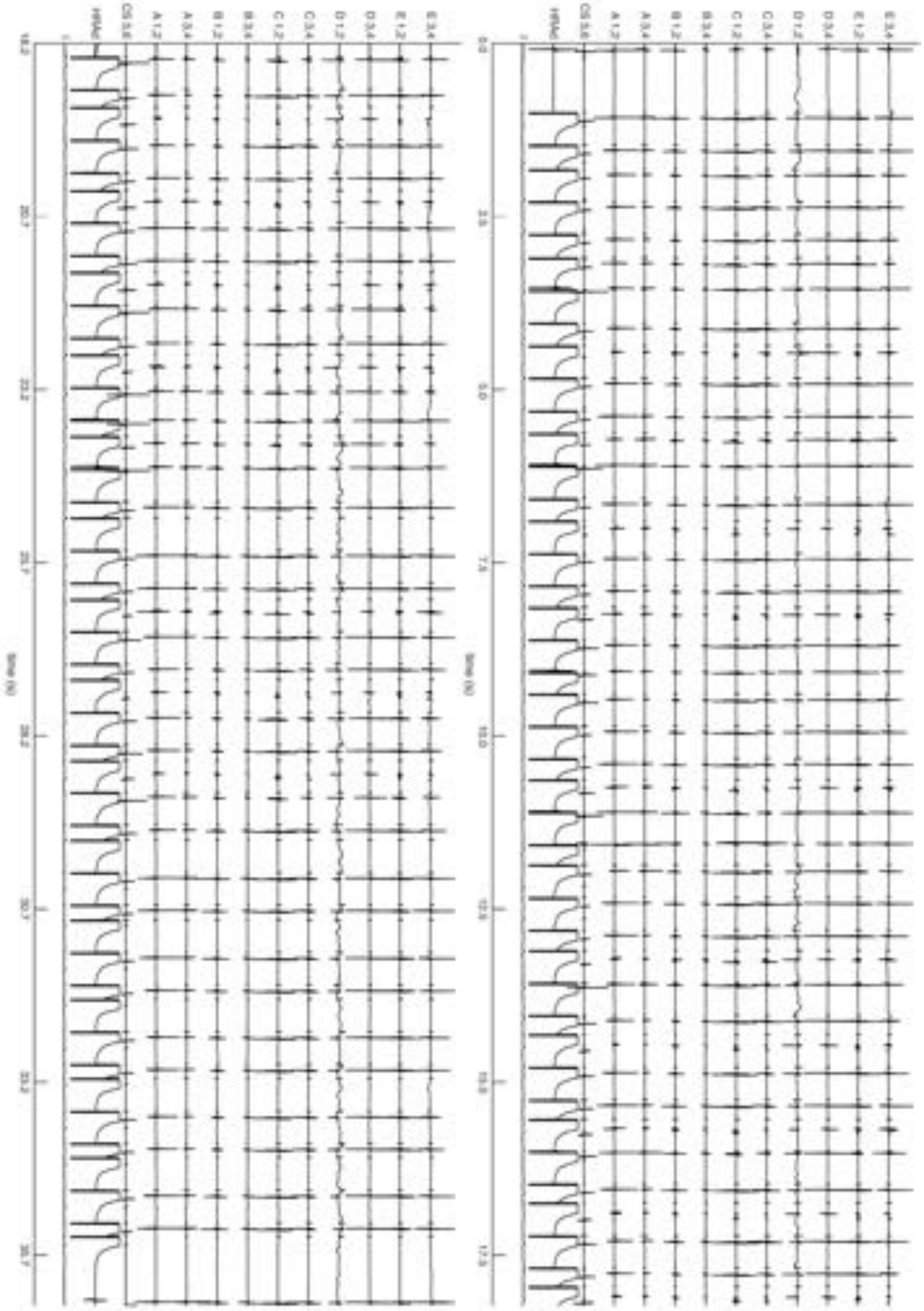

Case 14 – HRA pacing

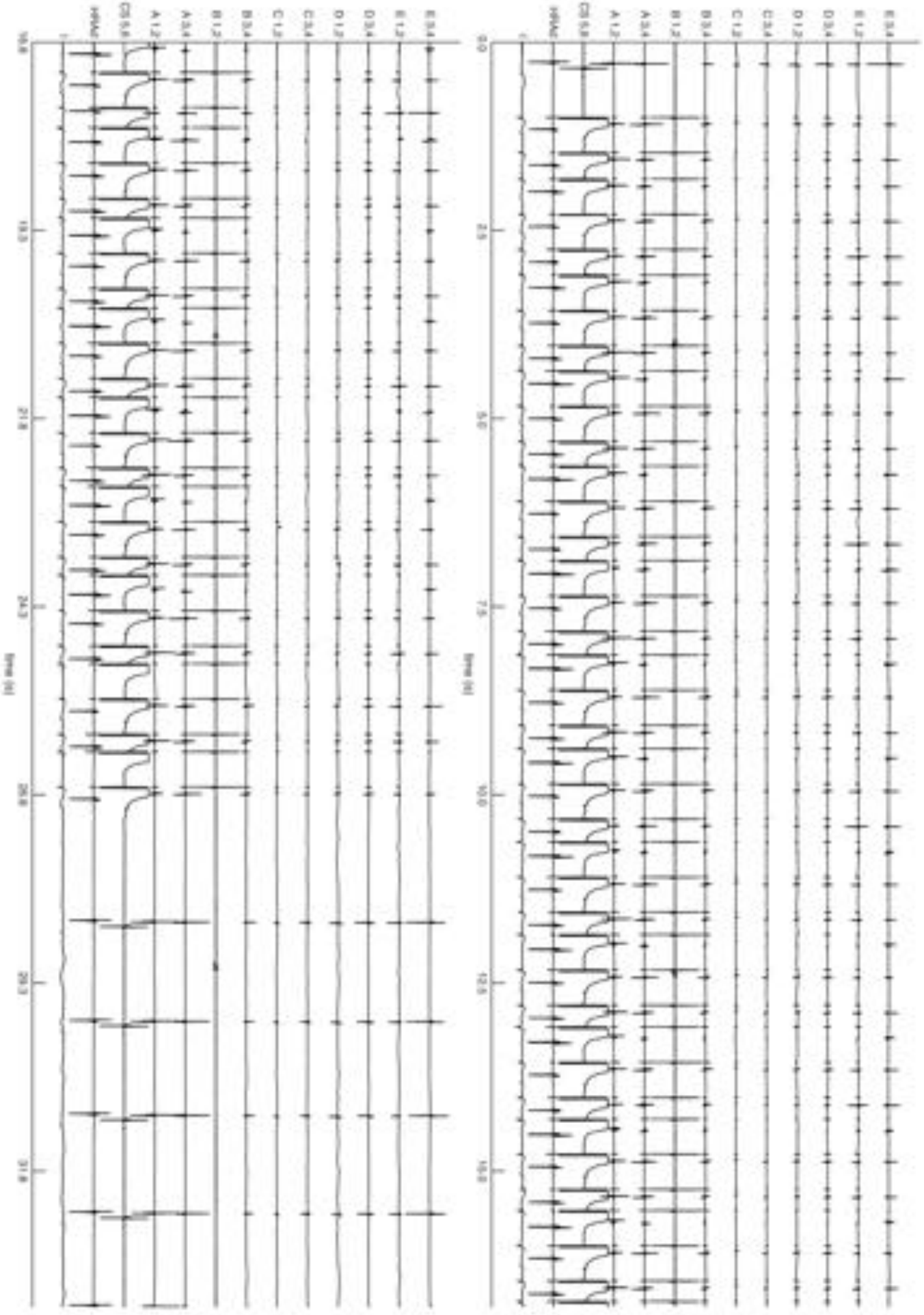

Case 15 – CS pacing

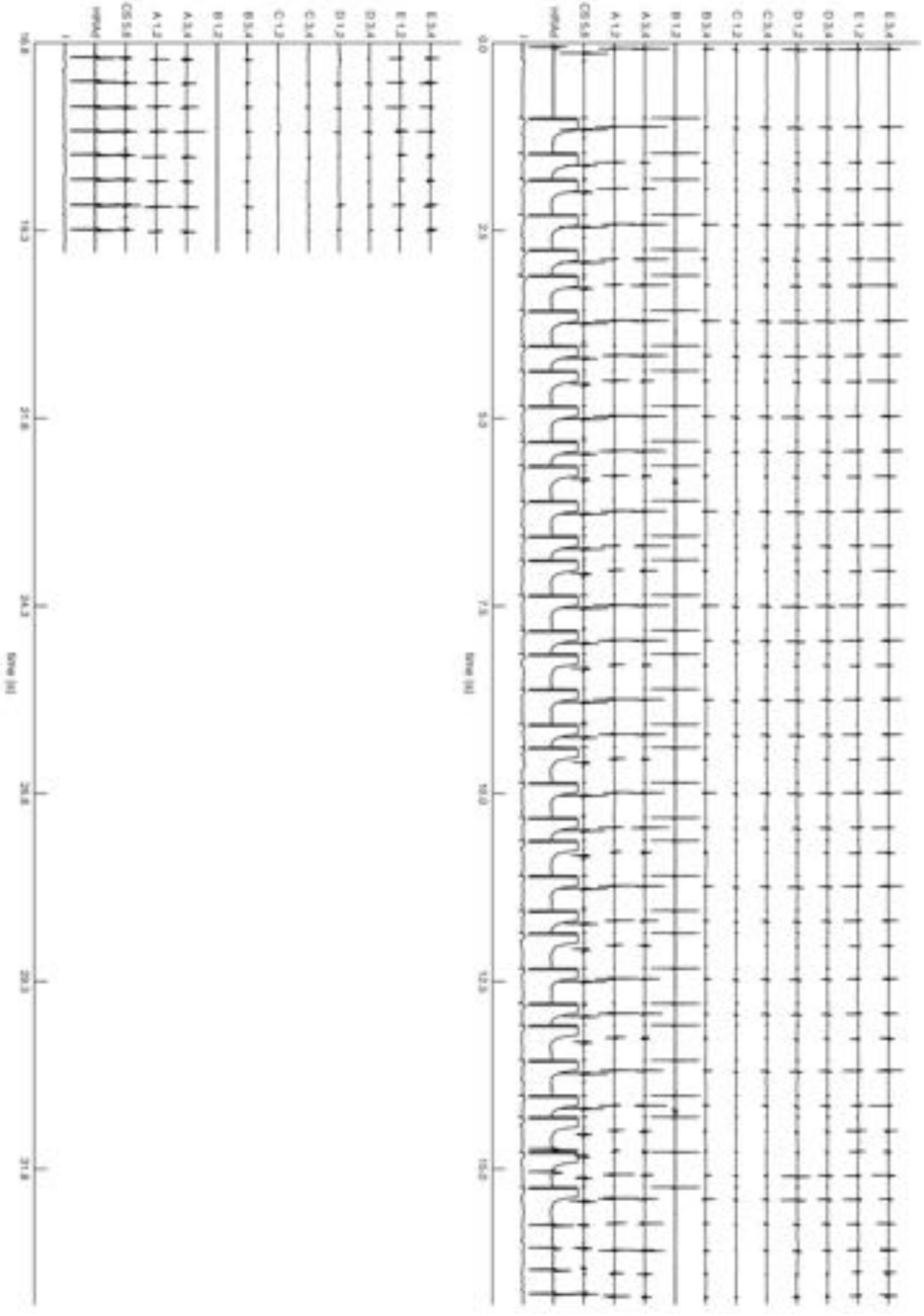

Case 15 – HRA pacing

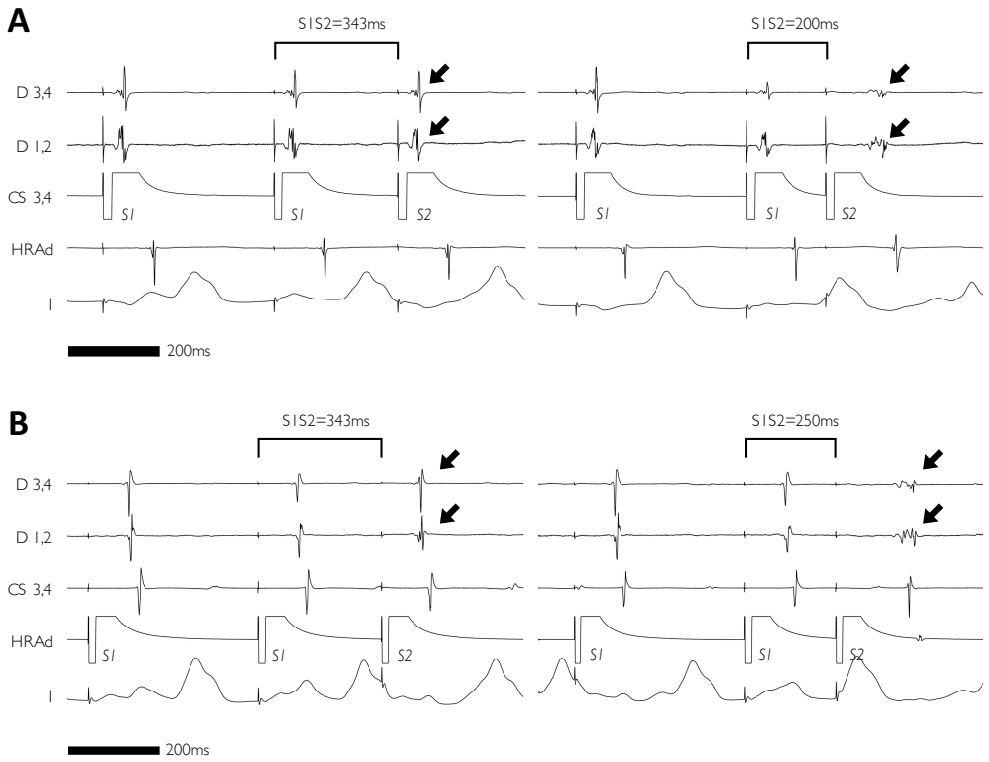

Figure 4-8. Bidirectional Paced Electrogram Fractionation

Paced electrograms recorded from a single LA site from Case 8 (see pages 116-117) showing fractionation of A2 electrograms (arrowed) during both CS pacing (panel **A**) and HRA pacing (panel **B**).

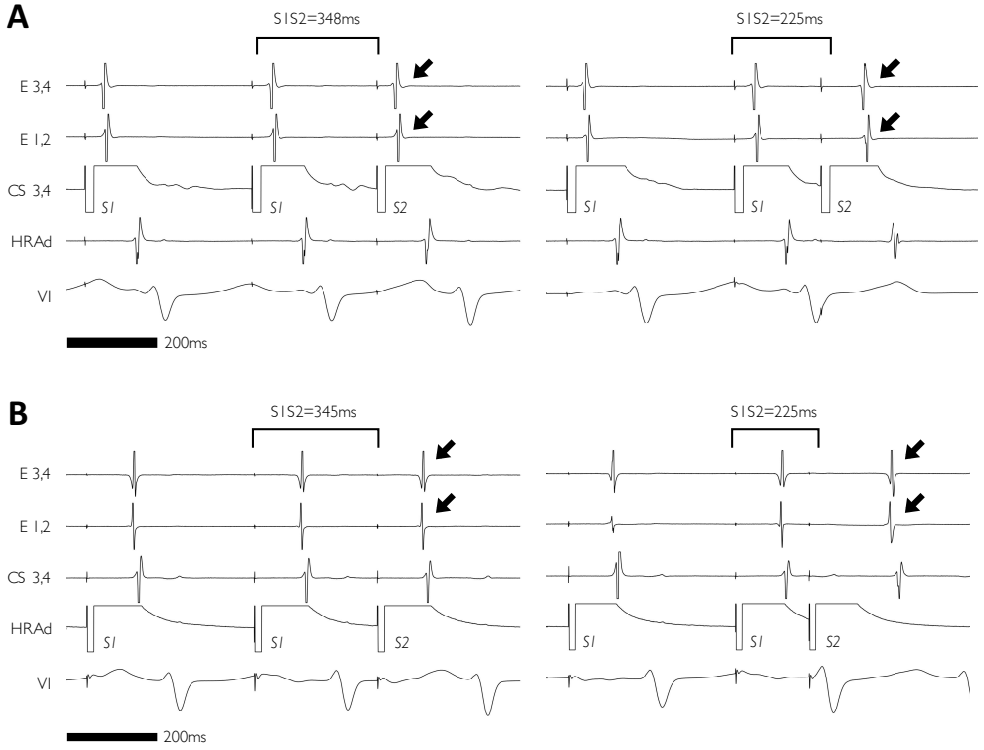

Figure 4-9. Absence of Paced Electrogram Fractionation

Paced electrograms recorded from a single LA site from Case 13 (see pages 126-127) showing no fractionation of A2 electrograms (arrowed) during either CS pacing (panel **A**) or HRA pacing (panel **B**).

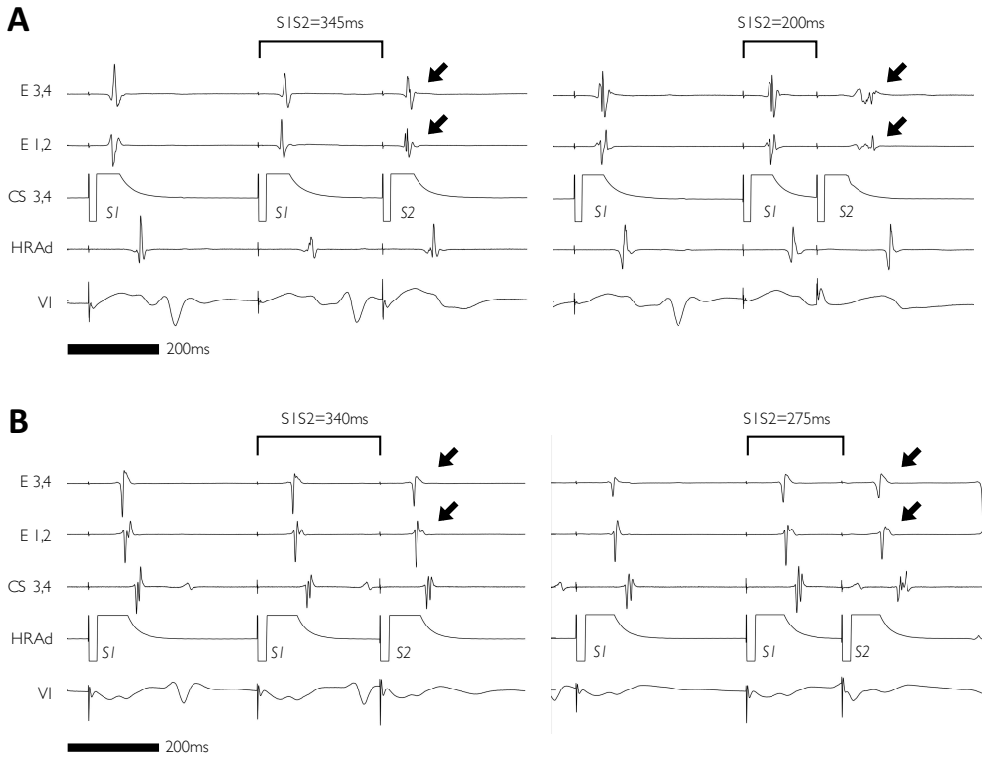

Figure 4-10. Unidirectional Paced Electrogram Fractionation from CS pacing

Paced electrograms recorded from a single LA site from Case 4 (see pages 108-109) showing fractionation of A2 electrograms (arrowed) during CS pacing (panel **A**) but not HRA pacing (panel **B**).

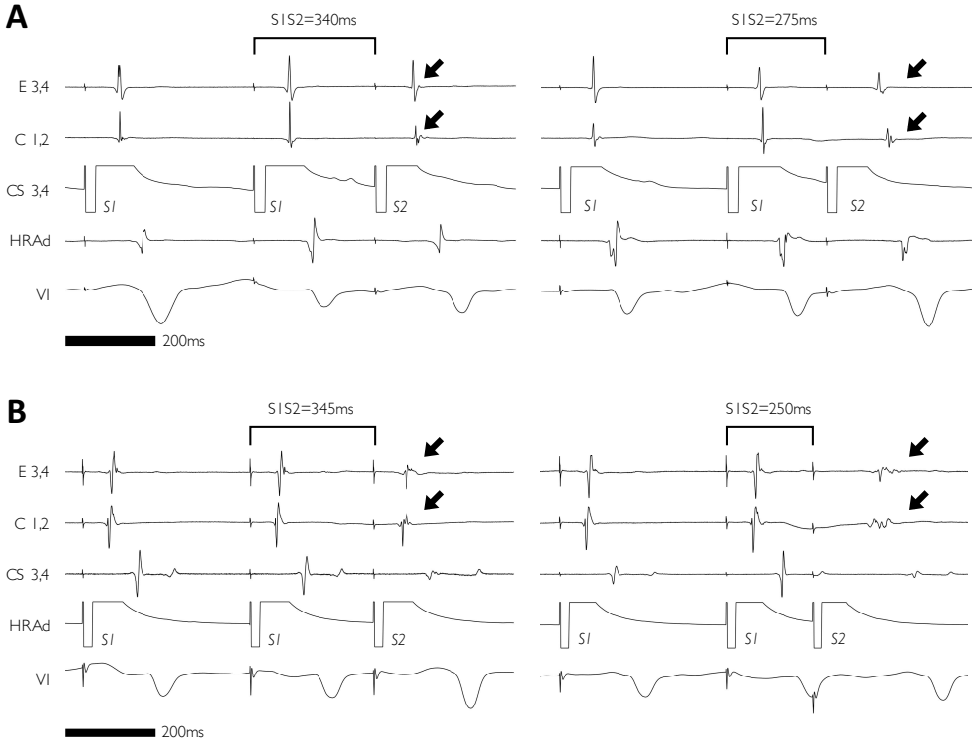

Figure 4-11. Unidirectional Paced Electrogram Fractionation from HRA pacing

Paced electrograms recorded from a single LA site from Case 11 (see pages 122-123) showing fractionation of A2 electrograms (arrowed) during HRA pacing (panel **B**) but not CS pacing (panel **A**).

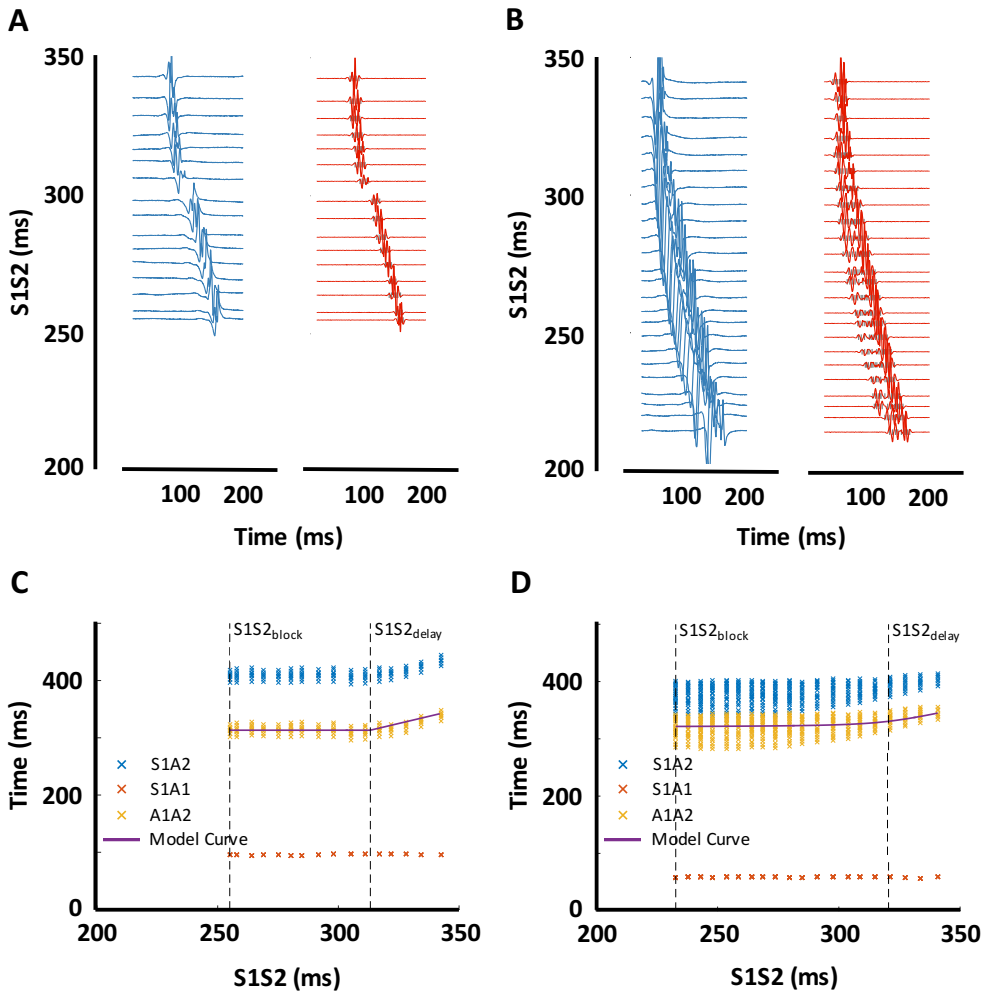

Figure 4-12. Electrogram Morphologies and S1S2-A1A2 Conduction Curves

A, **B** – Examples of early conduction delay and block with limited fractionation and later conduction delay and block with marked electrogram fractionation. Blue - unfiltered electrograms; Red - bandpass filtered electrograms (30-500Hz). **C**, **D** – S1S2-A1A2 conduction curves created by timing each A2 electrogram to its preceding A1 electrogram. Purple lines indicate a three-part curve fitted to the peaks to allow identification of $S1S2_{delay}$ and $S1S2_{block}$.

Conduction Delay, Conduction Block and Pacing Latency

The distribution of conduction delay parameters measured across the whole population is shown in Figure 4-13. $S1S2_{block}$ was relatively evenly distributed on the range 200-300ms for both HRA pacing and CS pacing. $S1S2_{delay}$ showed a bimodal distribution with peaks for HRA / CS pacing at 275±11 / 271±11ms and 326±13 / 319±16ms. Within a single case, measured $S1S2_{delay}$ was uniform across the left atrium, and independent of activation direction (HRA vs. CS $S1S2_{delay}$ R^2=0.7274, p<0.0001). Conversely, $S1S2_{block}$ varied with both pacing site (Figure 4-13C) and between LA regions. These findings suggest that $S1S2_{block}$ is significantly influenced by both pacing-site and left atrial electrophysiological properties, although the relative contributions of refractoriness and

intra-atrial conduction block are uncertain. In contrast, $S1S2_{delay}$ is more independent of pacing-site related properties. LA maps of $S1S2_{delay}$ and $S1S2_{block}$ are shown in Figure 4-14. In order to determine where along the pathway of conduction (i.e. from pacing site to LA recording site) that conduction delay occurred a number of observations are made in Figure 4-15. Firstly, conduction delay close to the pacing site (termed 'pacing latency') was quantified as the delay between stimulation and earliest local electrogram on the next nearest bipole. Although pacing latency was significantly correlated with LA conduction delay (Figure 4-15A), it was insufficient alone to explain the overall conduction delay seen (compare circles and triangles in Figure 4-15B). Next, considering that intra-atrial conduction delay must therefore be present, individual local LA activation times were plotted against the preceding coupling interval (S1S2 time) and grouped according to the conduction path length (termed 'Distance' in Figure 4-15C and D). In the majority of cases, left atrial LAT was incrementally delayed as the recording site moved more distant from the stimulation site (Figure 4-15C), however a number of cases showed reduced or absent decrement (Figure 4-15D). These findings are summarised in Figure 4-15E and Figure 4-15F indicating that change in activation time was significantly larger for recording sites greater than 60mm from earliest LA activation. A distance of 60mm was chosen since this represented the overall midpoint of path length distributions.

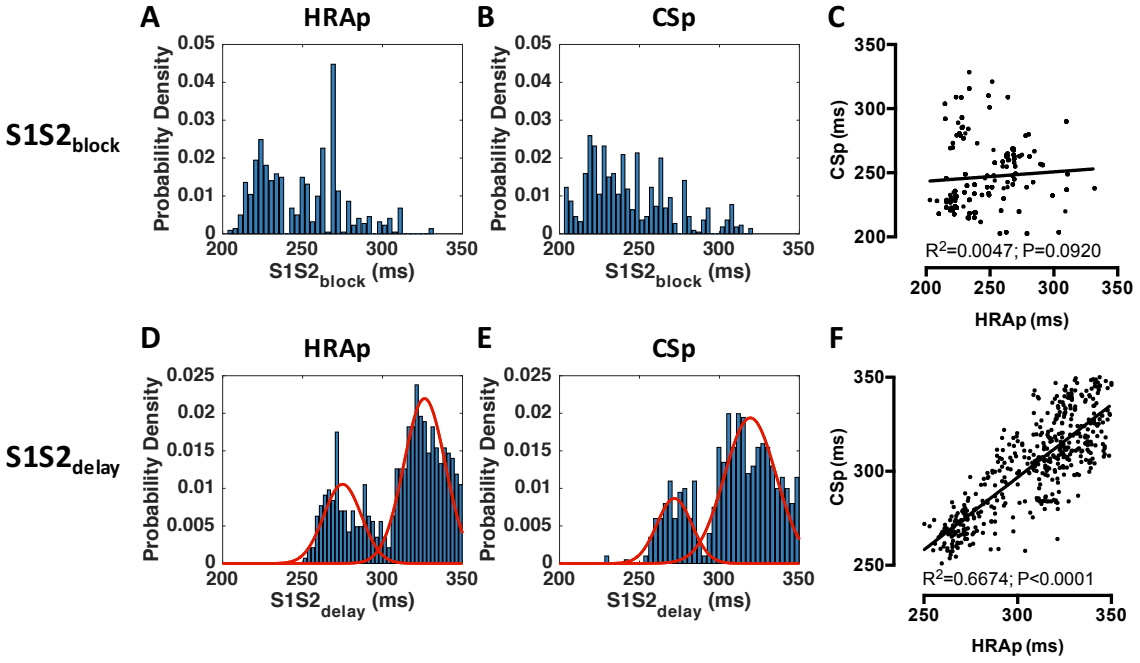

Figure 4-13. Conduction Delay Frequency Distributions

Overall distributions are shown for HRA (HRAp) and CS pacing (CSp). ERP did not confirm to any tested distributions. RRP and FRP showed bimodal distributions suitably represented by a Gaussian mixed model.

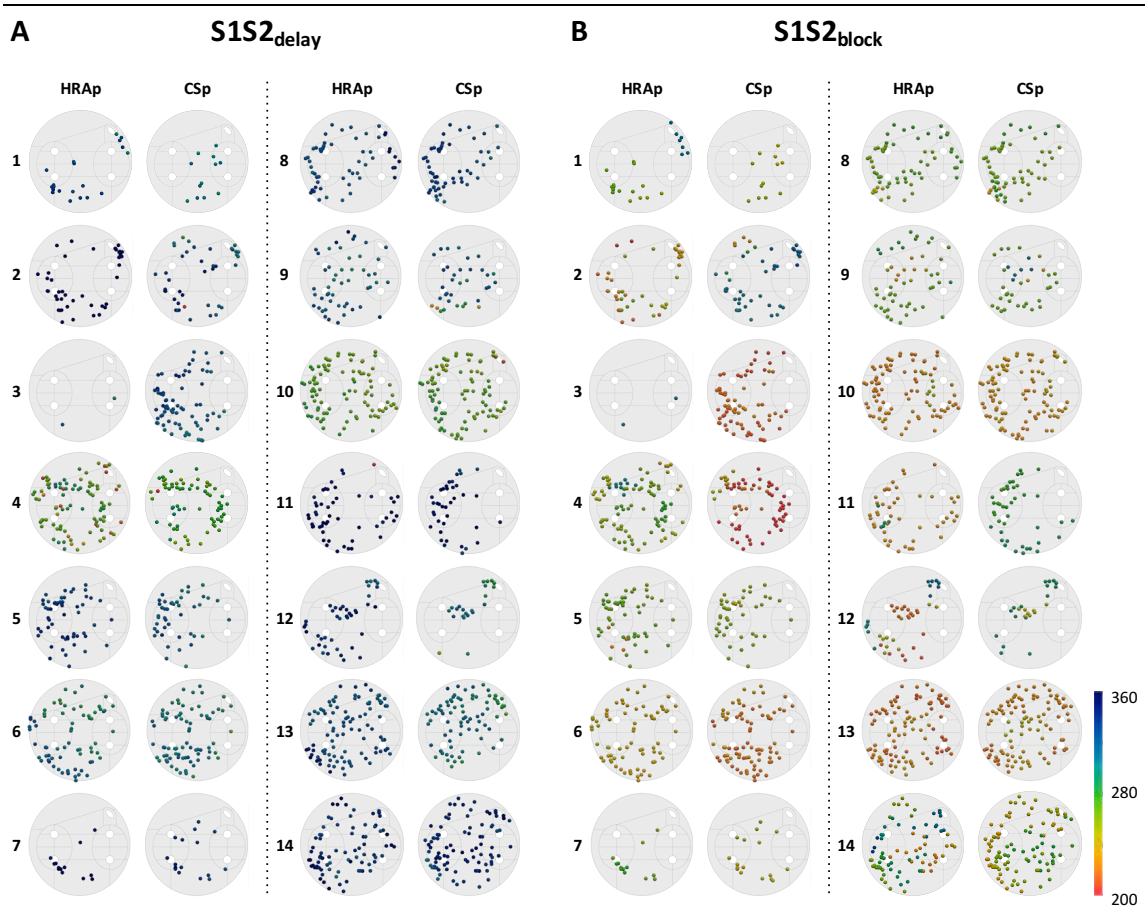

Figure 4-14. $S1S2_{delay}$ and $S1S2_{block}$ Distributions

Atrial unfold maps (for processing steps see Figure 5-2) are shown for HRA and CS pacing.

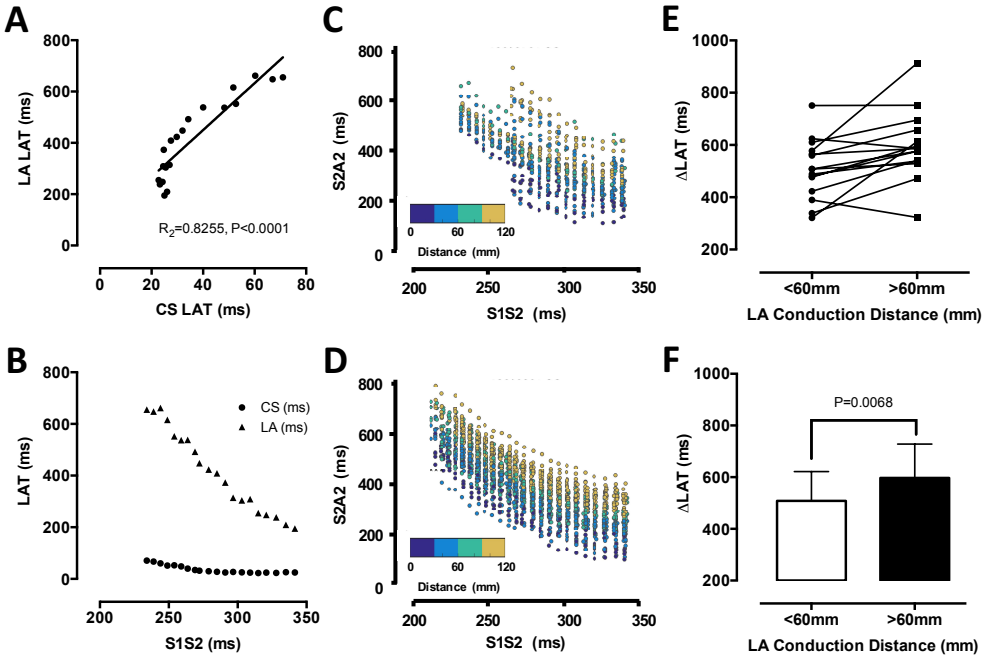

Figure 4-15. Components of Intra-Atrial Conduction Delay

A, B – Pacing latency; **C, D** – Conduction curves coloured by path length distance; **E, F** – ΔLAT represents the difference between earliest and latest LA activation for regions of the chamber less than and greater than 60mm from the earliest LA activation site.

Electrogram Duration

Electrogram duration is a marker of abnormal conduction, with electrogram prolongation seen in regions of microfibrosis (277). Therefore, electrogram duration was quantified using two parameters from the S1S2-A1A2 curves for each LA region: 1) electrogram duration at baseline S1S2=343ms (ED, ms); and 2) maximal increase in electrogram duration compared to baseline (ΔED, ms). Frequency distribution histograms for ED and ΔED are given in Figure 4-16.

Mean ED across the population ranged from 11-57ms (HRA pacing) and 8-65ms (CS pacing). Considering the population as a whole there were generally no significant differences in regional ED under HRA pacing vs. CS pacing. The one exception was the anterior LA region where ED was significantly longer under HRA pacing, consistent with activation of this site from two directions originating from the septum and Bachman's bundle (Figure 4-17B). ED did however vary significantly between LA regions for both HRA and CS pacing with longer ED universally seen in the LA septum compared to the four other regions (Figure 4-17B). Overall, there was a weak but significant correlation between HRA pacing ED and CS pacing ED (Figure 4-17A) indicating that ED is to a certain extent independent of wave front activation direction and possibly related to local LA myocardial properties (e.g. microfibrosis or multiple conducting pathways).

Mean ΔED varied throughout the population with ranges of 0.3-53ms (HRA pacing) and 3-57ms (CS pacing) and, as for ED, there was no overall difference in mean regional ΔEDs under HRA pacing as compared to CS pacing (Figure 4-17D). Considering the whole population ΔEDs recorded under HRA pacing were weakly correlated with ΔEDs recorded under CS pacing, although given the strength and significance of this association (R^2=0.0217, P=0.0347) were both negligible (Figure 4-17C). As for ED, ΔED varied significantly between LA regions for both HRA and CS pacing, again with greater ΔED seen in septal regions. Examining patients individually revealed there to be some cases with very close ΔEDs comparing HRA to CS pacing (ΔED variation<10ms) and others with much greater variation in ΔED (ΔED variation>10ms). This finding indicates that, for some patients, ΔED is an activation direction-dependent phenomenon (which may therefore be functional in nature), whilst for other patients ΔED at a single recording site is independent of activation direction and may reflect local LA remodelling.

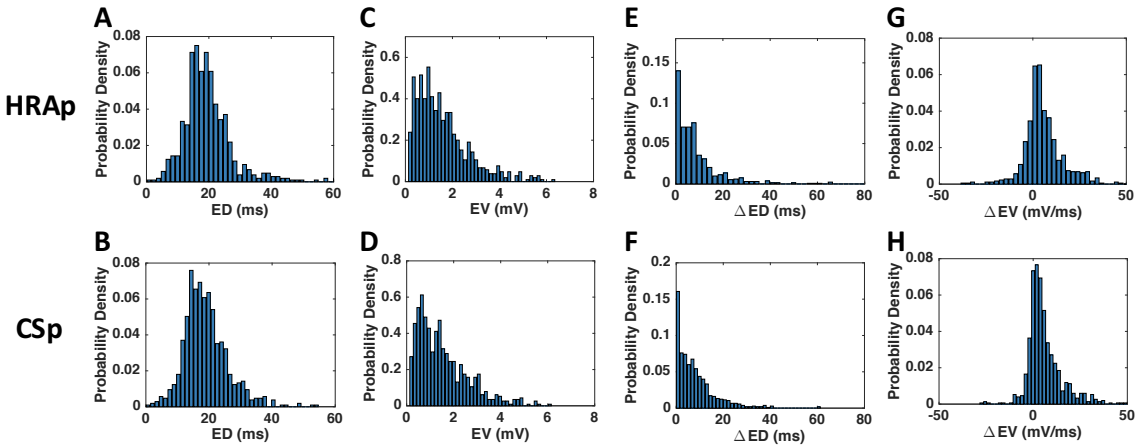

Figure 4-16. Electrogram Duration Frequency Distributions

Overall electrogram duration and electrogram voltage distributions are shown for HRA pacing (HRAp) and CS pacing (CSp). **A**, **B** – electrogram duration (ED); **C**, **D** – electrogram voltage (EV); **E**, **F** – increase in electrogram duration with coupling interval (ΔED); **G**, **H** – change in electrogram voltage with coupling interval (ΔEV)

Electrogram Voltage

Electrogram voltage is a marker of abnormal atrial substrate, with reduced EV seen in regions of sodium channel blockade and reduced coupling (277). Therefore, electrogram voltage was quantified using two parameters from the S1S2-A1A2 curves for each LA region: 1) electrogram voltage at baseline S1S2=343ms (EV, mV); and 2) rate of change of electrogram voltage with S1S2 coupling interval (ΔEV, mV/s). Frequency distribution histograms for EV and ΔEV are given in Figure 4-16.

Mean EV across the population ranged from 0.7-2.7mV (HRA pacing) and 1.0-2.4mV (CS pacing). Considering the population as a whole there were no significant differences in regional EV under HRA pacing vs. CS pacing (Figure 4-17F). Furthermore, EV varied between LA regions only under HRA pacing and not CS pacing. One possible explanation for this observation is wave front collision in the LA during HRA pacing with multiple RA-LA breakthrough sites. Consistent with the observation of greater septal ED, septal EV was however significantly lower than other LA regions, indicating that electrograms in this region are generally longer in duration and lower in amplitude than in other parts of the LA. Overall there was a significant correlation between HRA pacing EV and CS pacing EV (Figure 4-17E) indicating that EV is to a certain extent agnostic of activation direction and therefore likely to be influenced largely by local LA properties.

Mean case ΔEV varied throughout the population with ranges of -2 to 11mV/s (HRA pacing) and 3 to 11mV/s (CS pacing) and, as for EV, there was no overall difference in

mean regional ΔEVs under HRA pacing as compared to CS pacing (Figure 4-17H). Considering the population as a whole ΔEVs recorded under HRA pacing were weakly correlated with ΔEVs recorded under CS pacing (Figure 4-17G) but, as for ΔED, the strength of the correlation was negligible (R^2=0.02, P=0.0002). There were no intra-atrial regional variations in ΔEV for HRA pacing and regional variations in ΔEV for CS pacing were minimal (Figure 4-17H). Examining patients individually revealed there to be some cases with very close ΔEVs comparing HRA to CS pacing (ΔEV variation<4mV/s) and others with much greater variation in ΔEV (ΔEV variation>4mV/s). This finding indicates that, for some patients, ΔEV is partially activation direction-independent. One mechanism for this observation may be an underlying atrial myopathy with loss of recruitment of myocytes at shorter coupling intervals resulting in lower bipolar electrogram voltages at these sites.

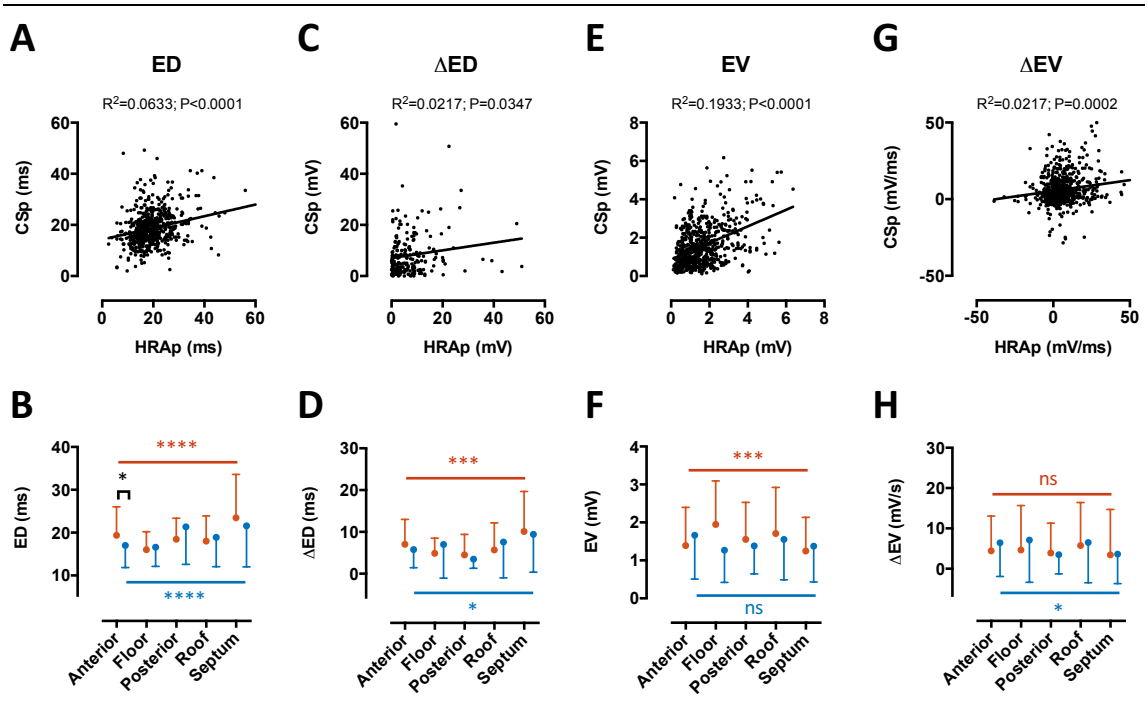

Figure 4-17. Electrogram Voltage and Duration

Top row – correlation between electrogram voltage and duration parameters between HRA pacing and CS pacing. Bottom row – regional distributions of electrogram voltage and duration parameters. Red lines and significance notations refer to HRA pacing; Blue lines and significance notations refer to CS pacing. Black significance notations refer to HRA pacing vs. CS pacing. **A**, **B** – electrogram duration (ED); **C**, **D** – increase in electrogram duration with coupling interval (ΔED); **E**, **F** – electrogram voltage (EV); **G**, **H** – change in electrogram voltage with coupling interval (ΔEV).

AF Inducibility

Overall, the study protocol induced atrial fibrillation in 9/15 (60%) of patients. HRA pacing induced AF more often than CS pacing (8/15 (53%) vs. 4/15 (27%)) but this

difference was not statistically significant (P=0.2635). Of the cases where AF was induced, the majority of AF was triggered by HRA pacing alone (5/9 cases), followed by HRA and CS pacing (3/9 cases) and finally by CS pacing alone (1/9 cases). The mean S2 coupling interval at which AF was induced was 281±25ms. There was no difference in the S2 interval at AF induction between HRA pacing and CS pacing (287±20ms vs. 272±33ms). There was no significant difference in $S1S2_{delay}$, $S1S2_{block}$, electrogram voltage or electrogram duration between patients in whom the study protocol induced AF and those in whom AF was not induced for either HRA pacing or CS pacing (see Table 4-2). However, dispersion of LA activation during extrastimulus testing was significantly greater amongst patients in whom AF was induced vs. those in whom AF was not induced (Figure 4-18). This difference was only evident at sites distant (>60mm) from earliest LA activation, suggesting that discontinuous conduction is likely to be present resulting in accumulation of conduction delay as propagation proceeds throughout the LA in patients with greater electrical remodelling.

Table 4-2. Electrical Substrate in Patients with and without AF Induction

	Study parameter	AF Inducible	AF Non-Inducible	Unpaired t test, P=
HRAp	**$S1S2_{block}$ (ms)**	246 ± 12	234 ± 19	0.2293
	$S1S2_{delay}$ (ms)	323 ± 27	308 ± 24	0.3482
	EV (mV)	1.4 ± 0.6	1.6 ± 0.4	0.4971
	ED (ms)	29.0 ± 4.7	29.4 ± 4.9	0.8969
	ΔEV (mV/s)	5.9 ± 4.5	4.5 ± 4.2	0.5573
	ΔED (ms/ms)	25.4 ± 16.0	27.6 ± 12.0	0.7866
CSp	**$S1S2_{block}$ (ms)**	239 ± 24	243 ± 28	0.7493
	$S1S2_{delay}$ (ms)	320 ± 23	304 ± 19	0.1883
	EV (mV)	1.5 ± 0.5	1.5 ± 0.3	0.8091
	ED (ms)	30.7 ± 8.5	34.1 ± 6.3	0.4302
	ΔEV (mV/s)	6.2 ± 2.9	6.3 ± 2.2	0.9602
	ΔED (ms/ms)	29.2 ± 17.6	23.3 ± 11.2	0.4879

ERP, effective refractory period; RRP relative refractory period; FRP, functional refractory period; EV, electrogram voltage; ED, electrogram duration; ΔEV, change in electrogram voltage with pacing rate; ΔED, change in electrogram duration with pacing rate; HRAp, HRA pacing; CSp, CS pacing. Results are presented as mean values for each case, with standard deviations describing the variation between cases.

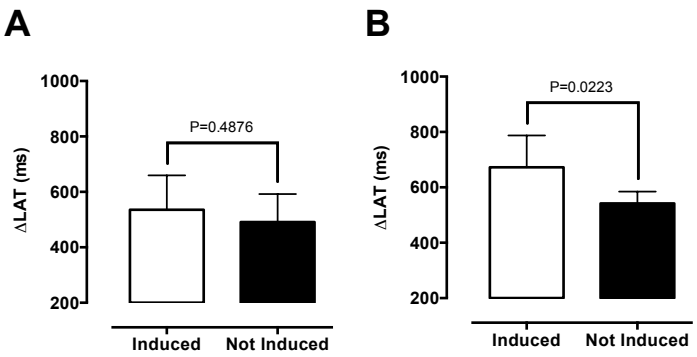

Figure 4-18. Dispersion of LA Activation During Extrastimulus Testing

Delay between earliest and latest LA activation (ΔLAT) is given for patients in whom AF was inducible (white bars) and non-inducible (black bars). **A** – LA sites with conduction path length <60mm; **B** – LA sites with conduction path length >60mm. See Figure 4-15 for calculation of ΔLAT.

Insights from Computational Modelling

In the first experiment a 4x4cm atrial monolayer was created with fibre orientation perpendicular to one edge. By pacing from two sites, planar activation waves were created travelling parallel to and perpendicular to the fibre orientation. Typical S1S2-A1A2 curves from two patients representing long conduction delay (Remodelling –) and short conduction delay (Remodelling +) are shown in Figure 4-19E and F for comparison. Introducing previously published reductions in I_{to}, I_{Kur}, and $I_{Ca,L}$ to the cell model resulted in shortening and flattening of the single-cell action potential (Figure 4-19B). The model was interrogated to question 1) whether these changes in APD could account for the spectrum of S1S2-A1A2 curves seen across the population and 2) whether changing the incidence wave/fibre orientation angle could account for the differences seen in $S1S2_{block}$ (but not $S1S2_{delay}$) between HRA pacing and CS pacing. As can be seen in Figure 4-19C, the standard Courtemanche cell model (SR AP) resulted in early conduction delay ($S1S2_{delay}$ ~300ms, $S1S2_{block}$ ~280ms) and an S1S2-A1A2 curve similar in morphology to 'Remodelling –' patients. In contrast, introducing the aforementioned channel conductance reductions into the cell model (AF AP, Figure 4-19D) resulted in much shorter conduction delay ($S1S2_{delay}$ ~230ms, $S1S2_{block}$ ~210ms) with an S1S2-A1A2 curve more similar in morphology to that seen in 'Remodelling +' patients. Longitudinal vs. transverse wave incidence angle had no effect on conduction curve morphology or conduction delay for either SR AP or AF AP (compare open and closed triangles in Figure 4-19C and D).

In the second experiment, two recording sites were used, separated by 1.5cm and parallel to the direction of activation. As before, the same S1S2 protocol as in the human studies was applied and activation times were recorded at both sites. The experiment was repeated using the SR AP, the AF AP and the AF AP with further reductions in I_{Na}. In Figure 4-20A, B and C increasing degrees of 'AF electrical remodelling' result in conduction curves with progressively increasing conduction delay, consistent with the spectrum of activation seen clinically in Figure 4-15. Electrical remodelling in this model was associated with flatter conduction velocity restitution curves (Figure 4-20D, E and F), with significantly reduced maximal CV restitution slope (Figure 4-20J). As previously described, APD restitution curves were also flattened by electrical remodelling (Figure 4-20G, H, I), although the introduction of additional sodium channel blockade had no additive effect on APD restitution flattening.

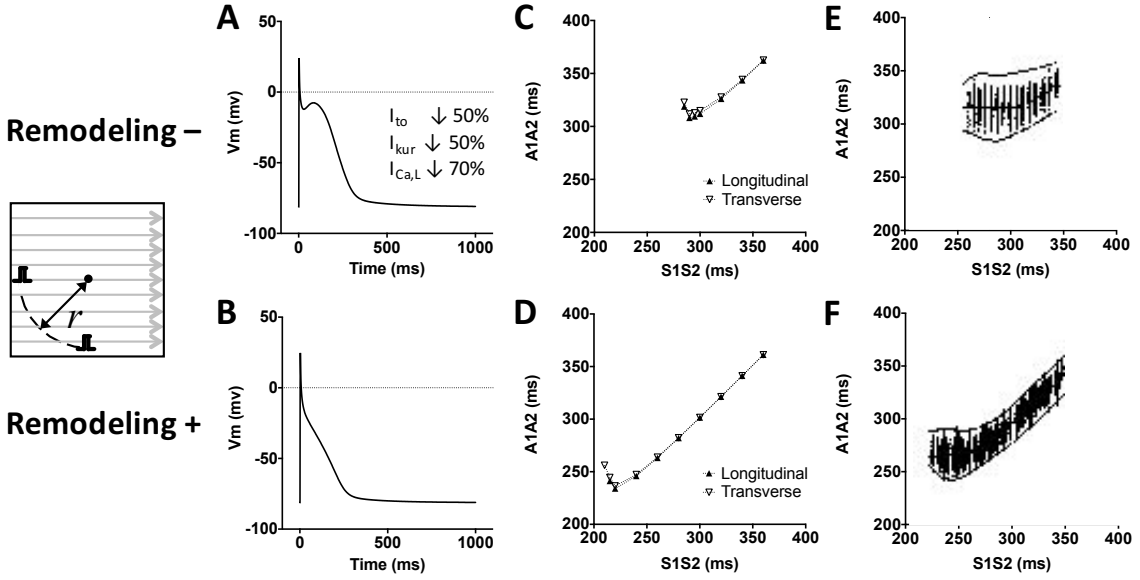

Figure 4-19. Relationship between Action Potential Duration and Conduction Curves

(Inset, left) Schematic showing the configuration of the experiment, *r*=18mm. **A** – Action potential for the sinus rhythm (SR) Courtemanche cell model and with modifications to I_{to}, I_{Kur}, and $I_{Ca,L}$ resulting in an 'AF' morphology action potential (**B**). **C**, **D** – Simulated S1S2-A1A2 curves demonstrating that reductions in I_{to}, I_{Kur}, and $I_{Ca,L}$ can account for the differing conduction curves seen clinically. **E**, **F** – Typical S1S2-A1A2 curves from two PAF cases with early and late conduction delay, respectively.

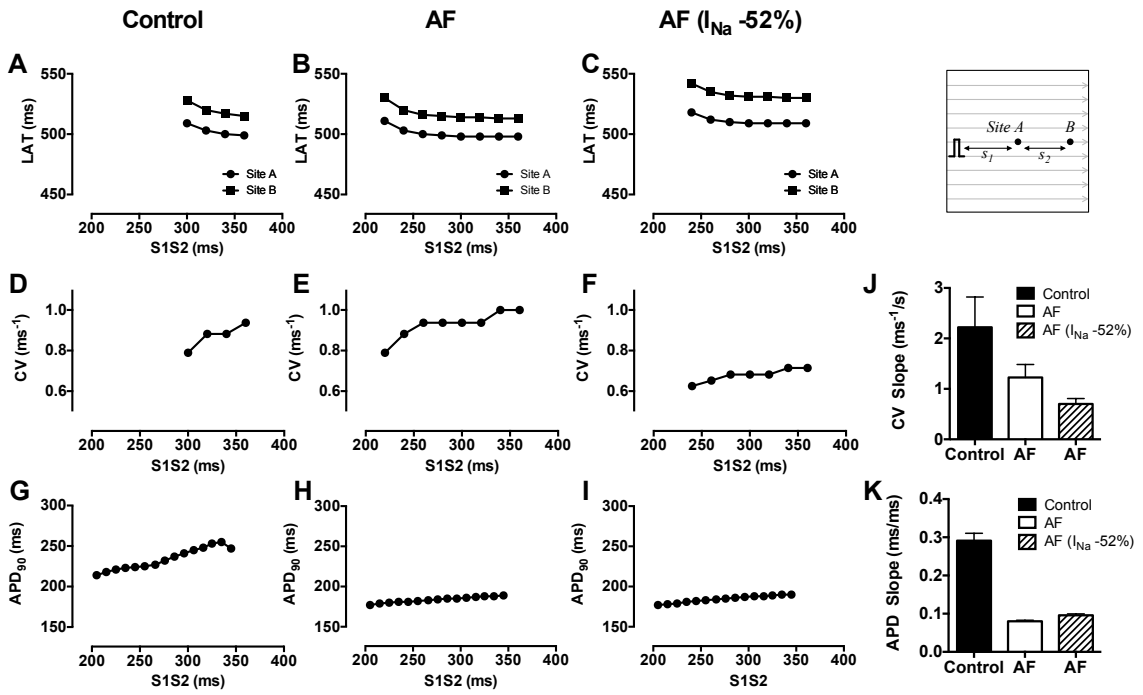

Figure 4-20. Conduction Velocity and Action Potential Restitution Properties

(Inset, left) Schematic showing the configuration of the experiment, s_1=18mm/s_2=15mm. **A**, **B**, **C** – Conduction curves recorded from Sites A and B in response to pacing of the control, AF and AF (reduced I_{Na}) cell models. **D**, **E**, **F** – Conduction velocity restitution curves. **G**, **H**, **I** – APD_{90} restitution curves. **J**, **K** – Maximal slope of CV and APD restitution curves, respectively.

4.4 Discussion

This study used a detailed extrastimulus mapping technique to characterise conduction and rate-dependent changes in electrogram voltage and duration throughout the left atrium. The main findings of this study are as follows: 1) left atrial conduction delay is bimodally distributed amongst patients with PAF; 2) baseline electrogram duration and voltage show significant variation between patients and LA regions; 3) extrastimulus-dependent changes in electrogram duration and voltage are more uniform throughout the LA but often change with activation direction. In a subset of patients both can however be independent of pacing site, perhaps suggesting the presence of local discontinuous LA conduction at these sites; and 4) patients with inducible AF at the time of electrophysiological testing have significantly greater dispersion of LA activation times suggesting the presence of more advanced electrical remodelling in these patients. Overall, these clinical findings document for the first time significant electrophysiological variation between PAF cases undergoing first-time pulmonary vein isolation. Computational modelling illustrates that this variation could be explained in terms of

action potential remodelling resulting in 1) shortened refractoriness and 2) flattened conduction velocity restitution.

Comparison to Previous Studies of PEFA

PEFA has previously been used to identify areas of abnormal electrical propagation in the ventricle (269, 280) arising due to myocardial fibrosis and action potential remodelling (276). In turn, PEFA applied in the atrium showed that such remodelling leads to increased intra-atrial conduction delay between the right atrium and coronary sinus in patients with AF as compared to controls (278). Similarly, right atrial electrogram prolongation has been shown to be increased in patients with atrial flutter/fibrillation (279). The results presented here agree with and extend these findings to indicate that within a clinically similar group of paroxysmal AF patients, a spectrum of electrical responses can be identified which are explained by varying degrees of LA electrical remodelling. In both of the prior studies the authors identify the critical S1S2 interval at which electrogram duration starts to prolong ($S1S2_{delay}$). In both of the prior studies, $S1S2_{delay}$ was shown to be significantly longer in AF patients compared to controls (i.e. electrogram duration started to prolong at significantly longer coupling intervals). This finding is compared to the present data where shortening of the action potential duration (consistent with AF) can explain reductions in $S1S2_{delay}$ seen clinically and would suggest that $S1S2_{delay}$ could be expected to be shorter not longer in patients with significant LA electrical remodelling. The fact that $S1S2_{delay}$ was in fact longer in two prior studies may be explained by concomitant structural remodelling resulting in conduction delay, or by greater activation latency seen in some patients (286).

Atrial Conduction Delay and Block

Simulation studies have shown that atrial electrical remodelling in AF decreases the action potential duration (APD, for which ERP is a surrogate), resulting in shortening of the AF wavelength and increased duration of AF (265). In previous clinical studies of atrial refractoriness, ERP has been shown to increase with both age (287) and hypertension (284) in the absence of AF. In the presence of AF, ERP has also been shown to variably prolong as compared to controls (268), but as AF progresses from paroxysmal to persistent, measured ERP universally shortens (245). Therefore, prolongation of refractoriness appears to be an adaptive mechanism preventing the formation of AF in at-risk states (age, hypertension) but shortening of refractoriness is associated with more severe forms of AF.

In the present study, $S1S2_{block}$ for an individual LA site was defined as the shortest S1S2 coupling interval conducting from pacing catheter (positioned in HRA or CS) to that site in the LA. $S1S2_{block}$ represents conduction over a range of tissues, comprising tissue local to the pacing site, conducting tissue between pacing site and recording site and tissue local to the recording site. Pacing site refractoriness, conduction path refractoriness and conduction delay or functional block may all impact $S1S2_{block}$. The findings presented here therefore indicate that the recording site of the 'output' interval can have a significant impact on measured ERP ($S1S2_{block}$ varied significantly throughout the LA chamber despite use of a single pacing site). Furthermore, there was no correlation between $S1S2_{block}$ measured at a single output site under differing incident wave directions ($S1S2_{block}$ for HRA pacing showed no correlation with $S1S2_{block}$ for CS pacing). Hence ERP measured in clinical studies depends not only on pacing site APD but also on conduction to the recording site, which itself may be influenced by regions of functional block or conduction delay. This finding may explain some of the variation seen in previous clinical studies of ERP responses in AF.

In contrast, in the present study $S1S2_{delay}$ was uniform throughout the left atrium and independent of activation direction. Theoretical components of $S1S2_{delay}$ again include pacing site refractoriness and delay but also conduction delay along the LA conducting path. Prior studies have identified significant pacing site latency (286, 288) as a cause of intra-atrial conduction delay but in the present study pacing site latency (defined as conduction time within the CS) was insufficient to explain activation delay to the left atrium. Given its uniformity throughout the LA and close correlation under HRA and CS pacing conditions it is tempting to speculate that $S1S2_{delay}$ may provide a more reliable measure of the action potential response to changes in coupling interval. Indeed, by simulating activation proceeding along longitudinal and transverse fibre orientations this study shows that incorporating experimentally-measured reductions in I_{to}, I_{kur} and $I_{Ca,L}$ conductances can explain the bimodal distributions of $S1S2_{delay}$ seen in the patients studied here.

Conduction delay within the left atrium was also quantified by determining the spread of activation times seen within two 'halves' of the LA defined by the intraatrial conducting path length. Overall, sites within 60mm of earliest LA activation showed significantly less dispersion of activation than sites farther than 60mm from earliest LA activation, but with significant inter-individual differences. Cases showing less dispersion of activation

may be associated with flattened CV restitution as indicated by atrial electrical remodelling in the second simulation study. Conversely in the clinical study cases showing greater dispersion of activation were more likely to be AF-inducible at EP study. This later observation is entirely consistent with prior work indicating that the absence of conduction velocity restitution is protective against fibrillatory conduction / AF initiation (289) and suggests a potential role for these recording techniques in risk-stratification of PAF patients.

Baseline Electrogram Voltage and Duration (EV, ED)

A number of previous studies have identified reductions in sinus rhythm atrial voltages in patients with AF (266), patients with increasing severity of AF (245, 256) and patients with risk factors for AF, including age (287), hypertension (284) and congestive heart failure (290). However, other studies have failed to identify any difference between global and regional LA voltages between patients with and without AF (267), suggesting that voltage alone may be insufficient to define the electrical substrate for atrial fibrillation. Indeed in considering hypertension, LA voltage does not decrease (266), but other markers of atrial remodelling are increased (reduced RA conduction velocity and increased AF inducibility) (284) showing that LA voltage is a poor marker of electrophysiological substrate. The results presented here are in agreement with previous studies showing a spectrum of mean LA voltages between patients. Overall, mean chamber voltage was independent of activation direction. Previous studies found higher voltage in the posterior wall of the LA (291) or lower voltage in the posterior wall and septum (266). This study showed a minor regional variation (higher in the floor, posterior and roof regions) in voltage during HRA pacing which did not reach significance during CS pacing. Overall the variability of these findings suggests that baseline electrogram voltage is a poor marker of left atrial remodelling.

Electrogram duration has been used as a marker of electrogram complexity in numerous previous studies (292). Mounting evidence suggests that fractionation during atrial fibrillation is functional in nature rather than indicative of the presence of a specific electrical substrate (246, 267, 293). In contrast complex fractionated signals with prolonged duration (>50ms) during sinus rhythm have been associated with increasing age, lower voltage and slower conduction velocity and may therefore represent the development of fibrotic change in the atrium with age (294). Given these findings it is

notable that in the present study electrogram duration varied significantly throughout the LA with septal regions typically having longest electrogram duration.

Although histological and imaging studies have identified regional variation in fibrotic remodelling in the LA in AF (78, 295), these prior studies have shown the posterior wall to be predominantly affected by fibrosis, which is in contrast to the data presented here. Other histological studies have shown that fibrosis is a diffuse process affecting the atria uniformly (296). Furthermore, the present data also shows that there was limited correlation between local left atrial electrogram durations under different activation directions (HRA vs. CS pacing), which is in agreement with previous work demonstrating a lack of relationship between electrogram fractionation in sinus rhythm as compared to CS pacing (293). These findings suggest that, as for baseline voltage, prolonged baseline electrogram duration may be a passive phenomenon, for example related to wave collision, rather than indicative of a specific underlying electrical substrate.

Rate-dependent Change in Voltage and Duration (ΔEV, ΔED)

Maintenance of atrial fibrillation has previously been shown to depend on continually changing regions of slow conduction, functional conduction block and wave break (283, 297–300). Whilst functional in nature, this AF substrate is critically dependent on the presence of conduction delay and action potential abnormalities (301). In this context, variations in electrogram voltage and electrogram duration in response to activation rate may detect abnormal or discontinuous conduction properties crucial to the maintenance of AF. ΔEV showed a rightward skewed normal distribution throughout the whole population, indicating that overall, ΔEV decreased with pacing rate but with significant inter-site variation. ΔEV was largely constant between left atrial regions however overall ΔED was significantly greater in the septum, consistent with the baseline voltage and duration data presented above. ΔEV and ΔED both showed very small but significant correlations between HRA pacing and CS pacing. Notably, examining individual patients revealed that the population dichotomised into patients with significant directional variation in ΔED and ΔEV and patients without significant directional variation in ΔED and ΔEV. Put another way, ΔEV and ΔED were markedly dependent on activation direction in some, but not all, patients. The presence of such dependence of electrogram duration on activation direction may suggest the presence of discontinuous conduction in these patients (302) indicative of more advanced disease.

Regional Variation of the LA substrate

Previous studies have shown that electrical remodelling is non-uniform throughout the left atrium. The findings presented here are in agreement with this finding. Specifically, 1) conduction at $S1S2_{block}$ (but not $S1S2_{delay}$) varied throughout the atrium indicating that intra-atrial conduction is non-uniform; 2) baseline electrogram duration and baseline electrogram voltage varied throughout the atrium. Variation in AF electrical substrate has also previously been confirmed by ECGI. Using this technique, relative homogeneity is seen in the paroxysmal group compared to relative heterogeneity in the persistent group (72). The present study agrees with these findings but also extends them to indicate that relative heterogeneity may also be seen within paroxysmal AF patients. The impact of that heterogeneity on clinical outcomes remains to be determined.

Limitations

A number of limitations of the current study should be acknowledged. Data collection preceeded the adoption of force-sensing catheters and it is uncertain if variations in electrode-tissue contact may have impacted on the voltage data. Bipolar voltage may be significantly affected by incidence wave orientation and it is not clear to what extent, if any, standardisation for wave incidence angle would have altered the results. The stimulation protocol necessarily used a short (2-beat) drive train in order to permit mapping of the entire LA chamber. Some studies have identified cardiac memory in atrial myocytes (303, 304) and may have altered the response of the chamber towards the end of the pacing train compared to the start of the pacing train. The magnitude (if any) of this effect in the present study is unknown. Finally, no follow-up data is presented here. Future studies should correlate the electrophysiological properties described with AF duration, burden and response to AAD/ablation therapy.

4.5 Conclusions

In this chapter I have developed a methodology for substrate assessment in atrial fibrillation utilizing a simple pacing protocol to determine a number of electrophysiological parameters. Simulation work shows that variation in these parameters can be explained in terms of electrical remodelling in AF. Another approach to characterising the atrial substrate in atrial fibrillation is the use of CMR imaging. In the next chapter the relationship between atrial fibrosis measured with CMR and the electrical substrate defined with the techniques described here are examined. In doing so

Aim C4 (e*xamine the role of CMR in predicting the electrical substrate in patients with a spectrum of AF disease severity*) is addressed.

5 Imaging: The Relationship Between Atrial Structural Remodelling and AF Electrophysiological Substrate

5.1 Introduction

In the previous chapter a pacing protocol was developed to identify a number of dynamic (i.e. rate-dependent) properties of atrial tissue including conduction delay, change in electrogram amplitude with extrastimulus coupling interval and change in electrogram duration with extrastimulus coupling interval. Each of these parameters showed a spectrum of values between AF patients, and, owing to a similar spectrum of activation profiles in AF cell models, suggest a possible relationship between the measured electrical properties and disease severity. In this chapter the relationship between atrial structural remodelling (both fibrotic and geometric) determined by CMR imaging and these electrical parameters is examined.

Evidence from both animal models and human studies implicates atrial fibrosis in the pathogenesis of atrial fibrillation. In canine models of AF triggered by rapid atrial pacing (305), congestive heart failure (169, 175) and mitral regurgitation (306), atrial fibrosis is associated with significantly increased AF duration. Similarly, tissue samples from AF patients undergoing cardiothoracic surgery or post-mortem examination indicate that atrial fibrosis is associated with both the presence (172, 307) and severity (296, 308) of AF. Such changes in the extracellular matrix may be mediated via cardiomyocyte control of fibroblast function (174), and show a varied distribution between regions of the left atrium (295).

Despite the consistency of these findings, the relationship between atrial fibrosis and atrial electrophysiological properties is less clear. For example, effective refractory period (ERP) has been shown to both increase (306) and decrease (169, 305) following rapid atrial pacing in canine models. Similar disagreement exists over the effect of atrial fibrosis on conduction velocity. In simulation studies, atrial fibrosis is associated with decreased conduction velocity, consistent with gap junction decoupling by bands of fibrosis (265). Whilst this finding is supported by some animal studies (305), others have

failed to demonstrate a relationship between atrial fibrosis and conduction slowing (169, 306). In addition to atrial fibrosis, atrial structural remodelling manifest as left atrial enlargement (geometric remodelling) has long been known to be associated with the occurrence and persistence of atrial fibrillation (309–312). These findings have been confirmed with cross-sectional imaging studies showing LA enlargement in unselected patients with atrial fibrillation (313) and in patients with AF recurrence after pulmonary vein isolation procedures (314). Furthermore, geometric remodelling may be a reversible process following pulmonary vein isolation with restoration of sinus rhythm resulting in a significant and progressive decline in LA diastolic and systolic volumes (314) as well as reversal of atrial dilatation (268).

Against this background, late gadolinium enhancement CMR imaging (DE-MRI) has emerged as a candidate clinical tool to stage AF severity and guide therapeutic intervention. In clinical studies increasing fibrosis burden on DE-MRI (classified as mild (<15%), moderate (15-35%) and severe (>35%)) has been associated with increased post-ablation AF recurrence rates (78, 90, 91). Similarly DE-MRI LA wall signal intensity is correlated with both time in continuous AF, and the presence of persistent or longstanding AF (315, 316). Whilst LA geometry has traditionally been assessed with 2D dimensions or 3D volumes, more recently the shape of the LA has been examined. 'Left Atrial Sphericity' (LASP) is a metric defining how closely the LA confirms to a best-fit sphere, and increasing LASP (i.e. more spherical LA geometry) has been shown to be an independent predictor of AF recurrence after ablation (317). Both LA volume and LASP decrease after pulmonary vein isolation (318).

Providing a mechanistic explanation for these clinical findings has proved more challenging. Although post-ablation LA fibrosis, as defined by DE-MRI, is associated with reduced bipolar voltage on electroanatomic mapping (319–321) greater uncertainty exists around the ability of pre-ablation DE-MRI to predict pre-ablation LA voltage. Considering the LA chamber as a whole, the extent of fibrosis defined by DE-MRI has been weakly associated with the extent of fibrosis defined by low voltage on EAM (R^2=0.61) (78), whilst in a mixed population (pre- and post-ablation), normalized LA wall signal intensity shows a log-linear relationship with bipolar voltage in some, but not all, patients (315). Furthermore, examining the relationship between 'dense' and 'patchy' left atrial DE-MRI indicates that areas of low bipolar voltage may be seen in all fibrosis densities as well as in regions of healthy tissue (247). Finally, other studies have failed to

demonstrate any relationship between LA voltage and DE-MRI (322) casting doubt on the direct relationship between DE-MRI and LA voltage in the pre-ablation setting.

Given the conflicting data supporting the interplay between atrial electrical and structural remodelling, this study examines the relationship between the dynamic atrial electrophysiological properties defined in the previous chapter, atrial fibrosis (as determined by DE-MRI imaging) and atrial geometric remodelling. Three CMR output metrics are studied: 1) The image intensity ratio (IIR) is the mean atrial wall signal intensity divided by mean blood pool signal intensity; 2) LGE area is the percentage of LA wall above an IIR of 0.97; 3) LA sphericity (LASP) is an index describing the degree to which the left atrium conforms to a spherical shape.

5.2 Methods

12 consecutive patients undergoing first time ablation for paroxysmal atrial fibrillation (n=8) and persistent atrial fibrillation (n=4) were studied. Patients were excluded from the study if there was a history of ischemic heart disease, cardiac surgery or structural heart disease. Anti-arrhythmic drugs, including calcium channel blockers, were stopped at least 5 half-lives before ablation (6 months in the case of Amiodarone).

Cardiac Magnetic Resonance

Late-gadolinium enhancement CMR was performed 25±21 days prior to EP study using a 1.5T MR system (Achieva, Phillips Medical Systems, Best, The Netherlands) and a 32-element cardiac phased array coil. First, survey and sensitivity encoding reference scans were obtained, followed by a 2D multi-cardiac phase cine scan acquired in a four-chamber orientation. From this scan, the trigger delay was determined for all subsequent scans in order to minimize artefacts from atrial wall motion. Twenty minutes after administration of 0.2ml/kg Gadovist (Bayer HealthCare Pharmaceuticals, Berlin, Germany), axial 3D LGE imaging was performed [respiratory-navigated, ECG-triggered inversion recovery turbo field echo acquisition; spatial resolution = 1.3x1.3x4mm^3 (reconstructed to 0.6x0.6x2 mm^3); TE/TR = 3.0/6.2ms; flip angle = 25°]. The inversion time was determined using a preceding Look-Locker sequence to achieve optimal suppression of the left ventricular myocardium.

LGE Intensity Quantification

For regional LGE intensity calculations, the left atrial blood pool was manually segmented from the LGE sequences using ITK-Snap 3.0 (323) and a 3-dimensional surface shell representing the endocardium was created. For each vertex, the mean of the signal intensity values along a normal projection 3mm internal and external to the shell was determined (taken to represent the left atrial wall), before the shell was 'flattened' onto a 2-dimensional disc bounded by the mitral annulus (324). A mean projection normal to the shell was taken in order to take account of LGE signal intensity throughout the left atrial wall as previously described (315). The image intensity ratio (IIR) at each vertex on the flattened LA map was calculated as the mean regional signal intensity divided by the mean signal intensity of the left atrial blood pool.

LGE Area Quantification

For each LA region, the percentage LA wall with an IIR (mean wall divided by mean blood pool signal intensity) above 0.97 was determined. An IIR of >0.97 has previously been identified as an appropriate threshold to identify fibrotic LA tissue (315).

LA Sphericity Quantification

The LA sphericity (LASP) was obtained as previously described (317). Briefly, a 3D segmentation of the LA (excluding the left atrial appendage and pulmonary veins) was created manually using ITK-Snap 3.0 (323). The manual segmentation was smoothed using a well-known mesh smoothing technique known as Laplacian smoothing. In this technique, each mesh point was relocated to a new position based on the mean of its neighbours' positions. The centre and average radius (AR) of a sphere best fitting the smoothed LA shell were calculated as the centre of mass of all the surface points (centre) and the mean of the distances between all points and that centre (radius). The LASP was then given by Equation 5-1:

$$LASP = \left(1 - \frac{AR\ standard\ deviation}{AR}\right) \times 100 \qquad \textbf{Equation 5-1}$$

Hence, an LASP of 100 indicates a perfectly spherical LA, whilst decreasing LASP indicates progressively non-spherical LA geometry.

Electrophysiological Parameters

All parameters (conduction curve block and delay ($S1S2_{block}$ and $S1S2_{delay}$), baseline electrogram voltage (EV), baseline electrogram duration (ED), change in voltage with coupling interval (ΔEV) and maximal increase in electrogram duration with coupling interval (ΔED)) were measured as described in Chapter 4. Mean electrophysiological parameters were calculated for each region of each chamber. For comparision between electrophysiological parameters and LA sphericity, mean parameters were calculated for the entire chamber.

Statistical Tests

Data analysis was performed using GraphPad Prism version 6.0c (GraphPad Software, San Diego, California, USA, www.graphpad.com). Data are represented as mean±SD throughout. Categorical variables were compared with the Fisher's exact test. Continuous variables were compared using a two-tailed Student's T-test or the Mann-Whitney U test for data not normally distributed (normality determined by the D'Agostino & Pearson test). In all cases, a significance level of $P<0.05$ was considered statistically significant.

5.3 Results

Patient Characteristics

Patient characteristics are shown in Table 5-1. Paroxysmal and persistent AF patients were identical clinically with the only significant difference being serum creatinine level.

Table 5-1. Characteristics of Study Patients

	Paroxysmal AF (n=8)	Persistent AF (n=4)	P
Age	62 ± 11	62 ± 12	0.9598
Male Sex	2 (25%)	4 (100%)	0.0606
Duration of AF (years)	3.4 ± 3.6	3.0 ± 0.8	0.8439
LA diameter (cm)	3.8 ± 0.6	4.2 ± 0.8	0.3732
LVEF (%)	62 ± 4	58 ± 6	0.1495
Hypertension	3 (37.5%)	2 (50%)	1.0000
Diabetes mellitus	0 (0%)	0 (0%)	1.0000
CHA_2DS_2Vasc	0.5 ± 0.8	0.5 ± 0.6	0.9999
Creatinine (µmol/l)	76 ± 16	105 ± 6	0.006 *
eGFR (ml/min)	77 ± 21	62 ± 2	0.1980
Hb (g/dl)	134 ± 14	130 ± 12	0.3250
Prior AADs (n)	2.1 ± 0.8	2.5 ± 1.0	0.5059

AF, Atrial Fibrillation; LA, Left Atrium; AAD, antiarrhythmic drug; LVEF, left ventricular ejection fraction; Hb, haemoglobin

CMR Quantification

Manual segmentations of the LA are shown in Figure 5-1 and processing steps in a case with anterior LGE in Figure 5-2A. Regional LGE was identifiable in all cases studied. To minimise interpretation of high signal from the respiratory navigator and/or aortic wall as regional enhancement, two oval regions of exclusion were included on the unfold maps prior to quantitative analysis (Figure 5-2B). One case (case 2) with significant respiratory navigator artefact was excluded from further analysis. Following this processing, regional differences in LA enhancement were identifiable with significantly lower signal intensity ratios seen in the floor and posterior regions as compared to the anterior, roof and septal regions of the LA (Figure 5-3). The distributions of signal intensity, LGE area and sphericity were assessed within the population subgroups (paroxysmal AF, n=8; persistent AF, n=4). As shown in Figure 5-4 there was no difference in any of the CMR output metrics between the paroxysmal and persistent AF patients.

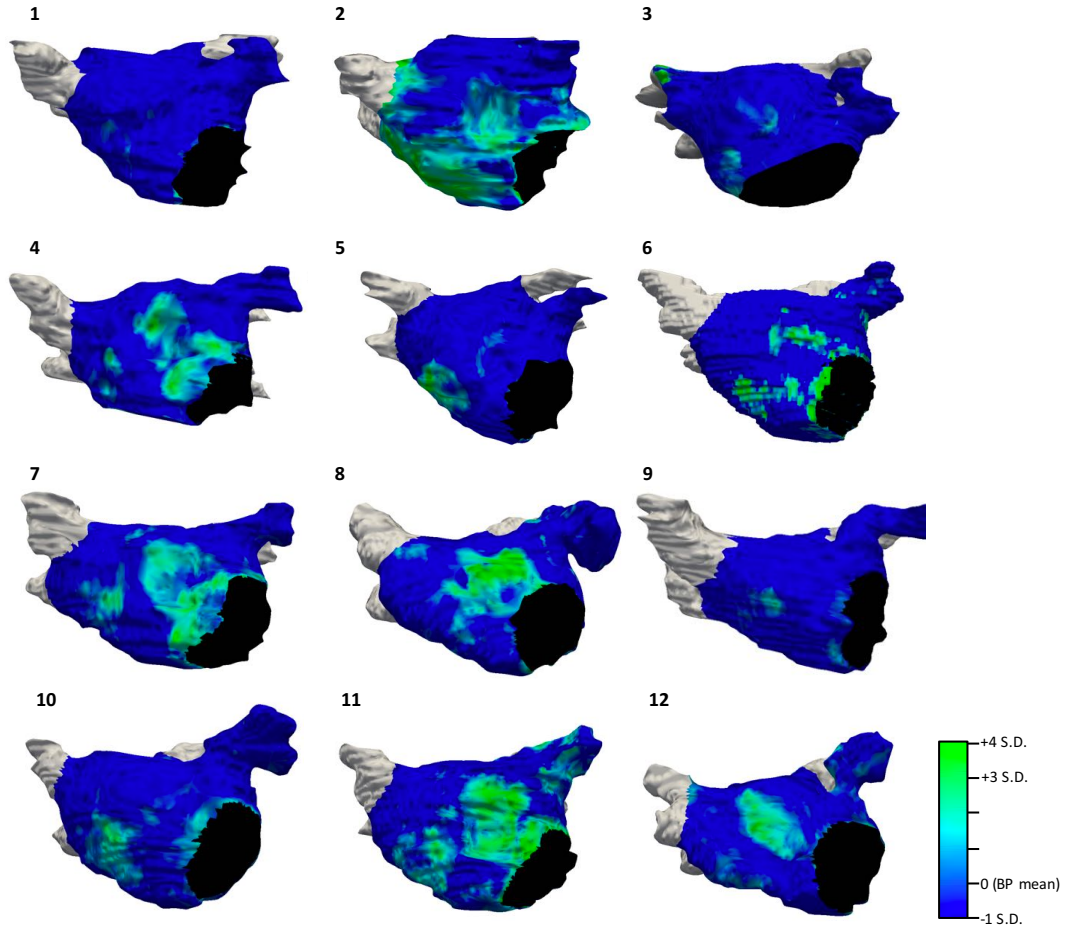

Figure 5-1. LA CMR Shells with Variation in Shape and Late Gadolinium Enhancement

Shells created form the LA blood pool and coloured according to late gadolinium enhancement are shown for all cases studied. Case 2 was excluded from further analysis owing to significant respiratory navigator artefact affecting large portions of the chamber.

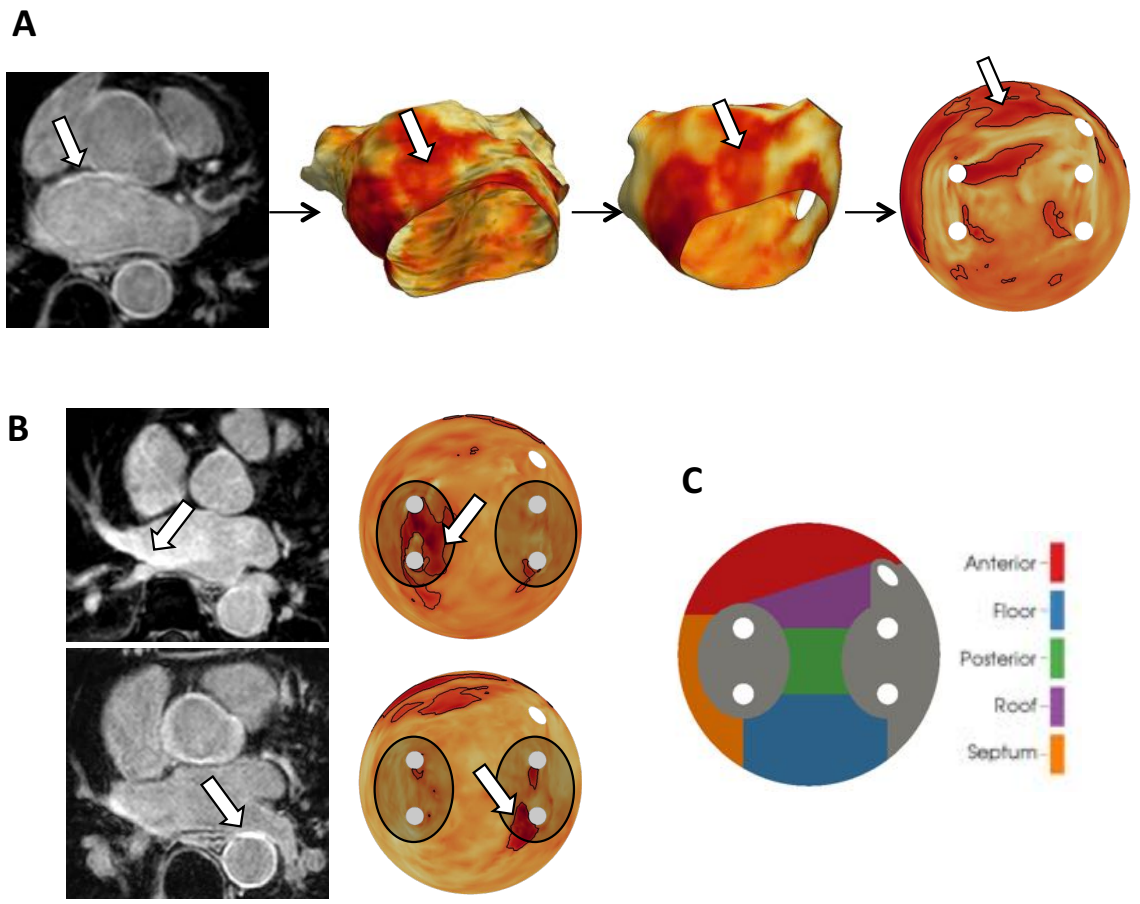

Figure 5-2. LGE CMR Processing Steps

A – LA LGE CMR with anterior enhancement (white arrows) is first manually segmented before being registered and projected onto a model LA, in turn allowing creation of the unfold map bounded by the mitral annulus. The colour scale is normalised to the LA signal intensities (brightest LGE = red; darkest LGE = yellow). **B** – Respiratory navigator artefact at the right pulmonary venous inflow and fibrous aorta artefact adjacent to the lower left pulmonary vein are both minimised by applying two oval regions of exclusion around the pulmonary venous ostia on the atrial unfold maps (grey). **C** – LA region definitions.

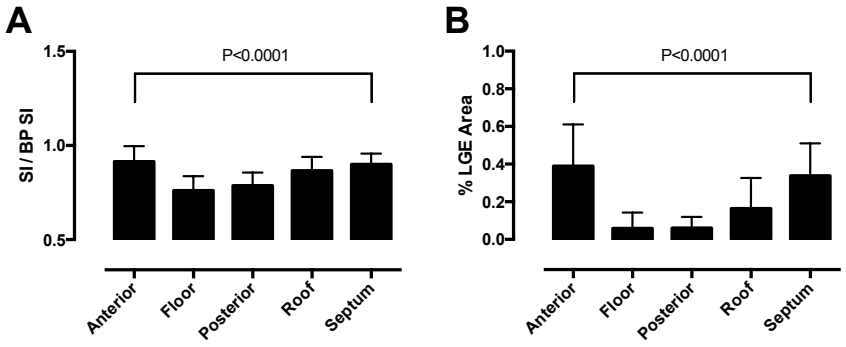

Figure 5-3. Regional Variation in LGE Signal Intensity and LGE Area

A – Regional signal intensities are shown for 'mean' intensity projections, normalised to the blood pool signal intensity. **B** – Regional LGE Areas are shown for 'mean' intensity projections, representing the percentage of LA wall above an IIR of 0.97.

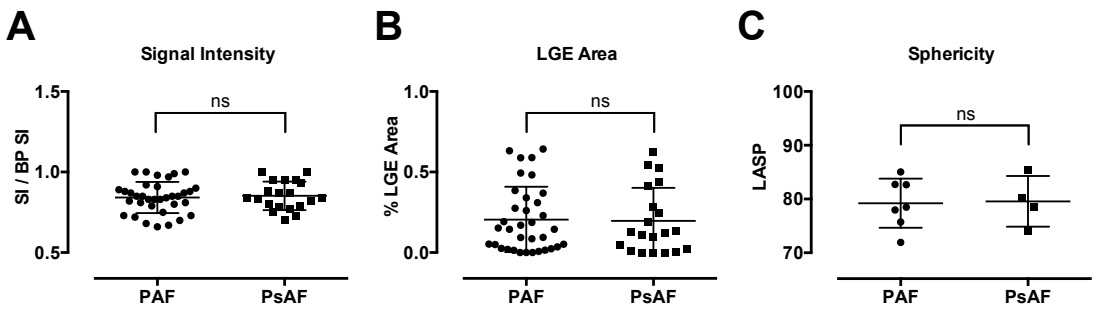

Figure 5-4. CMR Quantification for Paroxysmal and Persistent AF Subgroups

A – Normalised signal intensities for each LA region (anterior, floor, posterior, roof, septum) for paroxysmal (PAF, n=8) and persistent (PsAF, n=4) AF cases. **B** – LGE Area (% LA wall with image intensity ratio > 0.97) for each LA region for PAF and PsAF cases. **C** – Sphericity indices for each PAF and PsAF case.

Spectrum of Electrogram Morphologies

A range of electrogram morphologies was seen ranging from early conduction delay with minimal decrement through much later conduction delay and significant stimulation site to recording site decrement. However, qualitatively there was no relationship between the degree of left atrial fibrosis (as defined by CMR LGE) and the type of electrical response seen globally in the chamber. As shown in Figure 5-5, a spectrum of conduction curve morphologies was identifiable in patients with similar CMR findings.

CMR LGE and Electrical Remodelling

Overall on a point-by-point basis there was no correlation between LGE signal intensity and conduction delay ($S1S2_{block}$ / $S1S2_{delay}$), electrogram voltage (EV / ΔEV) or electrogram duration (ED / ΔED) (Table 5-2). Similarly, again on a point-by-point basis there was no correlation between LGE Area and conduction delay ($S1S2_{block}$ / $S1S2_{delay}$), electrogram voltage (EV / ΔEV) or electrogram duration (ED / ΔED). However, baseline electrogram voltage (EV) was significantly lower in regions of high LGE signal intensity (IIR>0.97) as compared to regions of low LGE signal intensity (IIR<0.97) (Figure 5-6A). This finding indicates that there is a weak but significant correlation between atrial fibrosis (defined by a previously validated LGE signal intensity threshold) and atrial bipolar voltage, although it is important to acknowledge that a range of bipolar voltages is seen at all LGE signal intensities. Although there was a trend towards increasing ΔED at regions of high signal intensity, this observation did not reach significance (Figure 5-6D). There was no difference between the other electrophysiological parameters (ED, ΔEV, S1S2delay, $S1S2_{block}$) at regions of low vs. high LGE signal intensity.

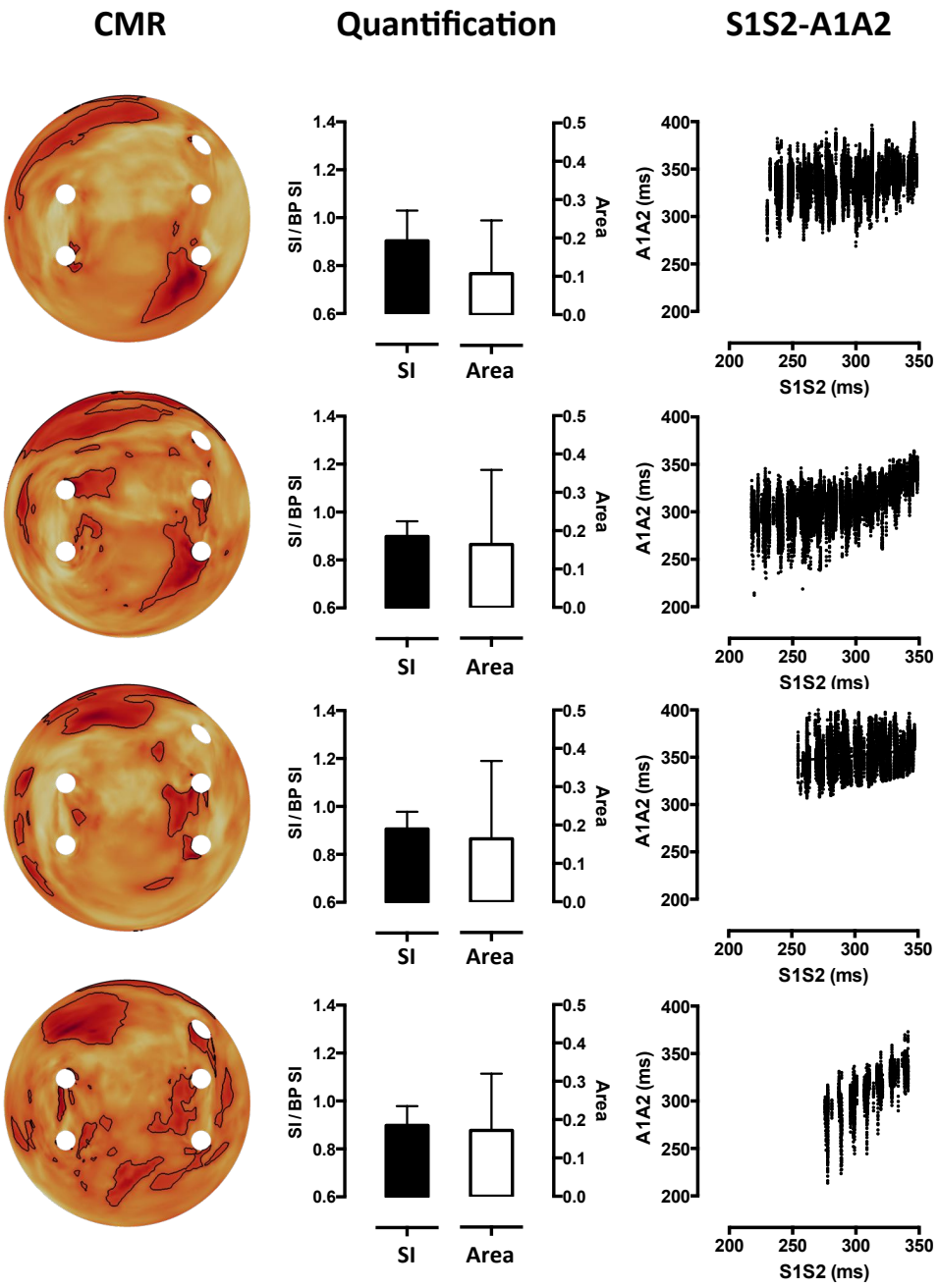

Figure 5-5. Varying Electrical Responses Despite Similar LA LGE

Four example cases are shown demonstrating a range of electrical responses (right column) to pacing despite similar atrial LGE seen qualitatively (left column) and quantified as IIR or area of enhancement (middle column).

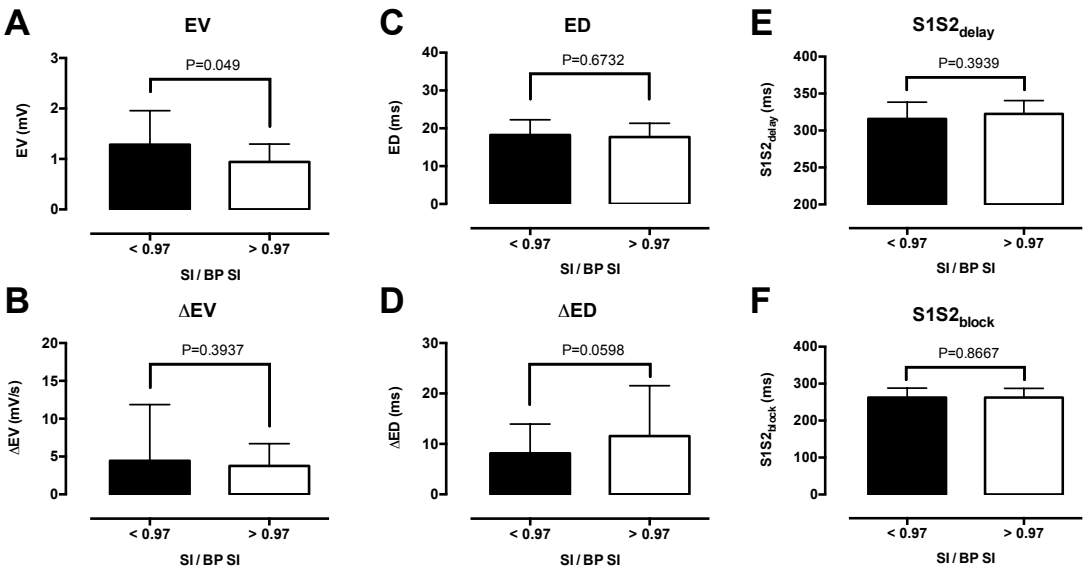

Figure 5-6. Effect of LGE Signal Intensity on Electrogram Voltage, Duration and Conduction

Variation in electrophysiological parameters between regions of low LGE signal intensity (IIR<0.97) and high LGE signal intensity (IIR>0.97) for EV (**A**), ΔEV (**B**), ED (**C**), ΔED (**D**), S1S2delay (**E**) and S1S2block (**F**).

Table 5-2. Correlation Between LGE Signal Intensity and Electrical Remodelling

	HRA Pacing		CS Pacing	
	R^2	P	R^2	P
EV	0.0027	ns	0.0009	ns
ED	0.0209	ns	0.0038	ns
ΔEV	0.0059	ns	0.0309	ns
ΔED	0.0016	ns	0.0256	ns
$S1S2_{delay}$	0.0244	ns	0.0019	ns
$S1S2_{block}$	0.0024	ns	$2.5x10^{-7}$	ns

EV, Electrogram voltage; ED, Electrogram duration; ΔED, Increase in electrogram duration with coupling interval; ΔEV, Change in electrogram voltage with coupling interval; S1S2delay / S1S2block, Extrastimulus coupling intervals at which local decrement or loss of conduction occur.

Table 5-3. Correlation Between LGE Area and Electrical Remodelling

	HRA Pacing		CS Pacing	
	R^2	P	R^2	P
EV	$4.8 x10^{-6}$	ns	0.0009	ns
ED	0.0404	ns	$1.6 x10^{-5}$	ns
ΔEV	0.0100	ns	0.0097	ns
ΔED	0.0037	ns	0.0224	ns
$S1S2_{delay}$	0.0044	ns	0.0176	ns
$S1S2_{block}$	$3.7 x10^{-5}$	ns	0.0034	ns

EV, Electrogram voltage; ED, Electrogram duration; ΔED, Increase in electrogram duration with coupling interval; ΔEV, Change in electrogram voltage with coupling interval; S1S2delay / S1S2block, Extrastimulus coupling intervals at which local decrement or loss of conduction occur.

LA Sphericity and Electrical Remodelling

Structural remodelling (quantified by LA sphericity) showed no correlation with conduction delay / block ($S1S2_{delay}$, $S1S2_{block}$), electrogram voltage (EV, ΔEV) or electrogram duration (ED, ΔED), as shown in Figure 5-7.

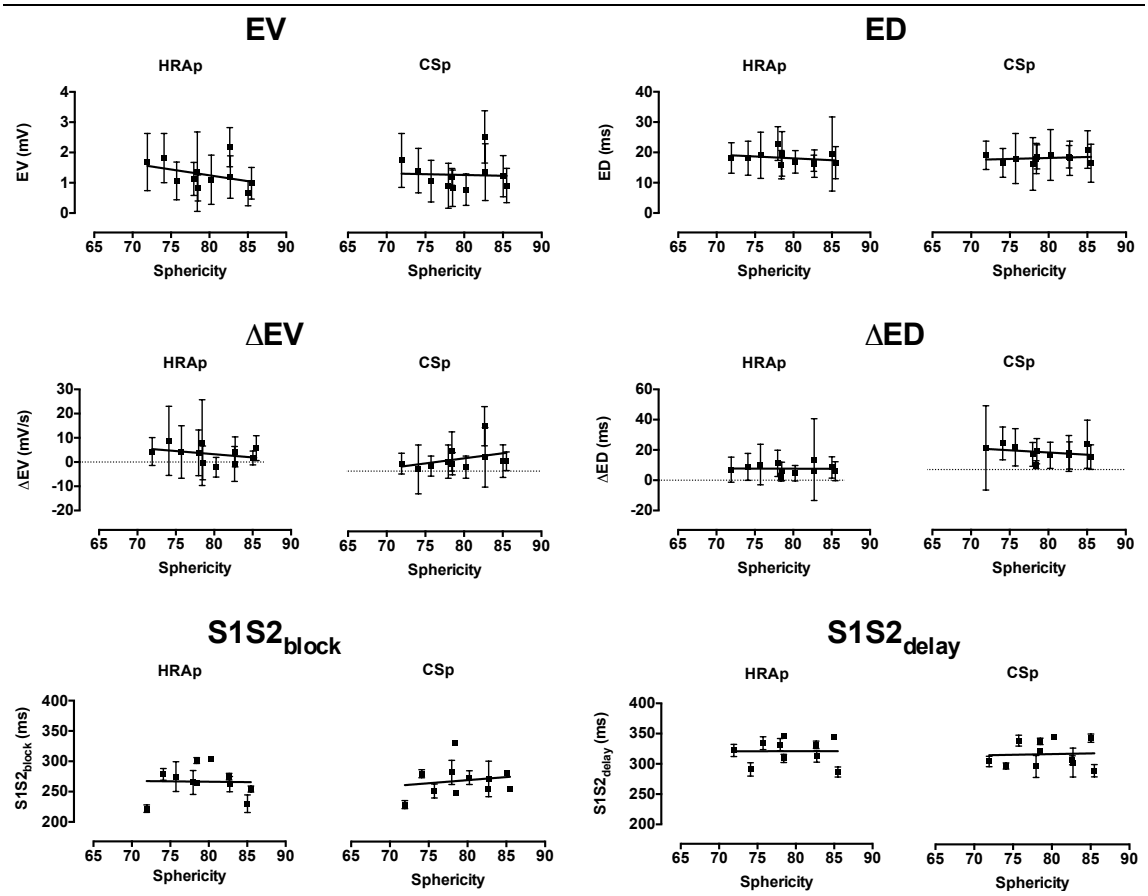

Figure 5-7. Relationship between LA sphericity and study parameters

Relationship between electrogram voltage (EV), electrogram duration (ED), change in electrogram voltage and duration with coupling interval (ΔEV, ΔED) and conduction delay ($S1S2_{block}$ and $S1S2_{delay}$) and LA sphericity is shown for each case. Error bars represent standard deviations for the means of each region within each case.

5.4 Discussion

This study examined the relationship between atrial shape and fibrosis (assessed by CMR imaging) and AF electrical substrate (assessed by extra-stimulus mapping). In order to assess this relationship across a spectrum of AF disease severities, a mixed population was studied including paroxysmal and persistent patients with AF duration ranging from 1 to 11 years. The main findings of the study are as follows. 1) In patients with AF a spectrum of LA late gadolinium enhancement is seen with signal intensity varying between patients. 2) Within the left atrium, distribution of LGE enhancement is non-

uniform with anteroseptal regions associated with highest signal intensity and LGE area. 3) Although electrogram voltage was significantly lower at sites of high LGE signal intensity, neither LGE signal intensity nor LA sphericity were predictive of electrogram duration or conduction delay. Taken together, these findings suggest that although DE-MRI varies between patients with AF, this variation is not predictive of LA tissue electrical responses. As such, it remains possible that an electrical substrate for atrial fibrillation may be present regardless of the quantification of imaging findings.

Atrial Remodelling and Clinical Outcomes

A number of studies have investigated the utility of left atrial CMR imaging to predict clinical outcomes in atrial fibrillation. Pre-ablation left atrial scarring/fibrosis (defined by DE-MRI) has been associated with increased duration of AF (316), AF recurrence after ablation (78, 90, 320) and reduced success of AF ablation (91). However, not all studies report a positive association between DE-MRI and clinical outcomes (322), and DE-MRI has been shown to be independent of traditional risk factors for AF in some studies (91). The same observations are made for geometrical LA structural remodelling. LA size determined by MRI is predictive of clinical outcome to ablation (325), and greater pre-ablation scar is associated with LA dilatation in some (320), but not all (322) studies.

In this context, it is notable that the findings presented here indicate a disconnect between electrical and structural remodelling in AF (as defined by DE-MRI), with a spectrum of electrical responses seen in clinically similar patients as defined by DE-MRI. This is in agreement with the above studies indicating variable success in using DE-MRI to predict clinical outcomes and indicates that varying degrees of electrical and structural remodelling may be responsible for the initiation and/or maintenance of AF in these patients. Indeed the observation of variable electrical remodelling demonstrated with extrastimulus mapping in these patients (independent of LA structural remodelling) may go some way to explain the observation that even in the presence of DE-MRI structural remodelling AF ablation can be successful, whereas in the absence of DE-MRI structural remodelling AF ablation may still fail (81.82% success has been reported in patients with wall fibrosis ≤5%) (91).

Atrial Fibrosis, Dilation and Electrical Remodelling

In order to identify a mechanistic explanation for these variable clinical findings, a number of previous studies have investigated the relationship between CMR-defined LA

structural remodelling and invasively determined LA electrical parameters. These studies have primarily focussed on voltage mapping as a surrogate for left atrial fibrosis although the relationship with electrogram morphological changes has also been assessed. In doing so a number of studies have identified strong relationships between DE-MRI and LA bipolar voltage (247, 315, 326), but as for clinical outcomes this finding is not repeated by all studies (322), and the data appear to indicate significant overlap between DE-MRI between voltage groups (320). The present study is consistent with this data indicating that bipolar voltage is indeed lower at regions of high LGE signal intensity. The strength of this relationship is however low and there are significant overlaps between the groups. Consistent with the lack of a relationship between DE-MRI and electrogram duration presented here is the clinical observation that electrogram fractionation may actually be reduced at sites of atrial fibrosis defined by DE-MRI (247).

Several observations suggest that atrial dilatation is implicated in the pathogenesis of AF. Using CT studies, LA volume has been shown to be larger in patients with recurrence after AF ablation than in patients without recurrence (327). Similarly, reversal of left atrial remodelling (characterised by decreased LA diastolic and systolic volumes as well as increased LA ejection fraction) has been demonstrated after successful, but not unsuccessful, AF ablation (314). Furthermore, LA volume assessed by CMR (diastolic cut-off >112ml) is predictive of freedom from AF at 1 year post ablation with a sensitivity of 80% and specificity of 70% (325). The results presented here failed to show a relationship between electrical remodelling and atrial dilatation (defined by the sphericity index). The observation that there was no relationship between atrial conduction indices and atrial dilatation in this clinical study is consistent with previous studies in a goat model of chronic atrial dilatation (328). Importantly however, AF stability in this model was related to intra-atrial conduction delay rather than reduced refractoriness or fibrosis (329).

Regional LGE

The population studied here showed significant regional differences in DE-MRI throughout the LA chamber. Most notably, the normalized signal intensity and fibrosis burdens were greater in the anterior, roof and septal regions as compared to the floor and posterior regions (both $P<0.0001$). This finding is consistent with previous reports indicating that LA fibrosis is non-uniform throughout the LA chamber, as determined both by DE-MRI imaging (78) and histological assessment (295). It is however in

disagreement with a detailed histological assessment of the LA roof, posterior and floor regions showing no difference in the amount of fibrosis (296).

Limitations

A number of limitations must be acknowledged in the present study. Firstly, the sample size is small and the population of patients is heterogeneous, with a spectrum of AF disease severities studied. This approach was taken in order to maximise the opportunity for identifying a spectrum of CMR-electrical correlates although whether the same findings would be present with a more homogeneous population is not known. Future work would also benefit from an animal model in which to test the underlying mechanisms for the observations made (e.g. imaging and electrical correlations with histologically-defined atrial fibrosis).

It must also be acknowledged that left atrial LGE imaging is technically challenging and fundamentally limited by the current resolution of the scanning techniques available. The voxel size employed in the current study was 1.3x1.3x4mm^3 (reconstructed to 0.6x0.6x2 mm^3) which may be approximately the LA wall thickness in certain regions. Although there are limited histological correlates of atrial LGE (330), LGE imaging of the atrium is likely to be limited in sensitivity and this observation may at least partially explain some of the negative findings presented above.

A variety of techniques have been employed to quantify pre-ablation LA fibrosis using LGE CMR. By necessity, all techniques require a frame of reference and previous studies have either used the atrial blood pool (315), the LV myocardium (326) or the fibrotic mitral valve (326) as signal intensity references. In this study, the atrial blood pool for a number of reasons. Firstly, the blood pool is a large region not open to partial volume effects. Secondly, in comparison to the atrial wall, the blood pool is large enough so as to be more easily defined. Whether a different analysis would impact on the results is not certain, but given the qualitative disparity between the unprocessed scans and spectrum of electrical responses it seems unlikely.

Calculation of the IIR requires manual segmentation of the left atrial wall, before dividing the mean signal intensity for each LA region by the mean signal intensity of the blood pool (315). Delineation of the LA wall from blood pool is an error-prone process, especially where increased LA wall signal intensity (i.e. late gadolinium enhancement) renders the wall signal intensity equivalent to the blood pool signal intensity. To eliminate

potential bias introduced during manual segmentation, the segmentations used here were instead performed on the LA blood pool. It is possible however that different segmentation techniques may account for some of the variation between this work and published literature described above.

5.5 Conclusions

In summary, the data presented here provide evidence that electrical remodelling in atrial fibrillation may occur independently of left atrial fibrosis, as determined by late gadolinium enhancement CMR and show that inter-patient variability of the AF substrate can be detected in the absence of significant qualitative or quantitative differences in late gadolinium CMR findings. The contribution of the described electrical remodelling to predicting clinical outcomes compared to the published DE-MRI studies remains to be determined.

Having now examined three independent modalities (surface ECG, intra-cardiac mapping and CMR imaging) in characterising arrhythmia substrates, the next chapter integrates multiple modalities (intra-cardiac mapping, imaging and histology) together for arrhythmia substrate characterisation. Incomplete linear ablation is a major determinant of the occurrence of post-ablation atrial tachycardias, so these techniques are now used to consider factors important in the success of linear ablation. In doing so Aim C5 (*to assess the impact of contact force in the creation of effective linear ablation lesions*) is addressed.

6 Multi-modality Substrate Characterisation: Impact of Catheter-Myocardium Contact Force on Atrial Radiofrequency Ablation Lesion Formation

6.1 Introduction

Catheter-tissue contact force is a key determinant of radiofrequency (RF) ablation lesion formation in both *ex vivo* (331–334) and *in vivo* non-myocardial (335–337) ablation models. Similarly, increasing CF leads to increased lesion depth and diameter *in vivo* in the canine ventricle (338). Whilst high contact force has been associated with increased ventricular lesion size, whether the same is true of the thin-walled left atrium is not known.

Procedural safety profiles are also affected by CF. Risk of tamponade is directly related to applied contact force with a minimum force of 38g being sufficient for perforation in *ex vivo* human atrial tissue (339). In a study of porcine atrial ablation, application of radiofrequency energy reduced the perforating force by 23% (340) and perforating forces were significantly lower through recently ablated than non-ablated atrial tissue (341). Furthermore, contact force itself is an independent predictor of steam pops and thrombus formation (336). Ideal CF targets for atrial ablation must therefore balance both lesion effectiveness and safety of application.

Notably the majority of ablation models have utilized power-controlled generator settings, which deliver fixed power output regardless of catheter tip temperature. Meanwhile, temperature-controlled ablation has been shown to reduce the incidence of impedance rise, steam pops and charring/thrombus formation (342), and has become the standard approach to left atrial ablation in some centres. This study therefore explored the relationship between catheter myocardium contact force and lesion formation in an *in vivo* chronic porcine atrial ablation model. The model was designed to replicate human atrial ablation and utilized standard clinical-grade ablation equipment throughout. By controlling for all ablation-related parameters, including catheter stability, the effect of contact force on ablation lesion creation is determined in isolation.

6.2 Methods

Animal Model and Protocol

Animal studies complied fully with Danish law on animal experiments. Eight male Göttingen mini-pigs (41.2±7.2kg) were pre-sedated with intramuscular azaperone (4mg/kg) and midazolam (0.5mg/kg). General anesthesia was induced with intravenous ketamine (5mg/kg) and midazolam (0.5mg/kg), and the animals were intubated and mechanically ventilated. Anesthesia was maintained with a continuous intravenous infusion of propofol (3mg/kg/h) and fentanyl (15μg/kg/h).

Two of the eight mini-pigs underwent pre-ablation cardiovascular magnetic resonance (CMR) imaging and all eight mini-pigs subsequently underwent electroanatomic mapping (EAM) and ablation according to the protocols described below. Immediately post-ablation all animals were transferred for CMR imaging before being recovered from anesthesia and returned to the farm for 2 months. Mini-pigs were used to ensure minimal growth during the recovery period. After 2 months, animals were anesthetized according to the same protocol and underwent chronic CMR imaging followed by EAM. Subsequently a midline sternotomy was performed in all animals, the hearts were removed en bloc and perfusion fixed ready for subsequent analysis.

Electroanatomic Maps and Ablation

Two 8F sheaths were placed percutaneously into the right femoral vein, followed by an intravenous injection of 100IU/kg heparin. A 6F decapolar reference catheter was positioned in the coronary sinus (CS). An 8F ablation catheter (ThermoCool SmartTouch, D curve, Biosense Webster, Diamond Bar, CA, USA) was advanced to the right atrium (RA). A 3D geometry of the RA was created using Carto3-MEM (Biosense Webster, Diamond Bar, CA, USA) and a high-density pre-ablation peak-to-peak bipolar voltage map was constructed during proximal CS pacing.

Linear RF ablation (42°C, 30W, 17ml/min irrigation) was performed from the superior vena cava (SVC) to the inferior vena cava (IVC) along the posterior wall of the RA. The RA intercaval region was selected since this region can be accessed with minimal catheter manipulation, is uniform in wall thickness and easily accessible for subsequent dissection (343). Prior to ablation, smooth catheter movement along the proposed line was confirmed. RF energy was delivered in temperature-controlled mode between the distal

electrode of the ablation catheter (3.5mm) and a reference patch affixed to the skin overlying the thigh muscle. A 5.3±1.5mm gap was left in the ablation line mid-chamber, and alternate ends of the ablation line were delivered at either 'high' (HF, >20g) or 'low' (LF, <10g) contact force. Ablation was performed as a continuous drag with the catheter moved every 30s. Following completion of the inter-caval linear lesion, a second high-density voltage map was immediately acquired during proximal CS pacing. Delivery of effective ablation was confirmed by the absence of pace capture (3mA output, 2ms pulse-width) along the ablation line and the presence of a new activation detour during CS pacing. Following recovery (2-months) post-ablation chronic voltage maps were created following the same protocol.

Cardiac Magnetic Resonance

Cardiac magnetic resonance was performed on a 1.5T MR system (Achieva, Phillips Medical Systems, Best, The Netherlands) and a five-element cardiac phased array coil. First, survey and sensitivity encoding reference scans were obtained, followed by a 2D multi-cardiac phase cine scan acquired in a four-chamber orientation. From this scan, the trigger delay was determined for all subsequent scans in order to minimize artefacts from atrial wall motion.

Sagittal T2W images were acquired [multi-slice turbo spin echo with a double inversion recovery pre-pulse and spectral pre-saturation with inversion recovery fat suppression; effective echo time (TE) = 45ms; repetition time (TR) = twice the cardiac cycle length; spatial resolution = 1.5 x 1.5mm^2 (reconstructed to 1.0x1.0mm^2); slice thickness = 3mm] using the respiratory navigator to minimize motion artefacts and to ensure acquisition at end-expiration for all slices.

Thirty minutes after administration of 0.2ml/kg Gadovist (Bayer HealthCare Pharmaceuticals, Berlin, Germany), axial 3D LGE imaging was performed [respiratory-navigated, ECG-triggered inversion recovery turbo field echo acquisition; spatial resolution = 1.3x1.3x4mm^3 (reconstructed to 0.6x0.6x2 mm^3); TE/TR = 3.0ms/6.2ms; flip angle = 25°]. The inversion time was determined using a preceding Look-Locker sequence to achieve optimal suppression of the atrial blood pool signal.

Macroscopic and Microscopic Examination

After the animals were euthanized, the hearts were explanted and suspended in normal saline. The aorta and main pulmonary artery were cannulated and the pulmonary veins, IVC and SVC were cross-clamped. Retrograde perfusion fixation of each whole heart was performed using 1 litre of Karnovsky's fixative (Solmedia Ltd, Shrewsbury, UK) per heart. The ablation line and surrounding tissue were excised *en bloc* and mounted in plastic frames, allowing two 5mm sections to be removed from the caudal and cranial ends of the ablation line. Each section was photographed then dehydrated, embedded in paraffin, sectioned (5μm sections), and stained with Masson's Trichrome for microscopic examination.

Data Analysis

Catheter Stability

Catheter stability at each end of the ablation line was determined using the Carto3 Visitag module, with stability filters set to 2.5mm/10seconds. The number of Visitags created during ablation per unit length of ablation line was taken to represent catheter stability within that ablation region.

Electroanatomic Mapping

Chronic voltage maps were registered to post-ablation maps by 3D translation and rotation using the SVC, IVC, RA appendage and azygos veins as registration landmarks. Short axis clipping planes were applied to remove the SVC above the right atrial appendage, to remove the IVC below the coronary sinus and to divide the chamber through the centre of the ablation gap. Low voltage (<0.5mV) area arising from ablation was quantified using the ablation index (AI). For each half of the chamber, AI was defined as the post-ablation low voltage area minus the pre-ablation low voltage area divided by ablation area. Pre- and post-ablation low voltage area was defined as the area of the caudal or cranial ends of the shell <0.5mV. Ablation area was defined as the area of the shell indicated by Carto ablation tags. AI was calculated for post-ablation acute (AI_{acute}) and chronic ($AI_{chronic}$) voltage maps, as shown in Figure 6-1. Scar density and mean ablation region voltage were calculated as follows. First, 3D scar regions were removed from the Carto3 geometries using a box clipping function (Kitware Inc, New York, USA). The resulting 3-dimensional posterior RA regions were resolved to 2-dimensions using a

surface parameterization technique (324). Ablation regions were thereby determined by projecting the ablation region (determined by intra-procedural ablation tags) onto the post-ablation acute and chronic patches to allow quantification of the voltages recorded within the ablation region.

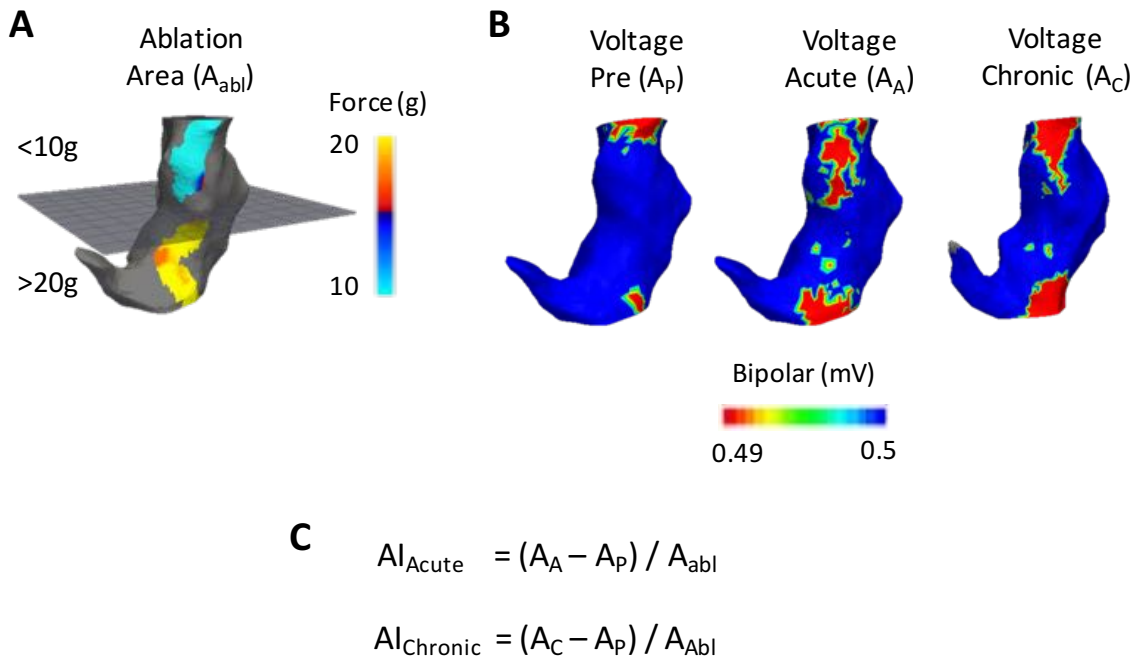

Figure 6-1. Ablation Index Calculation.

The Ablation Index was calculated at acute (AI_{Acute}) and chronic ($AI_{Chronic}$) timepoints by indexing the area of new low voltage within cranial and caudal ends of the chamber to the area ablated. **A** – ablation area; **B** – low voltage area pre- and post- ablation; **C** – calculation of the ablation index.

Cardiac Magnetic Resonance

Acute and chronic wall thickness was measured manually on axial T2W images. Chronic LGE enhancement was quantified by two metrics. Ablation volume at each end of the ablation line was determined as follows. First, a region of interest encompassing the entire posterior RA wall was manually created on the axial LGE images. Next, enhancement within the region of interest was identified by applying automatic signal intensity thresholds at a range of standard deviations above the mean atrial blood pool signal intensity. Finally, the image slice representing the centre of ablation gap was identified as the middle slice on the thresholded isosurface at which the distance of the apparent gap was minimized. From this standardized reference a 1cm region was taken either side of the central ablation gap thereby allowing relative ablation volumes to be compared between the animals at 3SD above the blood pool mean for chronic LGE images. Fibrosis intensity was quantified as the maximum and mean LGE signal intensity found within the

posterior RA region of interest. Intensities are presented as the image intensity ratio (IIR), being the ratio of ablation region signal intensity divided by the mean right atrial blood pool signal intensity. Mean IIR was simply defined as the mean of the IIRs for each voxel in the 1cm region of interest defined above. Peak IIR was determined by manually drawing a 2-dimensional region of interest in the posterior RA wall for each slice of the axial LGE image. The maximal intensity within these regions for each imaging slice was plotted against distance along the ablation line, thereby allowing peak IIR to be determined for caudal and cranial ends of the ablation line.

Microscopic Examination

Ablation scar was defined as transmural where a contiguous region of scar was evident from endocardial to epicardial aspects on the transverse sections. Fibrosis scoring of the ablation scar was determined as follows. Whole sections were digitized (10x magnification) using a scanning brightfield microscope (Leica Microsystems, Milton Keynes, UK). The ratio of blue to red staining of three rectangular zones within the ablation scar was quantified using an image ImageJ macro as previously described (344):

```
run("Brightness/Contrast...");
run("RGB Stack");
run("Convert Stack to Images");
run("Image Calculator...", "image1=Blue operation=Divide image2=Red create 32-bit");
run("Brightness/Contrast...");
run("Subtract...", "value=1.2");
run("Multiply...", "value=10000000");
run("Brightness/Contrast...");
run("Max...", "value=1");
run("Min...", "value=0");
run("Measure");
```

Statistical Analysis

Data analysis was performed using GraphPad Prism version 6.0c (GraphPad Software, San Diego, California, USA, www.graphpad.com). Results are presented as mean±SD. Student's unpaired *t*-test was used to compare group means between HF and LF regions. One-way analysis of variance was used to compare group means when considering caudal and cranial HF and LF regions separately. In all cases, a significance level of $P<0.05$ was considered statistically significant.

6.3 Results

Procedural and Ablation Parameters

All 8 animals survived until the end of the protocol and no animals were excluded from analysis due to premature death. No procedural complications occurred. Mean applied contact force was 22.6±11.4g in HF zones and 7.8±4.0g in LF zones ($P<0.0001$, Figure 6-2A and B) resulting in average force-time integrals of 1170±509gs (HF) and 272±94gs (LF) (Figure 6-2C and D). Total ablation time for the lines was 16±4 minutes. Catheter stability was identical between HF and LF zones with mean VisiTag densities of 3.87±0.65 tags/cm and 3.84±0.94 tags/cm, respectively ($P=0.7508$). Contact force resulted in a significant increase in impedance (measured mid-chamber) from baseline, up to 25g, with a plateau thereafter (Figure 6-2E). Overall, a significantly greater proportion of ablation lesions was delivered at maximum power output at regions of LF compared to regions of HF ablation (Figure 6-2F) and this difference was seen in every animal. Mean power during ablation was 24.8±6.6W vs. 28.7±4.0W in the HF and LF zones, respectively ($p<0.0001$).

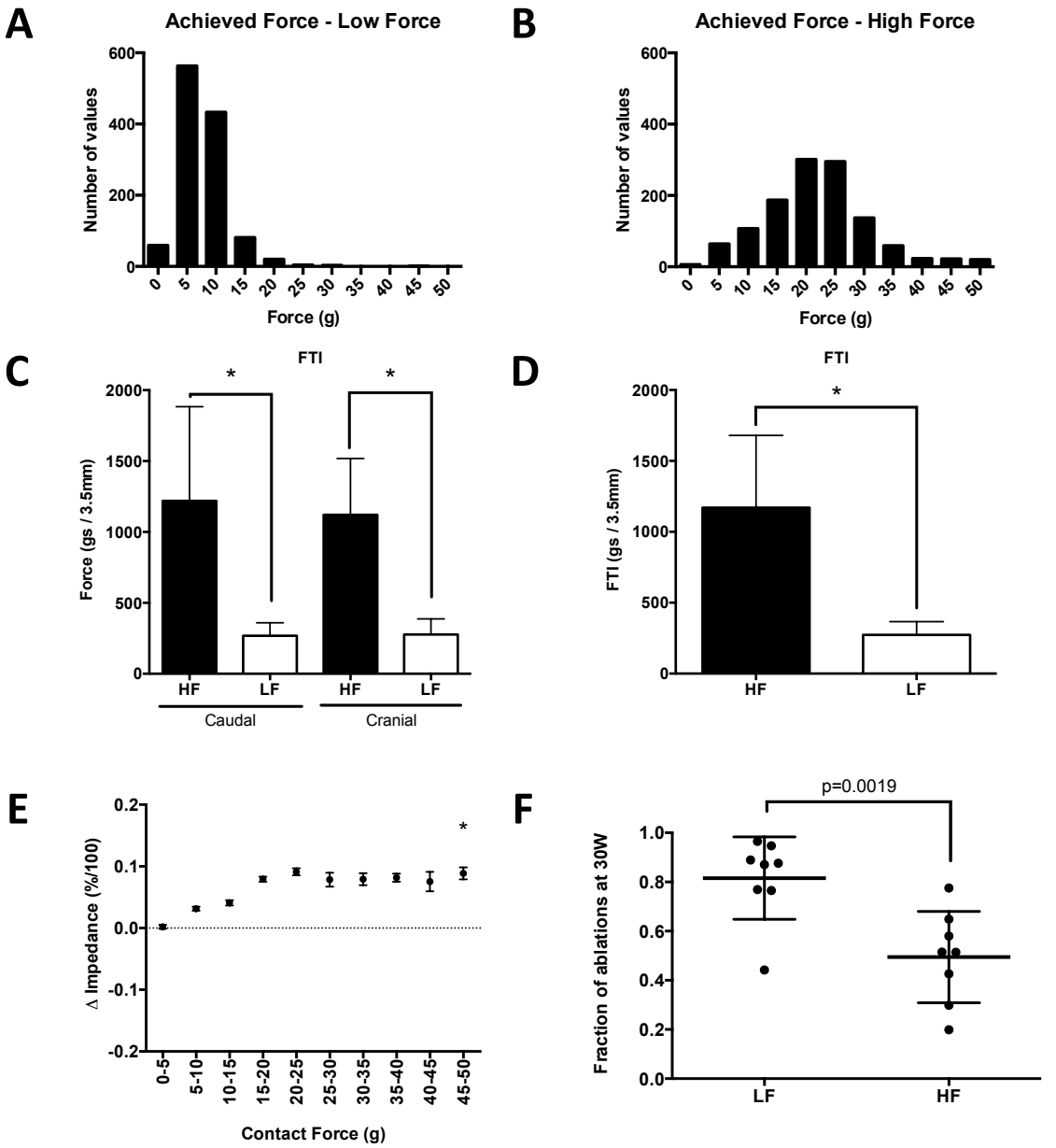

Figure 6-2. Ablation Parameters

A, B – Contact force distribution during LF and HF ablation. **C**, **D** – Calculated force-time integrals for HF and LF ablation at separate ends of the ablation line (**C**) and for both endscombined (**D**). **E** – Change in impedance with catheter-myocardium contact force. **F** – Maximal power output (30W) during ablation for LF and HF regions.

Electroanatomic Mapping

Pre-ablation, post-ablation and chronic mapping was performed in all animals, resulting in a total of 24 electroanatomic maps with an average of 1161 points per map. Achieved ablation size was quantified for acute and chronic post-ablation maps using the Ablation Index (AI), which represents the area of new low voltage on post-ablation voltage maps indexed to the area of RF energy application. There was no difference in AI_{acute} or $AI_{chronic}$ between HF and LF ablation regions (Figure 6-3). Scar density was quantified on

electroanatomic mapping as the proportion of the ablation zone below 0.5mV. There was no excess reduction in scar density between acute and chronic time points for scar created with LF ablation as compared to HF ablation (Figure 6-4). Similarly, there was no increase in ablation region voltage between acute and chronic time points for either HF or LF ablation (Figure 6-5).

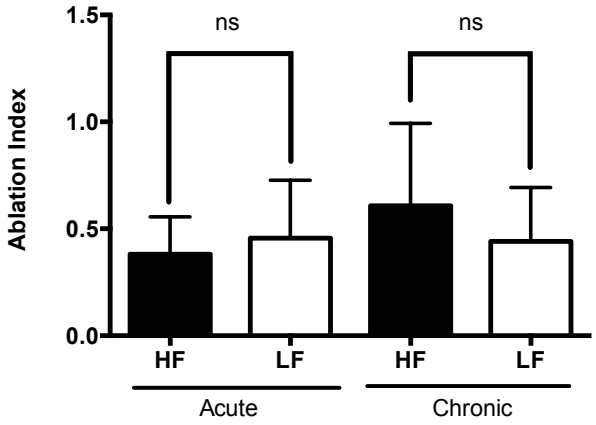

Figure 6-3. Ablation Index

The ablation index quantifies the area of applied radiofrequency ablation that is converted into low voltage scar on bipolar voltage mapping. There was no significant difference between the ablation index at either acute or chronic time points.

Cardiac Magnetic Resonance

Consistent with prior experience, no appreciable pre-ablation T2W or LGE enhancement was seen in either pig undergoing pre-ablation imaging (343). Acute T2W wall thickness was significantly greater for HF vs. LF ablation, and this difference persisted when cranial and caudal ends of the ablation line were considered separately (Figure 6-6). In contrast, there was no difference in chronic LGE scar volume between HF and LF ablation regions (Figure 6-7). Similarly, there was no difference in mean (Figure 6-8A) or peak (Figure 6-8B) LGE IIR between HF and LF ablation regions.

Macroscopic and Microscopic Examination

Macroscopic photographs of chronic ablation lesions following perfusion fixation are shown in Figure 6-9. The ablation line was sectioned perpendicular to the axis of ablation through HF and LF regions, resulting in 16 sections (Figure 6-10). In all 16 sections, replacement of normal atrial wall with fibrous scar tissue was identified. Transmural scar was seen in 14 out of 16 sections with both non-transmural ablation scars occurring in

HF ablation zones. There was no significant difference in quantified fibrosis density between HF and LF regions (59.1% vs. 68.1%, P=0.3059).

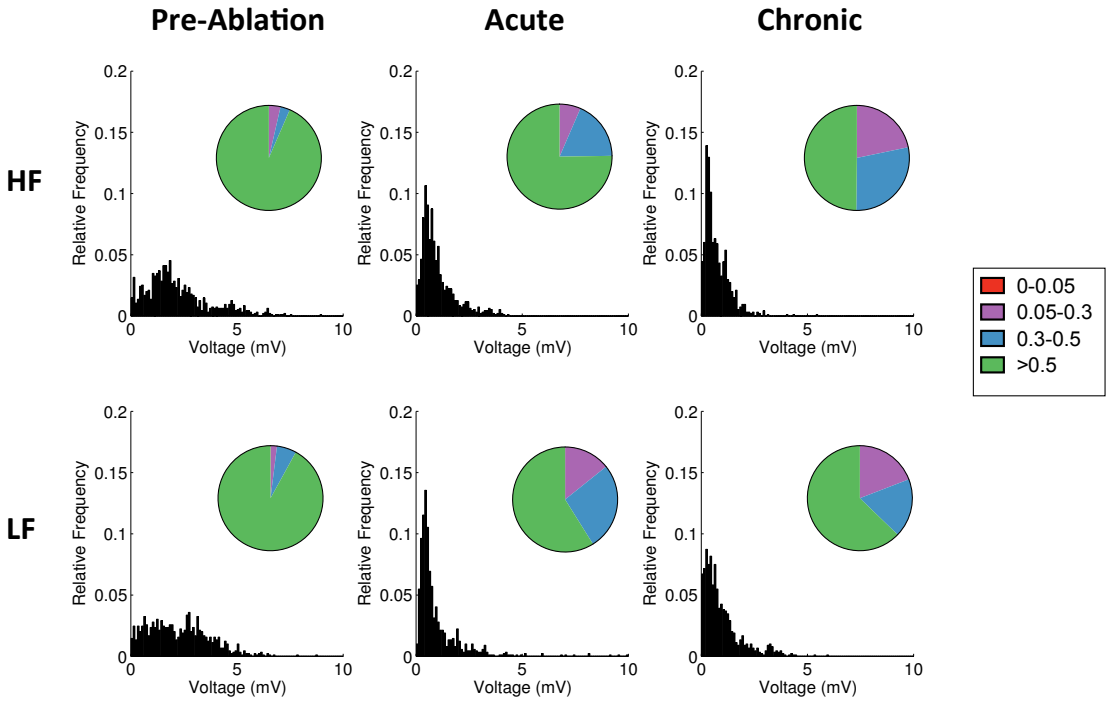

Figure 6-4. Ablation Region Voltage Distribution

Compared to pre-ablation voltage distributions, post-ablation voltage distributions show a leftward skew that is similar for both high force (HF) and low force (LF) ablation regions. Comparing acute to chronic time points, there is no excess increase in voltage recovery for LF as compared to HF regions.

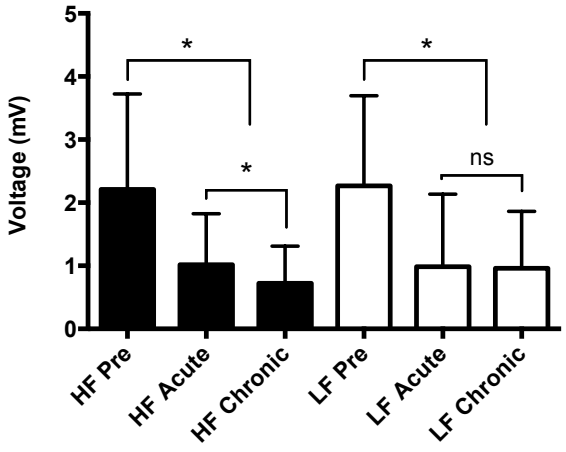

Figure 6-5. Ablation Region Mean Voltages

Mean voltages were similar post-ablation and pre-ablation for both high force (HF) and low force (LF) zones. There was no excess increase in mean voltage at chronic time points compared to acute time points for either HF or LF zones.

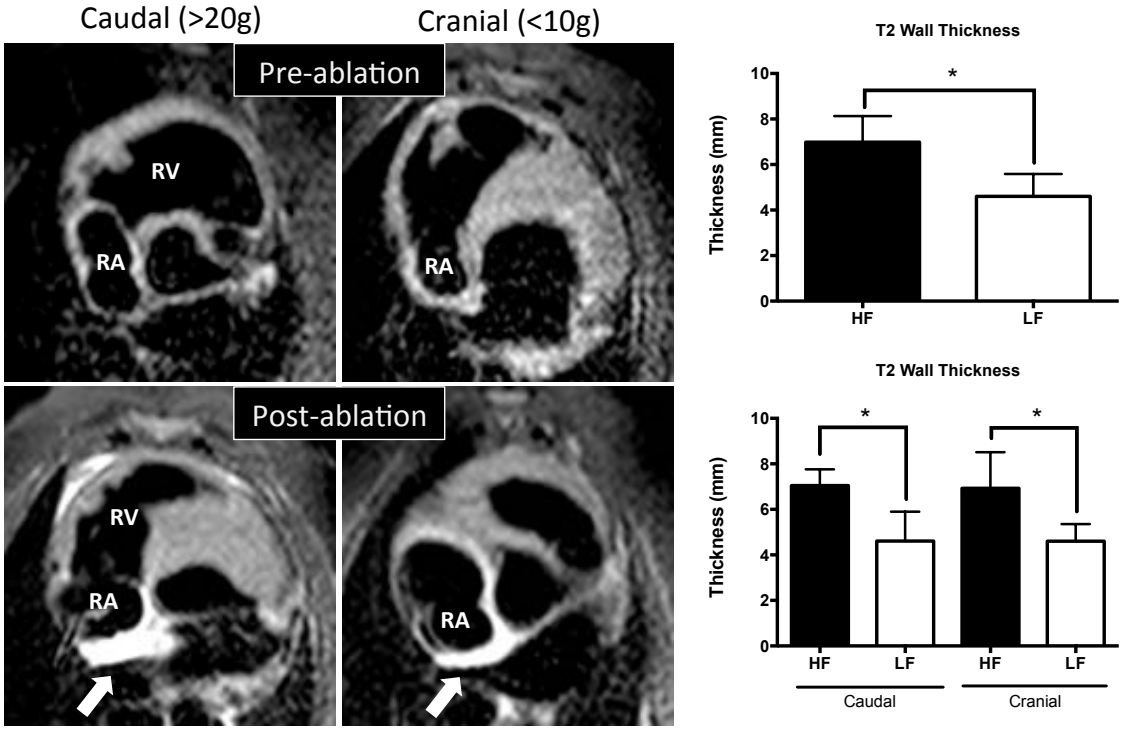

Figure 6-6. T2-Weighted Wall Thickness

Posterior right atrial wall thickness measured on T2-weighted images was increased post-ablation (left, arrows). T2W wall thickness was significantly greater for regions of high force (HF) than low force (LF) for both caudal and cranial ablation zones (right).

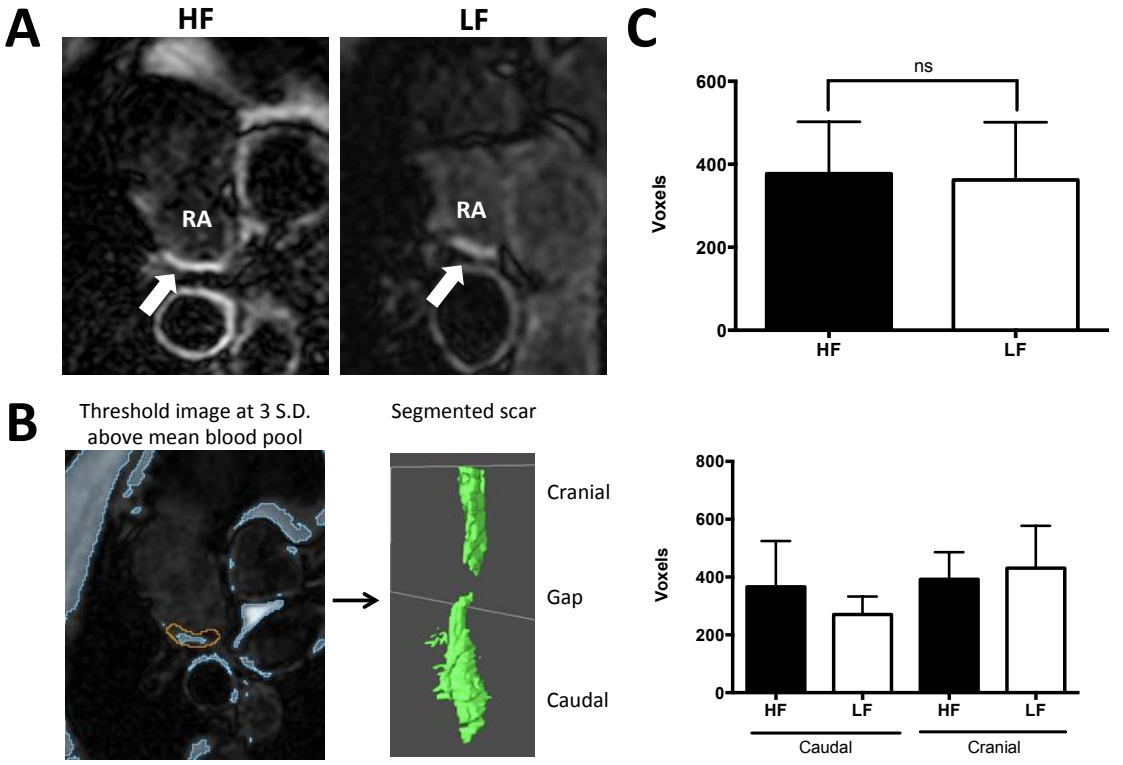

Figure 6-7. Chronic LGE Lesion Volume

A – LGE appearances (white arrows) for high force (HF) and low force (LF) ablation regions. **B** – Standardised assessment of lesion volume involved manual segmentation of the posterior RA wall

(yellow) and automatic segmentation of the entire volumetric image at 3SD above atrial blood pool mean. Combining regions resulted in the ablation scar segmentation (green). **C** – There was no difference in ablation volume between HF and LF ablation zones.

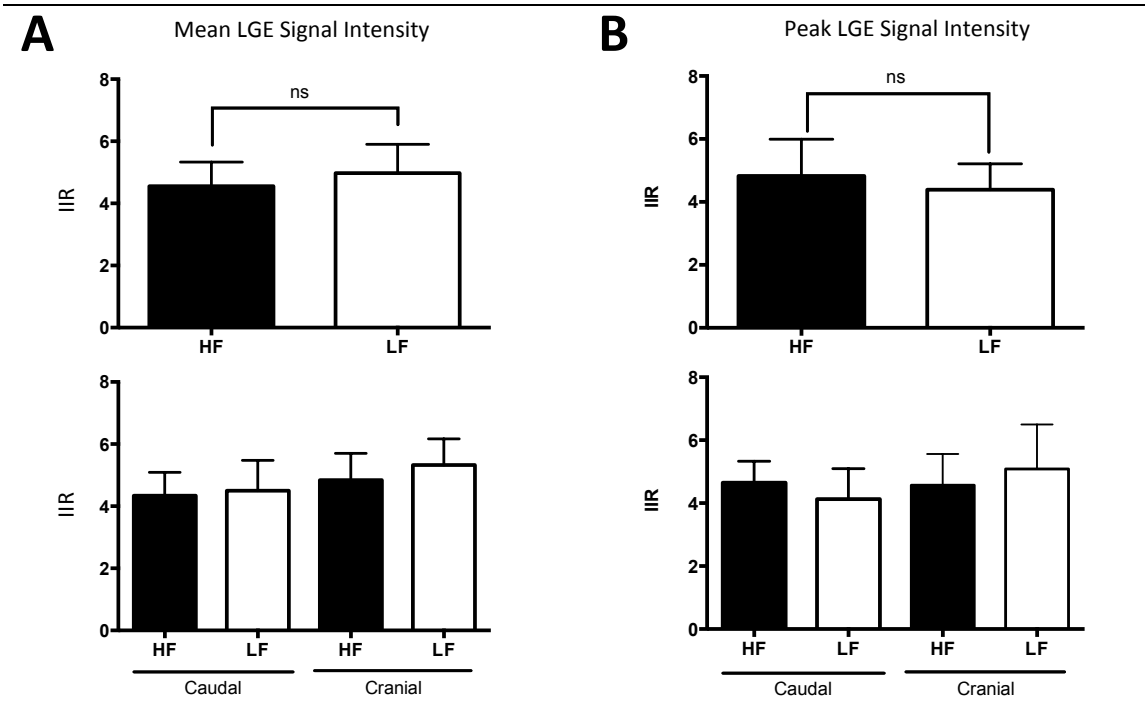

Figure 6-8. Chronic LGE signal intensity

A – Mean signal intensity was calculated for the ablation zones as defined in Figure 6-7B. **B** – Peak signal intensity was measured from cranial-caudal signal intensity contours along the ablation line.

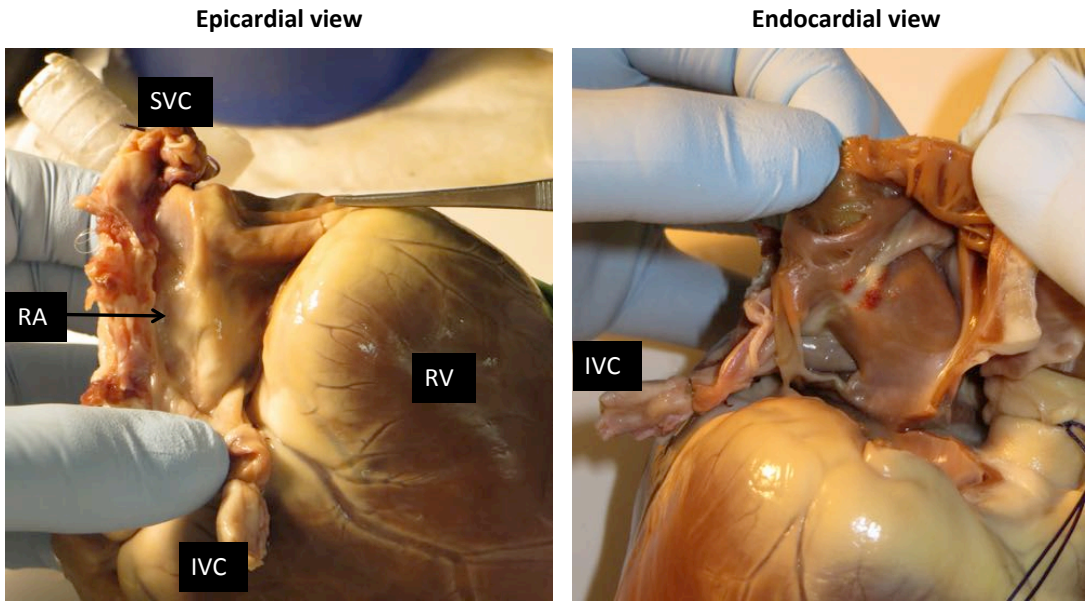

Figure 6-9. Macroscopic Appearances of the Ablation Line

Left panel - epicardial view. Right panel - endocardial view. The ablation line gap can be seen just before ablation continues into the inferior vena cava.

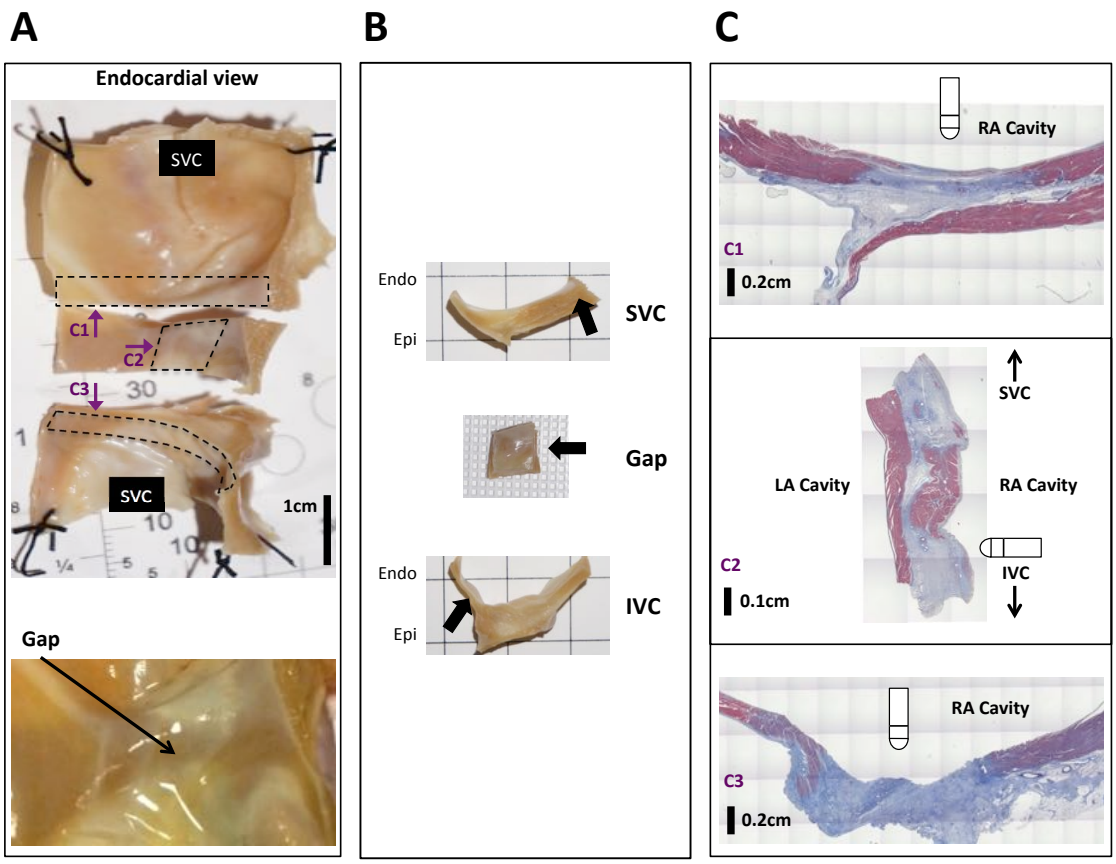

Figure 6-10. Microscopic Appearances of the Ablation Line

A – endocardial view showing cranial, mid and caudal ends of the ablation line. Dotted lines indicated primary cuts to prepare specimens for sectioning. **B** – specimens prepared for sectioning. Black arrows are orthogonal to the sectioning planes. **C** – Masson's trichrome stain of cranial, gap and caudal regions of the ablation line. The cranial and caudal specimens are sectioned transverse to the line with the gap specimen sectioned longitudinal to the line.

6.4 Discussion

The main findings of this study are: 1) Low force ablation results in equivalent RF ablation lesion size, quality and transmurality as high force ablation; 2) Catheter-myocardium-blood pool interface impedance is proportional to contact force within the range 0-25g and reaches a plateau thereafter; 3) During temperature-controlled RF energy delivery, higher generator power output may compensate for reduced catheter-myocardium energy transfer at low contact force.

With the advent of intra-procedural contact force monitoring catheters, it has become possible to not only confirm contact of the catheter tip with a physical barrier (i.e., myocardium) but also to directly measure the force (magnitude and direction) exerted by that barrier on the catheter tip. In clinical studies the use of contact force monitoring has been associated with improved procedural outcomes, regardless of the contact force

applied (345), and low contact force has been associated both with procedural failure (346) and with sites of pulmonary venous reconnection (347). Despite these findings, use of contact force sensing technology does not universally lead to improved procedural outcomes (348), raising the possibility that other confounding factors may at least partially explain the relationship between contact force and outcome in clinical studies.

Examining lesion sizes created in the *ex-vivo* studies lends further weight to this argument. As can be seen in Figure 6-11, most studies show a linear relationship between CF and lesion depth at low contact forces before reaching a plateau somewhere between 10 and 20g. Of particular importance however is that even at minimal contact force even the shortest duration applications achieved a lesion depth of almost 4mm. Considering the typical thickness of the human LA wall ranging up to 3-4mm (349, 350) it follows that even low force ablation can achieve transmural scarring in atrial ablation. This hypothesis is supported by *in vivo* studies of ventricular radiofrequency ablation (demonstrating 5.0mm to 5.9mm lesion depth even at low contact force (338)), but has not been tested in an *in vivo* atrial model.

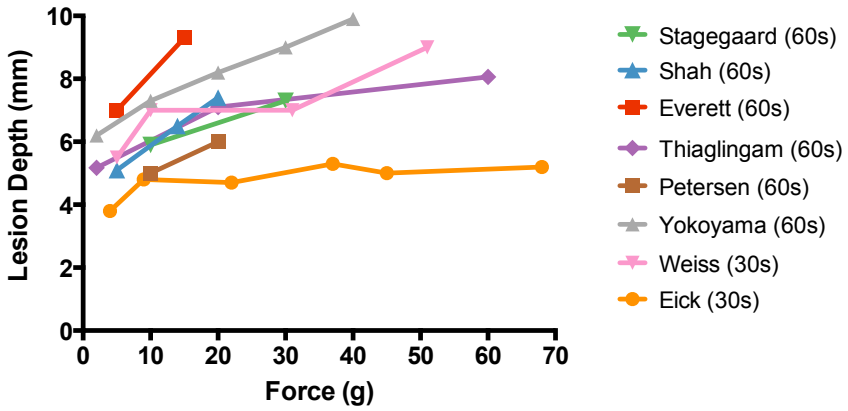

Figure 6-11. Contact Force / Lesion Depth Reiationship in Prior Studies

Lesion depth is plotted against contact force for prior ex-vivo and in-vivo non-myocardial studies. RF application durations are shown in parentheses.

Based on these observations, the present study aimed to assess the size, quality and transmurality of atrial ablation lesions created at low force (<10g, mean 7.8g) as compared to lesions created at high force (>20g, mean 22.6g). A previously validated porcine right atrial ablation model, representing an ablation site similar in thickness to the human left atrium (351), was used. The low force and high force targets were selected based on previous work demonstrating consistent contact at 9.9±8.6g and tissue tenting

at 25.0±14.0g of contact force (352). Crucially, equal stability was ensured between low and high force regions by using the Visitag module in the Carto-3 mapping system, and any effect of regional variation in tissue characteristics was negated by performing ablation in counterbalanced order with both high and low force being used at caudal and cranial ends of the ablation line. Under these controlled conditions, there were no differences in lesion size, quality or transmurality either acutely or at 2 months post-ablation between the low force and high force strategies. Therefore, equivalent procedural success should be achievable with low force ablation, whenever consistent catheter-myocardium contact can be established.

Whilst our study was not powered to detect procedural complications, it is logical that increased contact force may be associated with complications, especially cardiac perforation, tamponade and damage to extra-cardiac structures. Although studies examining perforating forces have generally identified higher minimum perforating forces than those used in our study it is still desirable to utilize the minimum contact force required in order to increase the safety margin. A recent *ex vivo* human study demonstrated that perforating forces are reduced by radiofrequency ablation, and that forces as low as 38g could result in atrial myocardial perforation (339). Given that AF was absent in all but one patient in this study, and that atrial wall thinning has been identified in AF (353), the minimum perforating contact force may well have been overestimated in the above study.

Of note in our study, T2-weighted wall thickness was significantly greater at regions of high force than low force. Two possible hypotheses are suggested for this finding. Firstly, even though low force achieved transmurality, high force may still have resulted in greater (unnecessary) energy transfer leading to more atrial wall oedema. Secondly, since tissue tenting has been identified on intracardiac ultrasound with forces around 25g (352), high force ablation in this study may have resulted in heating and oedema of extra-cardiac structures. This finding is consistent with previous work identifying an independent role for catheter-myocardium contact force in oesophageal injury during left atrial ablation (354), as well as CMR studies identifying increased aortic and oesophageal LGE post-LA ablation (355, 356).

Limitations

1) The results presented here describe the effect of contact force on linear ablation in an animal model. Given the similarity of wall thickness and profile of the porcine RA to the human LA, similar findings would be expected in the human LA. However it is acknowledged that this extrapolation is a limitation of any animal model of human cardiac tissue.

2) In order to most closely resemble clinical practice, drag lesions rather than point lesions were created. It is possible that the lesions will therefore overlap, resulting in a cumulative effect on tissue heating.

3) By performing ablation solely at the posterior RA the range of contact force vectors is limited. While this is necessary to isolate the effect of contact force on lesion formation it is acknowledged that this is a limitation of the data when extrapolating the findings to human LA ablation with a larger range of force vectors.

4) Since the animals were anaesthetised during ablation, the respiratory cycle was uniform and likely contributed to the ability to achieve good catheter stability. This may not always be the case during human atrial ablation, especially in the absence of general anaesthesia. Similarly variations in contact force may be required to achieve equal stability around the pulmonary venous ostia in human left atrial ablation.

6.5 Conclusions

In summary, by using a combined electro-anatomical mapping, imaging and histological examination approach this study demonstrated equivalent chronic ablation lesion formation at low and high catheter-myocardium contact force. Appropriate contact force targets for left atrial ablation may be lower than previously described, especially with concomitant use of novel stability-sensing technologies, and adoption of lower force targets may lead to improved procedure safety.

This study concludes the thesis section on arrhythmia substrate characterisation. I have shown the role of surface ECG, intracardiac contact mapping and imaging in characterising a variety of arrhythmia substrates. In the next section I explore problems and solutions related to the visualisation and display of such arrhythmia substrates.

SECTION THREE: REPRESENTATION OF ARRHYTHMIA SUBSTRATES

7 Arrhythmia Substrate Representation: Dot Mapping

7.1 Introduction

Substrate-based catheter ablation strategies form the cornerstone of treatment of multiple atrial and ventricular arrhythmias. In identifying the arrhythmia substrate a variety of physiological parameters are used, for example post-pacing interval and late potentials in ventricular tachycardia or complex fractionated electrograms and dominant frequency in atrial fibrillation. In certain situations combinations of multiple such datasets become especially valuable, for example bipolar voltage combined with local activation time in macro-re-entrant atrial tachycardia and ventricular tachycardia. Furthermore, emerging technologies such as non-invasive body surface mapping and contact rotor mapping provide novel physiological information describing the arrhythmia substrate. In addition to these electrical parameters, pre-procedural assessment with both atrial and ventricular imaging identifies areas of scar or fibrosis, which may be crucial to arrhythmogenesis. See Arrhythmia Substrate Characterisation Techniques, p. 27, for a full discussion of these techniques.

Despite this array of complimentary clinical datasets, no contemporary electro-anatomic mapping technologies are available to concurrently and statically display more than one dataset on a single cardiac chamber model. In this chapter I therefore develop such a technology, and demonstrate its use in data representation for both atrial and ventricular arrhythmias. The underlying aim is to represent multiple scalar datasets within a single spatial domain whilst minimizing 1) any loss of fidelity in the original datasets and 2) any operator-dependent manual segmentation or threshold selection of either dataset.

7.2 Methods

Dot Mapping

The technology developed here (Dot Mapping) represents the first dataset by chamber surface shading with a colour spectrum proportionally related to the scalar value of the first dataset. For surface models, the second dataset is represented with single-pixel-sized

white dots drawn just above the underlying coloured surface. For volumetric models, the second dataset is represented with single-pixel sized white dots drawn throughout the chamber wall. The dots are related to the dataset in two ways: 1) the location of the dots represents the location of the scalar dataset value being represented; 2) the density of the dots is proportional to the underlying scalar value. Examples of such scalar values might be late gadolinium signal intensity from CMR imaging or bipolar voltage from electro-anatomical contact mapping. Importantly, since only a fraction of available screen space is used to represent the second dataset (dots), it remains possible to 'see through' the dots to the underlying surface in order to retain the ability to perceive the first data set represented by surface colour shading. Dot Mapping was implemented using a commercial software package (MATLAB 8.2, The Mathworks Inc., Natick, MA). Source code for the Dot Mapping software is given in Appendix B.8.

The input datasets must be represented as either surface or volumetric meshes with associated scalar fields encoding the physiological parameter(s) of interest. Each element within the mesh is assigned a weight (λ) based on the area (or volume) of the element (A), the scalar field value for the element (S) and the ratio of the squares of the starting distance to the object (D) to the current distance to the object (D'):

$$\lambda = \frac{A \times S \times D^2}{D'^2} \qquad \textbf{Equation 7-1}$$

A random number X is then chosen from the set of positive integers (i.e. $k \in \mathbb{N}_1$) such that the probability of $X = k$ is given by the Poisson distribution with mean and variance λ:

$$P(X = k) = \frac{\lambda^k e^{-k}}{k!} \qquad \textbf{Equation 7-2}$$

In this way, an integer number of dots (x_i) is drawn within each element i, based on the scalar field value for that element but additionally corrected for element size and viewing position. The coordinates of each dot are calculated based on a random spatial distribution within each element. For each triangular element ABC this spatial distribution is given by:

$$P = \left(1 - \sqrt{r_1}\right)A + \sqrt{r_1}(1 - r_2)B + \sqrt{r_1}r_2C \qquad \textbf{Equation 7-3}$$

Where, r_1 and r_2 are two numbers chosen from a uniform distribution of random numbers in the interval [0,1]. For each tetrahedral element $ABCD$ the spatial distribution is calculated in a two-step process. Let R be a three-element array where r_1, r_2, and r_3 are three numbers chosen from a uniform distribution of random numbers in the interval [0,1]. R' and R'' are then defined as:

$$R' = \begin{cases} R & if\ r_1 + r_2 \leq 1 \\ \begin{bmatrix} 1 - r_1 \\ 1 - r_2 \\ r_3 \end{bmatrix} & if\ r_1 + r_2 > 1 \end{cases} \quad \textbf{Equation 7-4}$$

$$R'' = \begin{cases} R' & if\ r_1' + r_2' + r_3' \leq 1 \\ \begin{bmatrix} r_1' \\ 1 - r_3' \\ 1 - r_1' - r_2' \end{bmatrix} & if\ r_1' + r_2' + r_3' > 1\ and\ r_2' + r_3' > 1 \\ \begin{bmatrix} 1 - r_2' - r_3' \\ r_2' \\ r_1' + r_2' + r_3' - 1 \end{bmatrix} & if\ r_1' + r_2' + r_3' > 1\ and\ r_2' + r_3' \leq 1 \end{cases} \quad \textbf{Equation 7-5}$$

Then, the Cartesian co-ordinates (P) of the random points for the dots are given by:

$$P = \begin{bmatrix} A \\ B \\ C \\ D \end{bmatrix} \circ \begin{bmatrix} 1 - \sum R'' \\ r_1'' \\ r_2'' \\ r_3'' \end{bmatrix} \quad \textbf{Equation 7-6}$$

The Dot Mapping interface allows the user to adjust the 'brightness' and 'contrast' of the Dot Map by adjusting a constant (b), and power (c), applied to each element weight (λ) to result in a new element weight (λ_{adj}):

$$\lambda_{adj} = b\lambda^c \quad \textbf{Equation 7-7}$$

This new element weight is then used as the mean and variance of the Poisson distribution (Equation 7-2). Further controls allow the user to toggle display of one or both datasets as well as perform the standard manipulation functions of rotate, pan and zoom.

Optionally, to improve computational efficiency, the algorithm can determine whether the number of dots for any one simplex should be limited. If A is the area or volume of the simplices, and q is a system-defined constant, then the maximum number of dots for each simplex (N) is given by:

$$N = qA \qquad \textbf{Equation 7-8}$$

If the required number of dots (x_i, Equation 7-2) for a simplex, i, is greater than n_i, then the number of dots for that simplex is limited to n_i. The constant q is chosen such that 'dot-density' curves remain flat within expected operational zoom, brightness and contrast levels.

Data Perception

To test the simultaneous perception of dual datasets with Dot Mapping the sample problems shown in Figure 7-1 were displayed. Orientation of two uniformly changing scalar fields across a circular geometry was varied and the perceived angle of the axis of maximum rate of change of the dataset was recorded for colour alone, dots alone and combined Dot Mapping (100 repetitions). In a second test, correct localisation of a focal source was determined with traditional colour mapping and Dot Mapping (100 repetitions). Finally, propagation direction perception accuracy (colour) was determined in the presence and absence of a randomly located region of scar represented by Dot Mapping (100 repetitions).

Clinical Data Collection and Pre-Processing

Atrial Cases

Two patients requiring atrial catheter instrumentation were studied. One patient had previously undergone LA catheter ablation for persistent AF using a stepwise approach incorporating wide area pulmonary vein encirclement and linear ablation at the mitral isthmus (case 1). The other patient had previously undergone surgical correction of RVOT and LVOT obstruction requiring right and left atriotomies. As part of the clinical procedures for both cases a 3D geometry of the left atrium was created using the Carto 3 mapping system (Biosense Webster, Diamond Bar, CA, USA). High-density pre-ablation peak-to-peak bipolar voltage and local activation time maps were constructed using points acquired with the ablation catheter in order to give coverage of the entire left atrium. Case 1 underwent CMR imaging 3 weeks prior to catheter ablation, including 3D

balanced steady-state free precession (b-SSFP) and 3D late gadolinium enhancement (LGE) imaging. CMR images were processed according to previously described methods (357). Briefly, after semi-automatic segmentation of the atrial blood pool, the LGE images were registered to the b-SSFP images and a 3D manifold 'shell' of the LA was created with surface LGE data calculated by maximum intensity projection normal to the shell. CMR LGE data was registered to the endocardial EAM geometry using landmark registration followed by an iterative closest point algorithm.

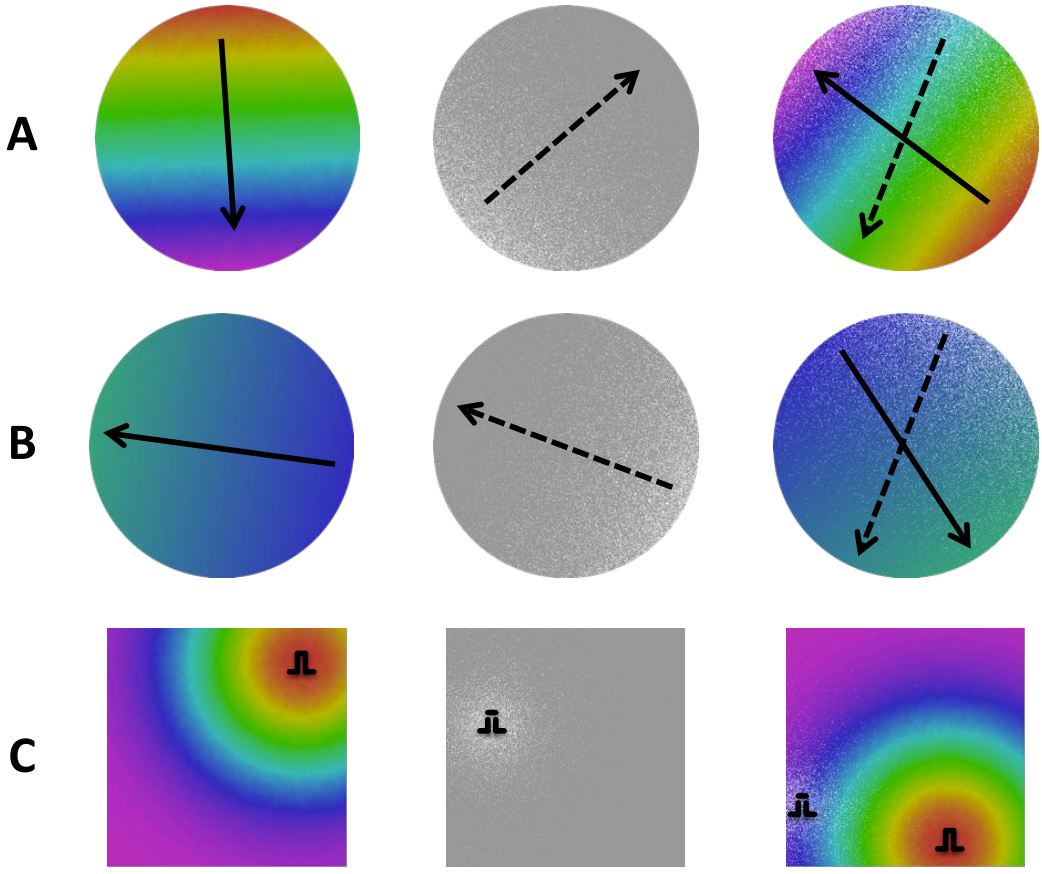

Figure 7-1. Test Datasets for Data Perception Experiments

A – Combination of two linear activation patterns represented with Dot Mapping and the rainbow colour scale. **B** – Combination of two linear activation patterns represented with the blue-green colour scale. Solid arrows represent the propagation direction of the dataset represented with colour. Dotted arrows represent the propagation direction of the dataset represented with dots. **C** – Focal activation sites identified with colour mapping (left), dots (middle) and combined colour-Dot Mapping (right).

Ventricular cases

A patient requiring left ventricular instrumentation for catheter ablation of ischaemic heart disease-related ventricular tachycardia was studied. Endocardial access was obtained using a retrograde aortic approach and pericardial access was obtained using a

subxiphoid percutaneous approach. Using the Carto 3 EAM system (Biosense Webster, Diamond Bar, CA, USA) 3D geometries representing the endocardial and epicardial surfaces of the left ventricle were created. High-density peak-to-peak bipolar voltage maps were constructed during sinus rhythm. Prior to ablation the patient underwent CMR imaging including high-resolution 3D LGE imaging. The left ventricular myocardium was segmented on a slice-by-slice basis using Seg3D (Scientific Computing and Imaging Institute, University of Utah) to create a 3D binary image. A tetrahedral mesh was created from the binary image with mean signal intensity within each tetrahedron represented as the absolute signal intensity value above the mean blood pool value. Finally, the endocardial Carto 3 maps were registered to the endocardial surface of the CMR segmentation using landmark registration followed by an iterative closest point algorithm.

Operator Experience

Operator experience using Dot Mapping was assessed in three domains (diagnostic accuracy, dataset fidelity and ease of use) and compared with traditional display techniques. Each domain was assessed using two atrial paired datasets (electrogram voltage vs. local activation time). Operators (n=15) reviewed the paired datasets with and without Dot Mapping for 1 minute and, after each 1-minute period, the three domains were assessed using a 4-point Likert scale with 5 items per domain (Table 7-1).

Table 7-1. Likert Items for the User Experience Assessment Scale

Domain	Likert Items
Diagnostic accuracy	The display system maximizes the diagnostic utility of the underlying datasets.
	The display system fully facilitates accurate diagnosis.
	The display system faithfully represents the first dataset.
	The display system faithfully represents the second dataset.
	The display system increases the combined value of the underlying datasets
Display fidelity	The first dataset is displayed with high fidelity.
	The second dataset is displayed with high fidelity.
	The overall fidelity of the display system is high.
	There is no loss of fidelity of the datasets as a result of the display system.
	Registration accuracy between the datasets is maximized.
Ease of use	It is easy to relate the first dataset to the second dataset.
	It is easy to relate the second dataset to the first dataset
	It is easy to visualize both datasets together.
	The system does not rely on user recollection of the dataset(s).
	The system allows rapid assessment of the combined datasets.

Users rated each Likert item using the 4-point scale: 0=strongly agree, 1=agree, 2=disagree, 3=strongly disagree.

Statistics

Data analysis was performed using GraphPad Prism version 6.0c (GraphPad Software, San Diego, California, USA, www.graphpad.com). Continuous variables are expressed as mean±standard deviation. Groups were compared using the one-way analysis of variance (ANOVA) with Tukey's multiple comparisons test used post-hoc to identify differences between groups. Likert score results are presented as median scores and differences were assessed with the Wilcoxon two-sample signed rank test.

7.3 Results

Dot Mapping Graphical User Interface

The Dot Mapping Graphical User Interface (GUI) was implemented within the MATLAB programming environment (MATLAB 8.2, The Mathworks Inc., Natick, MA) and a screenshot is shown in Figure 7-2. Key components of the GUI include the display window and the control bar. Within the display window a colour scale for the colour-represented dataset is indicated. The control bar contains a variety of control elements for loading data and manipulating the Dot Map. Other controls allow the Dot Map and the colour map to be toggled independently. Further detlails of the controls are given in the figure legend.

Dot Mapping Algorithm Performance

To test the performance of the Dot Mapping algorithm, a simple 2-dimensional test case was created as shown in Figure 7-3A consisting of 16 identical isosceles triangles with signal intensities between 1/3rd and 1.0. The Dot Mapping software defaults to brightness and contrast of 1.5 ($b = 1.5$, $c = 1.5$, Equation 7-7). The effect of adjusting b and c on the ranges 1.5-2.5 is shown in Figure 7-3B. Typically, a brightness of <1.5 and contrast ~2-2.5 achieves good image contrast whilst allowing adequate perception of the underlying colour datasets (shown as uniform black in Figure 7-3B).

A core aim of the Dot Mapping algorithm is to ensure that the screen dot density (that is the number of dots per unit screen area) remains constant for each simplex (or region of simplices with uniform signal intensity) regardless of the zoom level of the scene. In Figure 7-4A, a flat 'screen dot density' curve is demonstrated for a region of uniform

signal intensity on the 2-dimensional test case. Operational zoom levels are restricted by adjusting q (Equation 7-8) first to 100,000 (Figure 7-4B) and then to 20,000 (Figure 7-4C). For the cases presented later, no dot restrictions are applied ($q = \infty$).

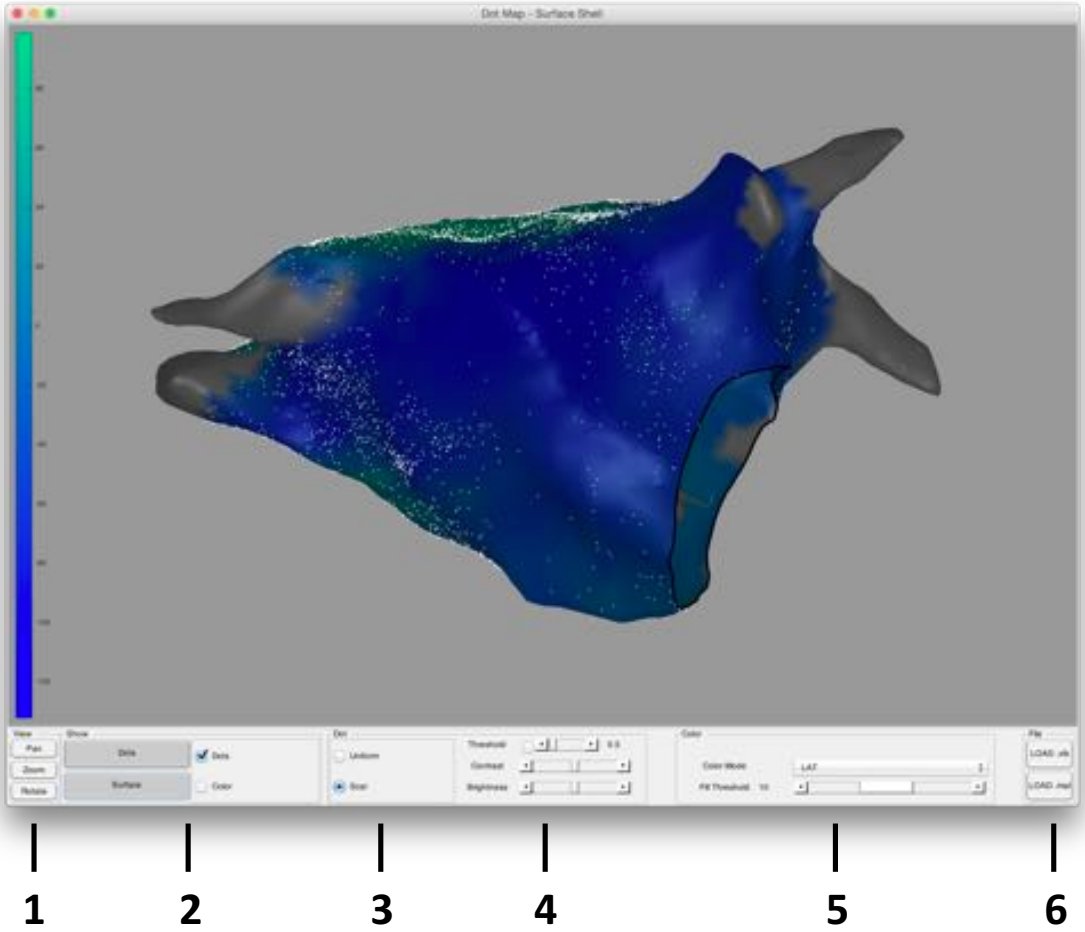

Figure 7-2. Dot Mapping Graphical User Interface

The Dot Map GUI is shown for a surface shell. The control bar forms the lower portion of the screen. Key controls are as follows: **1** – image manipulation controls; **2** – controls to toggle on/off the Dot Map, the colour shell and any feature edges (e.g. in the above example, the mitral valve annulus); **3** – setting to determine whether the Dot Map is uniform in density or proportional to the underlying dataset; **4** – controls for the brightness, contrast and threshold of the Dot Map; **5** – controls for the colour map including fill threshold for interpolation; **6** – data loading controls.

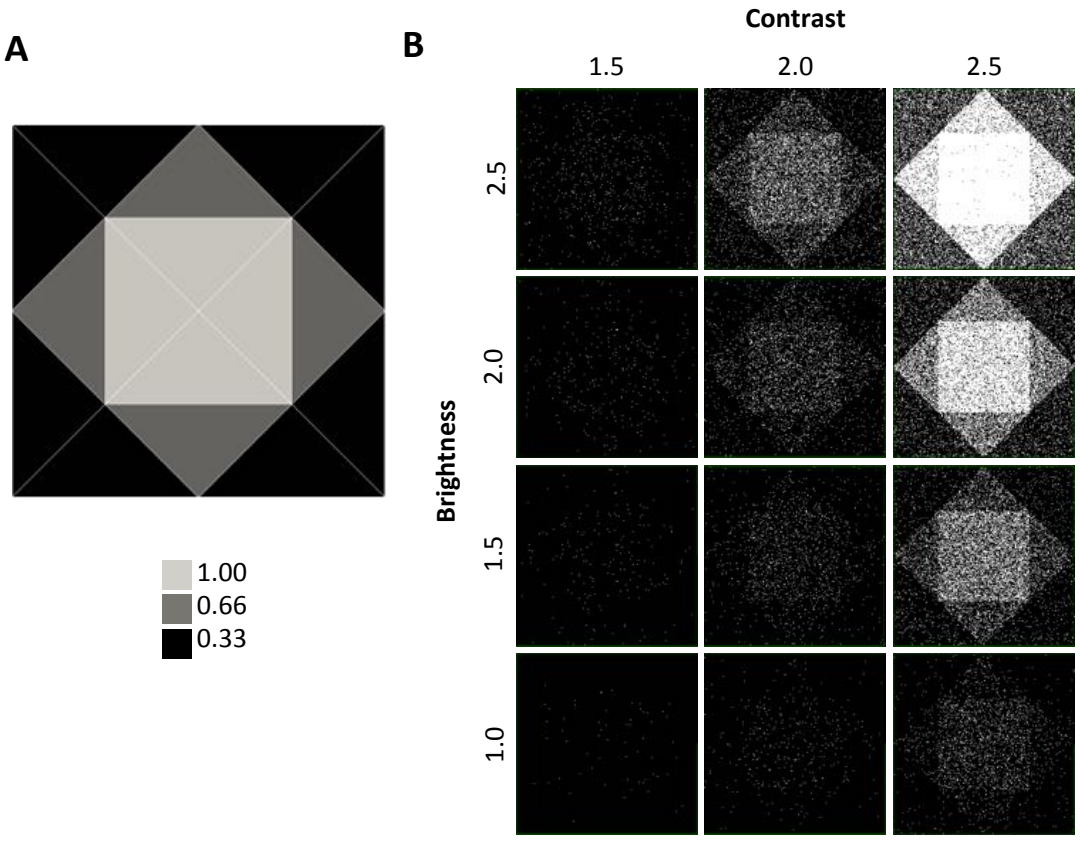

Figure 7-3. Dot Mapping Algorithm Performance.

A - Test dataset. **B** - Representations of the test dataset using Dot Mapping with varying brightness and contrast settings.

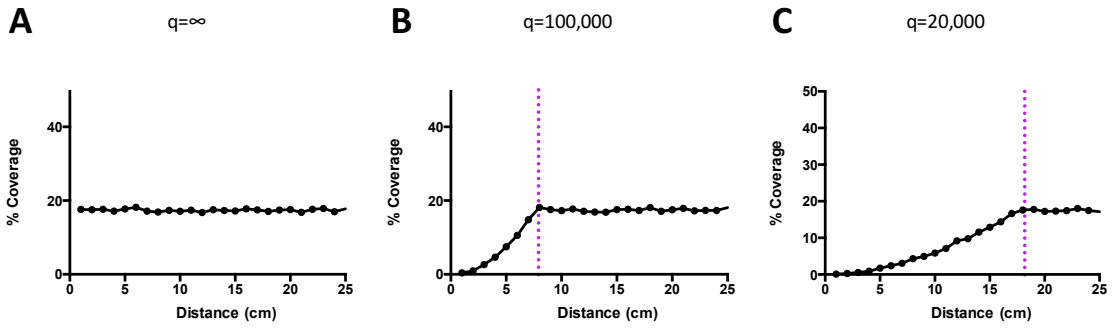

Figure 7-4. Effect of Zooming on Data Representation

A – The Dot Mapping algorithm maintains the screen density of dots regardless of the distance from viewpoint to chamber model (i.e. zoom factor). **B**, **C** – Introducing a limit on the maximum number of dots reduces the effective operational range of zooming factors that can be accurately represented (to the right of the purple dotted lines).

Dataset Perception

In the tests of dataset perception, two colour scales were examined. The rainbow colour scale (e.g. Figure 7-1A) varying from red to purple is typically used in electroanatomic mapping systems and incorporates the full visible colour spectrum This colour spectrum

tends to introduce the perception of artificial zones in uniform data. A simple two-hue colour scale (e.g. blue-green, Figure 7-1B) provides a smoother transition consistent with the gradient of underlying data, and whilst it has found use in representation of imaging data it is yet to be employed in electroanatomic mapping systems. In the tests of propagation perception, colour mapping out-performed Dot Mapping when using the rainbow colour scale, but not the blue-green colour scale where propagation perception using dots was superior (Figure 7-5).

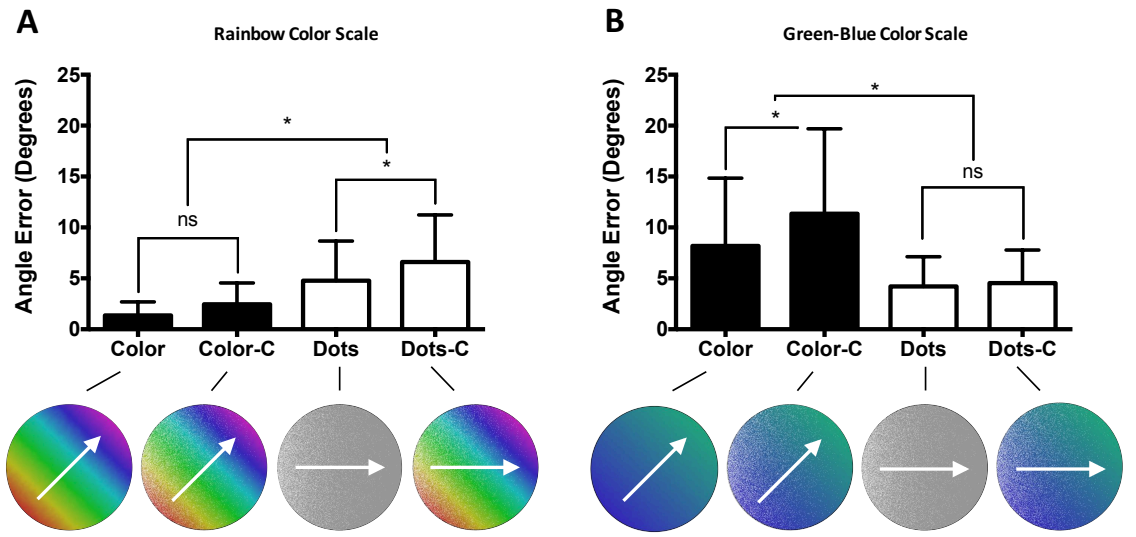

Figure 7-5. Propagation Direction Perception Accuracy

Absolute error in the perception of the angle of propagation (degrees) is shown for datasets represented with colour and dots alone (Colour, Dots) and combined (Colour-C, Dots-C). Lower panels represent examples of the test cases, with propagation represented by colour preceding towards 45˚ and propagation represented by dots preceding towards 90˚. White arrows indicate a user response with 0˚ angle error for traditional colour map perception (Colour), traditional colour map perception in the presence of dots (Colour-C), dot map perception (Dots) and dot map perception in the presence of colour (Colour-C). **A** – Colour maps drawn with rainbow colour map. **B** – Colour maps drawn with blue-green colour map. * $P < 0.05$, One-way Analysis of Variance.

There was no difference between perception accuracy of the Dot Map in the presence or absence of an additional propagation colour dataset when that dataset was represented with the blue-green colour scale. There was only a slight decrease in propagation direction perception accuracy using Dot Mapping when the rainbow colour scale was employed (4.8° vs. 6.6°, p=0.0005). Localisation of a focal source was slightly more accurate using colour mapping than Dot Mapping (Figure 7-6), but the difference in error was less than 1mm. Importantly, when dual datasets were represented using colour mapping and Dot Mapping, localisation accuracy with each modality was maintained compared to individual dataset representation. Finally, the inclusion of a localised dataset (e.g.

representing electrogram voltage or scar) had no effect on the perception of the underlying colour propagation direction.

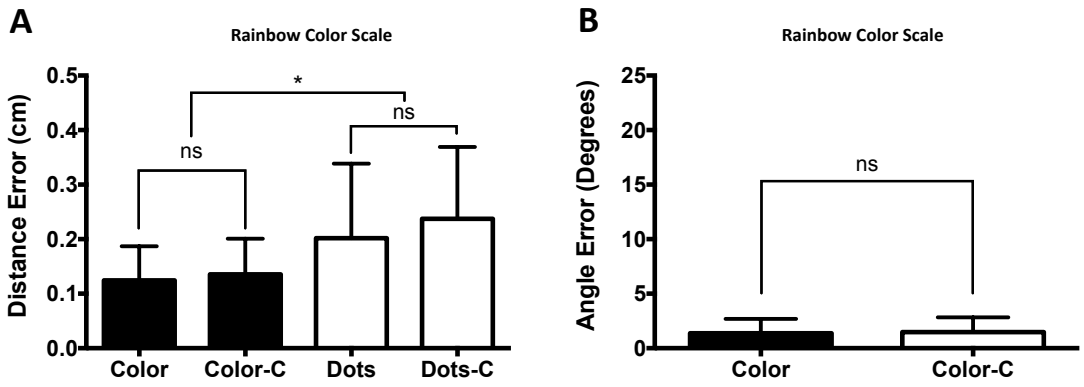

Figure 7-6. Focal Region Perception Accuracy

A – Absolute error in the perception of the location of a focal source (mm) is shown for datasets represented with colour and dots alone (Colour, Dots) and combined (Colour-C, Dots-C). **B** – Absolute error in the perception of the angle of propagation (degrees) of a dataset represented with colour (rainbow colour map) is shown for a colour dataset alone (Colour) and a colour dataset combined with a focal dataset represented with dots (Colour-C).

Clinical Cases

In the following sections, three clinical cases (two atrial and one ventricular) are used to demonstrate applications of Dot Mapping for representing various types of electrical and imaging data.

Right Atrial Electrogram Voltage with Local Activation Time

Figure 7-7 shows an example of Dot Mapping representing electro-anatomical mapping data. In (A) a traditional isochronal activation map created by point-by-point mapping of the right atrium is shown. The activation pattern is consistent with typical right atrial flutter. In (B) a voltage map is shown with a threshold of 0.5mV applied, revealing a lateral scar (purple) consistent with the previous atriotomy. In (C) the combination of voltage and activation data highlights a possible second circuit involving the region of scar in the lateral right atrium. Entrainment in this case confirmed that this was in fact the primary tachycardia circuit.

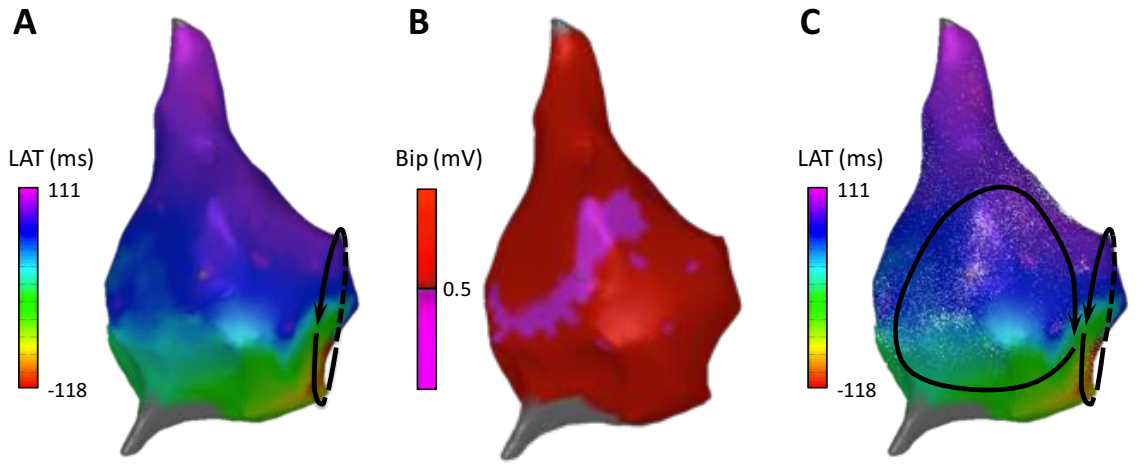

Figure 7-7. Dot Mapping to Combine Atrial Local Activation Time and Bipolar Voltage

A – Right atrial local activation time (LAT) map. **B** – Right atrial voltage map (purple = <0.5mV). **C** – Combined LAT/voltage represented with Dot Mapping. LAT, local activation time; Bip, bipolar voltage.

Left Atrial Electrogram Voltage and CMR Late Gadolinium Enhancement

Dot mapping can be used to combine datasets from multiple modalities. In Figure 7-8, a left atrial chamber model from a patient with post-ablation atrial tachycardia is shown. In (A) the EAM bipolar voltage map created in sinus rhythm demonstrated clearly delineated zones of low voltage around the pulmonary veins. In (B) the late gadolinium enhancement shell shows similar enhancement (green). The combination of both datasets in (C) using Dot Mapping allows the qualitative relationship between scar and voltage to be perceived. In particular, the density of the scar can be perceived with dot density reflecting the underlying signal intensity. Furthermore, by turning off the colour shell and displaying only the LGE data with Dot Mapping, it becomes possible to simultaneously see the 3-dimensional relationship of regions of scar on both anterior and posterior aspects of the chamber.

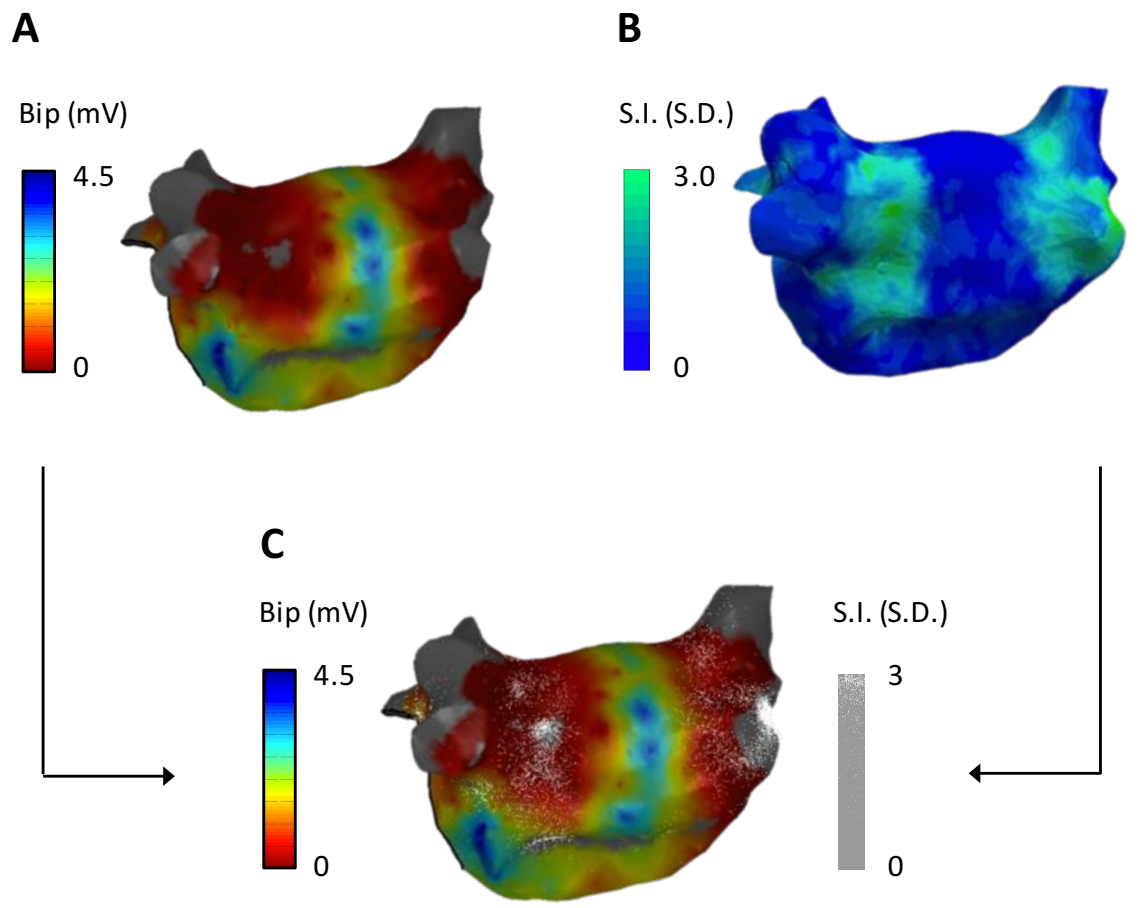

Figure 7-8. Dot Mapping to Combine Bipolar Voltage and LGE CMR

A – Left atrial bipolar voltage map. **B** – Left atrial LGE CMR shell (green = high signal intensity, >3 standard deviations above the atrial blood pool mean). **C** – Combined voltage map/LGE CMR represented with Dot Mapping, where densely spaced dots correspond to >3 standard deviations above the atrial blood pool mean (green in Figure **B**). Bip, bipolar voltage; S.I., LGE signal intensity; S.D., standard deviation.

Ventricular Endocardial and Epicardial Voltage Maps

In the atrial cases discussed above the Dot Map is drawn a small distance above the surface of the shell. Extending this approach can allow the Dot Map to be drawn some distance from the surface of the underlying colour shell allowing the technique to be applied to ventricular endocardial and epicardial mapping. In this setting, a solid grey background is used to retain contrast with any dots not overlying the solid colour chamber. In Figure 7-9, combined endocardial and epicardial voltage maps are shown using Dot Mapping. Compared to the individual colour shells (A - endocardial, B - epicardial), Dot Mapping (C) allows continued perception of the endocardial voltage map even when it is overlaid with the epicardial map. Furthermore, by manipulating the orientation of the combined Dot Map, it becomes possible to perceive the relationship between endocardial scar (red colour) and epicardial scar (dense dots).

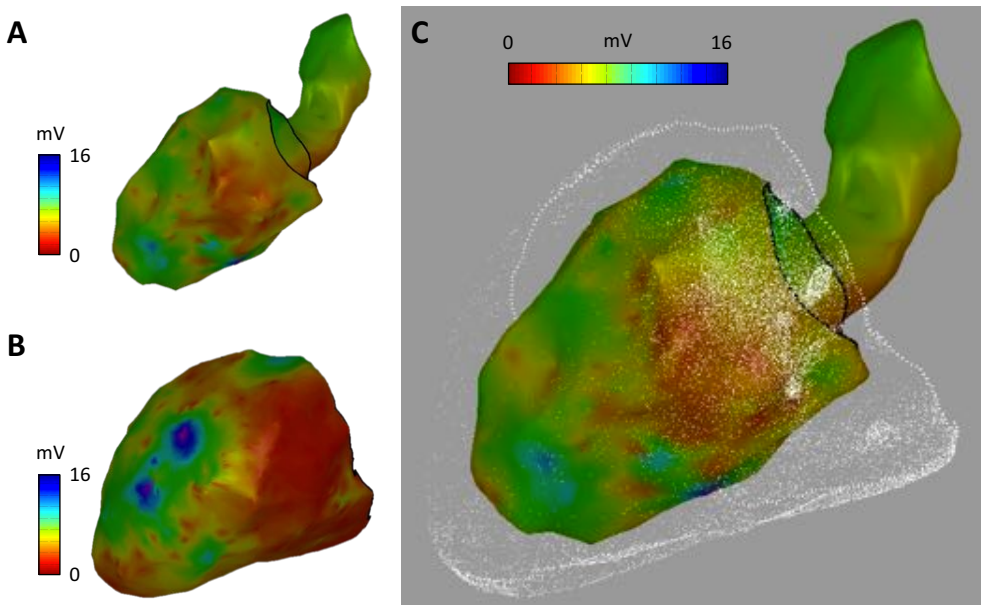

Figure 7-9. Dot Mapping to Combine Epicardial and Endocardial Voltage Maps

A – Left ventricular endocardial voltage map. **B** – Left ventricular epicardial voltage map. **C** – Combined endocardial/epicardial voltage maps represented with Dot Mapping.

Ventricular Voltage Mapping and LGE CMR

The Dot Mapping software accepts volumetric datasets in addition to surface shells. In Figure 7-10 the same case as in Figure 7-9 is displayed using Dot Mapping to display a combination of endocardial voltage and late gadolinium enhancement CMR. The pre-ablation CMR scan in this patient identified a 75% thickness subendocardial scar in the mid to basal inferolateral wall (white arrows, A). By representing the CMR data with volumetric Dot Mapping it becomes possible to perceive the relationship between the ischaemic scar and endocardial low voltage regions.

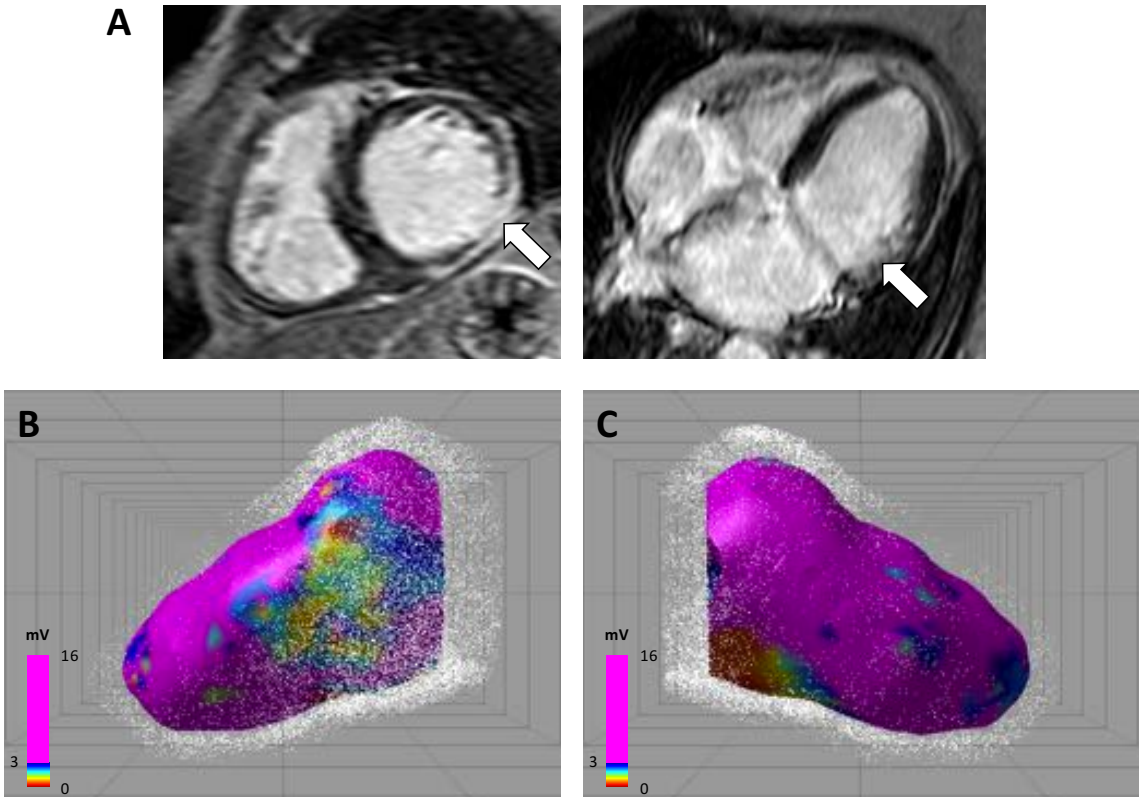

Figure 7-10. Dot Mapping to Combine Bipolar Voltage and Volumetric LGE CMR Data

A – Short and long axis LGE images shown inferolateral subendocardial enhancement (white arrows). **B**, **C** – Combined endocardial voltage map/LGE CMR represented with Dot Mapping. Purple represents any voltage >3mV.

Operator Experience

With 5 items in each domain, the maximum score per domain is 25. Dot Mapping outperformed traditional colour mapping in the "Dataset co-registration" domain (median score 24.5 vs. 10, $p<0.05$). "Diagnostic accuracy" (17 vs. 21) and "Display fidelity" (18 vs. 20) scored similarly; indicating that Dot Mapping software faithfully represents the input datasets and is therefore non-inferior to the separate display of the individual datasets.

7.4 Discussion

The main findings of this study are as follows. 1) Dot Mapping is a new technique which can display the combination of at least two independent datasets within a common spatial domain whilst minimizing loss of fidelity of either dataset; 2) Dot Mapping can be successfully applied to electrophysiological and imaging datasets in both the atrium and the ventricle; and 3) Dot Mapping can facilitate the clinical interpretation of a second

dataset in the context of a first dataset. The underlying aim of Dot Mapping is to facilitate the simultaneous display of multiple datasets in a single spatial domain.

Motivation

Three developments over the course of the last two decades have promoted the design of the Dot Mapping system. Firstly, the quantity of data available to support clinical diagnoses of arrhythmia mechanisms in electrophysiology procedures is increasing. In early ablation procedures, activation times at a limited number of electrodes were used to diagnose the arrhythmia and demonstrate successful application of RF energy (133), but in modern procedures, mapping may be achieved using catheters with tens or even hundreds of electrodes. The corresponding increase in the quantity of clinical data has led to techniques to summarise this data, reducing the number of dimensions involved and facilitating its display on 3-dimensional representations of the cardiac chamber in question (see Electroanatomic Map Display, p. 59). Secondly, with greater geometrical, position and electrical accuracy of mapping systems, the opportunity has arisen to interpret the basic electrograms in an increasing number of ways, including amplitude (voltage), timing (local activation time), complexity (fractionation) and under an increasing number of conditions (e.g. sinus rhythm, during tachyarrhythmia and during pacing). Finally, with an increased understanding of underlying arrhythmia mechanisms has come a requirement to consider combinations of these parameters simultaneously (e.g. voltage or imaging-derived scar and local activation time) in order to reach a clinical diagnosis.

A limited number of techniques have previously been used to facilitate the co-display of more than one dataset across a spatial domain. Some of these are specific to electrophysiological procedures whilst some are not. They include surface transparency, linked scenes and the Ripple Mapping system. All of these have disadvantages for the co-display of scalar fields in electrophysiology. The use of surface transparency does allow simultaneous colouring of a shell to represent two datasets, but combinations of colours result in confusion for interpretation and in practice this technique limits the number of colours that can be used in one (or both) datasets. Displaying linked scenes, with two copies of the same geometry coloured differently and either side-by-side or toggled on user selection relies on greater geometrical perception by the operator. Finally, in the Ripple Mapping system, neither of these limitations applies, but the system specifically represents electrogram voltage over time along with one other dataset, and requires the

display to be played as a moving scene, the spatial perception of which requires habituation to interpret the data.

Rationale

Considering the requirement for multiple data set display in electrophysiological procedures and the aforementioned limitations of the existing techniques, this study aimed to develop a system that could display at least two independent scalar fields across the surface of a single cardiac chamber shell. One dataset is represented using a colour field whilst the second dataset is represented using finely spaced dots of uniform colour. In doing so, perception of the datasets depends on the entirely different visual inputs of colour or quantity. That the dots are displayed as single pixels with a limited maximum density is a deliberate approach to ensure at all times that the underlying colour data set can still be perceived.

Future Work

Although the Dot Mapping software can display volumetric datasets (for example Figure 7-10), the perception of the position of the dots requires additional input. This can be in the form of automatic or manual map movement, but new technologies for three-dimensional visualisation could circumvent such input.

7.5 Conclusions

This study has developed a new technology that facilitates the display and clinical interpretation of multiple datasets related to electrophysiological procedures. In doing so Aims R1 (d*evelop a system for concomitant representation of multiple electrophysiological parameters within a 3D geometry*) and R2 (*validate that system to assess dataset display fidelity and ease of dataset integration*) have been met. Future work should assess the utility of Dot Mapping in improving clinical workflow, diagnosis and treatment of arrhythmias.

SECTION FOUR: CONCLUDING REMARKS

8 Conclusions and Future Directions

In this thesis I have explored diverse aspects of the characterisation of arrhythmia substrates. By considering arrhythmia characterisation techniques of a range of complexities from surface ECG, through intra-cardiac mapping and cardiac magnetic resonance imaging I have examined only a subset of the currently available modalities. In the course of the last 100 years, tremendous advances have been made in both the characterisation and representation of arrhythmia substrates. I provided an overview of the key technologies in use before developing new applications of existing techniques (surface ECG, intra-cardiac mapping and CMR imaging) for the characterisation of arrhythmia substrates. I further developed a system for representation of complex datasets in electroanatomic mapping systems.

The aims of this thesis (introduced in Section 1.5) were subdivided into arrhythmia characterisation and arrhythmia representation techniques. They are summarised below.

Characterisation of Arrhythmia Substrates

C1 *Examine the role of surface ECG in characterising the arrhythmia substrate in the context of idiopathic ventricular fibrillation.*

C2 *Determine the optimal point sampling density for intra-cardiac contact mapping in the diagnosis of tachycardia mechanism in a variety of atrial tachycardias.*

C3 *Develop a tool to quantify electrical remodelling in paroxysmal AF and determine if population heterogeneities are present that could be used to predict response to catheter ablation.*

C4 *Examine the role of CMR in predicting the electrical substrate in patients with a spectrum of AF disease severity.*

C5 *Assess the impact of contact force in the creation of effective linear ablation lesions.*

Representation of Arrhythmia Substrates

R1 *Develop a system for concomitant representation of multiple electrophysiological parameters within a 3D geometry.*

R2 *Validate that system to assess dataset display fidelity and ease of dataset integration.*

These aims have been met as follows. In Chapter 2, I addressed Aim C1 by exploring the role of the surface ECG in characterising the arrhythmia substrate for idiopathic ventricular fibrillation. Idiopathic ventricular fibrillation has been associated with the early repolarisation ECG phenotype, which coincidently is the same phenotype seen during hypothermia. Taking influence from previous 'augmentation' techniques for the surface ECG (e.g. exercise testing or ajmaline testing) I studied whether the application of therapeutic hypothermia to patients with early repolarisation would identify patients at high risk of idiopathic ventricular fibrillation. The results indicated that although early repolarisation was more strongly associated with idiopathic ventricular fibrillation than coronary-artery disease related ventricular fibrillation, the magnitude of early repolarisation was most increased in coronary-artery disease related ventricular fibrillation survivors. As such hypothermia is unlikely to be a useful risk stratification tool, but the exact cellular pathways responsible for these different morphological changes remain to be determined.

In Chapter 3 I addressed Aim C2 by determining the optimal point sampling density for intra-cardiac mapping in atrial tachycardias. Contact mapping forms the cornerstone of diagnosis of atrial tachycardias, but frequently local activation time mapping can be challenging. One particular challenge is identifying when sufficient data has been collected to correctly diagnose the tachycardia mechanism. By using the combination of a modelling approach to simulate arrhythmias and retrospective analysis of local activation time maps from clinical procedures I was able to identify an optimal point sampling density of ~1.7 points/cm^2. This sampling density neither guarantees a diagnosis, nor is it necessarily required for diagnosis, but it does provide a useful 'end point' for mapping: if the diagnosis is not made once this density is reached, an alternative mapping approach may better serve the patient than continued data collection.

In Chapter 4 I addressed Aim C3 by developing a pacing technique and data analysis technique in order to characterise the electrical remodelling seen in atrial fibrillation. Specifically, changes in electrogram morphology with pacing rate together with

refractory periods were calculated. By applying computer simulations to the clinical data I was able to identify that electrical remodelling (i.e. changes in action potential current densities) could explain most of the variation seen within a clinically homogeneous population of atrial fibrillation patients. This is important, because whilst appearing similar through clinical metrics, patients with atrial fibrillation can follow very different clinical courses. The technique developed in Chapter 4 may allow future disease stratification to guide clinical interventions in certain patients with atrial fibrillation.

In Chapter 5, Aim C4 was addressed by taking the techniques for electrical AF substrates characterisation developed in Chapter 4 and examining the association with structural remodelling (geometrical and fibrotic) quantified with CMR imaging. CMR imaging has previously been shown to predict clinical course and procedural outcomes in atrial fibrillation, but significant variation is seen in the literature. As in Chapter 4 with clinical outcomes, in Chapter 5 I was able to show that in patients with very similar structural remodelling, a spectrum of electrical remodelling may be seen. This may therefore explain some of the discrepancies seen in the literature with CMR and clinical outcomes in atrial fibrillation.

In Chapter 6, Aim C5 was addressed by combining the above arrhythmia characterisation modalities to provide a detailed assessment of the effects of contact force on linear ablation lesion creation. This is important for the pathogenesis of post-ablation atrial tachycardias, and by using contact mapping together with imaging and histological assessment I was able to demonstrate that low force ablation is able to achieve equally effective, transmural lesions as high force ablation. This finding could have important implications for procedural safety as well as efficacy.

Moving on from arrhythmia characterisation techniques in the next section (Chapter 7) I examined technologies for representation of arrhythmia substrates. In doing so the final two aims of the thesis (R1 and R2) were addressed. Through the above work (and other work in the field) vast quantities of electrophysiological data are created, and it is becoming a challenge to display all that information in a clinically meaningful way. I focused in this chapter on the problem of displaying multiple datasets simultaneously and developed a new software tool (Dot Mapping) to meet this aim. I further demonstrated that Dot Mapping was effectively able to co-display two datasets in both atrial and ventricular arrhythmias without any significant loss of dataset fidelity.

The work presented in this thesis leads to a number of opportunities (and challenges) for future work. For example, whilst therapeutic hypothermia did not appear to be a useful candidate marker to dichotomise between benign and malignant early repolarisation, this was not tested in a prospective analysis of clinical outcomes. Regardless, as therapeutic hypothermia becomes less frequently used in post-resuscitation care, the opportunity to study hypothermia as a clinical risk marker for malignant arrhythmias is reducing. Other physiological ECG augmentation techniques (for example J-wave relationship with R-R interval (207, 228)) may instead prove to be more useful (and practical) for the risk stratification of patients with ER phenotype.

Similarly, the data presented on intracardiac mapping should be validated through translational clinical studies. The optimal activation sampling densities identified for atrial tachycardias should be prospectively assessed against the end points of tachycardia diagnosis and procedure duration. Such a clinical study would ideally recruit patients from multiple centres and operators. Likewise the AF substrate characterisation techniques require correlation with a variety of clinical parameters including AF duration, AF burden and freedom of AF post-PVI. These are important translational studies that, if positive, would have a substantial opportunity to improve the current management of AF. In agreement with the data presented in Chapter 5, other recent work has shown a disconnect between atrial fibrosis and electrical remodelling (358). Taken together these findings suggest that imaging and electrical assessment may ultimately contribute synergistically to substrate assessment in AF.

Likewise, imaging and electrical assessment were combined in Chapter 6 in the assessment of linear ablation lesions. I demonstrated that transmural lesion formation was possible at lower contact forces than currently recommended. Further work is therefore necessary in order to reconcile this finding with the relevant clinical studies of contact force in AF ablation (347, 359). As such, the next key question to be answered is the effect of contact force on lesion continuity (as opposed to transmurality). In a more general sense, the factors that affect lesion continuity should be the focus of future studies aiming to improve the success of atrial ablation procedures.

Finally, although the arrhythmia representation work presented here demonstrates that Dot Mapping is an effective software tool for co-representation of multiple datasets, it too requires validation in the clinical setting. Collaboration with EAM manufacturers will allow Dot Mapping to be assessed either within existing EAM platforms or as a stand-

alone device alongside EAM platforms. Whether Dot Mapping could result in tangible clinical benefits (i.e. reduced procedure time or improved procedure success) is likely to be highly dependent on clinician preference.

In summary this thesis has explored the characterisation and representation of arrhythmia substrates. Established characterisation techniques have been examined and expanded, and new characterisation techniques have been developed. Tools for the representation of the data thus created have been developed. Future work should test the clinical application of the tools and technologies created within this thesis.

Acknowledgements

This thesis was only made possible through the support, encouragement and wisdom of my supervisors, Professor Mark O'Neill and Dr Kawal Rhode. I would like to thank them for their time and dedication throughout this PhD, and look forward to our collaborations in the years to come.

I have been fortunate to work alongside many talented individuals at King's College London. In particular I would like to thank Dr Steven Niederer, Dr Henry Chubb, Dr James Harrison, Dr Nick Linton, Dr John Whitaker, Dr Christian Sohns, Stephen Sinclair, Annette Dahl, Dr Matthew Wright, Dr Michael Cooklin, Dr Aldo Rinaldi, Dr Rashed Karim, Professor Jaswinder Gill, Mohammed Ikram and Professor Alberto Smith and Professor Reza Razavi.

The animal work in this thesis was performed at Aarhus University Hospital, Skejby, and I am extremely grateful for expert help from Lars Ølgaard Bloch, Niels Peter Andersen, Høgni Dam, Dr Steen Fjord Pedersen, Professor Won Yong Kim and Dr Henrik Kjærulf Jensen.

I would also like to thank St Jude Medical and Biosense Webster who provided funding for this research through unrestricted educational grants.

Last, and by no means least, I would like to thank my family. To my parents, thank you for your unconditional support and advice over the years. To my fiancée (now wife), Caroline, a profound thank you for steering me through the many challenges brought by this thesis.

SECTION FIVE: APPENDICES

Appendix A. References

1. Issa ZF, Miller JM, Zipes DP. Clinical Arrhythmology and Electrophysiology: A Companion to Braunwald's Heart Disease. 2012.

2. Merideth J, Mendez C, Mueller WJ, Moe GK. Electrical Excitability of Atrioventricular Nodal Cells. Circ. Res. 1968;23:69–85.

3. Munk A a, Adjemian R a, Zhao J, Ogbaghebriel A, Shrier A. Electrophysiological properties of morphologically distinct cells isolated from the rabbit atrioventricular node. J. Physiol. 1996;493 (Pt 3:801–18.

4. Pu J, Boyden PA. Alterations of Na+ Currents in Myocytes From Epicardial Border Zone of the Infarcted Heart : A Possible Ionic Mechanism for Reduced Excitability and Postrepolarization Refractoriness. Circ. Res. 1997;81:110–119.

5. Rodríguez JF, Heidenreich E a, Romero L, Ferrero JM, Doblare M. Post-Repolarization Refractoriness in Human Ventricular Cardiac Cells. Comput. Cardiol. 2008;35:581–584.

6. Niwano S, Yoshizawa N, Inuo K, et al. Evaluation of Post-Repolarization Refractoriness for Conduction Block in Cardiac Muscle - Studies in an Artificial Isthmus in the Canine Right Atrium. Jpn. Circ. J. 2001;65:40–45.

7. Coronel R, Janse MJ, Opthof T, Wilde A a., Taggart P. Postrepolarization refractoriness in acute ischemia and after antiarrhythmic drug administration: Action potential duration is not always an index of the refractory period. Hear. Rhythm 2012;9:977–982.

8. DiFrancesco D. The role of the funny current in pacemaker activity. Circ. Res. 2010;106:434–446.

9. Robinson RB, Yu H, Chang F, Cohen IS. Developmental change in the voltage-dependence of the pacemaker current, i(f), in rat ventricle cells. Pflugers Arch. Eur. J. Physiol. 1997;433:533–535.

10. Cranefield PF. Action Potentials, Afterpotentials and Arrhythmias. Circ. Res. 1977;41:415–423.

11. Rosen MR. A short, biased history of triggered activity. Hellenic J. Cardiol. 2009;50:170–178.

12. Wit AL, Rosen MR. Cellular Electrophysiological and Genetic Mechanisms of Cardiac Arrhythmias. In: Macfarlane PW, van Oosterom A, Pahlm O, Kligfield P, Janse MJ, Camm J, editors. Comprehensive Electrocardiology. illustrate. Springer Science & Business Media, 2010:1084–1125.

13. Patterson E, Jackman WM, Beckman KJ, et al. Spontaneous Pulmonary Vein Firing in Man: Relationship to Tachycardia-Pause Early Afterdepolarizations and Triggered Arrhythmia in Canine Pulmonary Veins In Vitro. J. Cardiovasc. Electrophysiol. 2007;18:1067–1075.

14. Chen YJ, Chen S a., Chang MS, Lin CI. Arrhythmogenic activity of cardiac muscle in pulmonary veins of the dog: Implication for the genesis of atrial fibrillation. Cardiovasc. Res. 2000;48:265–273.

15. Wit AL, Boyden PA. Triggered activity and atrial fibrillation. Hear. Rhythm 2007;4:S17–S23.

16. Attwell D, Cohen I, Eisner D, Ohba M, Ojeda C. The steady state TTX-sensitive ("window") sodium current in cardiac Purkinje fibres. Pflügers Arch. Eur. J. Physiol. 1979;379:137–142.

17. Reuter H. Properties of Two Inward Membrane Currents in the Heart. Annu. Rev. Physiol. 1979;41:413–424.

18. Jurkiewicz NK, Sanguinetti MC. Rate-dependent prolongation of cardiac action potentials by a methanesulfonanilide class III antiarrhythmic agent. Specific block of rapidly activating delayed rectifier K+ current by dofetilide. Circ. Res. 1993;72:75–83.

19. Gadsby DC, Cranefield PF. Two levels of resting potential in cardiac Purkinje fibers. J. Gen. Physiol. 1977;70:725–746.

20. Zeng J, Rudy Y. Early afterdepolarizations in cardiac myocytes: mechanism and rate dependence. Biophys. J. 1995;68:949–964.

21. Brachmann J, Scherlag BJ, Rosenshtraukh L V, Lazzara R. Bradycardia-dependent triggered activity: relevance to drug-induced multiform ventricular tachycardia. Circulation 1983;68:846–856.

22. Ter Keurs HEDJ, Boyden PA. Calcium and arrhythmogenesis. Physiol. Rev. 2007;87:457–506.

23. Fabiato A, Fabiato F. Calcium-induced release of calcium from the sarcoplasmic reticulum of skinned cells from adult human, dog, cat, rabbit, rat, and frog hearts and from fetal and new-born rat ventricles. Ann. N. Y. Acad. Sci. 1978;307:491–522.

24. Verkerk AO, Veldkamp MW, Baartscheer A, et al. Ionic Mechanism of Delayed Afterdepolarizations in Ventricular Cells Isolated From Human End-Stage Failing Hearts. Circulation 2001;104:2728–2733.

25. Colquhoun D, Neher E, Reuter H, Stevens CF. Inward current channels activated by intracellular Ca in cultured cardiac cells. Nature 1981;294:752–754.

26. Ferrier GR. Digitalis arrhythmias: role of oscillatory afterpotentials. Prog. Cardiovasc. Dis. 1977;19:459–474.

27. Mary-Rabine L, Hordof AJ, Danilo P, Malm JR, Rosen MR. Mechanisms for impulse initiation in isolated human atrial fibers. Circ. Res. 1980;47:267–77.

28. Nathan D, Beeler G. Electrophysiologic Correlates of the Inotropic Effects of Isoproterenol in Canine Myocardium. J. Mol. Cell. Cardiol. 1975;7:1–15.

29. Wit AL, Cranefield PF. Triggered and automatic activity in the canine coronary sinus. Circ. Res. 1977;41:434–45.

30. Mines GR. On dynamic equilibrium in the heart. J. Physiol. 1913;46:349–383.

31. Kléber AG, Rudy Y. Basic mechanisms of cardiac impulse propagation and associated arrhythmias. Physiol. Rev. 2004;84:431–88.

32. Matteucci MC. Sur un phénomène physiologique produit par les muscles en contraction. Ann Chim Phys 1842;6:339–342.

33. von Kölliker A, Müller H. Nachweis der negativen Schwankung des Muskelstroms am natürlich sich kontrahierenden Herzen. Verhandlungen der Phys. Gesellschaft Würzbg. 1856;6.

34. Du Bois-Reymond EH. Untersuchungen über thierische elektricität. Berlin: G. Reimer; 1848.

35. Waller AD. A demonstration of man of electromotive changes accompanying the heart's beat. J Physiol 1887;8:229–234.

36. Bayliss W, Starling E. On the Electromotive Phenomena of the Mammalian Heart. Proc R Soc L. 1891;50:211–214.

37. Einthoven W. Ueber die Form des menschlichen electrocardiogramms. Pflügers Arch Eur J Physiol 1895;60:101–123.

38. Einthoven W. Un nouveau galvanometer. Arch Neerl Sc Ex Nat 1901;6:625–633.

39. Ernstene AC, Levine SA. A comparison of records taken with the einthoven string galvanometer and the amplifier-type electrocardiograph. Am. Heart J. 1929;4:725–731.

40. Lewis T. Auricular Fibrillation: a Common Clinical Condition. Br. Med. J. 1909;2:1528.

41. Pardee HEB. An Electrocardiographic Sign of Coronary Artery Obstruction. Arch. Intern. Med. 1920;26:244–257.

42. Wolferth C, Wood F. The electrocardiographic diagnosis of coronary occlusion by the use of chest leads. Am. Heart J. 1932;183:30–35.

43. Wilson FN, Johnston FD, Macleod AG, Barker PS. Electrocardiograms that represent the potential variations of a single electrode. Am. Heart J. 1934;9:447–458.

44. American Heart Association, Cardiac Society of Great Britain. Standardization of Precordial Leads. Am Hear. J 1938;15:235–239.

45. Goldberger E. A simple, indifferent, electrocardiographic electrode of zero potential and a technique of obtaining augmented, unipolar, extremity leads. Am. Heart J. 1942;23:483–492.

46. Wilson FN, Kossmann CE, Burch GE, et al. Recommendations for Standardization of Electrocardiographic and Vectorcardiographic Leads. Circulation 1954;10:564–573.

47. Erhardt LR, Sjögren a, Wahlberg I. Single right-sided precordial lead in the diagnosis of right ventricular involvement in inferior myocardial infarction. Am. Heart J. 1976;91:571–576.

48. Zalenski RJ, Cooke D, Rydman R, Sloan EP, Murphy DG. Assessing the diagnostic value of an ECG containing leads V4R, V8, and V9: the 15-lead ECG. Ann. Emerg. Med. 1993;22:786–793.

49. Finlay DD, Nugent CD, McCullagh PJ, Black ND. Mining for diagnostic information in body surface potential maps: a comparison of feature selection techniques. Biomed. Eng. Online 2005;4:51.

50. Stevenson WG, Soejima K. Recording Techniques for Clinical Electrophysiology. J Cardiovasc Electrophysiol 2005;16:1017–1022.

51. Spach MS, Dolber PC. Relating extracellular potentials and their derivatives to anisotropic propagation at a microscopic level in human cardiac muscle. Evidence for electrical uncoupling of side-to-side fiber connections with increasing age. Circ. Res. 1986;58:356–71.

52. Stevenson WG, Khan H, Sager P, et al. Identification of reentry circuit sites during catheter mapping and radiofrequency ablation of ventricular tachycardia late after myocardial infarction. Circulation 1993;88:1647–1670.

53. Okumura Y, Watanabe I, Ashino S, et al. Electrophysiologic and anatomical characteristics of the right atrial posterior wall in patients with and without atrial flutter: analysis by intracardiac echocardiography. Circ. J. 2007;71:636–642.

54. Tada H, Oral H, Sticherling C, et al. Double potentials along the ablation line as a guide to radiofrequency ablation of typical atrial flutter. J. Am. Coll. Cardiol. 2001;38:750–755.

55. Kalman JM, VanHare GF, Olgin JE, Saxon LA, Stark SI, Lesh MD. Ablation of `Incisional' Reentrant Atrial Tachycardia Complicating Surgery for Congenital Heart Disease : Use of Entrainment to Define a Critical Isthmus of Conduction. Circulation 1996;93:502–512.

56. Waldo A, MacLean W, Karp R, Kouchoukos N, James T. Entrainment and interruption of atrial flutter with atrial pacing: studies in man following open heart surgery. Circulation 1977;56:737–745.

57. Waldo AL. From bedside to bench: Entrainment and other stories. Hear. Rhythm 2004;1:94–106.

58. Linton NWF, Wilton SB, Scherr D, et al. A practical criterion for the rapid detection of single-loop and double-loop reentry tachycardias. J Cardiovasc Electrophysiol 2013;24:544–552.

59. Henthorn RW, Okumura K, Olshansky B, Plumb VJ, Hess PG, Waldo AL. A fourth criterion for transient entrainment: the electrogram equivalent of progressive fusion. Circulation 1988;77:1003–1012.

60. Sivagangabalan G, Pouliopoulos J, Huang K, et al. Comparison of electroanatomic contact and

noncontact mapping of ventricular scar in a postinfarct ovine model with intramural needle electrode recording and histological validation. Circ. Arrhythmia Electrophysiol. 2008;1:363–369.

61. Lambiase PD, Ahmed a. K, Ciaccio EJ, et al. High-density substrate mapping in brugada syndrome: Combined role of conduction and repolarization heterogeneities in arrhythmogenesis. Circulation 2009;120:106–117.

62. Salinet Jr J, Ahmad A, Brown PD, Stafford P, Ng GA, Schlindwein FS. Three-dimensional Frequency Mapping from the Noncontact Unipolar Electrograms in Atrial Fibrillation Leicester NIHR Biomedical Research Unit in Cardiovascular Disease , Glenfield Hospital , UK Faculty of Electrical Engineering , Universiti Teknologi Malay. Comput. Cardiol. 2010:745–748.

63. Zhao J, Yao Y, Huang W, et al. Novel methods for characterization of paroxysmal atrial fibrillation in human left atria. Open Biomed. Eng. J. 2013;7:29–40.

64. Oster HS, Taccardi B, Lux RL, Ershler PR, Rudy Y. Noninvasive Electrocardiographic Imaging : Reconstruction of Epicardial Potentials, Electrograms, and Isochrones and Localization of Single and Multiple Electrocardiac Events. Circulation 1997;96:1012–1024.

65. Messinger-Rapport BJ, Rudy Y. Noninvasive recovery of epicardial potentials in a realistic heart- torso geometry. Normal sinus rhythm. Circ. Res. 1990;66:1023–1039.

66. Ramanathan C, Jia P, Ghanem R, Calvetti D, Rudy Y. Noninvasive electrocardiographic imaging (ECGI): Application of the generalized minimal residual (GMRes) method. Ann. Biomed. Eng. 2003;31:981–994.

67. Ramanathan C, Ghanem RN, Jia P, Ryu K, Rudy Y. Noninvasive electrocardiographic imaging for cardiac electrophysiology and arrhythmia. Nat. Med. 2004;10:422–428.

68. Ghanem RN, Jia P, Ramanathan C, Ryu K, Markowitz A, Rudy Y. Noninvasive electrocardiographic imaging (ECGI): Comparison to intraoperative mapping in patients. Hear. Rhythm 2005;2:339–354.

69. Zhang X, Ramachandra I, Liu Z, Muneer B, Pogwizd SM, He B. Noninvasive three-dimensional electrocardiographic imaging of ventricular activation sequence. Am. J. Physiol. Heart Circ. Physiol. 2005;289:H2724–H2732.

70. Shah AJ, Hocini M, Xhaet O, et al. Validation of novel 3-dimensional electrocardiographic mapping of atrial tachycardias by invasive mapping and ablation: A multicenter study. J. Am. Coll. Cardiol. 2013;62:889–897.

71. Wang Y, Cuculich PS, Woodard PK, Lindsay BD, Rudy Y. Focal atrial tachycardia after pulmonary vein isolation: Noninvasive mapping with electrocardiographic imaging (ECGI). Hear. Rhythm 2007;4:1081–1084.

72. Cuculich PS, Wang Y, Lindsay BD, et al. Noninvasive characterization of epicardial activation in humans with diverse atrial fibrillation patterns. Circulation 2010;122:1364–1372.

73. Wang Y, Schuessler RB, Damiano RJ, Woodard PK, Rudy Y. Noninvasive electrocardiographic imaging (ECGI) of scar-related atypical atrial flutter. Hear. Rhythm 2007;4:1565–1567.

74. Haissaguerre M, Hocini M, Shah AJ, et al. Noninvasive panoramic mapping of human atrial fibrillation mechanisms: a feasibility report. J Cardiovasc Electrophysiol 2013;24:711–7.

75. Mewton N, Liu CY, Croisille P, Bluemke D, Lima JAC. Assessment of myocardial fibrosis with cardiovascular magnetic resonance. J. Am. Coll. Cardiol. 2011;57:891–903.

76. Peters DC, Wylie J V, Hauser TH, et al. Detection of pulmonary vein and left atrial scar after catheter ablation with three-dimensional navigator-gated delayed enhancement MR imaging: initial experience. Radiology 2007;243:690–5.

77. McGann CJ, Kholmovski EG, Oakes RS, et al. New magnetic resonance imaging-based method for defining the extent of left atrial wall injury after the ablation of atrial fibrillation. J. Am. Coll. Cardiol. 2008;52:1263–71.

78. Oakes RS, Badger TJ, Kholmovski EG, et al. Detection and quantification of left atrial structural remodeling with delayed-enhancement magnetic resonance imaging in patients with atrial fibrillation. Circulation 2009;119:1758–67.

79. Judd RM, Atalay MK, Rottman GA, Zerhouni EA. Effects of myocardial water exchange on T1 enhancement during bolus administration of MR contrast agents. Magn. Reson. Med. 1995;33:215–23.

80. Croisille P, Revel D, Saeed M. Contrast agents and cardiac MR imaging of myocardial ischemia: from bench to bedside. Eur. Radiol. 2006;16:1951–63.

81. Judd RM, Lugo-Olivieri CH, Arai M, et al. Physiological basis of myocardial contrast enhancement in fast magnetic resonance images of 2-day-old reperfused canine infarcts. Circulation 1995;92:1902–10.

82. Lima JAC, Judd RM, Bazille A, Schulman SP, Atalar E, Zerhouni EA. Regional Heterogeneity of Human Myocardial Infarcts Demonstrated by Contrast-Enhanced MRI. Circulation 1995;92:1117–1125.

83. Kim RJ, Wu E, Rafael A, et al. The use of contrast-enhanced magnetic resonance imaging to identify reversible myocardial dysfunction. N. Engl. J. Med. 2000;343:1445–53.

84. Kim RJ, Fieno DS, Parrish TB, et al. Relationship of MRI Delayed Contrast Enhancement to Irreversible Injury, Infarct Age, and Contractile Function. Circulation 1999;100:1992–2002.

85. Mahrholdt H, Wagner A, Holly TA, et al. Reproducibility of chronic infarct size measurement by contrast-enhanced magnetic resonance imaging. Circulation 2002;106:2322–7.

86. Karamitsos TD, Francis JM, Myerson S, Selvanayagam JB, Neubauer S. The role of cardiovascular magnetic resonance imaging in heart failure. J. Am. Coll. Cardiol. 2009;54:1407–24.

87. Mahrholdt H, Wagner A, Judd RM, Sechtem U, Kim RJ. Delayed enhancement cardiovascular magnetic resonance assessment of non-ischaemic cardiomyopathies. Eur. Heart J. 2005;26:1461–74.

88. McCrohon JA, Moon JC, Prasad SK, et al. Differentiation of heart failure related to dilated cardiomyopathy and coronary artery disease using gadolinium-enhanced cardiovascular magnetic resonance. Circulation 2003;108:54–9.

89. Segerson NM, Daccarett M, Badger TJ, et al. Magnetic resonance imaging-confirmed ablative debulking of the left atrial posterior wall and septum for treatment of persistent atrial fibrillation: rationale and initial experience. J Cardiovasc Electrophysiol 2010;21:126–32.

90. Akoum NW, Daccarett M, Mcgann CJ, et al. Atrial fibrosis helps select the appropriate patient and strategy in catheter ablation of atrial fibrillation: a DE-MRI guided approach. J Cardiovasc Electrophysiol 2011;22:16–22.

91. Mahnkopf C, Badger TJ, Burgon NS, et al. Evaluation of the left atrial substrate in patients with lone atrial fibrillation using delayed-enhanced MRI: implications for disease progression and response to catheter ablation. Hear. Rhythm 2010;7:1475–81.

92. Knowles BR, Caulfield D, Cooklin M, et al. 3-D visualization of acute RF ablation lesions using MRI for the simultaneous determination of the patterns of necrosis and edema. IEEE Trans. Biomed. Eng. 2010;57:1467–75.

93. Calkins H, Kuck KH, Cappato R, et al. 2012 HRS/EHRA/ECAS expert consensus statement on catheter and surgical ablation of atrial fibrillation: recommendations for patient selection, procedural techniques, patient management and follow-up, definitions, endpoints, and research trial design: a re. Hear. Rhythm 2012;9:632–696.e21.

94. Verma A, Wazni OM, Marrouche NF, et al. Pre-existent left atrial scarring in patients undergoing pulmonary vein antrum isolation: an independent predictor of procedural failure. J. Am. Coll. Cardiol. 2005;45:285–92.

95. Hodgkin AL, Huxley AF. A quantitative description of membrane current and its application to conduction and excitation in nerve. J. Physiol. 1952;117:500–44.

96. Courtemanche M, Ramirez RJ, Nattel S. Ionic mechanisms underlying human atrial action potential properties: insights from a mathematical model. Am. J. Physiol. - Hear. Circ. Physiol. 1998;275:H301–H321.

97. Nygren A, Leon LJ, Giles WR. Simulations of the human atrial action potential. Philos. Transsactions R. Soc. A 2001;359:1111–1125.

98. Courtemanche M, Ramirez RJ, Nattel S. Ionic targets for drug therapy and atrial fibrillation-induced electrical remodeling: insights from a mathematical model. Cardiovasc. Res. 1999;42:477–89.

99. Fenton FH, Cherry EM. Models of cardiac cell. 2008;3:1868.

100. Maleckar MM, Greenstein JL, Giles WR, Trayanova NA. K+ current changes account for the rate dependence of the action potential in the human atrial myocyte. Am. J. Physiol. - Hear. Circ. Physiol. 2009;297:H1398–410.

101. Koivumäki JT, Korhonen T, Tavi P. Impact of sarcoplasmic reticulum calcium release on calcium dynamics and action potential morphology in human atrial myocytes: a computational study. McCulloch AD, editor. PLoS Comput. Biol. 2011;7:e1001067.

102. Grandi E, Pandit S V, Voigt N, et al. Human atrial action potential and Ca2+ model: sinus rhythm and chronic atrial fibrillation. Circ. Res. 2011;109:1055–66.

103. Vigmond EJ, Weber dos Santos R, Prassl a J, Deo M, Plank G. Solvers for the cardiac bidomain equations. Prog. Biophys. Mol. Biol. 2008;96:3–18.

104. Niwano S, Wakisaka Y, Niwano H, et al. Prognostic significance of frequent premature ventricular contractions originating from the ventricular outflow tract in patients with normal left ventricular function. Heart 2009;95:1230–1237.

105. Yarlagadda RK, Iwai S, Stein KM, et al. Reversal of cardiomyopathy in patients with repetitive monomorphic ventricular ectopy originating from the right ventricular outflow tract. Circulation 2005;112:1092–1097.

106. Hasdemir C, Ulucan C, Yavuzgil O, et al. Tachycardia-induced cardiomyopathy in patients with idiopathic ventricular arrhythmias: The incidence, clinical and electrophysiologic characteristics, and the predictors. J Cardiovasc Electrophysiol 2011;22:663–668.

107. Takemoto M, Yoshimura H, Ohba Y, et al. Radiofrequency catheter ablation of premature ventricular complexes from right ventricular outflow tract improves left ventricular dilation and clinical status in patients without structural heart disease. J. Am. Coll. Cardiol. 2005;45:1259–1265.

108. Baman TS, Lange DC, Ilg KJ, et al. Relationship between burden of premature ventricular complexes and left ventricular function. Hear. Rhythm 2010;7:865–869.

109. Prystowsky EN, Padanilam BJ, Joshi S, Fogel RI. Ventricular arrhythmias in the absence of structural heart disease. J. Am. Coll. Cardiol. 2012;59:1733–1744.

110. Splawski I, Shen J, Timothy KW, et al. Spectrum of mutations in long-QT syndrome genes. KVLQT1, HERG, SCN5A, KCNE1, and KCNE2. Circulation 2000;102:1178–1185.

111. Schwartz PJ, Moss AJ, Vincent GM, Crampton RS. Diagnostic Criteria for the Long QT Syndrome. Circulation 1993;88:782–784.

112. Brugada P, Brugada J. Right bundle branch block, persistent ST segment elevation and sudden cardiac death: a distinct clinical and electrocardiographic syndrome. A multicenter report. J. Am. Coll. Cardiol. 1992;20:1391–1396.

113. Antzelevitch C, Brugada P, Borggrefe M, et al. Brugada Syndrome: Report of the second consensus conference. Circulation 2005;111:659–670.

114. Bezzina C, Veldkamp MW, van Den Berg MP, et al. A single Na(+) channel mutation causing both long-QT and Brugada syndromes. Circ. Res. 1999;85:1206–1213.

115. Grant AO, Carboni MP, Neplioueva V, et al. Long QT syndrome, Brugada syndrome, and conduction system disease are linked to a single sodium channel mutation. J. Clin. Invest. 2002;110:1201–1209.

116. Priori SG, Napolitano C, Gasparini M, et al. Natural history of Brugada syndrome: Insights for risk stratification and management. Circulation 2002;105:1342–1347.

117. Haïssaguerre M, Shoda M, Jaïs P, et al. Mapping and ablation of idiopathic ventricular fibrillation. Circulation 2002;106:962–967.

118. Haïssaguerre M, Derval N, Sacher F, et al. Sudden cardiac arrest associated with early repolarization. N Engl J Med 2008;358:2016–2023.

119. Tikkanen JT, Junttila MJ, Anttonen O, et al. Early repolarization: electrocardiographic phenotypes associated with favorable long-term outcome. Circulation 2011;123:2666–73.

120. Mizusawa Y, Bezzina CR. Early repolarization pattern: Its ECG characteristics, arrhythmogeneity and heritability. J. Interv. Card. Electrophysiol. 2014;39:185–192.

121. Saoudi N, Cosío F, Waldo AL, et al. A classification of atrial flutter and regular atrial tachycardia according to electrophysiological mechanisms and anatomical bases: A statement from a joint expert group from the working group of arrhythmias of the European society of cardiology and the . Eur. Heart J. 2001;22:1162–1182.

122. Jaïs P, Matsuo S, Knecht S, et al. A deductive mapping strategy for atrial tachycardia following atrial fibrillation ablation: Importance of localized reentry. J Cardiovasc Electrophysiol 2009;20:480–491.

123. Porter MJ, Morton JB, Denman R, et al. Influence of age and gender on the mechanism of supraventricular tachycardia. Hear. Rhythm 2004;1:393–396.

124. Rosso R, Kistler PM. Focal atrial tachycardia. Heart 2010;96:181–185.

125. Kistler PM, Roberts-Thomson KC, Haqqani HM, et al. P-Wave Morphology in Focal Atrial Tachycardia. Development of an Algorithm to Predict the Anatomic Site of Origin. J. Am. Coll. Cardiol. 2006;48:1010–1017.

126. Tang CW, Scheinman MM, Vanhare GF, et al. Use of P-Wave Configuration During Atrial Tachycardia To Predict Site of Origin. J. Am. Coll. Cardiol. 1995;26:1315–1324.

127. Blomstrom-Lundqvist C. ACC/AHA/ESC Guidelines for the Management of Patients With Supraventricular Arrhythmias*--Executive Summary: A Report of the American College of Cardiology/American Heart Association Task Force on Practice Guidelines and the European Society of Cardiology. 2003.

128. Poty H, Saoudi N, Haissaguerre M, Daou a, Clementy J, Letac B. Radiofrequency catheter ablation of atrial tachycardias. Am. Heart J. 1996;131:481–489.

129. Medi C, Kalman JM, Haqqani H, et al. Tachycardia-Mediated Cardiomyopathy Secondary to Focal Atrial Tachycardia. Long-Term Outcome After Catheter Ablation. J. Am. Coll. Cardiol. 2009;53:1791–1797.

130. Shah DC, Jaïs P, Haïssaguerre M, et al. Three-dimensional Mapping of the Common Atrial Flutter Circuit in the Right Atrium. Circulation 1997;96:3904–3912.

131. Kalman JM, Olgin JE, Saxon L a, Lee RJ, Scheinman MM, Lesh MD. Electrocardiographic and electrophysiologic characterization of atypical atrial flutter in man: use of activation and entrainment mapping and implications for catheter ablation. J Cardiovasc Electrophysiol 1997;8:121–144.

132. Feld GK, Fleck RP, Chen P, et al. Radiofrequency Catheter Ablation for the Treatment of Human Type 1 Atrial Flutter: Identification of a Critical Zone in the Reentrant Circuit by Endocardial Mapping Techniques. Circulation 1992;86:1233–1240.

133. Cosio FG, Lopez-Gil M, Goicolea a., Arribas F, Barroso JL. Radiofrequency ablation of the inferior vena cava-tricuspid valve isthmus in common atrial flutter. Am. J. Cardiol. 1993;71:705–709.

134. Brembilla-Perrot B, Huttin O, Manenti V, et al. Sex-related differences in peri- and post-ablation clinical data for patients with atrial flutter. Int. J. Cardiol. 2013;168:1951–1954.

135. Moubarak G, Pavin D, Laviolle B, et al. Incidence of atrial fibrillation during very long-term follow-up after radiofrequency ablation of typical atrial flutter. Arch. Cardiovasc. Dis. 2009;102:525–532.

136. Stevenson IH, Kistler PM, Spence SJ, et al. Scar-related right atrial macroreentrant tachycardia in patients without prior atrial surgery: Electroanatomic characterization and ablation outcome. Hear. Rhythm 2005;2:594–601.

137. Heck PM, Rosso R, Kistler PM. The challenging face of focal atrial tachycardia in the post AF ablation Era. J Cardiovasc Electrophysiol 2011;22:832–838.

138. Natale a, Newby KH, Pisanó E, et al. Prospective randomized comparison of antiarrhythmic therapy versus first-line radiofrequency ablation in patients with atrial flutter. J. Am. Coll. Cardiol. 2000;35:1898–1904.

139. Spector P, Reynolds MR, Calkins H, et al. Meta-analysis of ablation of atrial flutter and supraventricular tachycardia. Am. J. Cardiol. 2009;104:671–677.

140. Morady F. Catheter Ablation of Supraventricular: State of the Art. J Cardiovasc Electrophysiol 2004;15:124–39.

141. Haïssaguerre M, Hocini M, Sanders P, et al. Localized sources maintaining atrial fibrillation organized by prior ablation. Circulation 2006;113:616–25.

142. Fuster V, Rydén LE, Cannom DS, et al. 2011 ACCF/AHA/HRS focused updates incorporated into the ACC/AHA/ESC 2006 Guidelines for the management of patients with atrial fibrillation: a report of the American College of Cardiology Foundation/American Heart Association Task Force on Practice Guidel. J. Am. Coll. Cardiol. 2011;57:e101–98.

143. The National Collaborating Centre for Chronic Conditions. Atrial fibrillation: National Clinical Guideline For Management in Primary and Secondary Care. The Royal College of Physicians; 2006.

144. Ruigómez A, Johansson S, Wallander MA, Rodríguez LAG. Incidence of chronic atrial fibrillation in general practice and its treatment pattern. J. Clin. Epidemiol. 2002;55:358–63.

145. Stewart S, Murphy NF, Murphy N, Walker A, McGuire A, McMurray JJ V. Cost of an emerging epidemic: an economic analysis of atrial fibrillation in the UK. Heart 2004;90:286–92.

146. Friberg J, Scharling H, Gadsbøll N, Jensen GB. Sex-specific increase in the prevalence of atrial fibrillation (The Copenhagen City Heart Study). Am. J. Cardiol. 2003;92:1419–23.

147. Atrial Fibrillation Investigators. Risk factors for stroke and efficacy of antithrombotic therapy in atrial fibrillation. Analysis of pooled data from five randomized controlled trials. Arch. Intern. Med. 1994;154:1449–57.

148. Watson T, Shantsila E, Lip GYH. Mechanisms of thrombogenesis in atrial fibrillation: Virchow's triad revisited. Lancet 2009;373:155–66.

149. Wang TJ, Massaro JM, Levy D, et al. A risk score for predicting stroke or death in individuals with new-onset atrial fibrillation in the community: the Framingham Heart Study. JAMA 2003;290:1049–56.

150. Scherf D, Romano FJ, Terranova R. Experimental studies on auricular flutter and auricular fibrillation. Am. Heart J. 1948;36:241–51.

151. Jaïs P, Haïssaguerre M, Shah DC, et al. A focal source of atrial fibrillation treated by discrete radiofrequency ablation. Circulation 1997;95:572–6.

152. Haïssaguerre M, Jaïs P, Shah DC, et al. Spontaneous initiation of atrial fibrillation by ectopic beats originating in the pulmonary veins. N. Engl. J. Med. 1998;339:659–66.

153. Moe GK, Abildskov JA. Atrial fibrillation as a self-sustaining arrhythmia independent of focal discharge. Am. Heart J. 1959;58:59–70.

154. Mandapati R, Skanes A, Chen J, Berenfeld O, Jalife J. Stable microreentrant sources as a mechanism of atrial fibrillation in the isolated sheep heart. Circulation 2000;101:194–199.

155. Sanders P, Berenfeld O, Hocini M, et al. Spectral analysis identifies sites of high-frequency activity maintaining atrial fibrillation in humans. Circulation 2005;112:789–97.

156. Ramanna H, Hauer RN, Wittkampf FH, et al. Identification of the substrate of atrial vulnerability in patients with idiopathic atrial fibrillation. Circulation 2000;101:995–1001.

157. Nakao K, Seto S, Ueyama C, et al. Extended distribution of prolonged and fractionated right atrial electrograms predicts development of chronic atrial fibrillation in patients with idiopathic paroxysmal atrial fibrillation. J Cardiovasc Electrophysiol 2002;13:996–1002.

158. Akyürek O, Sayin T, Dinçer I, Karaoguz R, Güldal M, Oral D. Lengthening of intraatrial conduction time in atrial fibrillation and its relation with early recurrence of atrial fibrillation. Jpn. Heart J. 2001;42:575–84.

159. Everett TH, Wilson EE, Hulley GS, Olgin JE. Transmural characteristics of atrial fibrillation in canine models of structural and electrical atrial remodeling assessed by simultaneous epicardial and endocardial mapping. Hear. Rhythm 2010;7:506–17.

160. Everett TH, Wilson EE, Verheule S, Guerra JM, Foreman S, Olgin JE. Structural atrial remodeling alters the substrate and spatiotemporal organization of atrial fibrillation: a comparison in canine models of structural and electrical atrial remodeling. Am. J. Physiol. - Hear. Circ. Physiol. 2006;291:H2911–23.

161. Narayan SM, Krummen DE, Shivkumar K, Clopton P, Rappel W-J, Miller JM. Treatment of atrial fibrillation by the ablation of localized sources: CONFIRM (Conventional Ablation for Atrial Fibrillation With or Without Focal Impulse and Rotor Modulation) trial. J. Am. Coll. Cardiol. 2012;60:628–36.

162. Allessie MA, de Groot NMS, Houben RPM, et al. Electropathological substrate of long-standing persistent atrial fibrillation in patients with structural heart disease: longitudinal dissociation. Circ. Arrhythmia Electrophysiol. 2010;3:606–15.

163. Atienza F, Calvo D, Almendral J, et al. Mechanisms of fractionated electrograms formation in the posterior left atrium during paroxysmal atrial fibrillation in humans. J. Am. Coll. Cardiol. 2011;57:1081–92.

164. Wijffels MC, Kirchhof CJ, Dorland R, Allessie MA. Atrial fibrillation begets atrial fibrillation. A study in awake chronically instrumented goats. Circulation 1995;92:1954–68.

165. Morillo CA, Klein GJ, Jones DL, Guiraudon CM. Chronic rapid atrial pacing. Structural, functional, and electrophysiological characteristics of a new model of sustained atrial fibrillation. Circulation

1995;91:1588–95.

166. Franz MR, Karasik PL, Li C, Moubarak J, Chavez M. Electrical remodeling of the human atrium: similar effects in patients with chronic atrial fibrillation and atrial flutter. J. Am. Coll. Cardiol. 1997;30:1785–92.

167. Yu W-C, Lee SH, Tai C-T, et al. Reversal of atrial electrical remodeling following cardioversion of long-standing atrial fibrillation in man. Cardiovasc. Res. 1999;42:470–6.

168. Healey JS, Israel CW, Connolly SJ, et al. Relevance of electrical remodeling in human atrial fibrillation: results of the Asymptomatic Atrial Fibrillation and Stroke Evaluation in Pacemaker Patients and the Atrial Fibrillation Reduction Atrial Pacing Trial mechanisms of atrial fibrillation study. Circ. Arrhythmia Electrophysiol. 2012;5:626–31.

169. Li D, Fareh S, Leung TK, Nattel S. Promotion of atrial fibrillation by heart failure in dogs: atrial remodeling of a different sort. Circulation 1999;100:87–95.

170. Allessie MA, Ausma J, Schotten U. Electrical, contractile and structural remodeling during atrial fibrillation. Cardiovasc. Res. 2002;54:230–46.

171. Burstein B, Nattel S. Atrial fibrosis: mechanisms and clinical relevance in atrial fibrillation. J. Am. Coll. Cardiol. 2008;51:802–9.

172. Boldt A, Wetzel U, Lauschke J, et al. Fibrosis in left atrial tissue of patients with atrial fibrillation with and without underlying mitral valve disease. Heart 2004;90:400–5.

173. Frustaci A, Chimenti C, Bellocci F, Morgante E, Russo MA, Maseri A. Histological substrate of atrial biopsies in patients with lone atrial fibrillation. Circulation 1997;96:1180–4.

174. Burstein B, Qi X-Y, Yeh Y-H, Calderone A, Nattel S. Atrial cardiomyocyte tachycardia alters cardiac fibroblast function: a novel consideration in atrial remodeling. Cardiovasc. Res. 2007;76:442–52.

175. Shinagawa K, Shi Y-F, Tardif J-C, Leung T-K, Nattel S. Dynamic nature of atrial fibrillation substrate during development and reversal of heart failure in dogs. Circulation 2002;105:2672–8.

176. Corley SD, Epstein AE, DiMarco JP, et al. Relationships between sinus rhythm, treatment, and survival in the Atrial Fibrillation Follow-Up Investigation of Rhythm Management (AFFIRM) Study. Circulation 2004;109:1509–13.

177. Verma A. Atrial-fibrillation ablation should be considered first-line therapy for some patients. Curr. Opin. Cardiol. 2008;23:1–8.

178. Chen S-A, Hsieh MH, Tai C-T, et al. Initiation of atrial fibrillation by ectopic beats originating from the pulmonary veins: electrophysiological characteristics, pharmacological responses, and effects of radiofrequency ablation. Circulation 1999;100:1879–86.

179. Cappato R, Negroni S, Pecora D, et al. Prospective assessment of late conduction recurrence across radiofrequency lesions producing electrical disconnection at the pulmonary vein ostium in patients with atrial fibrillation. Circulation 2003;108:1599–604.

180. Nanthakumar K, Plumb VJ, Epstein AE, Veenhuyzen GD, Link D, Kay GN. Resumption of electrical conduction in previously isolated pulmonary veins: rationale for a different strategy? Circulation 2004;109:1226–9.

181. Arujuna A, Karim R, Caulfield D, et al. Acute pulmonary vein isolation is achieved by a combination of reversible and irreversible atrial injury after catheter ablation: evidence from magnetic resonance imaging. Circ. Arrhythmia Electrophysiol. 2012;5:691–700.

182. Lin W-S, Tai C-T, Hsieh M-H, et al. Catheter ablation of paroxysmal atrial fibrillation initiated by non-pulmonary vein ectopy. Circulation 2003;107:3176–83.

183. Hocini M, Sanders P, Jaïs P, et al. Techniques for curative treatment of atrial fibrillation. J Cardiovasc Electrophysiol 2004;15:1467–71.

184. Nademanee K, McKenzie J, Kosar E, et al. A new approach for catheter ablation of atrial fibrillation: mapping of the electrophysiologic substrate. J. Am. Coll. Cardiol. 2004;43:2044–53.

185. Verma A, Jiang C, Betts TR, et al. Approaches to Catheter Ablation for Persistent Atrial Fibrillation. N. Engl. J. Med. 2015;372:1812–1822.

186. Lippmann G. Relation entre les phénomènes électriques et capillaires. Ann. Chim. Phys. 1875;5:494–549.

187. Ader M. Sur un Nouvel Appareil enregistreur pour cables sous-marins. Comptes rendus l'Académie des Sci. 1897;124:1440–1442.

188. Rune E. Measuring instrument of the recording type. 1951.

189. Shannon C. Communication in the Presence of Noise. Proc Inst Radio Eng. 1949;37:10–21.

190. Nyquist H. Certain topics in telegraph transmission theory. Trans IEEE 1928;47:617–644.

191. Knecht S, Skali H, O'Neill MD, et al. Computed tomography-fluoroscopy overlay evaluation during catheter ablation of left atrial arrhythmia. Europace 2008;10:931–938.

192. Ben-Haim S a, Osadchy D, Schuster I, Gepstein L, Hayam G, Josephson ME. Nonfluoroscopic, in vivo navigation and mapping technology. Nat. Med. 1996;2:1393–1395.

193. Jiang Y, Farina D, Bar-Tal M, Dössel O. An impedance-based catheter positioning system for cardiac mapping and navigation. IEEE Trans. Biomed. Eng. 2009;56:1963–1970.

194. Wittkampf FH, Wever EF, Derksen R, et al. LocaLisa: new technique for real-time 3-dimensional localization of regular intracardiac electrodes. Circulation 1999;99:1312–1317.

195. Heist EK, Perna F, Chalhoub F, et al. Comparison of Electroanatomical Mapping Systems: Accuracy in Left Atrial Mapping. Pacing Clin Electrophysiol 2013;00:1–6.

196. Linton NWF, Koa-Wing M, Francis DP, et al. Cardiac ripple mapping: a novel three-dimensional visualization method for use with electroanatomic mapping of cardiac arrhythmias. Hear. Rhythm 2009;6:1754–62.

197. Jamil-Copley S, Linton N, Koa-Wing M, et al. Application of ripple mapping with an electroanatomic mapping system for diagnosis of atrial tachycardias. J Cardiovasc Electrophysiol 2013;24:1361–9.

198. Tikkanen JT, Anttonen O, Junttila MJ, et al. Long-term outcome associated with early repolarization on electrocardiography. N. Engl. J. Med. 2009;361:2529–37.

199. Sinner MF, Reinhard W, Müller M, et al. Association of early repolarization pattern on ECG with risk of cardiac and all-cause mortality: A population-based prospective cohort study (MONICA/KORA). PLoS Med. 2010;7.

200. Wasserburger RH, Alt WJ. The normal RS-T segment elevation variant. Am. J. Cardiol. 1961;8:184–92.

201. Klatsky AL, Oehm R, Cooper R a., Udaltsova N, Armstrong MA. The early repolarization normal variant electrocardiogram: Correlates and consequences. Am. J. Med. 2003;115:171–177.

202. Rosso R, Kogan E, Belhassen B, et al. J-point elevation in survivors of primary ventricular fibrillation and matched control subjects: incidence and clinical significance. J. Am. Coll. Cardiol. 2008;52:1231–8.

203. Haruta D, Matsuo K, Tsuneto A, et al. Incidence and prognostic value of early repolarization pattern in the 12-lead electrocardiogram. Circulation 2011;123:2931–2937.

204. Patel RB, Ng J, Reddy V, et al. Early repolarization associated with ventricular arrhythmias in patients with chronic coronary artery disease. Circ. Arrhythmia Electrophysiol. 2010;3:489–495.

205. Naruse Y, Tada H, Harimura Y, et al. Early repolarization is an independent predictor of occurrences of ventricular fibrillation in the very early phase of acute myocardial infarction. Circ. Arrhythmia Electrophysiol. 2012;5:506–513.

206. Rudic B, Veltmann C, Kuntz E, et al. Early repolarization pattern is associated with ventricular fibrillation in patients with acute myocardial infarction. Hear. Rhythm 2012;9:1295–1300.

207. Aizawa Y, Sato A, Watanabe H, et al. Dynamicity of the J-wave in idiopathic ventricular fibrillation with a special reference to pause-dependent augmentation of the J-wave. J. Am. Coll. Cardiol. 2012;59:1948–1953.

208. Antzelevitch C. Genetic, Molecular and Cellular Mechanisms Underlying the J Wave Syndromes. Circ. J. 2012;76:1054–1065.

209. Yan G-X, Antzelevitch C. Cellular Basis for the Electrocardiographic J Wave. Circulation 1996;93:372–379.

210. Tomaszewski W. Changements electrocardiographiques observes chez un homme mort de froid. Arch Mal Coer 1938;31:525.

211. Osborn J. Experimental Hypothermia: Respiratory and Blood pH Changes in Relation to Cardiac Function. Am. J. Physiol. 1953;175:389–398.

212. Ortega-Carnicer J, Benezet J, Calderón-Jiménez P, Yanes-Martín J. Hypothermia-induced Brugada-like electrocardiogram pattern. J. Electrocardiol. 2008;41:690–692.

213. Anon. Survivors of Out-of-Hospital Cardiac Arrest With Apparently Normal Heart: Need for definition and standardized clinical evaluation. Consensus Statement of the Joint Steering Committees of the Unexplained Cardiac Arrest Registry of Europe and of the Idiopa. Circulation 1997;95:265–272.

214. Rosso R, Glikson E, Belhassen B, et al. Distinguishing “benign” from “malignant early repolarization”: the value of the ST-segment morphology. Hear. Rhythm 2012;9:225–9.

215. Bastiaenen R, Hedley PL, Christiansen M, Behr ER. Therapeutic hypothermia and ventricular fibrillation storm in early repolarization syndrome. Hear. Rhythm 2010;7:832–4.

216. Rolfast CL, Lust EJ, de Cock CC. Electrocardiographic changes in therapeutic hypothermia. Crit. Care 2012;16:R100.

217. Vassallo SU, Delaney K a, Hoffman RS, Slater W, Goldfrank LR. A prospective evaluation of the electrocardiographic manifestations of hypothermia. Acad. Emerg. Med. 1999;6:1121–1126.

218. Mattu A, Brady WJ, Perron AD. Electrocardiographic manifestations of hypothermia. Am. J. Emerg. Med. 2002;20:314–326.

219. Lellouche N, Sacher F, Jorrot P, et al. Sudden cardiac arrest: ECG repolarization after resuscitation. J Cardiovasc Electrophysiol 2011;22:131–136.

220. Li R a, Leppo M, Miki T, Seino S, Marbán E. Molecular Basis of Electrocardiographic ST-Segment Elevation Ronald A. Li, Michelle Leppo, Takashi Miki, Susumu Seino and Eduardo Marbán Circulation Research 2000, 87:837-839. Animals 2000:837–839.

221. Yan GX, Antzelevitch C. Cellular basis for the Brugada syndrome and other mechanisms of arrhythmogenesis associated with ST-segment elevation. Circulation 1999;100:1660–1666.

222. Bastiaenen R, Behr ER. Letter by Bastiaenen and Behr regarding article, “Early repolarization: electrocardiographic phenotypes associated with favorable long-term outcome”. Circulation

2011;124:e899; author reply e900.

223. Piktel JS, Jeyaraj D, Said TH, Rosenbaum DS, Wilson LD. Enhanced dispersion of repolarization explains increased arrhythmogenesis in severe versus therapeutic hypothermia. Circ. Arrhythmia Electrophysiol. 2011;4:79–86.

224. Hsieh YC, Lin SF, Lin TC, Ting CT, Wu TJ. Therapeutic hypothermia (30 degrees C) enhances arrhythmogenic substrates, including spatially discordant alternans, and facilitates pacing-induced ventricular fibrillation in isolated rabbit hearts. Circ.J. 2009;73:2214–2222.

225. Long-Tian LI, Li-Bin Z, Yan-Li SI, et al. Effects of acute cooling / rewarming on membrane potential and K + currents in rat ventricular myocytes. Acta Physiol. Sin. 2008;60:311–319.

226. Piktel J, Rosenbaum D, Wilson L. Mild Hypothermia Decreases Arrhythmia Susceptibility in a Canine Model of Global Myocardial Ischemia. Crit Care Med 2012;13:1133–1145.

227. Gurabi Z, Koncz I, Patocskai B, Nesterenko V V, Antzelevitch C. Cellular mechanism underlying hypothermia-induced ventricular tachycardia/ventricular fibrillation in the setting of early repolarization and the protective effect of quinidine, cilostazol, and milrinone. Circ. Arrhythmia Electrophysiol. 2014;7:134–42.

228. Aizawa Y, Sato M, Kitazawa H, et al. Tachycardia-dependent augmentation of “notched J waves” in a general patient population without ventricular fibrillation or cardiac arrest: Not a repolarization but a depolarization abnormality? Hear. Rhythm 2015;12:376–383.

229. Takeuchi T, Tomita T, Yoshie K, Hioki H, Oguchi Y. Electrocardiographic J waves are associated with right ventricular morphology and function: evaluation by cardiac magnetic resonance imaging. Hear. Vessel. 2015;30:98–107.

230. Ghosh S, Cooper DH, Vijayakumar R, et al. Early repolarization associated with sudden death: Insights from noninvasive electrocardiographic imaging. Hear. Rhythm 2010;7:534–537.

231. Mahida S, Derval N, Sacher F, et al. History and clinical significance of early repolarization syndrome. Hear. Rhythm 2015;12:242–249.

232. Yan GX, Joshi A, Guo D, et al. Phase 2 reentry as a trigger to initiate ventricular fibrillation during early acute myocardial ischemia. Circulation 2004;110:1036–1041.

233. Greenfield JC, Rembert JC. The prevalence of lateral lead early repolarization in otherwise normal electrocardiograms as a function of age. J. Electrocardiol. 2013;46:334–335.

234. Koruth JS, Heist EK, Danik S, et al. Accuracy of left atrial anatomical maps acquired with a multielectrode catheter during catheter ablation for atrial fibrillation. J. Interv. Card. Electrophysiol. 2011;32:45–51.

235. Gepstein L, Hayam G, Ben-Haim SA. A Novel Method for Nonfluoroscopic Catheter-Based Electroanatomical Mapping of the Heart: In Vitro and In Vivo Accuracy Results. Circulation 1997;95:1611–1622.

236. Smeets JL, Ben-Haim S a, Rodriguez LM, Timmermans C, Wellens HJ. New method for nonfluoroscopic endocardial mapping in humans: accuracy assessment and first clinical results. Circulation 1998;97:2426–2432.

237. Del Carpio Munoz F, Buescher TL, Asirvatham SJ. Three-dimensional mapping of cardiac arrhythmias: what do the colors really mean? Circ. Arrhythmia Electrophysiol. 2010;3:e6–11.

238. Nakagawa H, Ikeda A, Sharma T, Lazzara R, Jackman WM. Rapid high resolution electroanatomical mapping: evaluation of a new system in a canine atrial linear lesion model. Circ. Arrhythmia Electrophysiol. 2012;5:417–24.

239. Faustino MM, Capuzzi D, Agricola T, et al. A new approach for catheter ablation of atrial tachycardia following atrial fibrillation ablation. J. Cardiovasc. Med. 2012;13:795–804.

240. Patel AM, d'Avila A, Neuzil P, et al. Atrial tachycardia after ablation of persistent atrial fibrillation: identification of the critical isthmus with a combination of multielectrode activation mapping and targeted entrainment mapping. Circ. Arrhythmia Electrophysiol. 2008;1:14–22.

241. Sanders P, Hocini M, Jaïs P, et al. Characterization of focal atrial tachycardia using high-density mapping. J. Am. Coll. Cardiol. 2005;46:2088–99.

242. Nygren a., Fiset C, Firek L, et al. Mathematical Model of an Adult Human Atrial Cell : The Role of K+ Currents in Repolarization. Circ. Res. 1998;82:63–81.

243. Biosense Webster. Carto® 3 MEM Software. Available at: https://www.biosensewebster.com/carto3.php#main.

244. Boston Scientific. Rhythmia™ Mapping System. Available at: http://www.bostonscientific.com/redefining-ep/rhythmia-mapping-system.html.

245. Teh AW, Kistler PM, Lee G, et al. Electroanatomic remodeling of the left atrium in paroxysmal and persistent atrial fibrillation patients without structural heart disease. J Cardiovasc Electrophysiol 2012;23:232–8.

246. Teh AW, Kistler PM, Lee G, et al. The relationship between complex fractionated electrograms and atrial low-voltage zones during atrial fibrillation and paced rhythm. Europace 2011;13:1709–16.

247. Jadidi AS, Cochet H, Shah AJ, et al. Inverse relationship between fractionated electrograms and atrial fibrosis in persistent atrial fibrillation: combined magnetic resonance imaging and high-density mapping. J. Am. Coll. Cardiol. 2013;62:802–12.

248. Wetzel U. A stepwise mapping approach for localization and ablation of ectopic right, left, and septal atrial foci using electroanatomic mapping. Eur. Heart J. 2002;23:1387–1393.

249. Narayan SM, Baykaner T, Clopton P, et al. Ablation of Rotor and Focal Sources Reduces Late Recurrence of Atrial Fibrillation Compared With Trigger Ablation Alone: Extended Follow-Up of the CONFIRM Trial (Conventional Ablation for Atrial Fibrillation With or Without Focal Impulse and Rotor Modulat. J. Am. Coll. Cardiol. 2014;63:1761–8.

250. Calvo CJ, Deo M, Zlochiver S, Millet J, Berenfeld O. Attraction of rotors to the pulmonary veins in paroxysmal atrial fibrillation: a modeling study. Biophys. J. 2014;106:1811–21.

251. Courtemanche M. Complex spiral wave dynamics in a spatially distributed ionic model of cardiac electrical activity. Chaos 1996;6:579–600.

252. Jones AR, Krummen DE, Narayan SM. Non-invasive identification of stable rotors and focal sources for human atrial fibrillation: mechanistic classification of atrial fibrillation from the electrocardiogram. Europace 2013;15:7–9.

253. Mandapati R, Buch E, Tung R, et al. Electrophysiological characterization of "rotor" sites identified by focal impulse and rotor modulation mapping. In: Heart Rhythm Scientific Sessions., 2014:S28.

254. Narayan SM, Krummen DE, Rappel W-J. Clinical mapping approach to diagnose electrical rotors and focal impulse sources for human atrial fibrillation. J Cardiovasc Electrophysiol 2012;23:447–54.

255. Nattel S, Burstein B, Dobrev D. Atrial remodeling and atrial fibrillation: mechanisms and implications. Circ. Arrhythmia Electrophysiol. 2008;1:62–73.

256. Chang SL, Tai CT, Lin YJ, et al. Biatrial substrate properties in patients with atrial fibrillation. J Cardiovasc Electrophysiol 2007;18:1134–1139.

257. Ganesan AN, Shipp NJ, Brooks AG, et al. Long-term outcomes of catheter ablation of atrial fibrillation: a systematic review and meta-analysis. J. Am. Heart Assoc. 2013;2.

258. Kerr CR, Humphries KH, Talajic M, et al. Progression to chronic atrial fibrillation after the initial diagnosis of paroxysmal atrial fibrillation: Results from the Canadian Registry of Atrial Fibrillation. Am. Heart J. 2005;149:489–496.

259. Kohári M, Zado E, Marchlinski FE, Callans DJ, Han Y. Left atrial volume best predicts recurrence after catheter ablation in patients with persistent and longstanding persistent atrial fibrillation. Pacing Clin Electrophysiol 2014;37:422–429.

260. Zhuang J, Wang Y, Tangi K, et al. Association between left atrial size and atrial fibrillation recurrence after single circumferential pulmonary vein isolation: a systematic review and meta-analysis of observational studies. Europace 2012;14:638–645.

261. Kiliszek M, Miazek N, Peller M, et al. Influence of left atrial size on the outcome of pulmonary vein isolation in patients with atrial fibrillation. Kardiol Pol 2014;72:1135–1140.

262. Costa FM, Ferreira AM, Oliveira S, et al. Left atrial volume is more important than the type of atrial fibrillation in predicting the long-term success of catheter ablation. Int. J. Cardiol. 2015;184:56–61.

263. Takahashi Y, Takahashi A, Kuwahara T, et al. Clinical characteristics of patients with persistent atrial fibrillation successfully treated by left atrial ablation. Circ. Arrhythmia Electrophysiol. 2010;3:465–71.

264. Lo L-W, Tai C-T, Lin Y-J, et al. Progressive remodeling of the atrial substrate - a novel finding from consecutive voltage mapping in patients with recurrence of atrial fibrillation after catheter ablation. J Cardiovasc Electrophysiol 2007;18:258–65.

265. Krogh-Madsen T, Abbott GW, Christini DJ. Effects of electrical and structural remodeling on atrial fibrillation maintenance: a simulation study. PLoS Comput. Biol. 2012;8:e1002390.

266. Marcus GM, Yang Y, Varosy PD, et al. Regional left atrial voltage in patients with atrial fibrillation. Hear. Rhythm 2007;4:138–44.

267. Saghy L, Callans DJ, Garcia F, et al. Is there a relationship between complex fractionated atrial electrograms recorded during atrial fibrillation and sinus rhythm fractionation? Hear. Rhythm 2011;9:181–188.

268. Teh AW, Kistler PM, Lee G, et al. Long-term effects of catheter ablation for lone atrial fibrillation: progressive atrial electroanatomic substrate remodeling despite successful ablation. Hear. Rhythm 2012;9:473–80.

269. Saumarez RC, Camm a J, Panagos a, et al. Ventricular fibrillation in hypertrophic cardiomyopathy is associated with increased fractionation of paced right ventricular electrograms. Circulation 1992;86:467–74.

270. Saumarez RC, Slade AK, Grace AA, Sadoul N, Camm AJ, McKenna WJ. The significance of paced electrogram fractionation in hypertrophic cardiomyopathy. A prospective study. Circulation 1995;91:2762–2768.

271. Saumarez RC. Sudden Death in Noncoronary Heart Disease Is Associated With Delayed Paced Ventricular Activation. Circulation 2003:2595–2601.

272. Saumarez RC, Pytkowski M, Sterlinski M, et al. Delayed paced ventricular activation in the long QT syndrome is associated with ventricular fibrillation. Hear. Rhythm 2006;3:771–8.

273. Spach MS, Dolber PC, Heidlage JF. Influence of the passive anisotropic properties on directional differences in propagation following modification of the sodium conductance in human atrial muscle. A model of reentry based on anisotropic discontinuous propagation. Circ. Res. 1988;62:811–832.

274. Spach MS, Miller WT, Geselowitz DB, Barr RC, Kootsey JM, Johnson E a. The discontinuous nature of propagation in normal canine cardiac muscle. Evidence for recurrent discontinuities of intracellular resistance that affect the membrane currents. Circ. Res. 1981;48:39–54.

275. Spach MS, Miller WT, Dolber PC, Kootsey JM, Sommer JR, Mosher CE. The functional role of structural complexities in the propagation of depolarization in the atrium of the dog. Cardiac conduction disturbances due to discontinuities of effective axial resistivity. Circ. Res. 1982;50:175–191.

276. Turner I, Huang CL-H, Saumarez RC. Numerical simulation of paced electrogram fractionation: relating clinical observations to changes in fibrosis and action potential duration. J Cardiovasc Electrophysiol 2005;16:151–61.

277. Jacquemet V, Henriquez CS. Genesis of complex fractionated atrial electrograms in zones of slow conduction: a computer model of microfibrosis. Hear. Rhythm 2009;6:803–10.

278. Pytkowski M, Jankowska A, Maciag A, et al. Paroxysmal atrial fibrillation is associated with increased intra-atrial conduction delay. Europace 2008;10:1415–20.

279. Tai C-T, Chen S-A, Tzeng JW, et al. Prolonged fractionation of paced right atrial electrograms in patients with atrial flutter and fibrillation. J. Am. Coll. Cardiol. 2001;37:1651–7.

280. Saumarez RC, Heald S, Gill J, et al. Primary ventricular fibrillation is associated with increased paced right ventricular electrogram fractionation. Circulation 1995;92:2565–2571.

281. Mitchell J, Mount D, Papadimitriou C. The discrete geodesic problem. SIAM J. Comput. 1987;16:647–668.

282. Surazhsky V, Surazhsky T, Kirsanov D, Gortler SJ, Hoppe H. Fast exact and approximate geodesics on meshes. In: ACM Trans. Graph.Vol 24., 2005:553.

283. Konings KT, Kirchhof CJ, Smeets JL, Wellens HJ, Penn OC, Allessie MA. High-density mapping of electrically induced atrial fibrillation in humans. Circulation 1994;89:1665–1680.

284. Medi C, Kalman JM, Spence SJ, et al. Atrial electrical and structural changes associated with longstanding hypertension in humans: Implications for the substrate for atrial fibrillation. J Cardiovasc Electrophysiol 2011;22:1317–1324.

285. Gaspo R, Bosch RF, Bou-Abboud E, Nattel S. Tachycardia-Induced Changes in Na+ Current in a Chronic Dog Model of Atrial Fibrillation. Circ. Res. 1997;81:1045–1052.

286. Koller BS, Karasik PE, Solomon a J, Franz MR. Prolongation of conduction time during premature stimulation in the human atrium is primarily caused by local stimulus response latency. Eur. Heart J. 1995;16:1920–4.

287. Kistler PM, Sanders P, Fynn SP, et al. Electrophysiologic and electroanatomic changes in the human atrium associated with age. J. Am. Coll. Cardiol. 2004;44:109–16.

288. Krummen DE, Bayer JD, Ho J, et al. Mechanisms of human atrial fibrillation initiation: clinical and computational studies of repolarization restitution and activation latency. Circ. Arrhythmia Electrophysiol. 2012;5:1149–59.

289. Lalani GG, Schricker A, Gibson M, Rostamian A, Krummen DE, Narayan SM. Atrial conduction slows immediately before the onset of human atrial fibrillation: a bi-atrial contact mapping study of transitions to atrial fibrillation. J. Am. Coll. Cardiol. 2012;59:595–606.

290. Sanders P, Morton JB, Davidson NC, et al. Electrical remodeling of the atria in congestive heart failure: Electrophysiological and electroanatomic mapping in humans. Circulation 2003;108:1461–1468.

291. Katritsis D, Sougiannis D, Giazitzoglou E, Kourlaba G, Ellenbogen KA. Regional endocardial left atrial voltage and electrogram fractionation in patients with atrial fibrillation. J Cardiovasc Electrophysiol

2008;19:1254–8.

292. Tanigawa M, Fukatani M, Konoe A, Isomoto S, Kadena M, Hashiba K. Prolonged and fractionated right atrial electrograms during sinus rhythm in patients with paroxysmal atrial fibrillation and sick sinus node syndrome. J. Am. Coll. Cardiol. 1991;17:403–408.

293. Jadidi AS, Duncan E, Miyazaki S, et al. Functional nature of electrogram fractionation demonstrated by left atrial high-density mapping. Circ. Arrhythmia Electrophysiol. 2012;5:32–42.

294. Roberts-Thomson KC, Kistler PM, Sanders P, et al. Fractionated atrial electrograms during sinus rhythm: relationship to age, voltage, and conduction velocity. Hear. Rhythm 2009;6:587–91.

295. Corradi D, Callegari S, Benussi S, et al. Myocyte changes and their left atrial distribution in patients with chronic atrial fibrillation related to mitral valve disease. Hum. Pathol. 2005;36:1080–1089.

296. Platonov P, Mitrofanova L, Orshanskaya V, Ho SY. Structural Abnormalities in Atrial Walls Are Associated With Presence and Persistency of Atrial Fibrillation But Not With Age. J. Am. Coll. Cardiol. 2011;58:2225–2232.

297. Wells JL, Karp RB, Kouchoukos NT, MacLean W a, James TN, Waldo AL. Characterization of atrial fibrillation in man: studies following open heart surgery. Pacing Clin Electrophysiol 1978;1:426–438.

298. Konings KT, Smeets JL, Penn OC, Wellens HJ-J, Allessie MA. Configuration of unipolar atrial electrograms during electrically induced atrial fibrillation in humans. Circulation 1997;95:1231–1241.

299. Yamabe H, Morihisa K, Tanaka Y, et al. Mechanisms of the maintenance of atrial fibrillation: Role of the complex fractionated atrial electrogram assessed by noncontact mapping. Hear. Rhythm 2009;6:1120–1128.

300. Yamabe H, Morihisa K, Koyama J, Enomoto K, Kanazawa H, Ogawa H. Analysis of the mechanisms initiating random wave propagation at the onset of atrial fibrillation using noncontact mapping: Role of complex fractionated electrogram region. Hear. Rhythm 2011;8:1228–1236.

301. Spach MS, Heidlage JF, Dolber PC, Barr RC. Mechanism of origin of conduction disturbances in aging human atrial bundles: experimental and model study. Hear. Rhythm 2007;4:175–85.

302. Kadish A, Balke CW, Levine JF, Moore EN, Spear JF. Activation patterns in healed experimental myocardial infarction. Circ. Res. 1989;65:1698–1709.

303. Herweg B, Chang F, Chandra P, Danilo P, Rosen MR. Cardiac memory in canine atrium : identification and implications. Circulation 2001;103:455–461.

304. Sanchez C, Pueyo E. Cardiac memory in human atria and relation to arrhythmogenesis. Comput. Cardiol. 2009;36:81–84.

305. Kumagai K, Nakashima H, Urata H, Gondo N, Arakawa K, Saku K. Effects of angiotensin II type 1 receptor antagonist on electrical and structural remodeling in atrial fibrillation. J. Am. Coll. Cardiol. 2003;41:2197–2204.

306. Verheule S, Wilson E, Everett T, Shanbhag S, Golden C, Olgin J. Alterations in atrial electrophysiology and tissue structure in a canine model of chronic atrial dilatation due to mitral regurgitation. Circulation 2003;107:2615–2622.

307. Hassink RJ, Aretz HT, Ruskin JN, Keane D. Morphology of atrial myocardium in human pulmonary veins: A postmortem analysis in patients with and without atrial fibrillation. J. Am. Coll. Cardiol. 2003;42:1108–1114.

308. Xu J, Cui G, Esmailian F, et al. Atrial extracellular matrix remodeling and the maintenance of atrial fibrillation. Circulation 2004;109:363–8.

309. Henry WL, Morganroth J, Pearlman a S, et al. Relation between echocardiographically determined left atrial size and atrial fibrillation. Circulation 1976;53:273–279.

310. Davies MJ, Pomerance a. Pathology of atrial fibrillation in man. Br. Heart J. 1972;34:520–525.

311. Probst P, Goldschlager N, Selzer a. Left atrial size and atrial fibrillation in mitral stenosis. Factors influencing their relationship. Circulation 1973;48:1282–1287.

312. Keren G, Etzion T, Sherez J, et al. Atrial fibrillation and atrial enlargement in patients with mitral stenosis. Am. Heart J. 1987;114:1146–1155.

313. Sohrabi S, Hope M, Saloner D, et al. Left Atrial Transverse Diameter on Computed Tomography Angiography Can Accurately Diagnose Left Atrial Enlargement in Patients With Atrial Fibrillation. J Thorac Imaging 2015;00:1–4.

314. Jahnke C, Fischer J, Gerds-li J, et al. Serial monitoring of reverse left-atrial remodeling after pulmonary vein isolation in patients with atrial fibrillation: A magnetic resonance imaging study. Int. J. Cardiol. 2011;153:42–46.

315. Khurram IM, Beinart R, Zipunnikov V, et al. Magnetic resonance image intensity ratio, a normalized measure to enable interpatient comparability of left atrial fibrosis. Hear. Rhythm 2014;11:85–92.

316. Dewire J, Khurram IM, Pashakhanloo F, et al. The Association of Pre-Existing Left Atrial Fibrosis with Clinical Variables in Patients Referred for Catheter Ablation of Atrial Fibrillation. Clin. Med. Insights Cardiol. 2014;8:11–15.

317. Bisbal F, Guiu E, Calvo N, et al. Left Atrial Sphericity: A New Method to Assess Atrial Remodeling. Impact on the Outcome of Atrial Fibrillation Ablation. J Cardiovasc Electrophysiol 2013.

318. Bisbal F, Guiu E, Cabanas P, et al. Reversal of spherical remodelling of the left atrium after pulmonary vein isolation: incidence and predictors. Europace 2014;16:840–847.

319. Kapa S, Desjardins B, Callans DJ, Marchlinski FE, Dixit S. Contact Electroanatomic Mapping Derived Voltage Criteria for Characterizing Left Atrial Scar in Patients Undergoing Ablation for Atrial Fibrillation. J Cardiovasc Electrophysiol 2014:1–9.

320. Malcolme-Lawes LC, Juli C, Karim R, et al. Automated analysis of atrial late gadolinium enhancement imaging that correlates with endocardial voltage and clinical outcomes: A 2-center study. Hear. Rhythm 2013;10:1184–1189.

321. Spragg DD, Khurram I, Zimmerman SL, et al. Initial experience with magnetic resonance imaging of atrial scar and co-registration with electroanatomic voltage mapping during atrial fibrillation: Success and limitations. Hear. Rhythm 2012:1–7.

322. Sramko M, Peichl P, Wichterle D, et al. Clinical value of assessment of left atrial late gadolinium enhancement in patients undergoing ablation of atrial fibrillation. Int. J. Cardiol. 2015;179:351–357.

323. Yushkevich P a., Piven J, Hazlett HC, et al. User-guided 3D active contour segmentation of anatomical structures: Significantly improved efficiency and reliability. Neuroimage 2006;31:1116–1128.

324. Karim R, Ma Y, Jang M, et al. Surface flattening of the human left atrium and proof-of-concept clinical applications. Comput. Med. Imaging Graph. 2014;38:251–66.

325. Jahnke C, Fischer J, Gonzalez Mirelis J, et al. Cardiovascular magnetic resonance imaging for accurate sizing of the left atrium: predictability of pulmonary vein isolation success in patients with atrial fibrillation. Jounrla Magn. Reson. Imaging 2011;463:455–463.

326. Hwang SH, Oh Y-W, Lee DI, Shim J, Park S-W, Kim Y-H. Evaluation of quantification methods for left arial late gadolinium enhancement based on different references in patients with atrial fibrillation. Int. J. Cardiovasc. Imaging 2014;ePub ahead.

327. Park JH, Pak H-N, Choi EJ, et al. The relationship between endocardial voltage and regional volume in electroanatomical remodeled left atria in patients with atrial fibrillation: comparison of three-dimensional computed tomographic images and voltage mapping. J Cardiovasc Electrophysiol 2009;20:1349–56.

328. Neuberger HR, Schotten U, Blaauw Y, et al. Chronic atrial dilation, electrical remodeling, and atrial fibrillation in the goat. J. Am. Coll. Cardiol. 2006;47:644–653.

329. Neuberger H-R, Schotten U, Verheule S, et al. Development of a substrate of atrial fibrillation during chronic atrioventricular block in the goat. Circulation 2005;111:30–7.

330. McGann C, Akoum N, Patel A, et al. Atrial fibrillation ablation outcome is predicted by left atrial remodeling on MRI. Circ. Arrhythmia Electrophysiol. 2014;7:23–30.

331. Thiagalingam A, D'Avila A, Foley L, et al. Importance of catheter contact force during irrigated radiofrequency ablation: evaluation in a porcine ex vivo model using a force-sensing catheter. J Cardiovasc Electrophysiol 2010;21:806–11.

332. Shah DC, Lambert H, Nakagawa H, Langenkamp A, Aeby N, Leo G. Area under the real-time contact force curve (force-time integral) predicts radiofrequency lesion size in an in vitro contractile model. J Cardiovasc Electrophysiol 2010;21:1038–43.

333. Stagegaard N, Petersen HH, Chen X, Svendsen JH. Indication of the radiofrequency induced lesion size by pre-ablation measurements. Europace 2005;7:525–534.

334. Eick OJ, Wittkampf FH, Bronneberg T, Schumacher B. The LETR-Principle: a novel method to assess electrode-tissue contact in radiofrequency ablation. J Cardiovasc Electrophysiol 1998;9:1180–5.

335. Weiss C, Antz M, Eick O, Eshagzaiy K, Meinertz T, Willems S. Radiofrequency catheter ablation using cooled electrodes: impact of irrigation flow rate and catheter contact pressure on lesion dimensions. Pacing Clin Electrophysiol 2002;25:463–469.

336. Yokoyama K, Nakagawa H, Shah DC, et al. Novel contact force sensor incorporated in irrigated radiofrequency ablation catheter predicts lesion size and incidence of steam pop and thrombus. Circ. Arrhythmia Electrophysiol. 2008;1:354–62.

337. Zheng X, Walcott GP, Hall JA, et al. Electrode impedance: an indicator of electrode-tissue contact and lesion dimensions during linear ablation. J. Interv. Card. Electrophysiol. 2000;4:645–54.

338. Ikeda A, Nakagawa H, Lambert H, et al. Relationship Between Catheter Contact Force and Radiofrequency Lesion Size and Incidence of Steam Pop in the Beating Canine Heart: Electrogram Amplitude, Impedance, and Electrode Temperature Are Poor Predictors of Electrode-Tissue Contact Force and Lesion. Circ. Arrhythmia Electrophysiol. 2014;7:1174–1180.

339. Quallich SG, Van Heel M, Iaizzo P a. Optimal contact forces to minimize cardiac perforations before, during, and/or after radiofrequency or cryoablation. Hear. Rhythm 2015;12:291–296.

340. Perna F, Heist EK, Danik SB, Barrett CD, Ruskin JN, Mansour M. Assessment of Catheter Tip Contact Force Resulting in Cardiac Perforation in Swine Atria Using Force Sensing Technology. Circ. Arrhythmia Electrophysiol. 2011;4:218–224.

341. Shah DC, Lambert H, Langenkamp A, et al. Catheter tip force required for mechanical perforation of porcine cardiac chambers. Europace 2011;13:277–83.

342. Thiagalingam A, D'Avila A, McPherson C, Malchano Z, Ruskin JN, Reddy VY. Impedance and temperature monitoring improve the safety of closed-loop irrigated-tip radiofrequency ablation. J Cardiovasc Electrophysiol 2007;18:318–25.

343. Harrison JL, Jensen HK, Peel S a, et al. Cardiac magnetic resonance and electroanatomical mapping of acute and chronic atrial ablation injury: a histological validation study. Eur. Heart J. 2014:1–10.

344. Kennedy DJ, Vetteth S, Periyasamy SM, et al. Central role for the cardiotonic steroid marinobufagenin in the pathogenesis of experimental uremic cardiomyopathy. Hypertension 2006;47:488–95.

345. Natale A, Reddy VY, Monir G, et al. Paroxysmal AF Catheter Ablation With a Contact Force Sensing Catheter: Results of the Prospective, Multicenter SMART-AF Trial. J. Am. Coll. Cardiol. 2014;64:647–56.

346. Reddy VY, Shah DC, Kautzner J, et al. The relationship between contact force and clinical outcome during radiofrequency catheter ablation of atrial fibrillation in the TOCCATA study. Hear. Rhythm 2012;9:1789–95.

347. Neuzil P, Reddy VY, Kautzner J, et al. Electrical reconnection after pulmonary vein isolation is contingent on contact force during initial treatment: results from the EFFICAS I study. Circ. Arrhythmia Electrophysiol. 2013;6:327–33.

348. Jarman JWE, Panikker S, Das M, et al. Relationship between contact force sensing technology and medium term outcome of atrial fibrillation ablation: A multicenter study of 600 patients. J Cardiovasc Electrophysiol 2014;ePub Ahead.

349. Wang K, Ho SY, Gibson DG, Anderson RH. Architecture of atrial musculature in humans. Br. Heart J. 1995;73:559–65.

350. Bishop MJ, Rajani R, Plank G, et al. Three-dimensional atrial wall thickness maps to inform catheter ablation procedures for atrial fibrillation. Europace 2015.

351. Harrison J, Bloch LØ, Grondal AK, et al. Magnetic resonance imaging of acute atrial ablation injury – a histological validation study. Europace 2012;14:iv4.

352. Okumura Y, Johnson SB, Bunch TJ, Henz BD, O'Brien CJ, Packer DL. A systematical analysis of in vivo contact forces on virtual catheter tip/tissue surface contact during cardiac mapping and intervention. J Cardiovasc Electrophysiol 2008;19:632–40.

353. Platonov PG, Ivanov V, Ho SY, Mitrofanova L. Left atrial posterior wall thickness in patients with and without atrial fibrillation: Data from 298 consecutive autopsies. J. Cardiovasc. Electrophysiol. 2008;19:689–692.

354. Nakagawa H, Ikeda A, Shah DC, et al. Role of Contact Force in Esophageal Injury During Left Atrial Radiofrequency Ablation. Hear. Rhythm 2008;5:S317.

355. Meng J, Peters DC, Hsing JM, et al. Late gadolinium enhancement of the esophagus is common on cardiac MR several months after pulmonary vein isolation: preliminary observations. Pacing Clin Electrophysiol 2010;33:661–666.

356. Tung P, Hong SN, Chan RH, et al. Aortic injury is common following pulmonary vein isolation. Hear. Rhythm 2013;10:653–658.

357. Harrison JL, Sohns C, Linton NW, et al. Repeat Left Atrial Catheter Ablation: Cardiac Magnetic Resonance Prediction of Endocardial Voltage and Gaps in Ablation Lesion Sets. Circ. Arrhythmia Electrophysiol. 2015.

358. Kirubakaran S, Chowdhury R a., Hall MCS, Patel PM, Garratt CJ, Peters NS. Fractionation of electrograms is caused by colocalized conduction block and connexin disorganization in the absence of fibrosis as AF becomes persistent in the goat model. Hear. Rhythm 2015;12:397–408.

359. Kuck K-H, Reddy VY, Schmidt B, et al. A novel radiofrequency ablation catheter using contact force sensing: TOCCATA study. Hear. Rhythm 2012;9:18–23.

360. Hadamard J. Lectures on Cauchy's problem in linear partial differential equations. Physiology 1923:334.

Appendix B. Computer Code

B.1 Dual-loop Re-entry Used in Chapter 3

File B-1 pentaray.par

```
num_gregions    =   2

gregion[0].num_IDs  =   6
gregion[0].name     =   "viable"
gregion[0].g_il =    0.28
gregion[0].g_it =    0.026
gregion[0].g_el         =       0.22
gregion[0].g_et         =       0.13
gregion[0].ID[0]    =   1
gregion[0].ID[1]    =   721
gregion[0].ID[2]    =   722
gregion[0].ID[3]    =   723
gregion[0].ID[4]    =   724
gregion[0].ID[5]    =   725

gregion[1].num_IDs  =   1
gregion[1].name     =   "scar"
gregion[1].g_il =    0
gregion[1].g_it =    0
gregion[1].g_el     =   0.22
gregion[1].g_et     =   0.13
gregion[1].ID[0]    =   921

# Equation

bidomain    = 0
dt      = 20    #microseconds
parab_solve     = 1
#ellip_solve     = 1
vm_per_phie     = 4

# I/O
spacedt     = 1
timedt      = 1 #milliseconds; ie 1 = 1kHz
gridout_i   = 2
#gridout_e  = 2

# Local Activation Times

num_LATs          = 2
lats[0].all       = 0
lats[0].measurand = 0
lats[0].method    = 1
lats[0].threshold = -20    #mV?
lats[0].ID        = "latfile"

lats[1].all   = 1
lats[1].measurand = 0
lats[1].method    = 1
lats[1].threshold = -20
lats[1].ID        = "latfile-all"

# Tag regions

numtagreg = 7

tagreg[0].name = tissue
tagreg[0].type = 2
tagreg[0].tag = 1
tagreg[0].p0[0] = 0
tagreg[0].p0[1] = 0
tagreg[0].p0[2] = 0
tagreg[0].p1[0] = 40000
tagreg[0].p1[1] = 40000
tagreg[0].p1[2] = 0

tagreg[1].name = scar
tagreg[1].type = 1
tagreg[1].tag = 921
```

```
tagreg[1].p0[0] = 20000
tagreg[1].p0[1] = 20000
tagreg[1].p0[2] = 0
tagreg[1].radius = 7500

tagreg[2].name = stim
tagreg[2].type = 2
tagreg[2].tag = 721
tagreg[2].p0[0] = 19000
tagreg[2].p0[1] = 20000
tagreg[2].p0[2] = 0
tagreg[2].p1[0] = 21000
tagreg[2].p1[1] = 21000
tagreg[2].p1[2] = 0

tagreg[3].name = ground
tagreg[3].type = 2
tagreg[3].tag = 722
tagreg[3].p0[0] = 19000
tagreg[3].p0[1] = 19000
tagreg[3].p0[2] = 0
tagreg[3].p1[0] = 21000
tagreg[3].p1[1] = 20000
tagreg[3].p1[2] = 0

tagreg[4].name = isthmus
tagreg[4].type = 2
tagreg[4].tag = 723
tagreg[4].p0[0] = 19000
tagreg[4].p0[1] = 0
tagreg[4].p0[2] = 0
tagreg[4].p1[0] = 21000
tagreg[4].p1[1] = 40000
tagreg[4].p1[2] = 0

tagreg[5].name = stimrentry
tagreg[5].type = 2
tagreg[5].tag = 724
tagreg[5].p0[0] = 19000
tagreg[5].p0[1] = 26500
tagreg[5].p0[2] = 0
tagreg[5].p1[0] = 21000
tagreg[5].p1[1] = 27500
tagreg[5].p1[2] = 0

tagreg[6].name = groundrentry
tagreg[6].type = 2
tagreg[6].tag = 725
tagreg[6].p0[0] = 19000
tagreg[6].p0[1] = 25500
tagreg[6].p0[2] = 0
tagreg[6].p1[0] = 21000
tagreg[6].p1[1] = 26500
tagreg[6].p1[2] = 0
```

File B-2. run_carp.sh

```
export NPROC=12
export LAUNCHER=mpirun

echo Set the file references ...
SIM_NAME=square
MESH_NAME=./geometry/square.1
PARAM_FILE=./pentaray.par
CARPEXECUTABLE=/home/localstn10/src/carp-dcse-pt/CARP/carp.petsc.pt

echo Set up the stimulus ...
VOLTAGE=1000
STIMDURATION=1

echo Define which runs to execute ...
DOBLOCKSTIM=0 # Initial stimulation
DOROTORINIT=0 # Rotor initialization
DOFINALRRUN=0 # Extra rotor run at end
DOLATMAPRUN=1 # Get the activation time

echo Set up the stimulus ...
STIM=2
GROUND=3
```

```
STIM_ROTOR=5
GROUND_ROTOR=6

echo Set up the t ends ...
t_1=1  # length of first stimulus
t_2=275 # length of first run
t_3=1  # length of second stimulus
t_4=10000 # length of second run
t_5=2500 # length of the final run for getting activation times, must be greater than TCL
t_6=370 # duration of the lat map run

DURATION_ACT=$t_1
DURATION_RUN=$(($DURATION_ACT+$t_2))
DURATION_ROTOR_ACT=$(($DURATION_RUN+$t_3))
DURATION_ROTOR_RUN=$(($DURATION_ROTOR_ACT+$t_4))
DURATION_ROTOR_RUN_FINAL=$(($DURATION_ROTOR_RUN+$t_5))
DURATION_LAT_MAP=$(($DURATION_ROTOR_ACT+t_6))

echo Set up the cell model ...
CELLMODEL=NYGREN

echo Set up the output directories ...
OUTPUTDIR_ACTIVATION=./${SIM_NAME}_act
OUTPUTDIR_RESTART=./${SIM_NAME}_run
OUTPUTDIR_ROTOR_ACTIVATION=./${SIM_NAME}_rotor_act
OUTPUTDIR_ROTOR_RESTART=./${SIM_NAME}_rotor_run
OUTPUTDIR_ROTOR_RESTART_FINAL=./${SIM_NAME}_rotor_final
OUTPUTDIR_LAT_MAP=./${SIM_NAME}_latmap

if [ $DOBLOCKSTIM == 1 ]
  then
    echo Launch CARP for the activation run ...
    $LAUNCHER -np $NPROC ${CARPEXECUTABLE} \
    +F $PARAM_FILE \
    -meshname $MESH_NAME \
    -simID $OUTPUTDIR_ACTIVATION \
    -num_tsav 2 \
    -tsav[0] $DURATION_ACT.0 \
    -tend $DURATION_ACT \
    -num_stim 1 \
    -stimulus[0].stimtype 3 \
    -stimulus[0].strength 0 \
    -stimulus[0].geometry $GROUND \
    -stimulus[0].duration $STIMDURATION \
    -stimulus[0].stimtype 0 \
    -stimulus[0].strength $VOLTAGE \
    -stimulus[0].start 0 \
    -stimulus[0].duration $STIMDURATION \
    -stimulus[0].geometry $STIM \
    -ellip_options_file ./amg_xl_opts \
    -parab_options_file ./ilu_cg_opts \
    -num_imp_regions 1 \
    -imp_region[0].im $CELLMODEL

    echo Launch CARP for the restart run ...
    RESTART=${OUTPUTDIR_ACTIVATION}/state.${DURATION_ACT}.0 #state
    $LAUNCHER -np $NPROC ${CARPEXECUTABLE} \
    +F $PARAM_FILE \
    -meshname $MESH_NAME \
    -simID $OUTPUTDIR_RESTART \
    -num_tsav 1 \
    -tsav[0] $DURATION_RUN.0 \
    -start_statef $RESTART \
    -tend $DURATION_RUN \
    -ellip_options_file ./amg_xl_opts \
    -parab_options_file ./ilu_cg_opts \
    -num_imp_regions 1 \
    -imp_region[0].im $CELLMODEL
fi

if [ $DOROTORINIT == 1 ]
  then
    echo Launch CARP for the rotor activation run ...
    RESTART_ROTOR_ACT=${OUTPUTDIR_RESTART}/state.${DURATION_RUN}.0 #state
    $LAUNCHER -np $NPROC ${CARPEXECUTABLE} \
    +F $PARAM_FILE \
    -meshname $MESH_NAME \
    -simID $OUTPUTDIR_ROTOR_ACTIVATION \
    -num_tsav 1 \
    -tsav[0] $DURATION_ROTOR_ACT.0 \
    -start_statef $RESTART_ROTOR_ACT \
    -tend $DURATION_ROTOR_ACT \
```

```
    -num_stim 2 \
    -stimulus[0].stimtype 3 \
    -stimulus[0].strength 0 \
    -stimulus[0].geometry $GROUND_ROTOR \
    -stimulus[0].duration $STIMDURATION \
    -stimulus[0].stimtype 0 \
    -stimulus[0].strength $VOLTAGE \
    -stimulus[0].geometry $STIM_ROTOR \
    -stimulus[0].start $(($DURATION_ROTOR_ACT-1)) \
    -stimulus[0].duration $STIMDURATION \
    -ellip_options_file ./amg_xl_opts \
    -parab_options_file ./ilu_cg_opts \
    -num_imp_regions 1 \
    -imp_region[0].im $CELLMODEL

    echo Launch CARP for the rotor restart run ...
    RESTART_ROTOR_RUN=${OUTPUTDIR_ROTOR_ACTIVATION}/state.${DURATION_ROTOR_ACT}.0 #state
    $LAUNCHER -np $NPROC ${CARPEXECUTABLE} \
    +F $PARAM_FILE \
    -meshname $MESH_NAME \
    -simID $OUTPUTDIR_ROTOR_RESTART \
    -num_tsav 1 -tsav[0] $DURATION_ROTOR_RUN.0 \
    -start_statef $RESTART_ROTOR_RUN \
    -tend $DURATION_ROTOR_RUN \
    -ellip_options_file ./amg_xl_opts \
    -parab_options_file ./ilu_cg_opts \
    -num_imp_regions 1 \
    -imp_region[0].im $CELLMODEL
fi

if [ $DOFINALRRUN == 1 ]
  then
    echo Launch CARP one final time to get activation times ...
    RESTART_ROTOR_RUN_FINAL=${OUTPUTDIR_ROTOR_RESTART}/state.${DURATION_ROTOR_RUN}.0
#state
    $LAUNCHER -np $NPROC ${CARPEXECUTABLE} \
    +F $PARAM_FILE \
    -meshname $MESH_NAME \
    -simID $OUTPUTDIR_ROTOR_RESTART_FINAL \
    -num_tsav 1 -tsav[0] $DURATION_ROTOR_RUN_FINAL.0 \
    -start_statef $RESTART_ROTOR_RUN_FINAL \
    -tend $DURATION_ROTOR_RUN_FINAL \
    -ellip_options_file ./amg_xl_opts \
    -parab_options_file ./ilu_cg_opts \
    -num_imp_regions 1 \
    -imp_region[0].im $CELLMODEL
fi

if [ $DOLATMAPRUN == 1 ]
  then
    echo Launch CARP again at the best time to get LATs for a map
    echo For dual loop, this is at the time of the second stimulus
    RESTART_ROTOR_RUN=${OUTPUTDIR_ROTOR_ACTIVATION}/state.${DURATION_ROTOR_ACT}.0 #
respecify
    $LAUNCHER -np $NPROC ${CARPEXECUTABLE} \
    +F $PARAM_FILE \
    -meshname $MESH_NAME \
    -simID $OUTPUTDIR_LAT_MAP \
    -start_statef $RESTART_ROTOR_RUN \
    -tend $DURATION_LAT_MAP \
    -ellip_options_file ./amg_xl_opts \
    -parab_options_file ./ilu_cg_opts \
    -num_imp_regions 1 \
    -imp_region[0].im $CELLMODEL
fi
```

B.2 Focal Activation Used in Chapter 3

File B-3. pentaray.par

```
num_gregions    =   1

gregion[0].num_IDs  =   3
gregion[0].name     =   "viable"
gregion[0].g_il =    0.28
gregion[0].g_it =    0.026
gregion[0].g_el         =       0.22
gregion[0].g_et         =       0.13
```

```
gregion[0].ID[0]    =   1
gregion[0].ID[1]        =       721
gregion[0].ID[2]        =       722

# Equation

bidomain    = 0
dt      = 10    #microseconds
parab_solve     = 1
#ellip_solve     = 1
vm_per_phie     = 4

# I/O
spacedt     = 1
timedt      = 1 #milliseconds; ie 1 = 1kHz
gridout_i   = 2
#gridout_e  = 2

# Local Activation Times

num_LATs          = 1
lats[0].all       = 0
lats[0].measurand = 0
lats[0].method    = 1
lats[0].threshold = -20    #mV?
lats[0].ID        = "latfile"

# Tag regions

numtagreg = 3

tagreg[0].name = tissue
tagreg[0].type = 2
tagreg[0].tag = 1
tagreg[0].p0[0] = 0
tagreg[0].p0[1] = 0
tagreg[0].p0[2] = 0
tagreg[0].p1[0] = 40000
tagreg[0].p1[1] = 40000
tagreg[0].p1[2] = 0

tagreg[1].name = stim
tagreg[1].type = 2
tagreg[1].tag = 721
tagreg[1].p0[0] = 23500
tagreg[1].p0[1] = 19500
tagreg[1].p0[2] = 0
tagreg[1].p1[0] = 24500
tagreg[1].p1[1] = 20500
tagreg[1].p1[2] = 0

tagreg[2].name = ground
tagreg[2].type = 2
tagreg[2].tag = 722
tagreg[2].p0[0] = 27500
tagreg[2].p0[1] = 19500
tagreg[2].p0[2] = 0
tagreg[2].p1[0] = 28500
tagreg[2].p1[1] = 20500
tagreg[2].p1[2] = 0
```

File B-4. run_carp.sh

```
export NPROC=12
export LAUNCHER=mpirun

echo Set the file references ...
SIM_NAME=square
MESH_NAME=./geometry/square.1
PARAM_FILE=./pentaray.par
CARPEXECUTABLE=/home/localstn10/src/carp-dcse-pt/CARP/carp.petsc.pt

echo Set up the stimulus ...
VOLTAGE=1000
STIMDURATION=1

echo Set up the stimulus ...
STIM=1
GROUND=2
```

```

echo Set up the t ends ...
t_1=1  # length of first stimulus
t_2=500 # length of first run

DURATION_ACT=$t_1
DURATION_RUN=$(($DURATION_ACT+$t_2))

echo Set up the cell model ...
CELLMODEL=NYGREN

echo Set up the output directories ...
OUTPUTDIR_ACTIVATION=./${SIM_NAME}_act
OUTPUTDIR_RESTART=./${SIM_NAME}_run

echo Launch CARP for the activation run ...
$LAUNCHER -np $NPROC ${CARPEXECUTABLE} \
+F $PARAM_FILE \
-meshname $MESH_NAME \
-simID $OUTPUTDIR_ACTIVATION \
-num_tsav 1 \
-tsav[0] $DURATION_ACT.0 \
-tend $DURATION_ACT \
-num_stim 2 \
-stimulus[0].stimtype 3 \
-stimulus[0].strength 0 \
-stimulus[0].geometry $GROUND \
-stimulus[0].duration $STIMDURATION \
-stimulus[1].stimtype 0 \
-stimulus[1].strength $VOLTAGE \
-stimulus[1].geometry $STIM \
-stimulus[1].start 0 \
-stimulus[1].duration $STIMDURATION \
-ellip_options_file ./amg_xl_opts \
-parab_options_file ./ilu_cg_opts \
-num_imp_regions 1 \
-imp_region[0].im $CELLMODEL

echo Launch CARP for the restart run ...
RESTART=${OUTPUTDIR_ACTIVATION}/state.${DURATION_ACT}.0
$LAUNCHER -np $NPROC ${CARPEXECUTABLE} \
+F $PARAM_FILE \
-meshname $MESH_NAME \
-simID $OUTPUTDIR_RESTART \
-num_tsav 1 \
-tsav[0] $DURATION_RUN.0 \
-start_statef $RESTART \
-tend $DURATION_RUN \
-ellip_options_file ./amg_xl_opts \
-parab_options_file ./ilu_cg_opts \
-num_imp_regions 1 \
-imp_region[0].im $CELLMODEL
```

B.3 Linear Activation Used in Chapter 3

File B-5. pentaray.par

```

num_gregions    =   1

gregion[0].num_IDs  =   3
gregion[0].name     =   "viable"
gregion[0].g_il =    0.28
gregion[0].g_it =    0.026
gregion[0].g_el         =       0.22
gregion[0].g_et         =       0.13
gregion[0].ID[0]    =   1
gregion[0].ID[1]    =   721
gregion[0].ID[2]    =   722

# Equation

bidomain    = 0
dt      = 20    #microseconds
parab_solve     = 1
#ellip_solve     = 1
vm_per_phie     = 4

# I/O
```

```
spacedt     = 1
timedt      = 1 #milliseconds; ie 1 = 1kHz
gridout_i   = 2
#gridout_e  = 2

# Local Activation Times

num_LATs          = 1
lats[0].all       = 0
lats[0].measurand = 0
lats[0].method    = 1
lats[0].threshold = -20    #mV?
lats[0].ID        = "latfile"

# Tag regions

numtagreg = 3

tagreg[0].name = tissue
tagreg[0].type = 2
tagreg[0].tag = 1
tagreg[0].p0[0] = 0
tagreg[0].p0[1] = 0
tagreg[0].p0[2] = 0
tagreg[0].p1[0] = 40000
tagreg[0].p1[1] = 40000
tagreg[0].p1[2] = 0

tagreg[1].name = stim
tagreg[1].type = 2
tagreg[1].tag = 721
tagreg[1].p0[0] = 1000
tagreg[1].p0[1] = 0
tagreg[1].p0[2] = 0
tagreg[1].p1[0] = 2000
tagreg[1].p1[1] = 40000
tagreg[1].p1[2] = 0

tagreg[2].name = ground
tagreg[2].type = 2
tagreg[2].tag = 721
tagreg[2].p0[0] = 0
tagreg[2].p0[1] = 0
tagreg[2].p0[2] = 0
tagreg[2].p1[0] = 1000
tagreg[2].p1[1] = 40000
tagreg[2].p1[2] = 0
```

File B-6. run_carp.sh

```
export NPROC=12
export LAUNCHER=mpirun

echo Set the file references ...
SIM_NAME=square
MESH_NAME=./geometry/square.1
PARAM_FILE=./pentaray.par
CARPEXECUTABLE=/home/localstn10/src/carp-dcse-pt/CARP/carp.petsc.pt

echo Set up the stimulus ...
VOLTAGE=1000
STIMDURATION=1

echo Set up the stim geometries ...
STIM=1
GROUND=2

echo Set up the t ends
t_1=1  # length of first stimulus
t_2=500 # length of first run

DURATION_ACT=$t_1
DURATION_RUN=$(($DURATION_ACT+$t_2))

echo Set up the cell model ...
CELLMODEL=NYGREN

echo Set up the output directories
OUTPUTDIR_ACTIVATION=./${SIM_NAME}_act
```

```
OUTPUTDIR_RESTART=./${SIM_NAME}_run

echo Launch CARP for the activation run ...
$LAUNCHER -np $NPROC ${CARPEXECUTABLE} \
+F $PARAM_FILE \
-meshname $MESH_NAME \
-simID $OUTPUTDIR_ACTIVATION \
-num_tsav 2 \
-tsav[0] $DURATION_ACT.0 \
-tend $DURATION_ACT \
-num_stim 1 \
-stimulus[0].stimtype 3 \
-stimulus[0].strength 0 \
-stimulus[0].geometry $GROUND \
-stimulus[0].duration $STIMDURATION \
-stimulus[0].stimtype 0 \
-stimulus[0].strength $VOLTAGE \
-stimulus[0].start 0 \
-stimulus[0].duration $STIMDURATION \
-stimulus[0].geometry $STIM \
-ellip_options_file ./amg_xl_opts \
-parab_options_file ./ilu_cg_opts \
-num_imp_regions 1 \
-imp_region[0].im $CELLMODEL

echo Launch CARP for the restart run ...
RESTART=${OUTPUTDIR_ACTIVATION}/state.${DURATION_ACT}.0 #state
$LAUNCHER -np $NPROC ${CARPEXECUTABLE} \
+F $PARAM_FILE \
-meshname $MESH_NAME \
-simID $OUTPUTDIR_RESTART \
-num_tsav 1 \
-tsav[0] $DURATION_RUN.0 \
-start_statef $RESTART \
-tend $DURATION_RUN \
-ellip_options_file ./amg_xl_opts \
-parab_options_file ./ilu_cg_opts \
-num_imp_regions 1 \
-imp_region[0].im $CELLMODEL
```

B.4 Spiral Wave Activation Used in Chapter 3

File B-7. pentaray.par

```
num_gregions    =   1

gregion[0].num_IDs  =   5
gregion[0].name     =   "viable"
gregion[0].g_il =    0.15
gregion[0].g_it =    0.15
gregion[0].g_el     =   0.15
gregion[0].g_et     =   0.15
gregion[0].ID[0]    =   1
gregion[0].ID[1]    =   721
gregion[0].ID[2]    =   722
gregion[0].ID[3]    =   723
gregion[0].ID[4]    =   724

# Equation

bidomain    = 0
dt      = 20    #microseconds
parab_solve     = 1
#ellip_solve     = 1
vm_per_phie     = 4

# I/O
spacedt     = 1
timedt      = 1 #milliseconds; ie 1 = 1kHz
gridout_i   = 2
#gridout_e  = 2

# Local Activation Times

num_LATs          = 2

lats[0].all       = 0
lats[0].measurand = 0
```

```
lats[0].method    = 1
lats[0].threshold = -20    #mV?
lats[0].ID        = "latfile"

lats[1].all       = 1
lats[1].measurand = 0
lats[1].method    = 1
lats[1].threshold = -20
lats[1].ID        = "latfile-all"

# Tag regions

numtagreg = 5

tagreg[0].name = tissue
tagreg[0].type = 2
tagreg[0].tag = 1
tagreg[0].p0[0] = 0
tagreg[0].p0[1] = 0
tagreg[0].p0[2] = 0
tagreg[0].p1[0] = 40000
tagreg[0].p1[1] = 40000
tagreg[0].p1[2] = 0

tagreg[1].name = stim
tagreg[1].type = 2
tagreg[1].tag = 721
tagreg[1].p0[0] = 1000
tagreg[1].p0[1] = 0
tagreg[1].p0[2] = 0
tagreg[1].p1[0] = 2000
tagreg[1].p1[1] = 40000
tagreg[1].p1[2] = 0

tagreg[2].name = ground
tagreg[2].type = 2
tagreg[2].tag = 722
tagreg[2].p0[0] = 0
tagreg[2].p0[1] = 0
tagreg[2].p0[2] = 0
tagreg[2].p1[0] = 1000
tagreg[2].p1[1] = 40000
tagreg[2].p1[2] = 0

tagreg[3].name = stimrotor
tagreg[3].type = 2
tagreg[3].tag = 723
tagreg[3].p0[0] = 19000
tagreg[3].p0[1] = 0
tagreg[3].p0[2] = 0
tagreg[3].p1[0] = 20000
tagreg[3].p1[1] = 30000
tagreg[3].p1[2] = 0

tagreg[4].name = groundrotor
tagreg[4].type = 2
tagreg[4].tag = 724
tagreg[4].p0[0] = 20000
tagreg[4].p0[1] = 0
tagreg[4].p0[2] = 0
tagreg[4].p1[0] = 21000
tagreg[4].p1[1] = 30000
tagreg[4].p1[2] = 0
```

File B-8. run_carp.sh

```
export NPROC=12
export LAUNCHER=mpirun

echo Set the file references ...
SIM_NAME=square
MESH_NAME=./geometry/square.1
PARAM_FILE=./pentaray.par
CARPEXECUTABLE=/home/localstn10/src/carp-dcse-pt/CARP/carp.petsc.pt

echo Set up the stimulus ...
VOLTAGE=1000
STIMDURATION=1

```

```
14 echo Define which runs to execute ...
15 DOBLOCKSTIM=1
16 DOROTORINIT=1
17
18 echo Set up the stimulus ...
19 STIM=1
20 STIM_ROTOR=3
21 GROUND=2
22 GROUND_ROTOR=4
23
24 echo Set up the t ends ...
25 t_1=1  # length of first stimulus
26 t_2=285 # length of first run
27 t_3=1  # length of second stimulus
28 t_4=10000 # length of second run
29 t_5=1000 # length of the final run for getting activation times, must be greater than TCL
30
31 DURATION_ACT=$t_1
32 DURATION_RUN=$(($DURATION_ACT+$t_2))
33 DURATION_ROTOR_ACT=$(($DURATION_RUN+$t_3))
34 DURATION_ROTOR_RUN=$(($DURATION_ROTOR_ACT+$t_4))
35 DURATION_ROTOR_RUN_FINAL=$(($DURATION_ROTOR_RUN+$t_5))
36
37 echo Set up the cell model ...
38 CELLMODEL=NYGREN
39
40 echo Set up the output directories ...
41 OUTPUTDIR_ACTIVATION=./${SIM_NAME}_act
42 OUTPUTDIR_RESTART=./${SIM_NAME}_run
43 OUTPUTDIR_ROTOR_ACTIVATION=./${SIM_NAME}_rotor_act
44 OUTPUTDIR_ROTOR_RESTART=./${SIM_NAME}_rotor_run
45 OUTPUTDIR_ROTOR_RESTART_FINAL=./${SIM_NAME}_rotor_final
46
47 if [ $DOBLOCKSTIM == 1 ]
48   then
49     echo Launch CARP for the activation run ...
50     $LAUNCHER -np $NPROC ${CARPEXECUTABLE} \
51     +F $PARAM_FILE \
52     -meshname $MESH_NAME \
53     -simID $OUTPUTDIR_ACTIVATION \
54     -num_tsav 2 \
55     -tsav[0] $DURATION_ACT.0 \
56     -tend $DURATION_ACT \
57     -num_stim 1 \
58     -stimulus[0].stimtype 3 \
59     -stimulus[0].strength 0 \
60     -stimulus[0].geometry $GROUND \
61     -stimulus[0].duration $STIMDURATION \
62     -stimulus[0].stimtype 0 \
63     -stimulus[0].strength $VOLTAGE \
64     -stimulus[0].start 0 \
65     -stimulus[0].duration $STIMDURATION \
66     -stimulus[0].geometry $STIM \
67     -ellip_options_file ./amg_xl_opts \
68     -parab_options_file ./ilu_cg_opts \
69     -num_imp_regions 1 \
70     -imp_region[0].im $CELLMODEL
71
72     echo Launch CARP for the restart run ...
73     RESTART=${OUTPUTDIR_ACTIVATION}/state.${DURATION_ACT}.0 #state
74     $LAUNCHER -np $NPROC ${CARPEXECUTABLE} \
75     +F $PARAM_FILE \
76     -meshname $MESH_NAME \
77     -simID $OUTPUTDIR_RESTART \
78     -num_tsav 1 \
79     -tsav[0] $DURATION_RUN.0 \
80     -start_statef $RESTART \
81     -tend $DURATION_RUN \
82     -ellip_options_file ./amg_xl_opts \
83     -parab_options_file ./ilu_cg_opts \
84     -num_imp_regions 1 \
85     -imp_region[0].im $CELLMODEL
86 fi
87
88 if [ $DOROTORINIT == 1 ]
89   then
90     echo Launch CARP for the rotor activation run ...
91     RESTART_ROTOR_ACT=${OUTPUTDIR_RESTART}/state.${DURATION_RUN}.0 #state
92     $LAUNCHER -np $NPROC ${CARPEXECUTABLE} \
93     +F $PARAM_FILE \
94     -meshname $MESH_NAME \
95     -simID $OUTPUTDIR_ROTOR_ACTIVATION \
```

```
    -num_tsav 1 \
    -tsav[0] $DURATION_ROTOR_ACT.0 \
    -start_statef $RESTART_ROTOR_ACT \
    -tend $DURATION_ROTOR_ACT \
    -num_stim 2 \
    -stimulus[0].stimtype 3 \
    -stimulus[0].strength 0 \
    -stimulus[0].geometry $GROUND_ROTOR \
    -stimulus[0].duration $STIMDURATION \
    -stimulus[0].stimtype 0 \
    -stimulus[0].strength $VOLTAGE \
    -stimulus[0].geometry $STIM_ROTOR \
    -stimulus[0].start $(($DURATION_ROTOR_ACT-1)) \
    -stimulus[0].duration $STIMDURATION \
    -ellip_options_file ./amg_xl_opts \
    -parab_options_file ./ilu_cg_opts \
    -num_imp_regions 1 \
    -imp_region[0].im $CELLMODEL

    echo Launch CARP for the rotor restart run ...
    RESTART_ROTOR_RUN=${OUTPUTDIR_ROTOR_ACTIVATION}/state.${DURATION_ROTOR_ACT}.0 #state
    $LAUNCHER -np $NPROC ${CARPEXECUTABLE} \
    +F $PARAM_FILE \
    -meshname $MESH_NAME \
    -simID $OUTPUTDIR_ROTOR_RESTART \
    -num_tsav 1 -tsav[0] $DURATION_ROTOR_RUN.0 \
    -start_statef $RESTART_ROTOR_RUN \
    -tend $DURATION_ROTOR_RUN \
    -ellip_options_file ./amg_xl_opts \
    -parab_options_file ./ilu_cg_opts \
    -num_imp_regions 1 \
    -imp_region[0].im $CELLMODEL
fi

echo Launch CARP one final time to get activation times ...
RESTART_ROTOR_RUN_FINAL=${OUTPUTDIR_ROTOR_RESTART}/state.${DURATION_ROTOR_RUN}.0 #state
$LAUNCHER -np $NPROC ${CARPEXECUTABLE} \
+F $PARAM_FILE \
-meshname $MESH_NAME \
-simID $OUTPUTDIR_ROTOR_RESTART_FINAL \
-num_tsav 1 -tsav[0] $DURATION_ROTOR_RUN_FINAL.0 \
-start_statef $RESTART_ROTOR_RUN_FINAL \
-tend $DURATION_ROTOR_RUN_FINAL \
-ellip_options_file ./amg_xl_opts \
-parab_options_file ./ilu_cg_opts \
-num_imp_regions 1 \
-imp_region[0].im $CELLMODEL
```

B.5 Single Loop Anisotropic Activation Used in Chapter 3

File B-9. pentaray.par

```
num_gregions    =   2

gregion[0].num_IDs  =   5
gregion[0].name     =   "viable"
gregion[0].g_il =    0.28
gregion[0].g_it =    0.026
gregion[0].g_el         =       0.22
gregion[0].g_et         =       0.13
gregion[0].ID[0]    =   1
gregion[0].ID[1]    =   721
gregion[0].ID[2]    =   722
gregion[0].ID[3]    =   723
gregion[0].ID[4]    =   724

gregion[1].num_IDs  =   1
gregion[1].name     =   "scar"
gregion[1].g_il =    0
gregion[1].g_it =    0
gregion[1].g_el     =   0.22
gregion[1].g_et     =   0.13
gregion[1].ID[0]    =   921

# Equation

bidomain    = 0
dt      = 20    #microseconds
```

```
parab_solve     = 1
#ellip_solve     = 1
vm_per_phie     = 4

# I/O
spacedt     = 1
timedt      = 1 #milliseconds; ie 1 = 1kHz
gridout_i   = 2
#gridout_e  = 2

# Local Activation Times

num_LATs          = 2

lats[0].all       = 0
lats[0].measurand = 0
lats[0].method    = 1
lats[0].threshold = -20    #mV?
lats[0].ID        = "latfile"

lats[1].all       = 1
lats[1].measurand = 0
lats[1].method    = 1
lats[1].threshold = -20
lats[1].ID        = "latfile-all"

# Tag regions

numtagreg = 6

tagreg[0].name = tissue
tagreg[0].type = 2
tagreg[0].tag = 1
tagreg[0].p0[0] = 0
tagreg[0].p0[1] = 0
tagreg[0].p0[2] = 0
tagreg[0].p1[0] = 40000
tagreg[0].p1[1] = 40000
tagreg[0].p1[2] = 0

tagreg[1].name = stim
tagreg[1].type = 2
tagreg[1].tag = 721
tagreg[1].p0[0] = 0
tagreg[1].p0[1] = 16000
tagreg[1].p0[2] = 0
tagreg[1].p1[0] = 20000
tagreg[1].p1[1] = 17000
tagreg[1].p1[2] = 0

tagreg[2].name = ground
tagreg[2].type = 2
tagreg[2].tag = 722
tagreg[2].p0[0] = 0
tagreg[2].p0[1] = 17000
tagreg[2].p0[2] = 0
tagreg[2].p1[0] = 20000
tagreg[2].p1[1] = 18000
tagreg[2].p1[2] = 0

tagreg[3].name = stimrentry
tagreg[3].type = 2
tagreg[3].tag = 723
tagreg[3].p0[0] = 0
tagreg[3].p0[1] = 22000
tagreg[3].p0[2] = 0
tagreg[3].p1[0] = 20000
tagreg[3].p1[1] = 23000
tagreg[3].p1[2] = 0

tagreg[4].name = groundrentry
tagreg[4].type = 2
tagreg[4].tag = 724
tagreg[4].p0[0] = 0
tagreg[4].p0[1] = 23000
tagreg[4].p0[2] = 0
tagreg[4].p1[0] = 20000
tagreg[4].p1[1] = 24000
tagreg[4].p1[2] = 0

tagreg[5].name = scar
tagreg[5].type = 1
```

```
tagreg[5].tag = 921
tagreg[5].p0[0] = 20000
tagreg[5].p0[1] = 20000
tagreg[5].p0[2] = 0
tagreg[5].radius = 7500
```

File B-10. run_carp.sh

```
export NPROC=12
export LAUNCHER=mpirun

echo Set the file references ...
SIM_NAME=square
MESH_NAME=./geometry/square.1
PARAM_FILE=./pentaray.par
CARPEXECUTABLE=/home/localstn10/src/carp-dcse-pt/CARP/carp.petsc.pt

echo Set up the stimulus ...
VOLTAGE=1000
STIMDURATION=1

echo Define which runs to execute ...
DOBLOCKSTIM=0 # Initial stimulation
DOROTORINIT=0 # Rotor initialisation
DOFINALRRUN=1 # Extra rotor run at end

echo Set up the stimulus ...
STIM=2
STIM_ROTOR=4
GROUND=3
GROUND_ROTOR=5

echo Set up the t ends ...
t_1=1  # length of first stimulus
t_2=250 # length of first run
t_3=1  # length of second stimulus
t_4=10000 # length of second run
t_5=500 # length of the final run for getting activation times, must be greater than TCL

DURATION_ACT=$t_1
DURATION_RUN=$(($DURATION_ACT+$t_2))
DURATION_ROTOR_ACT=$(($DURATION_RUN+$t_3))
DURATION_ROTOR_RUN=$(($DURATION_ROTOR_ACT+$t_4))
DURATION_ROTOR_RUN_FINAL=$(($DURATION_ROTOR_RUN+$t_5))

echo Set up the cell model ...
CELLMODEL=NYGREN

echo Set up the output directories ...
OUTPUTDIR_ACTIVATION=./${SIM_NAME}_act
OUTPUTDIR_RESTART=./${SIM_NAME}_run
OUTPUTDIR_ROTOR_ACTIVATION=./${SIM_NAME}_rotor_act
OUTPUTDIR_ROTOR_RESTART=./${SIM_NAME}_rotor_run
OUTPUTDIR_ROTOR_RESTART_FINAL=./${SIM_NAME}_rotor_final

if [ $DOBLOCKSTIM == 1 ]
  then
    echo Launch CARP for the activation run ...
    $LAUNCHER -np $NPROC ${CARPEXECUTABLE} \
    +F $PARAM_FILE \
    -meshname $MESH_NAME \
    -simID $OUTPUTDIR_ACTIVATION \
    -num_tsav 2 \
    -tsav[0] $DURATION_ACT.0 \
    -tend $DURATION_ACT \
    -num_stim 1 \
    -stimulus[0].stimtype 3 \
    -stimulus[0].strength 0 \
    -stimulus[0].geometry $GROUND \
    -stimulus[0].duration $STIMDURATION \
    -stimulus[0].stimtype 0 \
    -stimulus[0].strength $VOLTAGE \
    -stimulus[0].start 0 \
    -stimulus[0].duration $STIMDURATION \
    -stimulus[0].geometry $STIM \
    -ellip_options_file ./amg_xl_opts \
    -parab_options_file ./ilu_cg_opts \
    -num_imp_regions 1 \
    -imp_region[0].im $CELLMODEL

```

```
 73     echo Launch CARP for the restart run ...
 74     RESTART=${OUTPUTDIR_ACTIVATION}/state.${DURATION_ACT}.0 #state
 75     $LAUNCHER -np $NPROC ${CARPEXECUTABLE} \
 76     +F $PARAM_FILE \
 77     -meshname $MESH_NAME \
 78     -simID $OUTPUTDIR_RESTART \
 79     -num_tsav 1 \
 80     -tsav[0] $DURATION_RUN.0 \
 81     -start_statef $RESTART \
 82     -tend $DURATION_RUN \
 83     -ellip_options_file ./amg_xl_opts \
 84     -parab_options_file ./ilu_cg_opts \
 85     -num_imp_regions 1 \
 86     -imp_region[0].im $CELLMODEL
 87 fi
 88
 89 if [ $DOROTORINIT == 1 ]
 90   then
 91     echo Launch CARP for the rotor activation run ...
 92     RESTART_ROTOR_ACT=${OUTPUTDIR_RESTART}/state.${DURATION_RUN}.0 #state
 93     $LAUNCHER -np $NPROC ${CARPEXECUTABLE} \
 94     +F $PARAM_FILE \
 95     -meshname $MESH_NAME \
 96     -simID $OUTPUTDIR_ROTOR_ACTIVATION \
 97     -num_tsav 1 \
 98     -tsav[0] $DURATION_ROTOR_ACT.0 \
 99     -start_statef $RESTART_ROTOR_ACT \
100     -tend $DURATION_ROTOR_ACT \
101     -num_stim 2 \
102     -stimulus[0].stimtype 3 \
103     -stimulus[0].strength 0 \
104     -stimulus[0].geometry $GROUND_ROTOR \
105     -stimulus[0].duration $STIMDURATION \
106     -stimulus[0].stimtype 0 \
107     -stimulus[0].strength $VOLTAGE \
108     -stimulus[0].geometry $STIM_ROTOR \
109     -stimulus[0].start $(($DURATION_ROTOR_ACT-1)) \
110     -stimulus[0].duration $STIMDURATION \
111     -ellip_options_file ./amg_xl_opts \
112     -parab_options_file ./ilu_cg_opts \
113     -num_imp_regions 1 \
114     -imp_region[0].im $CELLMODEL
115
116     echo Launch CARP for the rotor restart run ...
117     RESTART_ROTOR_RUN=${OUTPUTDIR_ROTOR_ACTIVATION}/state.${DURATION_ROTOR_ACT}.0
#state
118     $LAUNCHER -np $NPROC ${CARPEXECUTABLE} \
119     +F $PARAM_FILE \
120     -meshname $MESH_NAME \
121     -simID $OUTPUTDIR_ROTOR_RESTART \
122     -num_tsav 1 -tsav[0] $DURATION_ROTOR_RUN.0 \
123     -start_statef $RESTART_ROTOR_RUN \
124     -tend $DURATION_ROTOR_RUN \
125     -ellip_options_file ./amg_xl_opts \
126     -parab_options_file ./ilu_cg_opts \
127     -num_imp_regions 1 \
128     -imp_region[0].im $CELLMODEL
129 fi
130
131 if [ $DOFINALRRUN == 1 ]
132   then
133     echo Launch CARP one final time to get activation times ...
134     RESTART_ROTOR_RUN_FINAL=${OUTPUTDIR_ROTOR_RESTART}/state.${DURATION_ROTOR_RUN}.0
#state
135     $LAUNCHER -np $NPROC ${CARPEXECUTABLE} \
136     +F $PARAM_FILE \
137     -meshname $MESH_NAME \
138     -simID $OUTPUTDIR_ROTOR_RESTART_FINAL \
139     -num_tsav 1 -tsav[0] $DURATION_ROTOR_RUN_FINAL.0 \
140     -start_statef $RESTART_ROTOR_RUN_FINAL \
141     -tend $DURATION_ROTOR_RUN_FINAL \
142     -ellip_options_file ./amg_xl_opts \
143     -parab_options_file ./ilu_cg_opts \
144     -num_imp_regions 1 \
145     -imp_region[0].im $CELLMODEL
146 fi
```

B.6 Single Loop Isotropic Activation Used in Chapter 3

File B-11. pentaray.par

```
num_gregions    =   2

gregion[0].num_IDs  =   5
gregion[0].name     =   "viable"
gregion[0].g_il =    0.15
gregion[0].g_it =    0.15
gregion[0].g_el         =       0.15
gregion[0].g_et         =       0.15
gregion[0].ID[0]    =   1
gregion[0].ID[1]    =   721
gregion[0].ID[2]    =   722
gregion[0].ID[3]    =   723
gregion[0].ID[4]    =   724

gregion[1].num_IDs  =   1
gregion[1].name     =   "scar"
gregion[1].g_il =    0
gregion[1].g_it =    0
gregion[1].g_el     =   0.22
gregion[1].g_et     =   0.13
gregion[1].ID[0]    =   921

# Equation

bidomain    = 0
dt      = 20    #microseconds
parab_solve     = 1
#ellip_solve     = 1
vm_per_phie     = 4

# I/O
spacedt     = 1
timedt      = 1 #milliseconds; ie 1 = 1kHz
gridout_i   = 2
#gridout_e  = 2

# Local Activation Times

num_LATs          = 2

lats[0].all       = 0
lats[0].measurand = 0
lats[0].method    = 1
lats[0].threshold = -20    #mV?
lats[0].ID        = "latfile"

lats[1].all       = 1
lats[1].measurand = 0
lats[1].method    = 1
lats[1].threshold = -20
lats[1].ID        = "latfile-all"

# Tag regions

numtagreg = 6

tagreg[0].name = tissue
tagreg[0].type = 2
tagreg[0].tag = 1
tagreg[0].p0[0] = 0
tagreg[0].p0[1] = 0
tagreg[0].p0[2] = 0
tagreg[0].p1[0] = 40000
tagreg[0].p1[1] = 40000
tagreg[0].p1[2] = 0

tagreg[1].name = stim
tagreg[1].type = 2
tagreg[1].tag = 721
tagreg[1].p0[0] = 0
tagreg[1].p0[1] = 16000
tagreg[1].p0[2] = 0
tagreg[1].p1[0] = 20000
tagreg[1].p1[1] = 17000
```

```
tagreg[1].p1[2] = 0

tagreg[2].name = ground
tagreg[2].type = 2
tagreg[2].tag = 722
tagreg[2].p0[0] = 0
tagreg[2].p0[1] = 17000
tagreg[2].p0[2] = 0
tagreg[2].p1[0] = 20000
tagreg[2].p1[1] = 18000
tagreg[2].p1[2] = 0

tagreg[3].name = stimrentry
tagreg[3].type = 2
tagreg[3].tag = 723
tagreg[3].p0[0] = 0
tagreg[3].p0[1] = 22000
tagreg[3].p0[2] = 0
tagreg[3].p1[0] = 20000
tagreg[3].p1[1] = 23000
tagreg[3].p1[2] = 0

tagreg[4].name = groundrentry
tagreg[4].type = 2
tagreg[4].tag = 724
tagreg[4].p0[0] = 0
tagreg[4].p0[1] = 23000
tagreg[4].p0[2] = 0
tagreg[4].p1[0] = 20000
tagreg[4].p1[1] = 24000
tagreg[4].p1[2] = 0

tagreg[5].name = scar
tagreg[5].type = 1
tagreg[5].tag = 921
tagreg[5].p0[0] = 20000
tagreg[5].p0[1] = 20000
tagreg[5].p0[2] = 0
tagreg[5].radius = 7500
```

File B-12. run_carp.sh

```
export NPROC=12
export LAUNCHER=mpirun

echo Set the file references ...
SIM_NAME=square
MESH_NAME=./geometry/square.1
PARAM_FILE=./pentaray.par
CARPEXECUTABLE=/home/localstn10/src/carp-dcse-pt/CARP/carp.petsc.pt

echo Set up the stimulus ...
VOLTAGE=1000
STIMDURATION=1

echo Define which runs to execute ...
DOBLOCKSTIM=1 # Initial stimulation
DOROTORINIT=1 # Rotor initialisation
DOFINALRRUN=1 # Extra rotor run at end

echo Set up the stimulus ...
STIM=2
STIM_ROTOR=4
GROUND=3
GROUND_ROTOR=5

echo Set up the t ends ...
t_1=1  # length of first stimulus
t_2=240 # length of first run
t_3=1  # length of second stimulus
t_4=1000 # length of second run
t_5=500 # length of the final run for getting activation times, must be greater than TCL

DURATION_ACT=$t_1
DURATION_RUN=$(($DURATION_ACT+$t_2))
DURATION_ROTOR_ACT=$(($DURATION_RUN+$t_3))
DURATION_ROTOR_RUN=$(($DURATION_ROTOR_ACT+$t_4))
DURATION_ROTOR_RUN_FINAL=$(($DURATION_ROTOR_RUN+$t_5))

```

```
38 echo Set up the cell model ...
39 CELLMODEL=NYGREN
40
41 echo Set up the output directories ...
42 OUTPUTDIR_ACTIVATION=./${SIM_NAME}_act
43 OUTPUTDIR_RESTART=./${SIM_NAME}_run
44 OUTPUTDIR_ROTOR_ACTIVATION=./${SIM_NAME}_rotor_act
45 OUTPUTDIR_ROTOR_RESTART=./${SIM_NAME}_rotor_run
46 OUTPUTDIR_ROTOR_RESTART_FINAL=./${SIM_NAME}_rotor_final
47
48 if [ $DOBLOCKSTIM == 1 ]
49   then
50     echo Launch CARP for the activation run ...
51     $LAUNCHER -np $NPROC ${CARPEXECUTABLE} \
52     +F $PARAM_FILE \
53     -meshname $MESH_NAME \
54     -simID $OUTPUTDIR_ACTIVATION \
55     -num_tsav 2 \
56     -tsav[0] $DURATION_ACT.0 \
57     -tend $DURATION_ACT \
58     -num_stim 1 \
59     -stimulus[0].stimtype 3 \
60     -stimulus[0].strength 0 \
61     -stimulus[0].geometry $GROUND \
62     -stimulus[0].duration $STIMDURATION \
63     -stimulus[0].stimtype 0 \
64     -stimulus[0].strength $VOLTAGE \
65     -stimulus[0].start 0 \
66     -stimulus[0].duration $STIMDURATION \
67     -stimulus[0].geometry $STIM \
68     -ellip_options_file ./amg_xl_opts \
69     -parab_options_file ./ilu_cg_opts \
70     -num_imp_regions 1 \
71     -imp_region[0].im $CELLMODEL
72
73     echo Launch CARP for the restart run ...
74     RESTART=${OUTPUTDIR_ACTIVATION}/state.${DURATION_ACT}.0 #state
75     $LAUNCHER -np $NPROC ${CARPEXECUTABLE} \
76     +F $PARAM_FILE \
77     -meshname $MESH_NAME \
78     -simID $OUTPUTDIR_RESTART \
79     -num_tsav 1 \
80     -tsav[0] $DURATION_RUN.0 \
81     -start_statef $RESTART \
82     -tend $DURATION_RUN \
83     -ellip_options_file ./amg_xl_opts \
84     -parab_options_file ./ilu_cg_opts \
85     -num_imp_regions 1 \
86     -imp_region[0].im $CELLMODEL
87 fi
88
89 if [ $DOROTORINIT == 1 ]
90   then
91     echo Launch CARP for the rotor activation run ...
92     RESTART_ROTOR_ACT=${OUTPUTDIR_RESTART}/state.${DURATION_RUN}.0 #state
93     $LAUNCHER -np $NPROC ${CARPEXECUTABLE} \
94     +F $PARAM_FILE \
95     -meshname $MESH_NAME \
96     -simID $OUTPUTDIR_ROTOR_ACTIVATION \
97     -num_tsav 1 \
98     -tsav[0] $DURATION_ROTOR_ACT.0 \
99     -start_statef $RESTART_ROTOR_ACT \
100    -tend $DURATION_ROTOR_ACT \
101    -num_stim 2 \
102    -stimulus[0].stimtype 3 \
103    -stimulus[0].strength 0 \
104    -stimulus[0].geometry $GROUND_ROTOR \
105    -stimulus[0].duration $STIMDURATION \
106    -stimulus[0].stimtype 0 \
107    -stimulus[0].strength $VOLTAGE \
108    -stimulus[0].geometry $STIM_ROTOR \
109    -stimulus[0].start $(($DURATION_ROTOR_ACT-1)) \
110    -stimulus[0].duration $STIMDURATION \
111    -ellip_options_file ./amg_xl_opts \
112    -parab_options_file ./ilu_cg_opts \
113    -num_imp_regions 1 \
114    -imp_region[0].im $CELLMODEL
115
116    echo Launch CARP for the rotor restart run ...
117    RESTART_ROTOR_RUN=${OUTPUTDIR_ROTOR_ACTIVATION}/state.${DURATION_ROTOR_ACT}.0 #state
118    $LAUNCHER -np $NPROC ${CARPEXECUTABLE} \
119    +F $PARAM_FILE \
```

```
    -meshname $MESH_NAME \
    -simID $OUTPUTDIR_ROTOR_RESTART \
    -num_tsav 1 -tsav[0] $DURATION_ROTOR_RUN.0 \
    -start_statef $RESTART_ROTOR_RUN \
    -tend $DURATION_ROTOR_RUN \
    -ellip_options_file ./amg_xl_opts \
    -parab_options_file ./ilu_cg_opts \
    -num_imp_regions 1 \
    -imp_region[0].im $CELLMODEL
fi

if [ $DOFINALRRUN == 1 ]
  then
    echo Launch CARP one final time to get activation times ...
    RESTART_ROTOR_RUN_FINAL=${OUTPUTDIR_ROTOR_RESTART}/state.${DURATION_ROTOR_RUN}.0
#state
    $LAUNCHER -np $NPROC ${CARPEXECUTABLE} \
    +F $PARAM_FILE \
    -meshname $MESH_NAME \
    -simID $OUTPUTDIR_ROTOR_RESTART_FINAL \
    -num_tsav 1 -tsav[0] $DURATION_ROTOR_RUN_FINAL.0 \
    -start_statef $RESTART_ROTOR_RUN_FINAL \
    -tend $DURATION_ROTOR_RUN_FINAL \
    -ellip_options_file ./amg_xl_opts \
    -parab_options_file ./ilu_cg_opts \
    -num_imp_regions 1 \
    -imp_region[0].im $CELLMODEL
fi
```

B.7 S1S2 Protocol Used in Chapter 4 APD/CV Restitution Experiments

File B-13. run_carp.sh – standard Courtemanche cell model; longitudinal fibre direction

```
export NPROC=12
export LAUNCHER=mpirun

echo Set the file references ...
SIM_NAME=square
MESH_NAME=./geometry/square.1
PARAM_FILE=./param_long.par
CARPEXECUTABLE=/home/localstn10/src/carp-dcse-pt/CARP/carp.petsc.pt

echo Set up the stimulus ...
VOLTAGE=1000
STIMDURATION=1
STIM=1
GROUND=2

echo Set up the t ends ...
t_1=1    # length of first stimulus
t_2=470  # length of first run
t_3=1    # length of the second stimulus
t_4=1    # length of the S2 stimulus
t_5=100  # length of the S2 runs
DURATION_ACT1=$t_1
DURATION_RUN1=$(($DURATION_ACT1+$t_2))
DURATION_ACT2=$(($DURATION_RUN1+$t_3))

echo Set up the cell model ...
CELLMODEL=COURTEMANCHE

echo Set up the output directories ...
OUTPUTDIR_ACTIVATION1=./${SIM_NAME}_act1
OUTPUTDIR_RESTART1=./${SIM_NAME}_run1
OUTPUTDIR_ACTIVATION2=./${SIM_NAME}_act2
OUTPUTDIR_RESTART2=./${SIM_NAME}_run2
OUTPUTDIR_S2_ACT=./S2_act
OUTPUTDIR_S2_RUN=./S2_run

echo Define the S2 coupling intevals
S2INTS=(295 290 285 280 275 270 265) # S2 CIs defined here

# First pace at 0ms and 470ms
echo Launch CARP for activation run 1 ...
$LAUNCHER -np $NPROC ${CARPEXECUTABLE} \
```

```
 43 +F $PARAM_FILE \
 44 -meshname $MESH_NAME \
 45 -simID $OUTPUTDIR_ACTIVATION1 \
 46 -num_tsav 1 \
 47 -tsav[0] $DURATION_ACT1.0 \
 48 -tend $DURATION_ACT1 \
 49 -num_stim 2 \
 50 -stimulus[0].stimtype 3 \
 51 -stimulus[0].strength 0 \
 52 -stimulus[0].geometry $GROUND \
 53 -stimulus[0].duration $STIMDURATION \
 54 -stimulus[1].stimtype 0 \
 55 -stimulus[1].strength $VOLTAGE \
 56 -stimulus[1].geometry $STIM \
 57 -stimulus[1].start 0 \
 58 -stimulus[1].duration $STIMDURATION \
 59 -ellip_options_file ./amg_xl_opts \
 60 -parab_options_file ./ilu_cg_opts \
 61 -num_imp_regions 1 \
 62 -imp_region[0].im $CELLMODEL
 63
 64 echo Launch CARP for restart run 1 ...
 65 RESTART=${OUTPUTDIR_ACTIVATION1}/state.${DURATION_ACT1}.0
 66 $LAUNCHER -np $NPROC ${CARPEXECUTABLE} \
 67 +F $PARAM_FILE \
 68 -meshname $MESH_NAME \
 69 -simID $OUTPUTDIR_RESTART1 \
 70 -num_tsav 1 \
 71 -tsav[0] $DURATION_RUN1.0 \
 72 -start_statef $RESTART \
 73 -tend $DURATION_RUN1 \
 74 -ellip_options_file ./amg_xl_opts \
 75 -parab_options_file ./ilu_cg_opts \
 76 -num_imp_regions 1 \
 77 -imp_region[0].im $CELLMODEL
 78
 79 echo Launch CARP for activation run 2 ...
 80 RESTART=${OUTPUTDIR_RESTART1}/state.${DURATION_RUN1}.0
 81 $LAUNCHER -np $NPROC ${CARPEXECUTABLE} \
 82 +F $PARAM_FILE \
 83 -meshname $MESH_NAME \
 84 -simID $OUTPUTDIR_ACTIVATION2 \
 85 -num_tsav 1 \
 86 -tsav[0] $DURATION_ACT2.0 \
 87 -start_statef $RESTART \
 88 -tend $DURATION_ACT2 \
 89 -num_stim 2 \
 90 -stimulus[0].stimtype 3 \
 91 -stimulus[0].strength 0 \
 92 -stimulus[0].geometry $GROUND \
 93 -stimulus[0].duration $STIMDURATION \
 94 -stimulus[1].stimtype 0 \
 95 -stimulus[1].strength $VOLTAGE \
 96 -stimulus[1].geometry $STIM \
 97 -stimulus[1].start $DURATION_RUN1 \
 98 -stimulus[1].duration $STIMDURATION \
 99 -ellip_options_file ./amg_xl_opts \
100 -parab_options_file ./ilu_cg_opts \
101 -num_imp_regions 1 \
102 -imp_region[0].im $CELLMODEL
103
104 # Restart after the second S1 stim, only run until required S2
105 for i in "${S2INTS[@]}"
106 do
107     DURATION_RUN2=$(($DURATION_ACT2+$i))
108     DURATION_S2_act=$(($DURATION_RUN2+$t_4))
109     DURATION_S2_run=$(($DURATION_S2_act+$t_5))
110
111     echo Launch CARP for restart run 2 ...
112     RESTART=${OUTPUTDIR_ACTIVATION2}/state.${DURATION_ACT2}.0
113     $LAUNCHER -np $NPROC ${CARPEXECUTABLE} \
114     +F $PARAM_FILE \
115     -meshname $MESH_NAME \
116     -simID $OUTPUTDIR_RESTART2 \
117     -num_tsav 1 \
118     -tsav[0] $DURATION_RUN2.0 \
119     -start_statef $RESTART \
120     -tend $DURATION_RUN2 \
121     -ellip_options_file ./amg_xl_opts \
122     -parab_options_file ./ilu_cg_opts \
123     -num_imp_regions 1 \
124     -imp_region[0].im $CELLMODEL
```

```
125
126     echo Launch CARP for S2 activation $i ...
127     RESTART=${OUTPUTDIR_RESTART2}/state.${DURATION_RUN2}.0
128     $LAUNCHER -np $NPROC ${CARPEXECUTABLE} \
129     +F $PARAM_FILE \
130     -meshname $MESH_NAME \
131     -simID ${OUTPUTDIR_S2_ACT}${i} \
132     -num_tsav 1 \
133     -tsav[0] $DURATION_S2_act.0 \
134     -start_statef $RESTART \
135     -tend $DURATION_S2_act \
136     -num_stim 2 \
137     -stimulus[0].stimtype 3 \
138     -stimulus[0].strength 0 \
139     -stimulus[0].geometry $GROUND \
140     -stimulus[0].duration $STIMDURATION \
141     -stimulus[1].stimtype 0 \
142     -stimulus[1].strength $VOLTAGE \
143     -stimulus[1].geometry $STIM \
144     -stimulus[1].start $DURATION_RUN2 \
145     -stimulus[1].duration $STIMDURATION \
146     -ellip_options_file ./amg_xl_opts \
147     -parab_options_file ./ilu_cg_opts \
148     -num_imp_regions 1 \
149     -imp_region[0].im $CELLMODEL
150
151     echo Launch CARP for S2 restart $i
152     RESTART=${OUTPUTDIR_S2_ACT}${i}/state.${DURATION_S2_act}.0
153     $LAUNCHER -np $NPROC ${CARPEXECUTABLE} \
154     +F $PARAM_FILE \
155     -meshname $MESH_NAME \
156     -simID ${OUTPUTDIR_S2_RUN}${i} \
157     -start_statef $RESTART \
158     -tend $DURATION_S2_run \
159     -ellip_options_file ./amg_xl_opts \
160     -parab_options_file ./ilu_cg_opts \
161     -num_imp_regions 1 \
162     -imp_region[0].im $CELLMODEL
163
164 done
```

File B-14. run_carp.sh – 'AF' Courtemanche cell model; longitudinal fibre direction

```
 1 export NPROC=12
 2 export LAUNCHER=mpirun
 3
 4 echo Set the file references ...
 5 SIM_NAME=square
 6 MESH_NAME=./geometry/square.1
 7 PARAM_FILE=./param_long.par
 8 CARPEXECUTABLE=/home/localstn10/src/carp-dcse-pt/CARP/carp.petsc.pt
 9
10 echo Set up the stimulus ...
11 VOLTAGE=1000
12 STIMDURATION=1
13 STIM=1
14 GROUND=2
15
16 echo Set up the t ends ...
17 t_1=1    # length of first stimulus
18 t_2=470  # length of first run
19 t_3=1    # length of the second stimulus
20 t_4=1    # length of the S2 stimulus
21 t_5=100  # length of the S2 runs
22 DURATION_ACT1=$t_1
23 DURATION_RUN1=$(($DURATION_ACT1+$t_2))
24 DURATION_ACT2=$(($DURATION_RUN1+$t_3))
25
26 echo Set up the cell model ...
27 CELLMODEL=COURTEMANCHE
28
29 echo Set up the output directories ...
30 OUTPUTDIR_ACTIVATION1=./${SIM_NAME}_act1
31 OUTPUTDIR_RESTART1=./${SIM_NAME}_run1
32 OUTPUTDIR_ACTIVATION2=./${SIM_NAME}_act2
33 OUTPUTDIR_RESTART2=./${SIM_NAME}_run2
34 OUTPUTDIR_S2_ACT=./S2_act
35 OUTPUTDIR_S2_RUN=./S2_run
36
```

```
echo Define the S2 coupling intevals
S2INTS=(295 290 285 280 275 270 265) # S2 CIs defined here

# First pace at 0ms and 470ms
echo Launch CARP for activation run 1 ...
$LAUNCHER -np $NPROC ${CARPEXECUTABLE} \
+F $PARAM_FILE \
-meshname $MESH_NAME \
-simID $OUTPUTDIR_ACTIVATION1 \
-num_tsav 1 \
-tsav[0] $DURATION_ACT1.0 \
-tend $DURATION_ACT1 \
-num_stim 2 \
-stimulus[0].stimtype 3 \
-stimulus[0].strength 0 \
-stimulus[0].geometry $GROUND \
-stimulus[0].duration $STIMDURATION \
-stimulus[1].stimtype 0 \
-stimulus[1].strength $VOLTAGE \
-stimulus[1].geometry $STIM \
-stimulus[1].start 0 \
-stimulus[1].duration $STIMDURATION \
-ellip_options_file ./amg_xl_opts \
-parab_options_file ./ilu_cg_opts \
-num_imp_regions 1 \
-imp_region[0].im $CELLMODEL -imp_region[0].im_param g_Kr-50%,g_CaL-70%,g_to-50%

echo Launch CARP for restart run 1 ...
RESTART=${OUTPUTDIR_ACTIVATION1}/state.${DURATION_ACT1}.0
$LAUNCHER -np $NPROC ${CARPEXECUTABLE} \
+F $PARAM_FILE \
-meshname $MESH_NAME \
-simID $OUTPUTDIR_RESTART1 \
-num_tsav 1 \
-tsav[0] $DURATION_RUN1.0 \
-start_statef $RESTART \
-tend $DURATION_RUN1 \
-ellip_options_file ./amg_xl_opts \
-parab_options_file ./ilu_cg_opts \
-num_imp_regions 1 \
-imp_region[0].im $CELLMODEL -imp_region[0].im_param g_Kr-50%,g_CaL-70%,g_to-50%

echo Launch CARP for activation run 2 ...
RESTART=${OUTPUTDIR_RESTART1}/state.${DURATION_RUN1}.0
$LAUNCHER -np $NPROC ${CARPEXECUTABLE} \
+F $PARAM_FILE \
-meshname $MESH_NAME \
-simID $OUTPUTDIR_ACTIVATION2 \
-num_tsav 1 \
-tsav[0] $DURATION_ACT2.0 \
-start_statef $RESTART \
-tend $DURATION_ACT2 \
-num_stim 2 \
-stimulus[0].stimtype 3 \
-stimulus[0].strength 0 \
-stimulus[0].geometry $GROUND \
-stimulus[0].duration $STIMDURATION \
-stimulus[1].stimtype 0 \
-stimulus[1].strength $VOLTAGE \
-stimulus[1].geometry $STIM \
-stimulus[1].start $DURATION_RUN1 \
-stimulus[1].duration $STIMDURATION \
-ellip_options_file ./amg_xl_opts \
-parab_options_file ./ilu_cg_opts \
-num_imp_regions 1 \
-imp_region[0].im $CELLMODEL -imp_region[0].im_param g_Kr-50%,g_CaL-70%,g_to-50%

# Restart after the second S1 stim, only run until required S2
for i in "${S2INTS[@]}"
do
    DURATION_RUN2=$(($DURATION_ACT2+$i))
    DURATION_S2_act=$(($DURATION_RUN2+$t_4))
    DURATION_S2_run=$(($DURATION_S2_act+$t_5))

    echo Launch CARP for restart run 2 ...
    RESTART=${OUTPUTDIR_ACTIVATION2}/state.${DURATION_ACT2}.0
    $LAUNCHER -np $NPROC ${CARPEXECUTABLE} \
    +F $PARAM_FILE \
    -meshname $MESH_NAME \
    -simID $OUTPUTDIR_RESTART2 \
    -num_tsav 1 \
    -tsav[0] $DURATION_RUN2.0 \
```

```
    -start_statef $RESTART \
    -tend $DURATION_RUN2 \
    -ellip_options_file ./amg_xl_opts \
    -parab_options_file ./ilu_cg_opts \
    -num_imp_regions 1 \
    -imp_region[0].im $CELLMODEL -imp_region[0].im_param g_Kr-50%,g_CaL-70%,g_to-50%

    echo Launch CARP for S2 activation $i ...
    RESTART=${OUTPUTDIR_RESTART2}/state.${DURATION_RUN2}.0
    $LAUNCHER -np $NPROC ${CARPEXECUTABLE} \
    +F $PARAM_FILE \
    -meshname $MESH_NAME \
    -simID ${OUTPUTDIR_S2_ACT}${i} \
    -num_tsav 1 \
    -tsav[0] $DURATION_S2_act.0 \
    -start_statef $RESTART \
    -tend $DURATION_S2_act \
    -num_stim 2 \
    -stimulus[0].stimtype 3 \
    -stimulus[0].strength 0 \
    -stimulus[0].geometry $GROUND \
    -stimulus[0].duration $STIMDURATION \
    -stimulus[1].stimtype 0 \
    -stimulus[1].strength $VOLTAGE \
    -stimulus[1].geometry $STIM \
    -stimulus[1].start $DURATION_RUN2 \
    -stimulus[1].duration $STIMDURATION \
    -ellip_options_file ./amg_xl_opts \
    -parab_options_file ./ilu_cg_opts \
    -num_imp_regions 1 \
    -imp_region[0].im $CELLMODEL -imp_region[0].im_param g_Kr-50%,g_CaL-70%,g_to-50%

    echo Launch CARP for S2 restart $i
    RESTART=${OUTPUTDIR_S2_ACT}${i}/state.${DURATION_S2_act}.0
    $LAUNCHER -np $NPROC ${CARPEXECUTABLE} \
    +F $PARAM_FILE \
    -meshname $MESH_NAME \
    -simID ${OUTPUTDIR_S2_RUN}${i} \
    -start_statef $RESTART \
    -tend $DURATION_S2_run \
    -ellip_options_file ./amg_xl_opts \
    -parab_options_file ./ilu_cg_opts \
    -num_imp_regions 1 \
    -imp_region[0].im $CELLMODEL -imp_region[0].im_param g_Kr-50%,g_CaL-70%,g_to-50%

done
```

File B-15. param_long.par

```
num_gregions    =   1

gregion[0].num_IDs  =   3
gregion[0].name     =   "viable"
gregion[0].g_il         =       0.5
gregion[0].g_it         =       0.25
gregion[0].g_el         =       0.5
gregion[0].g_et         =       0.25
gregion[0].ID[0]    =   1
gregion[0].ID[1]        =       721
gregion[0].ID[2]        =       722

# Equation

bidomain    = 0
dt      = 10    #microseconds
parab_solve     = 1
#ellip_solve     = 1
vm_per_phie     = 4

# I/O
spacedt     = 1
timedt      = 1 #milliseconds; ie 1 = 1kHz
gridout_i   = 2
#gridout_e  = 2

# Local Activation Times

num_LATs          = 1
lats[0].all       = 1
```

```
lats[0].measurand = 0
lats[0].method    = 1
lats[0].threshold = -20    #mV?
lats[0].ID        = "latfile"

# Tag regions

numtagreg = 3

tagreg[0].name = tissue
tagreg[0].type = 2
tagreg[0].tag = 1
tagreg[0].p0[0] = 0
tagreg[0].p0[1] = 0
tagreg[0].p0[2] = 0
tagreg[0].p1[0] = 40000
tagreg[0].p1[1] = 40000
tagreg[0].p1[2] = 0

tagreg[1].name = stim
tagreg[1].type = 2
tagreg[1].tag = 721
tagreg[1].p0[0] = 2000
tagreg[1].p0[1] = 19500
tagreg[1].p0[2] = 0
tagreg[1].p1[0] = 3000
tagreg[1].p1[1] = 20500
tagreg[1].p1[2] = 0

tagreg[2].name = ground
tagreg[2].type = 2
tagreg[2].tag = 722
tagreg[2].p0[0] = 39000
tagreg[2].p0[1] = 0
tagreg[2].p0[2] = 0
tagreg[2].p1[0] = 40000
tagreg[2].p1[1] = 40000
tagreg[2].p1[2] = 0
```

File B-16. param_trans.par

```
num_gregions    =   1

gregion[0].num_IDs  =   3
gregion[0].name     =   "viable"
gregion[0].g_il         =       0.5
gregion[0].g_it         =       0.25
gregion[0].g_el         =       0.5
gregion[0].g_et         =       0.25
gregion[0].ID[0]    =   1
gregion[0].ID[1]        =       721
gregion[0].ID[2]        =       722

# Equation

bidomain    = 0
dt      = 10    #microseconds
parab_solve     = 1
#ellip_solve     = 1
vm_per_phie     = 4

# I/O
spacedt     = 1
timedt      = 1 #milliseconds; ie 1 = 1kHz
gridout_i   = 2
#gridout_e  = 2

# Local Activation Times

num_LATs          = 1
lats[0].all       = 1
lats[0].measurand = 0
lats[0].method    = 1
lats[0].threshold = -20    #mV?
lats[0].ID        = "latfile"

# Tag regions

numtagreg = 3
```

```
39
40 tagreg[0].name = tissue
41 tagreg[0].type = 2
42 tagreg[0].tag = 1
43 tagreg[0].p0[0] = 0
44 tagreg[0].p0[1] = 0
45 tagreg[0].p0[2] = 0
46 tagreg[0].p1[0] = 40000
47 tagreg[0].p1[1] = 40000
48 tagreg[0].p1[2] = 0
49
50 tagreg[1].name = stim
51 tagreg[1].type = 2
52 tagreg[1].tag = 721
53 tagreg[1].p0[0] = 19500
54 tagreg[1].p0[1] = 2000
55 tagreg[1].p0[2] = 0
56 tagreg[1].p1[0] = 20500
57 tagreg[1].p1[1] = 3000
58 tagreg[1].p1[2] = 0
59
60 tagreg[2].name = ground
61 tagreg[2].type = 2
62 tagreg[2].tag = 722
63 tagreg[2].p0[0] = 39000
64 tagreg[2].p0[1] = 0
65 tagreg[2].p0[2] = 0
66 tagreg[2].p1[0] = 40000
67 tagreg[2].p1[1] = 40000
68 tagreg[2].p1[2] = 0
```

Activation times are read from file with the following commands:

```
more latfile-thresh.dat | grep "\<4\s" #centre node
more latfile-thresh.dat | grep "\<25942\s" #longitudinal conduction
more latfile-thresh.dat | grep "\<27513\s" #transverse conduction
```

B.8 Dot Mapping Software used in Chapter 7

File B-17. colorShell.m

```
function dataField = colorShell(hSurf, pts, data, t, varargin)
%     ********************************************************************
%     * The contents of this package are copyright (c) King's College London
%     *
%     * They may not be reproduced, distributed, modified or sold for any
%     * purpose
%     *
%     * Author:     Dr S. E. Williams
%     * Address:    Division of Imaging Sciences and Biomedical Engineering,
%     *             King's College London
%     *             St Thomas' Hospital
%     *
%     * March 2014
%     ********************************************************************

% COLORSHELL shades the surface hSurf according to the scalar field data
% given across pts
%
% Usage:
%   colorShell(hSurf, pts, data, t)
%   colorShell(..., 'propertyname', propertyvalue)
%
% Where:
%   hSurf - see plotVelocityGeometry
%   pts - the data position coordinates. Size mpts x ndim
%   data - the data at each location of pts. Size mpts x ndata
%   t - threshold distance greater than which shell will not be coloured
%
% COLORSHELL shades the surface of a shell according to the scalar field
% data. If the property-value pair coloraxis is set then color thresholding
% is performed:
```

```
%   triangles with |data|>max(caxis) - purple
%   triangles with |data|<min(caxis) - brown
% The property-value pair datatype is used to tell the colormap whether to
% flip or not (otherwise jet is back-to-front for isochronal maps)
%
% Properties:
%   showcolorbar        'show' | {'hide'}
%   colorbarlocation    'north' | 'south' | 'east' | {'west'} | 'northoutside' |
%                       'southoutside' | 'eastoutside' | 'westoutside'
%   coloraxis           [caxismin caxismax] | {[min(min(data)) max(max(data))]}
%   datatype            {'activation'} | 'force' | 'voltage'
%   interpolation       {'on'} | 'off'
%   colororder          {'forward'} | 'reverse'
%
% Author: Steven Williams (2013)
% Modifications -
%
% Info on Code Testing:
% ------------------------------------------------------------------
% % 1. Color by height
%     DISTANCETHRESH = 12;
%     [elec, hSurf, ~, ~] = plotVelocityGeometry(VelocityData, 'all', 'bip');
%     data = elec.Position(:,3);
%     colorShell(hSurf, elec.Position, data, DISTANCETHRESH);
%
% % 2. Color by a random dataset
%     DISTANCETHRESH = 12;
%     [elec, hSurf, ~, ~] = plotVelocityGeometry(VelocityData, 'all', 'bip');
%     data = rand(size(elec.Position(:,3)));
%     colorShell(hSurf, elec.Position, data, DISTANCETHRESH);
%
% % 3. Color by a single site with high values
%     SITE = 4;
%     DISTANCETHRESH = 12;
%     [elec, hSurf, ~, ~] = plotVelocityGeometry(VelocityData, 'all', 'bip');
%     data = zeros(size(elec.Position(:,3)));
%     data(1+10*SITE:10+10*SITE) = 1;
%     colorShell(hSurf, elec.Position, data, DISTANCETHRESH);
%
% % 4. Color by a number of different sites with high values and step thru
%     SITE = [1 2 3 4 5 6 7 8 9 10];
%     DISTANCETHRESH = 12;
%     [elec, hSurf, ~, ~] = plotVelocityGeometry(VelocityData, 'all', 'bip');
%     data = zeros(size(elec.Position(:,3)));
%     data = repmat(data, 1, numel(SITE));
%     for i = 1:numel(SITE)
%         data(10*(SITE(i)-1)+1:10+10*(SITE(i)-1), i) = 1;
%     end
%     colorShell(hSurf, elec.Position, data, DISTANCETHRESH);
%
% % 5. Color by individual points with high values and step thru
%     SITE = 1:100;
%     DISTANCETHRESH = 12;
%     [elec, hSurf, ~, ~] = plotVelocityGeometry(VelocityData, 'all', 'bip');
%     data = zeros(size(elec.Position(:,3)));
%     data = repmat(data, 1, numel(SITE));
%     for i = 1:numel(SITE)
%         data(SITE(i), i) = 1;
%     end
%     colorShell(hSurf, elec.Position, data, DISTANCETHRESH);
%
% % 6. Force shell
%     clf;
%     hSurf = trisurf(userdata.surface.triRep);
%     axis equal vis3d;
%     DISTANCETHRESH = 4;
%     colorShell(hSurf, userdata.electric.egmSurfX, userdata.electric.force.force,
DISTANCETHRESH ...
%       , 'showcolorbar', 'show' ...
%       , 'coloraxis', [1 40] ...
%       , 'datatype', 'force' ...
%     );
%
% % 7. Activation map based on interpolated Carto data
%     clf
%     hSurf = trisurf(userdata.surface.triRep);
%     axis equal vis3d
%     DISTANCETHRESH = 10;
%     t_min = min(userdata.surface.act_bip(:,1));
%     t_max = max(userdata.surface.act_bip(:,1));
%     colorShell(hSurf, userdata.electric.egmSurfX, userdata.surface.act_bip(:,1),
DISTANCETHRESH ...
```

```
%         , 'showcolorbar', 'show' ...
%         , 'coloraxis', [t_min t_max] ...
%         , 'datatype', 'activation' ...
%         , 'interpolation', 'off' ...
%         );
% ------------------------------------------------------------------
%
% ------------------------------------------------------------------
% code
% ------------------------------------------------------------------

% Validate input
p = inputParser;
p.addRequired('hSurf', @ishandle);
p.addRequired('pts', @isnumeric);
p.addRequired('data', @isnumeric);
p.addRequired('t', @isnumeric);
p.addParamValue('showcolorbar', 'hide', @(x)isstr(x) &&(strcmpi(x,'hide') || strcmpi(x,
'show')));
p.addParamValue('colorbarlocation', 'west', @(x)isstr(x) && (strcmpi(x, 'north') ...
    || strcmpi(x, 'south') || strcmpi(x, 'east') || strcmpi(x, 'west') ...
    || strcmpi(x, 'northoutside') || strcmpi(x, 'southoutside') ...
    || strcmpi(x, 'eastoutside') || strcmpi(x, 'westoutside') ...
    ));
p.addParamValue('coloraxis', [], @isnumeric);
p.addParamValue('datatype', 'activation', @isstr);
p.addParamValue('colororder', 'forward', @isstr);
p.addParamValue('interpolation', 'on', @isstr);
p.parse(hSurf, pts, data, t, varargin{:});
inputs = p.Results;
showcolorbar = inputs.showcolorbar;
colorbarlocation = inputs.colorbarlocation;
coloraxis = inputs.coloraxis;
datatype = inputs.datatype;
colororder = inputs.colororder;
doInterpolation = inputs.interpolation;

% Get a handle to the figure
hFig = get(get(hSurf,'parent'),'parent');

% Draw the sliderbar, if there is more than one dataset
if size(data,2)>1
    hSl = uicontrol(hFig, 'style', 'slider' ...
        , 'units', 'normalized' ...
        , 'position', [.8 .1 .15 .05] ...
        , 'callback', @adjustSlider ...
        , 'min', 1 ...
        , 'max', size(data,2) ...
        , 'value', 1 ...
        , 'sliderstep', [1/(size(data,2)-1) 1/(size(data,2)-1)] ...
        );
end

% Call adjust slider for the first time
adjustSlider();

    function adjustSlider(~, ~, ~)

        % Get the value of the sliderbar, if it exists
        if exist('hSl', 'var')
            i = round(get(hSl, 'value'));
        else
            i = 1;
        end

        % Every point in the surface - r for required.
        rPts = get(hSurf, 'Vertices');

        % If necessary perform interpolation
        switch doInterpolation
            case 'on'
                % Set up the interpolation
                warning('off','MATLAB:scatteredInterpolant:DupPtsAvValuesWarnId');
                tempdata = data(:,i);
                temppts = pts;
                indexRemove = isnan(tempdata);
                tempdata(indexRemove,:)=[];
                temppts(indexRemove,:)=[];
                F = scatteredInterpolant(temppts, tempdata ...
                    , 'natural' ... %interpolation method - linear, nearest or natural
                    , 'linear' ... %extrapolation method - linear, nearest or none
                    );
```

```
                dataField = F(rPts);
            case 'off'
                dataField = data(:,i);
                temppts = pts;
        end

        if isempty(dataField)
            return
        end

        % Find the shortest distance from every point in the surface to the dataset
        % pointcloud
        id = knnsearch(temppts, rPts);
        cPts = temppts(id,:); %c for closest
        d = distBetweenPoints(cPts, rPts);

        % if coloraxis has been specified set up for raw data thresholding now
        tAboveCAxis = zeros(size(d));
        tBelowCAxis = zeros(size(d));
        if ~isempty(coloraxis)
            tAboveCAxis(dataField>max(coloraxis)) = 1;
            tBelowCAxis(dataField<min(coloraxis)) = 1;
        end

        % Define magenta and brown
        magenta = [1 0 1];
        brown = [92 51 23]  /256;
        if strcmpi(colororder, 'reverse')
            disp('hi')
            tmp = brown;
            brown = magenta;
            magenta = tmp;
        end


        % Get the appropriate color map
        switch datatype
            case 'activation'
                colormap(ones([64,3]));
                cMap = hsv;
                if length(cMap)==64
                    cMap(end-8:end,:) = [];
                end
            case 'force'
                cMap = jet;
            case 'voltage'
                cMap = jet;
                %otherwise
                %    disp('IN OTHERWISE');
                %    cMap = hsv;
                %    if length(cMap)==64
                %        cMap(end-36:end,:) = [];
                %    end
                %    %assume activation if not specified
        end

        % Limit the size of the colormap
        if length(cMap) > 256;
            cMap = downsample(cMap, round(length(cMap)/256));
        end
        %set(gcf, 'colormap', cMap);
        colormap(cMap);
        disp(['Length of cMap is: ' num2str(length(cMap))]);

        scaledDataField = round(scaleData( dataField(~tAboveCAxis & ~tBelowCAxis), [1
size(cMap,1)] ));
        iC = ones(size(dataField));
        iC(find(~tAboveCAxis & ~tBelowCAxis)) = scaledDataField; %#ok<FNDSB>
        thresholdNaN = isnan(iC);
        iC(thresholdNaN) = 1;
        col = cMap(iC,:);

        % At this point the color map col is correct for all non-nan points
        % p satisfying the expression min(caxis)<dataField(p)<max(caxis)

        % threshold based on coloraxis
        if ~isempty(coloraxis)
            col(logical(tAboveCAxis),:) = repmat(magenta, [numel(find(tAboveCAxis)),1]);
            col(logical(tBelowCAxis),:) = repmat(brown, [numel(find(tBelowCAxis)),1]);
        end

        % Threshold based on the distance t
```

```
        thresholdDistance = zeros(size(d));
        thresholdDistance(d>t) = 1;

        % Create the color data matrix, making any vertex grey when it is greater
        % than t distance from the point cloud.
        col(logical(thresholdDistance),:) = .6; %ie [.6 .6 .6] grey
        col(logical(thresholdNaN),:) = .6; % ie [1 1 1] white

        % Update the color of the surface
        set(hSurf, 'FaceVertexCData', col ...
            ,'FaceColor', 'interp' ...
            ,'FaceAlpha', 1 ...
            );


        % Set the figure color axis
        colorAxis = [min(min(data)) max(max(data))];
        if ~isnan(colorAxis(1)) && ~isnan(colorAxis(2))
            caxis(colorAxis);


            % Create the figure color map
            if range(coloraxis)>0
                incrementOfCMap = length(cMap) / range(coloraxis);

                nMagenta = ceil( (max(data(:,i)) - max(coloraxis)) * incrementOfCMap );

                nBrown = ceil( (min(coloraxis) - min(data(:,i)) ) * incrementOfCMap );

                cMapMagenta = repmat(magenta, [nMagenta, 1]);
                cMapBrown = repmat(brown, [nBrown, 1]);
                figureCMap = vertcat(cMapBrown, cMap, cMapMagenta);

            else
                % there is a single threshold
                thresh = min(coloraxis);
                nColors = 256;
                nMagenta = ceil( ((max(data(:,i)) - thresh)/range(data(:,i))) * nColors );
                nBrown = ceil( ((thresh)/range(data(:,i))) * nColors );
                cMapMagenta = repmat(magenta, [nMagenta, 1]);
                cMapBrown = repmat(brown, [nBrown, 1]);
                figureCMap = vertcat(cMapBrown, cMapMagenta);
            end
            set(gcf, 'colormap', figureCMap);

        end

        % Show the colorbar
        if strcmpi(showcolorbar, 'show')
            % show the color bar
            colorbar('delete');
            colorbar('location', colorbarlocation);

        elseif strcmpi(showcolorbar, 'hide')
            % hide the color bar
            colorbar('delete');
        end

        % Return the scaledData if asked for
        if strcmpi(datatype,'force')
            dataField(logical(thresholdDistance),:) = 0;
            dataField(logical(thresholdNaN),:) = 0;
        end

    end %adjustSlider()
end %colorShell()
```

File B-18. distBetweenPoints.m

```
function D = distBetweenPoints(A, B, varargin)
%     ********************************************************************
%     * The contents of this package are copyright (c) King's College London
%     *
%     * They may not be reproduced, distributed, modified or sold for any
%     * purpose
%     *
%     * Author:     Dr S. E. Williams
%     * Address:    Division of Imaging Sciences and Biomedical Engineering,
%     *             King's College London
```

```
%     *             St Thomas' Hospital
%     *
%     * March 2014
%     ************************************************************************

% DISTBETWEENPOINTS Returns the distance from A to B.
% Usage:
%   D = DISTBETWEENPOINTS(A, B)
% Where:
%   A - is the first point(s)
%   B - is the second point(s)
%
% DISTBETWEENPOINTS returns the distance from A to B. A and B are specified
% as row vectors [x, y, z] or matrices, with rows representing different
% points.
%
% Author: Steven Williams (2013)
% Modifications -
%
% Info on Code Testing:
% ------------------------------------------------------------------
% test code
% ------------------------------------------------------------------
%
% ------------------------------------------------------------------
% code
% ------------------------------------------------------------------

if nargin==3
    warn = varargin{1};
else
    warn = false;
end
if size(A,2) ~= size(B,2);
    error('DISTBETWEENPOINTS: dimensions of points in A and B must be equal');
end
if size(A,1) ~= size(B,1);
    if size(A,1) ~= 1
        error('DISTBETWEENPOINTS: if npoints in A and B are different A must specify one and
only one point');
    else
        A = repmat(A, size(B,1), 1);
        if warn
            warning('DISTBETWEENPOINTS: A has been replicated size(B,1) times');
        end
    end
end

diffsq = (A - B).^2;

D = sqrt(sum(diffsq, 2));

end
```

File B-19. DotGuiStatic.m

```
classdef DotGuiStatic < hgsetget
%     ************************************************************************
%     * The contents of this package are copyright (c) King's College London
%     *
%     * They may not be reproduced, distributed, modified or sold for any
%     * purpose
%     *
%     * Author:     Dr S. E. Williams
%     * Address:    Division of Imaging Sciences and Biomedical Engineering,
%     *             King's College London
%     *             St Thomas' Hospital
%     *
%     * March 2014
%     ************************************************************************

    % DOTGUI objects draw scar datasets using Dot Mapping
    %
    % Usage:
    %   hDg = DotGui();
    %
    % Where:
    %   tf - is a boolean variable indicating whether headtracking is used
    %   hDg - is a handle to the DotGui object
```

```
%
% DOTGUI objects draw scar datasets using Dot Mapping. DOTGUI uses
% dialogue boxes to access either a VTK file or a MAT file. Details for
% for each are as follows:
%   (1) VTK file: input     - VTKReader object
%                 scar data - CellData of VTKReader
%   (2) MAT file: input     - Local function of pbhLoad_call() method
%                 scar data - inferred from bipolar voltage
%                             (userdata.surface.act_bip(:,2)
% - In the case of a VTK file only one data set is displayed (scar).
% - In the case of a MAT file, two datasets may be displayed (scar and
%   activation time).
%
% Possible Improvement - store two data sets in a .vtk file (LGE/scar
% information represented in CellData and voltage or activation time
% represented in PointsData.
%
% Having access the required dataset, DOTGUI reformats the shell
% (scaling to unit size, rotating as necessary to face the anterior
% wall and centering on the origin). The GUI is created
% programmatically.
%
% The DOTGUI constructor creates the following objects :
%   hDg.hDM     - DotMap
%   hDg.hP3D    - Pseudo3D
%   hDg.hVisAx  - VisualizerAxis
%
% Author: Steven Williams (2012)
% Modifications -
%
% Info on Code Testing:
% ---------------------
%
% ---------------------
%
% Use warnings with the following format
%    disp('DOTGUI: warning.')
%
% ------------------------------------------------------------------
% code
% ------------------------------------------------------------------

properties (SetAccess = private, GetAccess = public)
    Brightness = 1
    Contrast = 1
    Mode = 'scar'
    GeometryDOTS
    GeometryCOLOR
    SigIntensity = 1
    hDM
    IsVertexAtRim
    hLight
end

properties (SetAccess = public, GetAccess = public)
    S % structure of ui element handles
    DATASETCOLOR
    DATASETDOTS
    DATASETDOTS_processed
    DATASETCOLOR_processed
    SAMPLEPOSITIONSCOLOR
    SAMPLEPOSITIONSDOTS
    ColorMapType = 'activation'
    CvData
end


properties (SetAccess = private, GetAccess = private)
    AxisListener
end

methods
    % Constructor
    function hDg = DotGuiStatic(varargin)
        % Set up the GUI
        hDg.initialiseGui();

        % Set up the DotMap (sample data)
        sampleTr = TriRep([1 2 3], [0 0 0; 0 0 0; 0 0 0]);
        hDg.hDM = DotMapRim(sampleTr, 0);

        if numel(varargin)>0
```

```
            hDg.loadInitialisation(varargin{1});
        end

        % Set up the listner for camera position changes
        hDg.AxisListener = addlistener(hDg.S.ax, 'CameraPosition' ...
            , 'PostSet', @hDg.cameraMoved);
    end

    % Initialise the GUI
    function hDg = initialiseGui(hDg)
        % Figure window

        hDg.S.fh = figure('units', 'pixels' ...
            , 'position', [100 200 820 450] ...
            , 'menubar', 'none' ...
            , 'numbertitle', 'off' ...
            , 'name', 'Dot Map - Surface Shell' ...
            , 'resize', 'on' ...
            , 'renderer', 'zbuffer' ...
            );
        cameratoolbar(hDg.S.fh, 'setcoordsys', 'none');

        hDg.S.uip1 = uipanel(hDg.S.fh ...
            , 'units', 'normalized' ...
            , 'position', [0 .1 1 .9] ...
            , 'backgroundcolor', [.6 .6 .6] ...
            );
        hDg.S.uip2 = uipanel(hDg.S.fh ...
            , 'units', 'normalized' ...
            , 'position', [0 0 1 .1] ...
            );
        hDg.S.uip2a = uipanel(hDg.S.uip2 ...
            , 'units', 'normalized' ...
            , 'position', [0 0 .05 1] ...
            , 'title', 'View' ...
            );
        hDg.S.uip2b = uipanel(hDg.S.uip2 ...
            , 'units', 'normalized' ...
            , 'position', [.05 0 .1 1] ...
            , 'title', 'Show' ...
            );
        hDg.S.uip2c = uipanel(hDg.S.uip2 ...
            , 'units', 'normalized' ...
            , 'position', [.25 0 .4 1] ...
            , 'title', 'Dot' ...
            );
        hDg.S.uip2d = uipanel(hDg.S.uip2 ...
            , 'units', 'normalized' ...
            , 'position', [.65 0 .3 1] ...
            , 'title', 'Color' ...
            );
        hDg.S.uip2e = uipanel(hDg.S.uip2 ...
            , 'units', 'normalized' ...
            , 'position', [.95 0 .05 1] ...
            , 'title', 'File' ...
            );

        % Axis
        hDg.S.ax = axes('Parent', hDg.S.uip1 ...
            , 'units', 'normalized' ...
            , 'Position', [0 0 1 1] ...
            , 'xcolor','k' ...
            , 'ycolor','k' ...
            , 'xtick',[] ...
            , 'ytick',[] ...
            , 'Color', 'k' ...
            );
        hDg.hLight = light;


        % Popup Menu - Color
        hDg.S.pumColor = uicontrol(hDg.S.uip2d ...
            , 'Style', 'popup' ...
            , 'String', 'LAT|Voltage' ...
            , 'units', 'normalized' ...
            , 'position', [.1 1/3 .8 1/3] ...
            , 'callback', {@hDg.pumColor_call} ...
            );
        % Sliderbar - Color
        hDg.S.sbThreshCondVel = uicontrol(hDg.S.uip2d ...
            , 'Style', 'slider' ...
            , 'Units', 'normalized' ...
```

```
            , 'Position', [.1 2/3 .8 1/3] ...
            , 'value', 1500 ...
            , 'min', 1, 'max', 3000 ...
            , 'callback', {@hDg.sbThreshCondVel_call} ...
            , 'visible', 'off' ...
            );
        % Pushbutton - load .mat file
        hDg.S.pbhLoad = uicontrol(hDg.S.uip2e ...
            , 'Style', 'pushbutton' ...
            , 'String', 'LOAD .mat' ...
            , 'Units', 'normalized' ...
            , 'Position', [0 0 1 .5] ...
            , 'callback', {@hDg.pbhLoadMat_call} ...
            );
        % Pushbutton - load .vtk files
        hDg.S.pbhLoad = uicontrol(hDg.S.uip2e ...
            , 'Style', 'pushbutton' ...
            , 'String', 'LOAD .vtk' ...
            , 'Units', 'normalized' ...
            , 'Position', [0 .5 1 .5] ...
            , 'callback', {@hDg.pbhLoadVtk_call} ...
            );
        % Pushbutton - graph
        hDg.S.pbhGraph = uicontrol(hDg.S.uip2 ...
            , 'Style', 'pushbutton' ...
            , 'String', 'GRAPH' ...
            , 'Units', 'normalized' ...
            , 'Position', [0.17 0 0.06 1] ...
            , 'callback', {@hDg.pbhGraph_call} ...
            , 'visible', 'off' ...
            );
        % Pushbutton - rotate
        hDg.S.pbhRotate = uicontrol(hDg.S.uip2a ...
            , 'Style', 'pushbutton' ...
            , 'String','Rotate' ...
            , 'Units', 'normalized' ...
            , 'Position', [0 0 1 1/3] ...
            , 'callback', {@hDg.pbhRotate_call} ...
            );
        % Pushbutton - zoom
        hDg.S.pbhZoom = uicontrol(hDg.S.uip2a ...
            , 'Style', 'pushbutton' ...
            , 'String', 'Zoom' ...
            , 'Units', 'normalized' ...
            , 'Position', [0 1/3 1 1/3] ...
            , 'callback', {@hDg.pbhZoom_call} ...
            );
        % Pushbutton - pan
        hDg.S.pbhPan = uicontrol(hDg.S.uip2a ...
            , 'Style', 'pushbutton' ...
            , 'String','Pan' ...
            , 'Units', 'normalized' ...
            , 'Position', [0 2/3 1 1/3] ...
            , 'callback', {@hDg.pbhPan_call} ...
            );
        % Sliderbar - brightness
        hDg.S.sbBrightness = uicontrol(hDg.S.uip2c ...
            , 'Style', 'slider' ...
            , 'Units', 'normalized' ...
            , 'Position', [.6 0 .35 1/3] ...
            , 'value', 0.5 ...
            , 'callback', {@hDg.sbBrightness_call} ...
            );
        % Sliderbar - contrast
        hDg.S.sbContrast = uicontrol(hDg.S.uip2c ...
            , 'Style', 'slider' ...
            , 'Units', 'normalized' ...
            , 'Position', [.6 1/3 .35 1/3] ...
            , 'value', 0.5 ...
            , 'callback', {@hDg.sbContrast_call} ...
            );
        % Sliderbar - threshold
        hDg.S.cbThreshold = uicontrol(hDg.S.uip2c ...
            , 'Style', 'checkbox' ...
            , 'Units', 'normalized' ...
            , 'Position', [.6 0.75 .05 0.25] ...
            , 'Value', 0 ...
            , 'callback', {@hDg.cbThreshold_call} ...
            );
        hDg.S.sbThreshold = uicontrol(hDg.S.uip2c ...
            , 'Style', 'slider' ...
            , 'Units', 'normalized' ...
```

```
                , 'Position', [.65 2/3 .20 1/3] ...
                , 'min', 0 ...
                , 'max', 10 ...
                , 'value', 0.5 ...
                , 'callback', {@hDg.sbThreshold_call} ...
                );
            hDg.S.stThresholdValue = uicontrol(hDg.S.uip2c ...
                , 'Style', 'text' ...
                , 'Units', 'normalized' ...
                , 'Position', [.85 2/3 .1 1/3] ...
                );
            % Text
            hDg.S.stBrightness = uicontrol(hDg.S.uip2c ...
                , 'Style', 'text' ...
                , 'Units', 'normalized' ...
                , 'Position', [.4 0 .2 1/3] ...
                , 'String', 'Brightness' ...
                );
            hDg.S.stContrast = uicontrol(hDg.S.uip2c ...
                , 'Style', 'text' ...
                , 'Units', 'normalized' ...
                , 'Position', [.4 1/3 .2 1/3] ...
                , 'String', 'Contrast' ...
                );
            hDg.S.stThreshold = uicontrol(hDg.S.uip2c ...
                , 'Style', 'text' ...
                , 'Units', 'normalized' ...
                , 'Position', [.4 2/3 .2 1/3] ...
                , 'String', 'Threshold' ...
                );
            % Togglebutton - surface
            hDg.S.tbSurface = uicontrol(hDg.S.uip2b ...
                , 'Style', 'toggle' ...
                , 'Units', 'normalized' ...
                , 'Position', [0 0 1 .5] ...
                , 'String', 'Surface' ...
                , 'callback', {@hDg.tbSurface_call} ...
                );
            set(hDg.S.tbSurface, 'Value', get(hDg.S.tbSurface, 'Max'));
            % Togglebutton - dots
            hDg.S.tbDots = uicontrol(hDg.S.uip2b ...
                , 'Style', 'toggle' ...
                , 'Units', 'normalized' ...
                , 'Position', [0 .5 1 .5] ...
                , 'String', 'Dots' ...
                , 'callback', {@hDg.tbDots_call} ...
                );
            set(hDg.S.tbDots, 'Value', get(hDg.S.tbDots, 'Max'));
            % Radiobuttons - mode
            hDg.S.bghMode = uibuttongroup('Parent', hDg.S.uip2c ...
                , 'Title', '' ...
                , 'Units', 'normalized' ...
                , 'Position', [0 0 .4 1] ...
                , 'SelectionChangeFcn', {@hDg.bghMode_call} ...
                );
            hDg.S.rbhScar = uicontrol(hDg.S.bghMode ...
                , 'Style', 'radiobutton' ...
                , 'Units', 'normalized' ...
                , 'Position', [0 0 1 .5] ...
                , 'String', 'Scar' ...
                , 'Tag', 'dotsScar' ...
                );
            hDg.S.rbhUniform = uicontrol(hDg.S.bghMode ...
                , 'Style', 'radiobutton' ...
                , 'Units', 'normalized' ...
                , 'Position', [0 .5 1 .5] ...
                , 'String', 'Uniform' ...
                , 'Tag', 'dotsUniform' ...
                );
        end

        % reset instance variables
        function hDg = resetInstanceVariables(hDg)

            %variables
            hDg.Brightness = 1;
            hDg.Contrast = 1;
            hDg.Mode = 'scar';
            hDg.SigIntensity = 1;
            hDg.IsVertexAtRim = [];
            hDg.S % structure of ui element handles
            hDg.DATASETCOLOR = [];
```

```
            hDg.DATASETDOTS = [];
            hDg.DATASETDOTS_processed = [];
            hDg.DATASETCOLOR_processed = [];
            hDg.SAMPLEPOSITIONSCOLOR = [];
            hDg.SAMPLEPOSITIONSDOTS = [];
            hDg.ColorMapType = 'activation';
            hDg.CvData = [];

            %gui
            set(hDg.S.pumColor, 'value', 1);
            set(hDg.S.sbThreshCondVel, 'value', 1500);
            set(hDg.S.sbBrightness, 'value', 0.5);
            set(hDg.S.sbContrast, 'value', 0.5);
            set(hDg.S.cbThreshold, 'value', 0);
            set(hDg.S.sbThreshold, 'value', 0.5);
            set(hDg.S.tbDots, 'value', get(hDg.S.tbDots, 'max'));
            set(hDg.S.bghMode, 'selectedobject', hDg.S.rbhScar);

            % Set up the listner for camera position changes
            hDg.AxisListener = addlistener(hDg.S.ax, 'CameraPosition' ...
                , 'PostSet', @hDg.cameraMoved);
        end

        % // Callback // - CameraMoved: Called by the listener if cameraposition changes
        function cameraMoved(hDg, src, event) %#ok<INUSD>
            axis = hDg.S.ax;

            %Calculate the new distance from the camera to the target
            lightPosNew = get(axis, 'CameraPosition') .* 5;

            %Reposition the light
            set(hDg.hLight, 'position', lightPosNew);
        end

        % // Callback // - Load: Called by hDg.S.pbhLoadMat
        function pbhLoadMat_call(hDg, src, evt) %#ok<INUSD>
            % reset instance variables
            hDg.resetInstanceVariables();

            % Use a dialogue to get the .vtk or .mat file
            persistent openDir
            if isempty(openDir)
                openDir = stevematlabroot();
            end
            if ~isdir(openDir)
                openDir = stevematlabroot();
            end
            [filename, pathname] = uigetfile( ...
                {'*.mat','MatLab Files (*.mat)'} ...
                , 'Select a file' ...
                , openDir ...
                , 'MultiSelect', 'off');
            if isequal(filename,0) || isequal(pathname,0)
                return;
            else
                openDir = pathname;
                abspath = strcat(pathname, filesep(), filename);
            end

            load(abspath);

            % -- user selected a MAT file
            GeometryColor = userdata.surface.triRep;
            GeometryDots = userdata.surface.triRep;
            DataColor = userdata.surface.act_bip(:,1);
            DataDots = userdata.surface.act_bip(:,2);
            SamplePosColor = userdata.electric.egmSurfX;
            SamplePosDots = userdata.electric.egmSurfX;
            isVertexAtRim = userdata.surface.isVertexAtRim;

            hDg.loadInitialisation(GeometryColor, GeometryDots, DataColor, DataDots,
SamplePosColor, SamplePosDots, isVertexAtRim);
        end

        % // Callback // - Load: Called by hDg.S.pbhLoadVtk
        function pbhLoadVtk_call(hDg, scr, evt)
            % reset instance variables
            hDg.resetInstanceVariables();

           % Use a dialog to get the .vtk files
           persistent openDir
           if isempty(openDir)
```

```
            openDir = stevematlabroot();
        end
        if ~isdir(openDir)
            openDir = stevematlabroot();
        end
        [filename1, pathname1] = uigetfile( ...
            {'*.vtk', 'VTK Files (*.vtk)'} ...
            , 'Select the VTK file to be drawn in color' ...
            , openDir ...
            , 'MultiSelect', 'off');
        if isequal(filename1,0) || isequal(pathname1,0)
            return;
        else
            openDir = pathname1;
            absPathVtkFile1 = strcat(pathname1, filesep(), filename1);
        end
        [filename2, pathname2] = uigetfile( ...
            {'*.vtk', 'VTK Files (*.vtk)'} ...
            , 'Select the VTK file to be drawn in dots' ...
            , openDir ...
            , 'MultiSelect', 'off');
        if isequal(filename2,0) || isequal(pathname2,0)
            return;
        else
            openDir = pathname2;
            absPathVtkFile2 = strcat(pathname2, filesep(), filename2);
        end

        %load the vtk files
        vtk1 = VTKReader(absPathVtkFile1);
        vtk1.readAllData();
        vtk2 = VTKReader(absPathVtkFile2);
        vtk2.readAllData();

        % -- user selected a VTK file
         GeometryColor = TriRep(vtk1.Cells+1, vtk1.Points);
         GeometryDots = TriRep(vtk2.Cells+1, vtk2.Points);
         DataColor = vtk1.PointData;
         %DataDots = 1000 * (max(vtk2.PointData) - vtk2.PointData);
         DataDots = vtk2.PointData;

         SamplePosColor = GeometryColor.X; %pretend sampled at every point
         SamplePosDots = GeometryDots.X; %pretend sampled at every point
         isVertexAtRim = [];

         hDg.loadInitialisation(GeometryColor, GeometryDots, DataColor, DataDots,
SamplePosColor, SamplePosDots, isVertexAtRim);
    end

    function loadInitialisation(hDg, GeometryColor, GeometryDots, DataColor, DataDots,
SamplePosColor, SamplePosDots, isVertexAtRim)
        % The contract is that this method must set the following
        % properties in DotGuiStatic:
        %   hDg.Mode
        %   hDg.SAMPLEPOSITIONSCOLOR
        %   hDg.DATASETCOLOR_processed
        %   hDg.DATASETCOLOR
        %   hDg.IsVertexAtRim
        %   hDg.DATASETDOTS_processed
        %   hDg.DATASETDOTS
        %   hDg.GeometryCOLOR
        %   hDg.GeometryDOTS
        % The following properties must also be set in DotMapRim
        %   hDM.MmScale

        % Store the geometry
        points = GeometryColor.X;
        Rx = rotationmatrix(pi/2, pi, pi/2);
        [points, divFactor, centre] = local_rotateScaleCentre(points, Rx);
        hDg.GeometryCOLOR = TriRep(GeometryColor.Triangulation, points);
        samplePointsColor = local_rotateScaleCentre(SamplePosColor, Rx, divFactor,
centre);

        points = GeometryDots.X;
        [points, ~, ~] = local_rotateScaleCentre(points, Rx, divFactor, centre); % use
previous divFactor and centre
        hDg.GeometryDOTS = TriRep(GeometryDots.Triangulation, points);
        samplePointsDots = local_rotateScaleCentre(SamplePosDots, Rx, divFactor, centre);

        % Store the size of 1 mm in the new coordinate system
        hDg.hDM.MmScale = 1/divFactor;
```

```
            % Store the raw datasets
            hDg.DATASETCOLOR = DataColor;
            hDg.DATASETDOTS = DataDots;

            % Store and threshold the voltage
            state = get(hDg.S.cbThreshold, 'value');
            switch state
                case 0
                    threshold = Inf;
                case 1
                    threshold = get(hDg.S.sbThreshold, 'value');
            end
            hDg.DATASETDOTS_processed =
local_thresholdVertexDataAndConvertToFaceData(hDg.DATASETDOTS, hDg.GeometryDOTS, threshold);

            % Store the valve orifices
            if ~isempty(isVertexAtRim)
                hDg.IsVertexAtRim = isVertexAtRim;
            else
                hDg.IsVertexAtRim = [];
            end

            % By default, colour faces according to DATASETCOLOR, show scar
            hDg.DATASETCOLOR_processed = hDg.DATASETCOLOR;
            hDg.SAMPLEPOSITIONSCOLOR = samplePointsColor;
            hDg.SAMPLEPOSITIONSDOTS = samplePointsDots;
            hDg.Mode = 'scar';
            set(gca, 'CameraPosition', [10 0 0]);

            hDg.updateDotMap();
        end

        % --- Helper function to update the state of the DotMap object
        function hDg = updateDotMap(hDg)

            % set the state of Threshold
            state = get(hDg.S.cbThreshold, 'value');
            switch state
                case 0
                    hDg.hDM.Threshold = 'off';
                case 1
                    hDg.hDM.Threshold = 'on';
            end
            hDg.hDM.ThresholdValue = get(hDg.S.sbThreshold, 'value');

            % display the threshold value
            thresholdValue = get(hDg.S.sbThreshold, 'Value');
            set(hDg.S.stThresholdValue, 'String', thresholdValue);

            % display the colorbar
            colorbar('off')
            caxis([min(hDg.DATASETCOLOR_processed) max(hDg.DATASETCOLOR_processed)]);
            colorbar('west');

            % factor to scale brightness and contrast by
            brightness = hDg.Brightness * 1.5;
            contrast = hDg.Contrast * 1.5;

            % Set the values in DotMapRim
            hDg.hDM.IsVertexAtRim = hDg.IsVertexAtRim;
            hDg.hDM.ColorMapType = hDg.ColorMapType;
            hDg.hDM.DATASETCOLOR = hDg.DATASETCOLOR_processed;
            hDg.hDM.SAMPLEPOSITIONSCOLOR = hDg.SAMPLEPOSITIONSCOLOR;
            hDg.hDM.SAMPLEPOSITIONSDOTS = hDg.SAMPLEPOSITIONSDOTS;
            hDg.hDM.GeometryDOTS = hDg.GeometryDOTS;
            hDg.hDM.GeometryCOLOR = hDg.GeometryCOLOR;
            switch hDg.Mode
                case 'scar'
                    hDg.hDM.DATASETDOTS = (hDg.DATASETDOTS_processed * 100 * brightness) .^
contrast;
                case 'uniform'
                    hDg.hDM.DATASETDOTS = (100 * brightness) ^ contrast;
            end
        end

        % % IMAGE CONTROL % %
        function pbhRotate_call(hDg, src, evt) %#ok<INUSD>
            fig = hDg.S.fh;
            ax = hDg.S.ax;
            set(fig, 'WindowButtonDownFcn', {@moveCamera1, fig, ax, 'down', 'rotate'});
        end
        function pbhZoom_call(hDg, src, evt) %#ok<INUSD>
```

```
            fig = hDg.S.fh;
            ax = hDg.S.ax;
            set(fig, 'WindowButtonDownFcn', {@moveCamera1, fig, ax, 'down', 'zoom'});
        end
        function pbhPan_call(hDg, src, evt) %#ok<INUSD>
            fig = hDg.S.fh;
            ax = hDg.S.ax;
            set(fig, 'WindowButtonDownFcn', {@moveCamera1, fig, ax, 'down', 'pan'});
        end

        % % INTENSITY CONTROL % %
        function cbThreshold_call(hDg, src, evt)
            state = get(src, 'value');
            switch state
                case 0
                    hDg.DATASETDOTS_processed =
local_thresholdVertexDataAndConvertToFaceData(hDg.DATASETDOTS, hDg.GeometryDOTS, Inf);
                    hDg.updateDotMap();
                case 1
                    threshold = get(hDg.S.sbThreshold, 'Value');
                    hDg.DATASETDOTS_processed =
local_thresholdVertexDataAndConvertToFaceData(hDg.DATASETDOTS, hDg.GeometryDOTS, threshold);
                    hDg.updateDotMap();
            end
        end

        function sbThreshold_call(hDg, src, evt) %#ok<INUSD>
            state = get(hDg.S.cbThreshold, 'value');
            switch state
                case 0
                    threshold = Inf;
                case 1
                    threshold = get(src, 'value');
            end
            hDg.DATASETDOTS_processed =
local_thresholdVertexDataAndConvertToFaceData(hDg.DATASETDOTS, hDg.GeometryDOTS, threshold);
            hDg.updateDotMap();
        end
        function sbBrightness_call(hDg, src, evt) %#ok<INUSD>
            hDg.Brightness = ( 2 * get(src, 'Value') );
            hDg.updateDotMap();
        end
        function sbContrast_call(hDg, src, evt) %#ok<INUSD>
            hDg.Contrast = ( 2 * get(src, 'Value') );
            hDg.updateDotMap();
        end

        % % SETUP CONTROL % %
        function tbSurface_call(hDg, src, evt) %#ok<INUSD>
            hSurfState = get(src,'Value');
            if hSurfState == get(src,'Max')
                set(hDg.hDM.hSurf, 'Visible', 'on'); % -- surface is off, turn it on
            elseif hSurfState == get(src,'Min')
                set(hDg.hDM.hSurf, 'Visible', 'off'); % -- surface is on, turn it off
            end
        end
        function tbDots_call(hDg, src, evt) %#ok<INUSD>
            hLineState = get(src,'Value');
            if hLineState == get(src,'Max')
                set(hDg.hDM.hLine, 'Visible', 'on'); % -- dots are off, turn them on
            elseif hLineState == get(src,'Min')
                set(hDg.hDM.hLine, 'Visible', 'off'); % -- dots are on, turn them off
            end
        end
        function hDg = bghMode_call(hDg, src, evt) %#ok<INUSL>
            switch get(evt.NewValue, 'Tag')
                case 'dotsUniform'
                    hDg.Mode = 'uniform';
                case 'dotsScar'
                    hDg.Mode = 'scar';
            end
            hDg.updateDotMap();
        end

        % Color selection callback
        function pumColor_call(hDg, src, evt) %#ok<INUSD>
            val = get(src, 'Value');
            switch val
                case 1
                    hDg.DATASETCOLOR_processed = hDg.DATASETCOLOR;
                    hDg.ColorMapType = 'activation';
                case 2
```

```
                    hDg.DATASETCOLOR_processed = hDg.DATASETDOTS;
                    hDg.ColorMapType = 'voltage';
            end
            hDg.updateDotMap();
        end

        function sbThreshCondVel_call(hDg, src, evt) %#ok<INUSD>
            threshCV = get(src, 'Value');
            hDg.CvData = local_getCondVelData(hDg.DATASETCOLOR, hDg.GeometryCOLOR, threshCV);
            hDg.DATASETCOLOR_processed = hDg.CvData;
            hDg.updateDotMap();
        end
        % OUTPUT CONTROL
        function pbhGraph_call(hDg, src, evt)
           figure
           voltage = trVertToFaceData(hDg.GeometryDOTS, hDg.DATASETDOTS);
           cv = 1./hDg.CvData;
           scatter(voltage, cv);
        end
    end
end %classdef

function fDataThresholded = local_thresholdVertexDataAndConvertToFaceData(vData, tr,
threshold)
% local_thresholdVertexDataAndConvertToFaceData thresholds the data and
%   converts from vertex
% to face data.
% Usage:
%   tData = local_thresholdVertexDataAndConvertToFaceData(data, threshold)
% Where:
%   voltage - is an m*1 matrix of scalar values indexing into points of the
%             triangulation, tr
%   tr - is a Trirep
%   threshold - is the threshold above which dataset is considered
%               normal (e.g. no scar) and no dots will be drawn.
%   tData - is the thresholded data
%
% ------------------------------------------------------------------
% code
% ------------------------------------------------------------------

disp(['size(vData)=' num2str(size(vData))]);
disp(['min(vData)=' num2str(min(vData))]);
disp(['max(vData)=' num2str(max(vData))]);

vDataThresholded = vData;
vDataThresholded(vDataThresholded>threshold) = max(vData);
vDataThresholded(vDataThresholded==0) = NaN;
vDataThresholded = scaleData(max(vDataThresholded)./vDataThresholded, [0 9]);
vDataThresholded(isnan(vDataThresholded)) = 0;
fDataThresholded = trVertToFaceData(tr, vDataThresholded);

disp(['size(fDataThresholded)=' num2str(size(fDataThresholded))]);
disp(['min(fDataThresholded)=' num2str(min(fDataThresholded))]);
disp(['max(fDataThresholded)=' num2str(max(fDataThresholded))]);

end

function tCv = local_getCondVelData(DATASETCOLOR, tr, threshold)
% LOCAL_GETCONDVELDATA thresholds the conduction velocity data.
% Usage:
%   tCv = local_getCondVelData(data, threshold)
% Where:
%   DATASETCOLOR - is an m*1 matrix of scalar values indexing into points of the
%              triangulation, tr
%   tr - is a Trirep
%   threshold - is the conduction velocity threshold above which no data is drawn.
%
% ------------------------------------------------------------------
% code
% ------------------------------------------------------------------
% [cvloc cvgrad] = trigrad(tr, DATASETCOLOR);
% cvvec = cvgrad - cvloc;
% [~, ~, cv] = cart2sph(cvvec(:,1), cvvec(:,2), cvvec(:,3));
% cv(cv>threshold) = NaN;
% cv(isnan(cv)) = max(cv);
% tCv = cv;
threshold = threshold/1000;
disp(threshold);

[loc, cv] = lat2condvel(tr, DATASETCOLOR, threshold);
tCv = abs(cv);
```

```
tCv(tCv>threshold) = NaN;

end


function [points, divFactor, centre] = local_rotateScaleCentre(points, Rx, varargin)
% LOCAL_ROTATESCALECENTRE adjusts image data input for DotGui.
% Usage:
%   points = local_rotateScaleCentre(points, Rx)
% Where:
%   points - is an m*3 matrix of x,y,z coordinates of the vertices
%   Rx - is the required rotation matrix
%   points - is returned as the output
%   mm - is the size of 1 mm in the new system
% LOCAL_ROTATESCALECENTRE is used to standardise image data input for
% DotGui. A rotation, Rx, is applied to ensure the image is presented AP.
% The image is scaled to unit size and centred on the origin.
%
% ------------------------------------------------------------------
% code
% ------------------------------------------------------------------
points = points * Rx;

if nargin>=3
    %divFactor has been passed in
    divFactor = varargin{1};
    centre = varargin{2};
else
    diff = max(points) - min(points);
    divFactor = max(diff);
end
points = points ./ divFactor;
if nargin<4
    centre = mean ([min(points); max(points)]);
end
points = bsxfun(@minus, points, centre);
end
```

File B-20. DotMapRim.m

```
classdef DotMapRim < hgsetget
%     ************************************************************************
%     * The contents of this package are copyright (c) King's College London
%     *
%     * They may not be reproduced, distributed, modified or sold for any
%     * purpose
%     *
%     * Author:     Dr S. E. Williams
%     * Address:    Division of Imaging Sciences and Biomedical Engineering,
%     *             King's College London
%     *             St Thomas' Hospital
%     *
%     * March 2014
%     ************************************************************************

    % DOTMAP objects describe dot maps and plot them on an axis.n
    %
    % Usage:
    %   hDM = DotMap(tr, sigInt);
    % Where:
    %   tr - is a TriRep object to be dot mapped
    %   sigInt - is the signal intensity. If sigInt is a scalar value,
    %       uniform dot intensity is used. If sigInt is an m*1 array (where
    %       tr.Triangulation is m*3) varied dot intensity is used.
    %   hDM - is a handle to the dot map
    %
    % DOTMAP detailed description.
    %
    % Author: Steven Williams (2012)
    % Modifications -
    %
    % Info on Code Testing:
    % ---------------------
    % test code
    % ---------------------
    %
    % Use warnings with the following format
    %    disp('DOTMAP: warning.')
    %
    % ------------------------------------------------------------------
```

```
    % code
    % ------------------------------------------------------------------

    properties (SetAccess = private, GetAccess = public)
        hDotAx
        hDotFig
        hLine
        hLine2
        hSurf
        hValve
        SigIntensity
        DataListener    % -- listens for GeometryDOTS or DATASETDOTS changes
        AxisListener    % -- listens for axis camera property changes

    end

    properties (SetObservable, AbortSet)
        % Can define PreSet/PostSet property listeners for these properties
        %OrigSigIntensity %has been changed to DATASETDOTS
        %VertexActTime %has been changed to DATASETCOLOR
        DATASETDOTS
        DATASETCOLOR
        GeometryDOTS
        GeometryCOLOR
        IsVertexAtRim
        SAMPLEPOSITIONSCOLOR
        SAMPLEPOSITIONSDOTS
        MmScale
        ColorMapType
        Threshold
        ThresholdValue
    end

    properties (SetAccess = private, GetAccess = public)
        points
        nT
        area
        tricentroids
        fn
        p1
        p2
        p3
        camDistOrigSq   % -- previous camera position (updated as camera moves)
        camDistStartSq  % -- starting camera position (never changes)
    end

    methods
        % Constructor
        function hDM = DotMapRim(tr, sigIntensity)
            % Assign data to instance variables
            hDM.GeometryDOTS = tr;
            hDM.DATASETDOTS = sigIntensity;

            hDM.hDotAx = gca();
            set(hDM.hDotAx ...
                , 'Visible' , 'off' ...
                , 'Color', [.6 .6 .6] ...
                , 'XColor','y' ...
                , 'YColor','y' ...
                , 'ZColor','y' ...
                , 'CameraTarget', [0 0 0] ...
                );
            axis(hDM.hDotAx, 'equal', 'vis3d');

            % Draw the dot map (one time only)
            hDM.hLine = line();

            platform = computer;
            switch platform(1)
                case 'P'
                    markersize = 1;
                otherwise
                    markersize = 1.5;
            end

            set(hDM.hLine ...
                , 'LineStyle', 'none' ...
                , 'Marker', 'o' ...
                , 'MarkerSize', markersize ...
                , 'MarkerEdgeColor', [1 1 1] ...
                , 'MarkerFaceColor', [1 1 1] ...
                );
```

```
            hDM.hSurf = patch('faces', [1 2 3] ...
                , 'vertices', [0 0 0; 0 0 0; 0 0 0] ...
                , 'facecolor', [0.1 0.7 0.3] ...
                , 'edgecolor', 'none' ...
                , 'facelighting', 'gouraud' ...
                , 'specularstrength', 0.2 ...
                , 'diffusestrength', 0.22 ...
                );

            % Draw the valve
            hDM.hValve = line();
            set(hDM.hValve ...
                , 'LineStyle', '-' ...
                , 'Color', 'r' ...
                , 'LineWidth', 2 ...
                );

            % During setup, provide the initial camDistOrigSq. Recorded
            % this for all time as camDistStartSq.
            camPosOrig = get(hDM.hDotAx, 'CameraPosition');
            camTarOrig = get(hDM.hDotAx, 'CameraTarget');
            hDM.camDistOrigSq = sum( (camPosOrig - camTarOrig).^2 );
            hDM.camDistStartSq = hDM.camDistOrigSq;

            % Perform the dot mapping calculations and update the line
            hDM.initialise();
            hDM.calcDotMap();

            % Set up the listener for anatomy changes
            propNamesAnatomy = {'GeometryDOTS', 'GeometryCOLOR', 'DATASETDOTS',
'DATASETCOLOR'};
            hDM.DataListener = addlistener(hDM, propNamesAnatomy ...
                , 'PostSet', @hDM.dataChanged);

            % Set up the listner for camera position changes
            propNamesCamera = {'CameraPosition','CameraTarget','CameraViewAngle'};
            hDM.AxisListener = addlistener(hDM.hDotAx, propNamesCamera ...
                , 'PostSet', @hDM.cameraMoved);
        end

        % INITIALISE() should be called if hDM GeometryDOTS or DATASETDOTS
        % properties have changed. INITIALISE() sets up the triangulation
        % parameters (nT, area, fn), the points arrays of X, Y and Z for
        % each simplex) and the signal intensity array (SigIntensity)
        function hDM = initialise(hDM)

            hDM.nT = size(hDM.GeometryDOTS.Triangulation);
            hDM.area = triarea(hDM.GeometryDOTS);
            hDM.fn = faceNormals(hDM.GeometryDOTS, (1:hDM.nT)');
            [~, hDM.tricentroids] = tricentroid(hDM.GeometryDOTS);

            hDM.p1 = hDM.GeometryDOTS.X(hDM.GeometryDOTS.Triangulation(:,1),:);
            hDM.p2 = hDM.GeometryDOTS.X(hDM.GeometryDOTS.Triangulation(:,2),:);
            hDM.p3 = hDM.GeometryDOTS.X(hDM.GeometryDOTS.Triangulation(:,3),:);

            %Generate the sigIntensity array if needed, or assign if passed
            disp(['size(hDM.DATASETDOTS)=' num2str(size(hDM.DATASETDOTS))]);
            disp(['min(hDM.DATASETDOTS)=' num2str(min(hDM.DATASETDOTS))]);
            disp(['max(hDM.DATASETDOTS)=' num2str(max(hDM.DATASETDOTS))]);

            if isscalar(hDM.DATASETDOTS)
                hDM.SigIntensity = repmat(hDM.DATASETDOTS, ...
                    [size(hDM.GeometryDOTS.Triangulation,1) 1]);
            else
                hDM.SigIntensity = hDM.DATASETDOTS;
            end

            % If camDisgStartSq and camDistOrigSq are different then camera
            % has moved from its starting position so adjust SigIntensity
            if round(hDM.camDistStartSq) == round(hDM.camDistOrigSq)
                return;
            else
                hDM.SigIntensity = hDM.SigIntensity .*
((hDM.camDistStartSq/hDM.camDistOrigSq));
            end

            %Update the surface
            % A field, originalPoints, is added to UserData for
            % compatibility with VisualizerAxis
            u.originalPoints = hDM.GeometryCOLOR.X .* 0.99;

            set(hDM.hSurf, 'faces', hDM.GeometryCOLOR.Triangulation ...
```

```
                , 'vertices', hDM.GeometryCOLOR.X .* 0.99 ...
                , 'userdata', u ...
                );

            DISTANCETHRESH = 10 * hDM.MmScale;
            t_min = min(hDM.DATASETCOLOR);
            t_max = max(hDM.DATASETCOLOR);

            switch hDM.Threshold
                case 'on'
                    switch hDM.ColorMapType
                        case 'voltage'
                            coloraxis = hDM.ThresholdValue;
                            colororder = 'reverse';
                        case 'activation'
                            coloraxis = [t_min t_max];
                            colororder = 'forward';
                    end
                case 'off'
                    switch hDM.ColorMapType
                        case 'voltage'
                            coloraxis = [t_min t_max];
                            colororder = 'reverse';
                        case 'activation'
                            coloraxis = [t_min t_max];
                            colororder = 'forward';
                    end
            end

            if ~isempty(hDM.SAMPLEPOSITIONSCOLOR)
            colorShell(hDM.hSurf, hDM.SAMPLEPOSITIONSCOLOR, hDM.DATASETCOLOR, DISTANCETHRESH
...
                , 'showcolorbar', 'show' ...
                , 'coloraxis', coloraxis ...
                , 'colororder', colororder ...
                , 'datatype', hDM.ColorMapType ...
                , 'interpolation', 'off' ...
            );
            end

            % draw a line around the valves
            if ~isempty(hDM.IsVertexAtRim)
                % make a local copy
                isVertexAtRim = hDM.IsVertexAtRim;

                e = edges(hDM.GeometryCOLOR);
                edgeIsRim = isVertexAtRim(e);
                edgeIsRim = edgeIsRim(:,1) & edgeIsRim(:,2);

                rimEdges = e(edgeIsRim,:);

                n = size(rimEdges,1);
                x = nan(3*n,1);
                y = nan(size(x));
                z = nan(size(x));

                for i = 0:(n-1);
                    loc1 = hDM.GeometryCOLOR.X(rimEdges(i+1,1),:);
                    loc2 = hDM.GeometryCOLOR.X(rimEdges(i+1,2),:);

                    x(3*i+1) = loc1(1);
                    y(3*i+1) = loc1(2);
                    z(3*i+1) = loc1(3);

                    x(3*i+2) = loc2(1);
                    y(3*i+2) = loc2(2);
                    z(3*i+2) = loc2(3);
                end
                set(hDM.hValve ...
                    , 'XData', x .* 0.99 ...
                    , 'YData', y .* 0.99 ...
                    , 'ZData', z .* 0.99 ...
                    , 'LineWidth', 3 ...
                    , 'Color', [0 64 0]/256 ...
                    , 'visible', 'on' ...
                    );

                pos = get(hDM.hDotAx, 'CameraPosition');
                va = get(hDM.hDotAx, 'CameraViewAngle');

                camva(va);
                campos(pos);
```

```
            else
                set(hDM.hValve, 'visible', 'off');
            end
        end

        % CALCDOTMAP() should be called if the hDM hDotAx camera properties
        % have changed. CALCDOTMAP() creates n random coordinates within
        % each triangle simplex of hDM.GeometryDOTS where n is a random integer
        % from the Poisson distribution with parameter lambda. Lambda is
        % weighted dependent on the triangle area and signal intensity for
        % that triangle. CALCDOTMAP() assigns the x, y and z values to the
        % hDM properties XData, yData and ZData.
        function hDM = calcDotMap(hDM)
            % Calculate number of dots per triangle using Poisson distribution
            lambda = hDM.area .* hDM.SigIntensity;
            nDots = poissrnd(lambda);

            maxDots = floor(hDM.area .* 200000);
            iTooMany = nDots>maxDots;
            if any(iTooMany)
                nDots(iTooMany) = maxDots(iTooMany);
                disp('Dot Numbers restricted')
            end

            activeTriangles = (1:hDM.nT)';

            % TODO: CHANGE TO SAMPLEPOSITIONSDOTS IN THIS BLOCK OF CODE
            if ~isempty(hDM.SAMPLEPOSITIONSDOTS)
                % remove triangles greater than DISTANCETHRESH
                DISTANCETHRESH = 10 * hDM.MmScale;
                % Find the shortest distance from every point in the surface to
                % the dataset pointcloud
                id = knnsearch(hDM.SAMPLEPOSITIONSDOTS, hDM.tricentroids);
                cPts = hDM.SAMPLEPOSITIONSDOTS(id,:); %c for closest
                d = distBetweenPoints(cPts, hDM.tricentroids);
                % Threshold based on the distance t
                thresholdDistance = ones(size(d));
                thresholdDistance(d>DISTANCETHRESH) = 0;
                activeTriangles = activeTriangles(logical(thresholdDistance));
                nDots = nDots(logical(thresholdDistance));
            end

            % remove triangles with no dots
            kInactive = (nDots<=0);
            activeTriangles(kInactive) = [];
            nDots(kInactive) = [];

            if isempty(nDots)
                set([hDM.hLine hDM.hLine2],    'XData', [] ...
                    , 'YData', [] ...
                    , 'ZData', [] ...
                    );
                return
            end

            cumNDots = cumsum(nDots);
            iStart = [ 1 ; 1+cumNDots(1:(end-1))];
            totalDots = cumNDots(end);

            % Now create a vector of length totalDots, where the value of
            % iDot2iTri(iDot) gives the ACTIVE triangle in which iDot lies,
            % i.e. iDot2iTri = [1 1 1 1 1  2 2 2 2 2 2 2  3 3 3 3  4 4 4 4
            % .... ] where the number of 1's is nDots(1), the number of 2's
            % is nDots(2) etc.
            iDot2iTri = zeros(totalDots,1);
            iDot2iTri(iStart) = 1;
            iDot2iTri = cumsum(iDot2iTri);

            % Now get back the original indices
            iDot2iTri = activeTriangles(iDot2iTri);

            % Create two vectors of random numbers in (0,1) for each dot
            p = rand(totalDots,1);
            q = rand(totalDots,1);
            sqP = sqrt( p ); % numel = totalDots

            % Calculate the set of random points for each triangle.
            k1 = 1 - sqP;
            k2 = sqP .* (1-q);      % k1,k2,k3 all have numel=totalDots
            k3 = q .* sqP;
```

```
            X = k1 .* hDM.p1(iDot2iTri,1)  +   k2 .* hDM.p2(iDot2iTri,1)  +  k3 .*
hDM.p3(iDot2iTri,1);
            Y = k1 .* hDM.p1(iDot2iTri,2)  +   k2 .* hDM.p2(iDot2iTri,2)  +  k3 .*
hDM.p3(iDot2iTri,2);
            Z = k1 .* hDM.p1(iDot2iTri,3)  +   k2 .* hDM.p2(iDot2iTri,3)  +  k3 .*
hDM.p3(iDot2iTri,3);

            % Set the XData, YData and ZData of hDM.hLine
            % A field, originalPoints, is added to UserData for
            % compatibility with VisualizerAxis
            u.originalPoints.x = X;
            u.originalPoints.y = Y;
            u.originalPoints.z = Z;
            set([hDM.hLine],    'XData', X ...
                , 'YData', Y ...
                , 'ZData', Z ...
                , 'UserData', u ...
                );
        end
    end

    methods (Static)
        % Called by the listener if GeometryDOTS or DATASETDOTS change
        function dataChanged(~, event)
            hDM = event.AffectedObject;

            hDM.initialise();
            hDM.calcDotMap();

        end
    end

    methods
        % Called by the listener if hDotAx camera properties change
        function cameraMoved(hDM, src, event) %#ok<INUSD>
            axis = hDM.hDotAx;

            %Calculate the new distance from the camera to the target
            camPosNew = get(axis, 'CameraPosition');
            camTarNew = get(axis, 'CameraTarget');
            camDistNewSq = sum( (camPosNew - camTarNew).^2 );

            %Work out if the distance has changed
            if round(hDM.camDistOrigSq) == round(camDistNewSq)
                return;
            else
                hDM.SigIntensity = hDM.SigIntensity * ((hDM.camDistOrigSq/camDistNewSq));
                hDM.calcDotMap();
                hDM.camDistOrigSq = camDistNewSq;
            end
        end
    end

end %classdef
```

File B-21. lat2condvel.m

```
function [loc, cv] = lat2condvel(tri, lat, threshold)
%     ************************************************************************
%     * The contents of this package are copyright (c) King's College London
%     *
%     * They may not be reproduced, distributed, modified or sold for any
%     * purpose
%     *
%     * Author:     Dr S. E. Williams
%     * Address:    Division of Imaging Sciences and Biomedical Engineering,
%     *             King's College London
%     *             St Thomas' Hospital
%     *
%     * March 2014
%     ************************************************************************

% LAT2CONDVEL returns the CV across a TriRep.
% Usage:
%   [loc condvel] = lat2condvel(tri, lat, threshold)
% Where:
%   tri - is the TriRep
%   lat - is the value of the LAT at each point in tri.X
%   threshold - the maximum conduction velocity possible
```

```
%   loc - contains the position at the centroid of each face in tri
%   cv - contains the conduction velocity at each point in loc
%
% LAT2CONDVEL converts local activation time (LAT) to conduction velocity
% (CV) using trigrad. Output units depends on the input units. If points in
% tri.X are described in meters and times in lat described in seconds then
% the units of cv are m/s.
%
% Author: Steven Williams (2012)
% Modifications -
%
% Info on Code Testing:
% ------------------------------------------------------------------
% test code
% ------------------------------------------------------------------
% % construct a linear trirep
% LENGTH = 200;
% %X = (-LENGTH/2:LENGTH-LENGTH/2) .* 0.1;
% X = (1:LENGTH) .* 0.1;
% for i = 1:LENGTH
%     iStart = i * 2 - 1;
%     iEnd = iStart + 1;
%     p(iStart:iEnd, 1) = X(i);
%     p(iStart,2) = 0;
%     p(iEnd,2) = 1;
% end
% p(:,3) = 0;
% for i = 1:LENGTH * 2 - 2
%    tri(i, :) = [i i+1 i+2];
% end
% tri = TriRep(tri,p);
%
% % Calculate the scalar field
% EXP = 1;
% K = 2;
% lat = K .* p(:,1) .^ EXP;
%
% % Calculate the gradient of the scalar field; convert to CV (x axis)
% [loc cv] = lat2condvel(tri, lat);
%
% % Plot the results
% subplot(4,1,1);
% trisurf(tri);axis equal vis3d;
% title('Surface');
%
% subplot(3,1,2);
% line(loc(:,1), lat(2:end-1));
% title(['Local Activation Time Field (x direction) t=s^' num2str(EXP)]);
% xlabel('Distance, s');ylabel('Time, t');
%
% subplot(3,1,3);
% line(loc(:,1),cv);
% title('Conduction Velocity (x direction) ds/dt = 1/dt/ds');
% xlabel('Distance, s');ylabel('Velocity, ds/dt');
%
% Use warnings with the following format
%    disp('MYFUNCTION: warning.')
%
% ------------------------------------------------------------------
% code
% ------------------------------------------------------------------

[loc, grad] = trigrad(tri,lat);
[~, ~, r] = cart2sph(grad(:,1), grad(:,2), grad(:,3));

cv = 1./r;
cv(cv>threshold) = threshold;
cv(isnan(cv)) = threshold;
end
```

File B-22. moveCamera1.m

```
function ret=moveCamera1(src, eventdata, hfig, haxes, arg, action) %#ok<INUSL>
%     ************************************************************************
%     * The contents of this package are copyright (c) King's College London
%     *
%     * They may not be reproduced, distributed, modified or sold for any
%     * purpose
%     *
```

```
%     * Author:     Dr S. E. Williams
%     * Address:    Division of Imaging Sciences and Biomedical Engineering,
%     *             King's College London
%     *             St Thomas' Hospital
%     *
%     * March 2014
%     ************************************************************************

% MOVECAMERA1 provides click to move functionality.
%
% Usage:
%   ret = moveCamera(src, eventdata, hfig, haxes, arg, action)
%
% Where:
%   src, event - mandatory inputs
%   hfig - handle to the figure containing the axis
%   haxes - handle to the axis for which the camera position is altered
%   arg - call with 'down'. Other options are for local calls only: 'motion', or 'up'
%   action - 'zoom', 'rotate' or 'pan'
%   ret - returns 1 after satisfactory completion
%
% MOVECAMERA provides a mechanism to access the camera toolbar functions
% through event listeners:
%   To move the camera forward/backward:-
%       set(fig, 'WindowButtonDownFcn', {@moveCamera1, fig, ax, 'down', 'zoom'});
%   To rotate the camera:-
%       set(fig, 'WindowButtonDownFcn', {@moveCamera1, fig, ax, 'down', 'rotate'});
%   To pan the camera:-
%       set(fig, 'WindowButtonDownFcn', {@moveCamera1, fig, ax, 'down', 'pan'});
% In this way, mouse movement is captured to control the desired function
% (rotate, zoom or pan). The event listeners could for example be called by
% pressing on a uicontrol or by listening in turn for mouse clicks.
%
% ------------------------------------------------------------------
% Examples:
% 1) Use the mouse buttons to control a figure. Use within another
% function.
%   % Set the WindowButtonDownFcn callback to respond to mouse clicks
%   set(fig, 'WindowButtonDownFcn', {@mouseButtonFcn, fig, ax});
%
%   function mouseButtonFcn(src, evt, fig, ax)
%       switch get(fig, 'selectiontype')
%           % left mouse button to rotate
%           case 'normal'
%               set(fig, 'WindowButtonMotionFcn', {@moveCamera1, fig, ax, 'down', 'rotate'})
%           % middle mouse button to pan
%           case 'extend'
%               set(fig, 'WindowButtonMotionFcn', {@moveCamera1, fig, ax, 'down', 'pan'})
%           % right mouse button to zoom
%           case 'alt'
%               set(hFig, 'WindowButtonMotionFcn', {@moveCamera1, hFig, hAx, 'down', 'zoom'})
%       end
%    end
% ------------------------------------------------------------------
%
% Author: Steven Williams (2013)
% Modifications -
%
% Use warnings with the following format
%    disp('MYFUNCTION: warning.')
%
% ------------------------------------------------------------------
% code
% ------------------------------------------------------------------

switch arg

    % Respond to WindowButtonDownFcn events. This is the only event that
    % should be called externally to this function. This section sets the
    % corresponding Up and Motion functions.
    case 'down'
        pt = hgconvertunits(hfig,[0 0 get(hfig,'CurrentPoint')], ...
            get(hfig,'Units'),'pixels',0);
        pt = pt(3:4);
        Udata.figStartPoint = pt;
        Udata.figLastPoint  = pt;
        Udata.moving = 0;
        Udata.coordsys = 'z';
        if strcmp(action, 'zoom')
            Udata.mode = 'dollyfb';
        elseif strcmp(action, 'rotate')
            Udata.mode = 'orbit';
```

```
        elseif strcmp(action, 'pan')
            Udata.mode = 'pan';
        end
        setUdata(hfig,Udata)
        %Set the WindowButtonUpFcn (call to self)
        set(hfig, 'WindowButtonUpFcn', {@moveCamera1, hfig, haxes, 'up'});
        %Set the WindowButtonMotionFcn (call to self)
        set(hfig, 'WindowButtonMotionFcn', {@moveCamera1, hfig, haxes, 'motion'} ...
            );

    case 'motion'
        Udata = getUdata(hfig);
        if isstruct(Udata)
            pt = hgconvertunits(hfig,[0 0 get(hfig,'CurrentPoint')],...
                get(hfig,'Units'),'pixels',0);
            pt = pt(3:4);
            deltaPix  = pt-Udata.figLastPoint;
            Udata.figLastPoint = pt;
            Udata.moving = 1;
            mode = lower(Udata.mode);
            setUdata(hfig,Udata)
            % Now perform the desired event from the rotation.
            switch mode
                case 'orbit'
                    orbitPangca(hfig,haxes,deltaPix, 'o');
                case 'pan'
                    orbitPangca(hfig,haxes,deltaPix, 'p');
                case 'dollyfb'
                    forwardBackgca(hfig,haxes,deltaPix, 'c');
            end
        end

    case 'up'
        Udata = getUdata(hfig);
        set(hfig,'WindowButtonMotionFcn','');
        Udata.moving = 0;
        pt = hgconvertunits(hfig,[0 0 get(hfig,'CurrentPoint')],...
            get(hfig,'Units'),'pixels',0);
        pt = pt(3:4);
        Udata.figLastPoint = pt;
        setUdata(hfig,Udata);

    otherwise
        error('MOVECAMERA:unrecognizedinput','Unknown action string.');

end
ret = 1;
end

function localDrawnow(hfig)
    % Calling drawnow will result in hang, see g201318
    Udata = getUdata(hfig);
    if feature('HGUsingMATLABClasses')
        drawnow update;
        return
    end
    if Udata.moving == 1
        drawnow;
    else
        drawnow expose
    end
end

function orbitPangca(hfig,haxes,xy, mode)
    %mode = 'o' -> orbit; mode = 'p' -> pan
    Udata = getUdata(hfig);
    coordsys = lower(Udata.coordsys);
    if coordsys(1)=='n'
        coordsysval = 0;
    else
        coordsysval = coordsys(1) - 'x' + 1;
    end
    xy = -xy;
    if mode=='p' %pan
        panxy = xy*camva(haxes)/500;
    end
    if coordsysval>0
        d = [0 0 0];
        d(coordsysval) = 1;
        up = camup(haxes);
        upsidedown = (up(coordsysval) < 0);
        if upsidedown
```

```
            xy(1) = -xy(1);
            d = -d;
        end
        % Check if the camera up vector is parallel with the view direction;
        % if not, set the up vector
        if any(crossSimple(d,campos(haxes)-camtarget(haxes)))
            camup(haxes,d)
        end
    end
    %while sum(abs(xy))> 0 && isstruct(Udata) && (flag || Udata.moving==1) &&
ishghandle(haxes)
    if Udata.moving==1
        %Udata = getUdata(hfig);
        if ishghandle(haxes)
            if mode=='o' %orbit
                if coordsysval==0 %unconstrained
                    camorbit(haxes,xy(1), xy(2), coordsys)
                else
                    camorbit(haxes,xy(1), xy(2), 'data', coordsys)
                end
            else %pan
                if coordsysval==0 %unconstrained
                    campan(haxes,panxy(1), panxy(2), coordsys)
                else
                    campan(haxes,panxy(1), panxy(2), 'data', coordsys)
                end
            end
            localDrawnow(hfig);
        end
    end
end

function forwardBackgca(hfig,haxes,xy, mode)
    q = max(-.9, min(.9, sum(xy)/70));
    if mode=='b'
        camdolly(haxes,0,0,q);
    else
        posOld = get(haxes,'CameraPosition');
        camdolly(haxes,0,0,q, 'f');
        %If the dolly puts us too close to the target, undo the move:
        dist = norm(get(haxes,'CameraPosition')-get(haxes,'CameraTarget'));
        if dist > 3.3316e+003 || dist < 0.4
            set(haxes,'CameraPosition',posOld);
        end
    end
    localDrawnow(hfig);
end

function Udata = getUdata(hfig)
    Udata = getappdata(hfig, 'ctb200jaz');
    % Since the camera toolbar IS NOT serialized by design, Udata will have
    % an invalid toolbar handle when opening a fig file since the figure
    % object, which IS serialized, stores the Udata.
    if isfield(Udata,'mainToolbarHandle') && ~any(ishghandle(Udata.mainToolbarHandle))
        Udata = [];
    end
end

function setUdata(hfig,Udata)
    setappdata(hfig, 'ctb200jaz', Udata);
end

% simple cross product
function c=crossSimple(a,b)
    c(1) = b(3)*a(2) - b(2)*a(3);
    c(2) = b(1)*a(3) - b(3)*a(1);
    c(3) = b(2)*a(1) - b(1)*a(2);
end
```

File B-23. scalarData.m

```
function [ newData ] = scaleData( data, limits )
%     ***************************************************************
%     * The contents of this package are copyright (c) King's College London
%     *
%     * They may not be reproduced, distributed, modified or sold for any
%     * purpose
%     *
%     * Author:     Dr S. E. Williams
```

```
%     * Address:    Division of Imaging Sciences and Biomedical Engineering,
%     *             King's College London
%     *         St Thomas' Hospital
%     *
%     * March 2014
%     ************************************************************************

%SCALEDATA performs linear scaling of a data series to the desired limits.
% Usage:
%   newData = scaleData(data, limits)
% Where:
%   data - is the input data series
%   limits - the desired bounds of the rescaled data series, [lower upper]
%
% SCALEDATA detailed description.
%
% Author: Steven Williams (2012)
% Modifications -
%
% Info on Code Testing:
% ---------------------
% test code
% ---------------------
%
% Use warnings with the following format
%    disp('SCALEDATA: warning.')
%
% ------------------------------------------------------------------
% code
% ------------------------------------------------------------------

% if the data has no range, return the data at max or min of limits
if nansum(diff(data))==0
    newData = data;
    if nanmin(data)>=limits(2)
        newData(~isnan(newData)) = limits(2);
    elseif nanmax(data)<=limits(1)
        newData(~isnan(newData)) = limits(1);
    end
    return;
end

% Scale the data onto [0 1]
n = (data - min(data(:))) / (max(data(:)) - min(data(:)));

% Scale the data onto range(limits)
n = n * range(limits);

% Start the data at limits(1)
newData = n + limits(1);

end
```

File B-24. trVertToFaceData.m

```
function [ faceData ] = trVertToFaceData( tr, vertexData )
%     ************************************************************************
%     * The contents of this package are copyright (c) King's College London
%     *
%     * They may not be reproduced, distributed, modified or sold for any
%     * purpose
%     *
%     * Author:     Dr S. E. Williams
%     * Address:    Division of Imaging Sciences and Biomedical Engineering,
%     *             King's College London
%     *             St Thomas' Hospital
%     *
%     * March 2014
%     ************************************************************************

% TRVERTTOFACEDATA converts vertex to face data for a TriRep object.
% Usage:
%   faceData = trVertToFaceData(tr, vertexData)
% Where:
%   tr - is a TriRep object with the following dimensions:
%           tr.Triangulation    q * 3
%           tr.X                p * 1
%   vertexData - is an p*1 array of scalar data (by vertex)
%   faceData - is a q*1 array of scalar data (by face)
```

```
%
% TRVERTTOFACEDATA detailed description.
%
% Author: Steven Williams (2012)
% Modifications -
%
% Info on Code Testing:
                        % ----------------------
                        % test code
                        % ----------------------
%
% Use warnings with the following format
%    disp('TRVERTTOFACEDATA: warning.')
%
% ------------------------------------------------------------------
% code
% ------------------------------------------------------------------

faceData = zeros(length(tr.Triangulation), 1);

for i = 1:length(tr.Triangulation);
    v1 = tr.Triangulation(i, 1);
    v2 = tr.Triangulation(i, 2);
    v3 = tr.Triangulation(i, 3);

    faceData(i) = mean([vertexData(v1) vertexData(v2) vertexData(v3)]);
end
```

File B-25. VTKReader.m

```
classdef VTKReader < hgsetget
%     ************************************************************************
%     * The contents of this package are copyright (c) King's College London
%     *
%     * They may not be reproduced, distributed, modified or sold for any
%     * purpose
%     *
%     * Author:     Dr S. E. Williams
%     * Address:    Division of Imaging Sciences and Biomedical Engineering,
%     *             King's College London
%     *         St Thomas' Hospital
%     *
%     * March 2014
%     ************************************************************************

% VTKREADER Reads VTK files.
% Usage:
%   hVTK = VTKReader(filename)
%   hVTK = VTKReader('openfile')
%
% Where:
%   a is the input
%   b is the output
%
% VTKREADER Methods:
%   readPoints
%   readPoly
%   readPointData
%   readCellData
%   readAllData
%
% Author: Steven Williams (2013)
% Modifications -
%
% Info on Code Testing:
% ------------------------------------------------------------------
% test code
% ------------------------------------------------------------------
%
% ------------------------------------------------------------------
% code
% ------------------------------------------------------------------

    properties
        Filename
        IndexPoint
        IndexPointData
        IndexCell
        IndexCellData
```

```
        IndexNormals
        Points
        PointNormals
        PointData
        Cells
        CellNormals
        CellData
    end

    methods

        function hVTK = VTKReader(filename)
            % CONSTRUCTOR loads and checks the file and populates the
            % indices
            if strcmpi(filename, 'openfile');
                [filename, pathname] = uigetfile('*.vtk', 'Select VTK file to open ...');
                filename = [pathname filename];
            end

            hVTK.Filename = filename;

            % Open the file
            [dataFileID, message] = fopen(hVTK.Filename, 'r');
            if dataFileID == (-1)
                disp('VTKREADER.M: There was a problem opening the file:')
                error(message)
            end

            % Check the file is a VTK file
            str = fgets(dataFileID);   % -1 if eof
            if ~strcmp(str(1:5), '# vtk')
                error('The file is not a valid VTK file.');
            end

            % Read the header and confirm that the dataset is POLYDATA
            str = fgets(dataFileID);
            str = fgets(dataFileID);
            str = fgets(dataFileID);
            if ~strcmp(str(9:16), 'POLYDATA')
                error('The file does not contain a polydata dataset');
            end

            % Scan the file finding indexes to the Points polygon, pointdata and celldata
sections
            fseek(dataFileID, 0, 'bof');

            %format = '%s %*[^\n]'; %read first word of each line
            format = '%s';

            %segarray = textscan(dataFileID,format);
            segarray = textscan(dataFileID, format, 'delimiter', '\n');

            for i = 1:size(segarray{1},1)
                firstSpace = regexpi(segarray{1}(i), ' ');

                if(size(firstSpace{1},1)==0)
                    firstSpace = length(segarray{1}{i}) + 1;
                else
                    firstSpace = firstSpace{1}(1);
                end

                holdingString = segarray{1}(i);
                holdingString = holdingString{1};

                word = holdingString(1:firstSpace-1);
                segarray{1}{i} = word;
            end

            identifiers = {'POINTS'
                'POLYGONS'
                'CELL_DATA'
                'POINT_DATA'
                'NORMALS'};

            for i = 1:5
                logical = strstartcmp(identifiers{i}, segarray{1});
                if sum(logical) == 1
                    index{i} = find(logical);
                elseif sum(logical) < 1
                    index{i} = NaN;
                    disp(strcat('VTKREADER: ', identifiers{i}, ' not found. NaN assigned to
index.'));
```

```
                elseif sum(logical) > 1 && i ~= 5
                    index{i} = NaN;
                    disp(strcat('VTKREADER: Multiple ', identifiers{i}, ' found. NaN assigned
to index.'));
                else
                    index{i} = find(logical);
                end


            end

            hVTK.IndexPoint = index{1};
            hVTK.IndexCell = index{2};
            hVTK.IndexCellData = index{3};
            hVTK.IndexPointData = index{4};
            hVTK.IndexNormals = index{5};

            % Close the file
            fclose (dataFileID);
        end

        function hVTK = readPoints(hVTK)
            if ~isnan(hVTK.IndexPoint)
                % Access a private external function to read the data
                [data,normals,dataCnt,normalsCnt] = readData('points' ...
                    , '%*s %d %*s' ...
                    , '%f %f %f' ...
                    , hVTK.IndexPoint ...
                    , hVTK.Filename ...
                    , 0 ...
                    , 3 ...
                    , true ...
                    , hVTK.IndexNormals ...
                    );
                data = reshape(data, 3, dataCnt/3);
                vertex = data.';
                % Assign the Points to the instance variable
                hVTK.Points = vertex;

                if normalsCnt~=0
                    normals = reshape(normals, 3, normalsCnt/3);
                    normals = normals.';
                    % Assign the normals data to the instance variable
                    hVTK.PointNormals = normals;
                end
            else
                hVTK.Points = [];
            end
        end

        function hVTK = readCells(hVTK)
            if ~isnan(hVTK.IndexCell)
                % Access a private external function to read the data
                [data,normals,dataCnt,normalsCnt] = readData('cells' ...
                    , '%*s %d %*d' ...
                    , '%*f %f %f %f' ...
                    , hVTK.IndexCell ...
                    , hVTK.Filename ...
                    , 0 ...
                    , 3 ...
                    , false ...
                    , hVTK.IndexNormals ...
                    );
                data = reshape(data, 3, dataCnt/3);
                polygon = data.';
                % Assign the Cells to the instance variable
                hVTK.Cells = polygon;

                if normalsCnt~=0
                    normals = reshape(normals, 3, normalsCnt/3);
                    normals = normals.';
                    % Assign the normals data to the instance variable
                    hVTK.CellNormals = normals;
                end
            else
                hVTK.Cells = [];
            end
        end

        function hVTK = readPointData(hVTK)
            if ~isnan(hVTK.IndexPointData)
                % Access a private external function to read the data
```

```
                [data,normals,dataCnt,normalsCnt] = readData('point data' ...
                    , '%*s %d' ...
                    , '%f' ...
                    , hVTK.IndexPointData ...
                    , hVTK.Filename ...
                    , 2 ...
                    , 1 ...
                    , false ...
                    , 0 ...
                    );
                data = reshape(data, 1, dataCnt);
                pointData = data.';
                % Assign the Cells to the instance variable
                hVTK.PointData = pointData;
            else
                hVTK.PointData = [];
            end
        end

        function hVTK = readCellData(hVTK)
            if ~isnan(hVTK.IndexCellData)
                % Access a private external function to read the data
                [data,normals,dataCnt,normalsCnt] = readData('cell data' ...
                    , '%*s %d' ...
                    , '%f' ...
                    , hVTK.IndexCellData ...
                    , hVTK.Filename ...
                    , 2 ...
                    , 1 ...
                    , false ...
                    , 0 ...
                    );
                data = reshape(data, 1, dataCnt);
                cellData = data.';
                % Assign the Cells to the instance variable
                hVTK.CellData = cellData;
            else
                hVTK.CellData = []
            end
        end

        function hVTK = readAllData(hVTK)
            readPoints(hVTK);
            readCells(hVTK);
            readPointData(hVTK);
            readCellData(hVTK);
        end

    end

end
```

File B-26. readData.m

```
function [data,normals,dataCnt,normalsCnt] = readData(dataName ...
                                            , indexFormat ...
                                            , dataFormat ...
                                            , filePosition ...
                                            , filename ...
                                            , offset ...
                                            , itemMultiplier ...
                                            , readNormals ...
                                            , indexNormals ...
                                             )
%     ********************************************************************
%     * The contents of this package are copyright (c) King's College London
%     *
%     * They may not be reproduced, distributed, modified or sold for any
%     * purpose
%     *
%     * Author:     Dr S. E. Williams
%     * Address:    Division of Imaging Sciences and Biomedical Engineering,
%     *             King's College London
%     *             St Thomas' Hospital
%     *
%     * March 2014
%     ********************************************************************

% @VTKREADER/READDATA is a helper method for objects of the class VTKReader
```

```
% which reads sections of data from a vtk file
%
% Usage:
%   Accessed only by objects of class VTKReader
%
% Where:
%   data - a column matrix of the read data
%   normals - a column matrix of the normals data
%   dataCnt - the number of entries in the column matrix of data
%   normalsCnt - the number of entries in the column matrix of normals
%   dataName - the name of the data that is being sought (only used for
%       error writing purposes
%   indexFormat - the format of the first line of the section (POINTS 28442
%       float would be described as %*s %d %*s), permitting the length of
%       the
%       section to be read from the VTK file
%   dataFormat - the format of the data in the section
%   filePosition - the line number that the section starts at
%   filename - the vtk file
%   offset - the number of lines to skip between section header and data
%   itemMultiplier - the number of data values per data item. For example a
%       triangular polygon would have itemMultiplier = 3 whilst a scaler
%       would have itemMultiplier = 1
%   readNormals - boolean to identify whether or not to read a NORMALS data
%   section immediately subsequent to the read data section

% Author: Steven Williams (2011)
% Modifications -

% Info on Code Testing:
% ------------------------------------------------------------------
%
% ------------------------------------------------------------------

% ------------------------------------------------------------------
% code
% ------------------------------------------------------------------
    % Open the file
    dataFileID = fopen(filename,'r');

    % Skip unwanted lines
    for i = 1:filePosition - 1
        fgetl(dataFileID);
    end

    % Get the section header and number of data items (nvert)
    if (~strcmp(indexFormat,'skip'))
        str = fgets(dataFileID);
        nvert = sscanf(str, indexFormat, 1);
    else
        nvert = 1;
    end

    % If necessary, skip lines between the header and the data
    while (offset~=0)
        fgetl(dataFileID);
        offset = offset - 1;
    end

    numDataItems = itemMultiplier * nvert;

    % Read the data
    [data,dataCnt] = fscanf(dataFileID, dataFormat, numDataItems);
    if dataCnt~=itemMultiplier*nvert
        warning(strcat('Problem reading :', dataName));
    end

    % Read the normals

    if (readNormals)

        fseek(dataFileID,0,'bof');

        if numel(indexNormals) == 0
            normals = 0;
            normalsCnt = 0;

        elseif numel(indexNormals) == 1 && strcmp(dataName, 'cells')
            normOffset = indexNormals(1);
            while (normOffset~=0)
                fgetl(dataFileID);
                normOffset = normOffset - 1;
```

```
            end
            % read data
            [normals,normalsCnt] = fscanf(dataFileID, '%f %f %f', numDataItems*3);
            if normalsCnt~=itemMultiplier*nvert
                warning(strcat('Problem reading :', dataName, ': NORMALS'));
            end

        elseif numel(indexNormals) == 1 && strcmp(dataName, 'points')
            normals = 0;
            normalsCnt = 0;

        elseif numel(indexNormals) == 2 && strcmp(dataName, 'cells')
            normOffset = indexNormals(1);
            while (normOffset~=0)
                fgetl(dataFileID);
                normOffset = normOffset - 1;
            end
            % read data
            [normals,normalsCnt] = fscanf(dataFileID, '%f %f %f', numDataItems*3);
            if normalsCnt~=itemMultiplier*nvert
                warning(strcat('Problem reading :', dataName, ': NORMALS'));
            end

        elseif numel(indexNormals) == 2 && strcmp(dataName, 'points')
            normOffset = indexNormals(2);
            while (normOffset~=0)
                fgetl(dataFileID);
                normOffset = normOffset - 1;
            end
            % read data
            [normals,normalsCnt] = fscanf(dataFileID, '%f %f %f', numDataItems*3);
            if normalsCnt~=itemMultiplier*nvert
                warning(strcat('Problem reading :', dataName, ': NORMALS'));
            end

        end
    else
        normals = 0;
        normalsCnt = 0;
    end

    % Close the file
    fclose(dataFileID);
end
```

Appendix C. Awards, Presentations and Publications

Awards

Young Investigator Award (Shortlisted), Heart Rhythm Congress, Birmingham, 2014

Innovation Poster Presenter, Heart Rhythm Society Scientific Sessions, Denver, 2013

Oral presentations

Williams SE, *et al*. High Accuracy Unipolar Activation Time Assignment to Facilitate Dense Multipolar Electrode Mapping. Heart Rhythm Congress, Birmingham, 2013.

Williams SE, *et al*. CMR Characterization of Linear Ablation Lesions with Varying Contact Force – a Chronic Porcine Model. Heart Rhythm Congress, Birmingham, 2014.

Williams SE, *et al*. Optimized Local Activation Time Sampling Density for Left Atrial Electroanatomic Mapping. Heart Rhythm Congress, Birmingham, 2014.

Williams SE, *et al*. Ripple Mapping to Assess Atrial Tachycardia. Heart Rhythm Society, Boston, 2012.

Williams SE, *et al*. Low Force vs. High Force Atrial RF Ablation in a Chronic Porcine Model: Effective Lesion Assessment by Voltage, Pathology and Cardiac MR. Heart Rhythm Society, Boston, 2015.

Poster presentations

Williams SE, *et al*. Bipolar Voltage Cut-Offs For Identifying Post-Ablation Atrial scar are Different at Acute and Chronic Time-Points. Cardiostim, Nice 2014.

Williams SE, *et al*. Cardiac Magnetic Resonance of Atrial Ablation Injury: Impact of Catheter-Myocardium Contact Force. SCMR, San Francisco, 2014.

Williams SE, *et al*. Dot Mapping: A Novel Method to Display Multiple Parameters on a Single Electroanatomical Chamber Model. Heart Rhythm Congress, Birmingham, 2013.

Williams SE, *et al*. In Vivo Method for Determining Patient-Specific Atrial Electrical Conductivities and Fiber Orientation. Heart Rhythm Congress, Birmingham, 2013.

Williams SE, *et al*. Abnormal Electrogram Populations are Revealed by Atrial Programmed Stimulation in Paroxysmal Atrial Fibrillation. Heart Rhythm Congress, Birmingham, 2014.

Williams SE, *et al*. High Accuracy Unipolar Local Activation Time Assignment to Facilitate Accurate Dense Multipolar Electrode Mapping. Heart Rhythm Society, Denver, 2013

Williams SE, *et al*. Dot Mapping: A Novel Method to Display Multiple Parameters on a Single Electroanatomical Chamber Model. Heart Rhythm Society, Denver, 2013

Williams SE, *et al*. RealTime Positional Adjustment of Electroanatomical Models to Improve Spatial Perception and Catheter Localization. Heart Rhythm Society, Denver, 2013

Williams SE, *et al*. Optimized Atrial Local Activation Time Sampling Density and Technique. Heart Rhythm Society, San Francisco, 2014.

Williams SE, *et al*. Pace-Capture Defined Bipolar Voltage Thresholds for Identifying Post-Ablation Scar. Heart Rhythm Society, San Francisco, 2014.

Williams SE, *et al*. CMR Characterisation of Linear Ablation Lesions with Varying Contact Force – A Porcine Model. Heart Rhythm Society, San Francisco, 2014.

Williams SE, *et al*. Voltage and Pace-Capture Mapping of Linear Ablation Lesions Overestimate Chronic Gap Size. Heart Rhythm Society, Boston, 2014.

Publications

Williams SE *et al*. The Effect of Contact Force in Atrial Radiofrequency Ablation: Electroanatomical, Cardiovascular Magnetic Resonance and Histological Assessment in a Chronic Porcine Model. JACC Clin Electrophysiol 2015; 1(5): 421-431.

Williams SE *et al*. Quantitative Assessment of the Effects of Therapeutic Hypothermia on Early Repolarization in Idiopathic Ventricular Fibrillation Survivors: A 7-Year Cohort Study. Circ Arrhythmia Electrophysiol 2014; 7(1): 120-6.

Williams SE *et al*. Ectopy and Supraventricular Tachycardia: Is There a Relationship. Pacing Clin Electrophysiol 2013; 36(4): 497-500.

Patents

WO application 2014132080. Williams SE *et al.* Method and System for Overlaying Images or Data. Published 2014-09-04. Assigned to King's College London.